
UNIVERSITY OF LIVERPOOL

Department of Electrical Engineering & Electronics

# Electron diagnostics of magnetron discharges

Thesis submitted in accordance with the requirements of the University of Liverpool for the degree of Doctor in Philosophy by

**Peter John Ryan**

September 2019

## Abstract

The magnetron is a weakly magnetised plasma source used for physical vapour deposition to produce high-quality thin films and coatings for technological applications. In this research, electron plasma property measurements were performed in conventional DC magnetron discharges and in high power impulse magnetron sputtering (HiPIMS) discharges. The two main topics of this thesis are: (i) a comparison of electron plasma property measurements made by Langmuir probe and incoherent laser Thomson scattering, and (ii) an investigation of electron dynamics in HiPIMS discharges using a combination of incoherent laser Thomson scattering and optical emission spectroscopy.

Electrons are responsible for driving many important processes in low temperature discharge plasmas, such as, plasma heating, ionisation and plasma chemistry. The Langmuir probe is commonly employed to measure electron plasma properties, but its data can be difficult to interpret, especially from magnetised plasma. The aim of the first part of the research was to assess the accuracy of electron plasma property measurements made by Langmuir probes in weakly magnetised plasma, by comparing the results from the probe measurements with reliable results obtained via laser Thomson scattering. Standard unmagnetised theories were used to interpret the probe data. The range of magnetic field strength, electron temperature and electron density in the study were $1 \lesssim B[\mathrm{mT}] \leqslant 33$, $0.1 \leqslant T_e[\mathrm{eV}] \leqslant 5.9$ and $4 \times 10^{16} \leqslant n_e[\mathrm{m}^{-3}] \leqslant 7 \times 10^{19}$, respectively.

The results showed that there was good agreement between the diagnostics during the pulse-on time of HiPIMS at all of the measurement positions. This is a significant outcome because previous Langmuir probe studies were, in general, restricted to regions where electron magnetisation was insignificant due to the difficulty of interpreting probe data and concerns over plasma perturbation. In contrast, large discrepancies were observed for the lower-density DC magnetron mode, even when the magnetic field strength was insignificant for electron magnetisation. For some discharge conditions, the electron density determined by laser Thomson scattering was over an order of magnitude greater than the plasma density obtained by the Langmuir probe, using both ion and electron collection theories. In addition, the low energy part of the electron energy distribution function determined by the probe was depleted at all of the measurement positions for the DC mode. The possible reasons for the discrepancies are discussed, with the conclusion being that the plasma was significantly perturbed by the probe stem.

HiPIMS discharges have a high ionisation fraction of sputtered atoms in the deposition

flux, which leads to improved film properties. Previous investigations have reported reliable electron plasma properties for only isolated spatial regions of the discharge. The aim of the second part of the research was to perform a comprehensive survey of electron dynamics in HiPIMS discharges. Electron plasma properties were measured using laser Thomson scattering, and optical emission spectroscopy provided information about excited atomic and ionic states. The combination of these two diagnostics gives an insight into the electron-heavy species interactions occurring in the plasma. The results were consistent with a dense ($n_e > 10^{19}$ m$^{-3}$), metal-rich plasma propagating along the axial direction from the magnetic trap region to a typical substrate position. The main outcomes from this research were experimental confirmation of the expected features of HiPIMS discharges using the reliable laser Thomson scattering technique, and validation of trends identified in previous Langmuir probe studies at a typical substrate position. Therefore, the results provide a solid foundation for the understanding of electron dynamics in HiPIMS.

## Publications

The research in this thesis has, so far, led to the following peer-reviewed publications:

1. **Ryan, P. J.**, Bradley, J. W., Bowden, M. D. Comparison of Langmuir probe and laser Thomson scattering for electron property measurements in magnetron discharges. *Physics of Plasmas* **26**, 073515 (2019). **Collections: Editor's Pick**. [1]

2. **Ryan, P. J.**, Bradley, J. W., Bowden, M. D. Comparison of Langmuir probe and laser Thomson scattering for plasma density and electron temperature measurements in HiPIMS plasma. *Physics of Plasmas* **26**, 040702 (2019). [2]

## Conferences

1. **Ryan, P. J.**, Bradley, J. W., Bowden, M. D. Comparison of Thomson scattering and Langmuir probe for electron property measurements in HiPIMS plasma. 10th International Conference on Fundamentals and Industrial Applications of HIPIMS, Braunschweig, Germany (2019). **Oral presentation**.

2. **Ryan, P. J.**, Bradley, J. W., Bowden, M. D. Plasma Parameter Determination in a HiPIMS Discharge Using Laser Thomson Scattering. 46th International Conference on Metallurgical Coatings and Thin Films, San Diego, USA (2019). **Oral presentation**.

3. Smith, M., **Ryan, P. J.**, Bryant, P. M. Langmuir probe RF compensation in low temperature plasmas. 46th IOP Plasma Physics Conference, Loughborough, UK (2019). **Poster**.

4. **Ryan, P. J.**, Bradley, J. W., Bowden, M. D. Comparison of Thomson scattering and Langmuir probe for electron property measurements in a DC magnetron plasma. 45th EPS Conference on Plasma Physics, Prague, Czech Republic (2018). **Poster**.

## Acknowledgements

I would like to express my gratitude and appreciation to my supervisor Dr Mark Bowden for the opportunity to conduct this research, and for his guidance and support throughout the project. In addition, I would like to thank Prof James Bradley for many useful discussions about magnetron physics, Dr Paul Bryant for sharing his Langmuir probe expertise, the staff of the electronics workshop and Mr Gareth Blacoe of the mechanical workshop for helping to build/fix equipment and answering my questions, and the staff in stores for their help.

Moreover, I would like to thank everyone who helped to make my time at the University of Liverpool an enjoyable experience, both on and away from campus. This includes my office mates, members of the lunchtime group, workers in the laboratories, companions on trips to conferences, and friends from outside of university.

Finally, I would like to thank my family for their love and encouragement during this PhD.

# Contents

# List of Figures

# List of Tables

# Symbols and abbreviations

## Symbols (SI units)

| | |
|---|---|
| $A_f$ | surface area of magnetic flux surface ($m^2$) |
| $A_{ul}$ | Einstein coefficient for spontaneous emission ($s^{-1}$) |
| $\mathbf{B}$; $B$ | magnetic field vector; magnitude (T) |
| $c$ | speed of light in vacuum ($2.99792458 \times 10^8$ $m \cdot s^{-1}$) |
| $c_s$ | ion sound speed ($m \cdot s^{-1}$) |
| $C_s$ | sheath capacitance (F) |
| $e$ | electron charge ($1.60217662 \times 10^{-19}$ C) |
| $\mathbf{E}$; $E$ | electric field vector; magnitude ($V \cdot m^{-1}$) |
| $E_l$ | lower energy level (J) |
| $E_{iz}$ | ionisation energy (J) |
| $E_u$ | upper energy level (J) |
| $h$ | Planck constant ($6.62607004 \times 10^{-34}$ J·s) |
| $i_d$ | displacement current (A) |
| $I$ | current (A), intensity of line emission (normalised units) |
| $I_d$ | discharge current (A) |
| $J_D$ | discharge current density ($A \cdot m^{-2}$) |
| $J_H$ | Hall current density ($A \cdot m^{-2}$) |
| $J_z$ | axial current density ($A \cdot m^{-2}$) |
| $J_\phi$ | azimuthal current density ($A \cdot m^{-2}$) |
| $k_B$ | Boltzmann constant ($1.38064852 \times 10^{-23}$ $J \cdot K^{-1}$) |
| $\mathbf{k}_i; k_i$ | incident wavevector in laboratory frame; magnitude ($m^{-1}$) |
| $\mathbf{k}_s; k_s$ | scattered wavevector in laboratory frame; magnitude ($m^{-1}$) |
| $\mathbf{k}$; $k$ | $\mathbf{k}_s - \mathbf{k}_i$; magnitude ($m^{-1}$) |
| $l_p$ | Langmuir probe tip length (m) |
| $L_B$ | distance parallel to the magnetic field from the measurement position to the target surface (m) |
| $n$ | number density ($m^{-3}$) |

| | |
|---|---|
| $n_{c,P}, n_{w,P}$ | Langmuir probe determined electron densities for a bi-Maxwellian electron velocity distribution function ($m^{-3}$) |
| $n_{c,T}, n_{w,T}$ | laser Thomson scattering determined electron densities for a bi-Maxwellian electron velocity distribution function ($m^{-3}$) |
| $n_{D,P}$ | Langmuir probe determined electron density using the Druyvesteyn method ($m^{-3}$) |
| $n_e$ | electron density ($m^{-3}$) |
| $n_{e,P}$ | Langmuir probe determined electron density ($m^{-3}$) |
| $n_{e,T}$ | laser Thomson scattering determined electron density ($m^{-3}$) |
| $n_i$ | ion density ($m^{-3}$) |
| $n_{i,P}$ | Langmuir probe determined ion density ($m^{-3}$) |
| $n_0$ | ground state number density of an atomic or ionic species ($m^{-3}$) |
| $m_e$ | electron mass (kg) |
| $m_i$ | ion mass (kg) |
| $P1, P2, P3$ | reference to the scattering geometry (defined in section 4.3.4) |
| $r$ | radial position from the centre of the magnetron (m) |
| $r_{g,e}$ | electron gyroradius (m) |
| $r_{g,i}$ | ion gyroradius (m) |
| $r_p$ | Langmuir probe tip radius (m) |
| $R_{ex}$ | excitation rate coefficient ($m^3 \cdot s^{-1}$) |
| $t$ | time (s) |
| $T_{c,P}, T_{w,P}$ | Langmuir probe determined electron temperatures for a bi-Maxwellian electron velocity distribution function (K) |
| $T_{c,T}, T_{w,T}$ | laser Thomson scattering determined electron temperatures for a bi-Maxwellian electron velocity distribution function (K) |
| $T_e$ | electron temperature (K) |
| $T_{e,P}$ | Langmuir probe determined electron temperature (K) |
| $T_{e,T}$ | laser Thomson scattering determined electron temperature (K) |
| $T_i$ | ion temperature (K) |
| $v_R$ | relative velocity magnitude ($m \cdot s^{-1}$) |
| $V$ | voltage (V) |
| $V_d$ | discharge voltage (V) |
| $V_f$ | floating potential (V) |
| $V_p$ | plasma potential (V) |
| $W_R$ | kinetic energy in the centre of mass frame (J) |
| $Y_{SS}$ | self-sputtering yield |
| $z$ | axial position from the magnetron surface (m) |
| $\Delta\lambda$ | $\lambda - \lambda_i$ (m) |
| $\epsilon_0$ | permittivity of free space ($8.85418782 \times 10^{-12}$ $F \cdot m^{-1}$) |
| $\lambda$ | wavelength (m) |

| | |
|---|---|
| $\lambda_D$ | Debye length (m) |
| $\lambda_i$ | laser wavelength in laboratory frame (m) |
| $\lambda_{me}$ | electron mean free path (m) |
| $\lambda_{mi}$ | ion mean free path (m) |
| $\lambda_{OML}$ | radial distance from the probe axis where an ion has its last collision and just grazes the probe's surface (m) |
| $\lambda_s$ | scattered wavelength in laboratory frame (m) |
| $\sigma$ | cross-section ($m^2$) |
| $\sigma_H$ | Hall conductivity ($S{\cdot}m^{-1}$) |
| $\sigma_P$ | Pedersen conductivity ($S{\cdot}m^{-1}$) |
| $\tau$ | decay timescale (s) |
| $\tau_e$ | electron momentum-exchange collision time (s) |
| $\tau_{n1}, \tau_{n2}$ | short- and long-term electron density exponential decay constants (s) |
| $\tau_{T1}, \tau_{T2}$ | short- and long-term electron temperature exponential decay constants (s) |
| $\omega_{g,e}$ | angular frequency of an electron's gyration in a magnetic field ($rad{\cdot}s^{-1}$) |

## Abbreviations

| | |
|---|---|
| ABR | Allen, Boyd and Reynolds |
| APD | avalanche photodiode |
| ECR | electron cyclotron resonance |
| EEDF | electron energy distribution function |
| EVDF | electron velocity distribution function |
| HiPIMS | high power impulse magnetron sputtering |
| iCCD | intensified charge-coupled device |
| ICP | inductively coupled plasma |
| IPVD | ionised physical vapour deposition |
| IRM | ionisation region model |
| JET | Joint European Torus |
| LIDAR | light detection and ranging |
| Nd:YAG | neodymium-doped yttrium aluminum garnet |
| OES | optical emission spectroscopy |
| OML | orbital motion limited |
| PIC | particle in cell |
| QE | quantum efficiency |
| SNR | signal-to-noise ratio |
| TGS | triple grating spectrometer |

# Chapter 1

# Introduction

This thesis is concerned with electron diagnostics of magnetron discharges [3] - a weakly magnetised, low temperature plasma source. Magnetron discharges are one of the most versatile and widely used methods of thin film and coating deposition in industry for technological applications. In this study, the magnetron was operated in two different regimes: a DC mode and a high-power pulsed-DC mode known as high power impulse magnetron sputtering (HiPIMS). The two main research topics are: (i) a diagnostic comparison study of electron plasma property measurements made by Langmuir probe and laser Thomson scattering in both DC and HiPIMS modes, and (ii) an investigation of electron dynamics in HiPIMS using a combination of laser Thomson scattering and optical emission spectroscopy. This chapter provides a basic introduction to the research aims of this thesis, which are stated in section 1.5. The thesis outline follows in section 1.6.

## 1.1 General introduction to plasma

The term plasma was coined by Langmuir in 1928 to describe a reactive mixture of ions, electrons and neutral species [4]. A plasma is generated when energy is transferred to a gas, and some or all of the bound electrons are excited above the ionisation level. The required ionisation energy significantly exceeds the average kinetic energy of a gas atom or molecule in the Earth's atmosphere, and so naturally occurring plasmas are far more common in astronomical bodies where temperatures reach millions of degrees Kelvin [5, p. 2].

An important property of a plasma is that it exhibits collective behaviour as a result of

the long-range electromagnetic force dominating over short-range gas kinetics. A plasma acts to reduce the spatial extent of an electric field induced by a charge perturbation by the process of Debye shielding. The Debye length ($\lambda_D$) characterises the decay of the electric potential from the charge perturbation to the shielded plasma. Consequently, on length scales $\gg \lambda_D$, the net electric field is approximately zero and the plasma is regarded as 'quasineutral'; but on length scales $\lesssim \lambda_D$, space-charge effects are important.

The most fundamental parameters for characterising a plasma are the particle density ($n_\star$) of each species ($\star = e, i, n$ for electrons, ions and neutrals, respectively) and their effective temperature ($T_\star$). Many types of man-made plasma sources have been developed to exploit different ranges and combinations of density and temperature for a variety of applications. Magnetic confinement devices for controlled thermonuclear fusion, such as tokamaks and stellarators, generate high temperature plasmas ($T_e > 1$ keV), which are fully ionised ($n_e, n_i \gg n_n$) and close to thermal equilibrium ($T_e \approx T_i$). The range of plasma density is $n_e = 10^{19} - 10^{21}$ m$^{-3}$ [6, p. 42]. On the other hand, low temperature plasmas ($T_e < 10$ eV) generated using electrical discharges for technological applications, are usually weakly ionised ($n_e, n_i \ll n_n$) and non-thermal.[1] The ion and neutral temperatures remain close to room temperature with the electron temperature significantly higher ($T_e \gg T_i, T_n \approx 300$ K), and the range of plasma density is $n_e = 10^{14} - 10^{25}$ m$^{-3}$ [7, pp. 8–9].

Low temperature plasmas generated at atmospheric pressure have chemistry related applications because the frequent collisions between charged particles and neutrals raises the chemical reactivity of the, often molecular, background gas. Examples include the removal of cells from biological tissue without thermal damage [8] and polymer surface modification [9]. Operation at low pressure is more expensive because of the vacuum system requirement; however, the plasma content can be precisely controlled and longer mean free paths in the system enable electrons/ions to obtain higher energies in an electric field before scattering. These low pressure sources are used for plasma etching, deposition, and surface modification [7]. Applications of these plasma processing techniques include the microelectronic fabrication of integrated circuits, and the production of coatings/thin films with specialised mechanical, optical and electrical properties [10].

[1] Although atmospheric arc discharges ($n_e \leqslant 10^{25}$ m$^{-3}$, $T_e = 0.1 - 2$ eV) satisfy $T_n \approx T_i \lesssim T_e$ [7, p. 8].

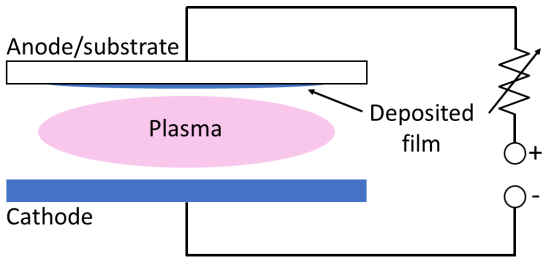


Figure 1.1: Schematic of a DC diode discharge. The cathode is sputtered by plasma ions and the sputtered atoms condense onto the anode/substrate.

## 1.2 Low pressure electrical discharges

Low pressure electrical discharges use electric fields to 'breakdown' an insulating gas into the conducting plasma state and produce a discharge current. Discharges that utilise DC or pulsed-DC (kHz) electric fields drive a conduction current, whereas radio-frequency sources (MHz) are dominated by displacement currents via capacitive/inductive coupling of the plasma to the electrodes. In either case, the input power is most efficiently transferred to the electrons, due to their greater mobility in the applied electric field compared to the ions; thus, non-thermal plasma is typically generated.

A simple discharge consists of a DC potential difference ($V_d$) across two parallel plate electrodes and a resistor in series to limit the current, as shown in figure 1.1. This configuration is called the DC diode discharge. These discharges are initiated by electron avalanches, whereby a cascade of electron impact ionisation is induced by a single electron as it drifts towards the anode. The initial seed electrons are supplied by an external source, such as photoionisation by a cosmic ray. A requirement for an electron avalanche is that the average gain of kinetic energy by an electron, between collisions with neutrals, must exceed the ionisation energy threshold. The relatively slow drifting ions do not significantly contribute to the ionisation process directly, but they cause secondary electron emission from the cathode surface, which then act as seeds for electron avalanches. The evolution of the breakdown phase is dependent on the type of gas, the gas pressure, the anode-cathode separation distance, the applied voltage and the resistor value [11, p. 15]. A self-sustaining discharge is generated if the average number of secondary electrons generated per drifting secondary electron is greater than or equal to one.

The resistor value and the supplied voltage determines the steady-state operating regime of a self-sustaining discharge after the breakdown phase [11, p. 3]. In the 'glow

discharge' regime ($V_d \sim 500$ V and an ion current density of $J_i \sim 10^{-5} - 10^{-3}$ A·cm$^{-2}$ [7, p. 538]), there is a strong electric field in the space-charge layer, or 'sheath', adjacent to the cathode surface, which causes ion (electron) acceleration towards (away) from the cathode surface. This electric field is much stronger than the electric field in the bulk plasma and in the anode sheath. The energisation of secondary electrons in the cathode sheath is an important process for sustaining the discharge because these electrons have enough kinetic energy to directly ionise the background gas, and they can also transfer their energy to the lower-energy electron population in the plasma bulk leading to subsequent ionisation. Another consequence of sheath formation is that energetic ion bombardment on the cathode causes the ejection of atoms from the surface via the process of sputtering [12]. The cathode is slowly eroded away and redeposited onto all surfaces inside the chamber; hence, this constitutes a basic plasma deposition device where the anode also serves as the substrate. Furthermore, the gas composition in the chamber can be manipulated so that the sputtered atoms participate in specific chemical reactions as they travel towards the substrate.

The main disadvantage of the DC diode discharge for plasma deposition[2] is the low deposition rate [7, p. 559]. This is caused by the low plasma density ($n_e \leqslant 10^{16}$ m$^{-3}$), and hence low sputtering rate; and the high background gas pressure ($\sim 5$ Pa), which is required to ignite the discharge, but it causes scattering of the sputtered atoms inside the chamber. The deposition rate, however, can be improved by using an external magnetic field to enhance the confinement of the plasma so that the discharge can be ignited at lower pressure. This is the design philosophy of the magnetron discharge. Furthermore, magnetic fields enable resonant electron heating in helicon discharges (MHz) and electron cyclotron resonance discharges (GHz) [7, p. 18][13]. In general, the magnetic field strength is sufficient to only strongly confine electrons, rather than the heavier ions, in plasma sources used for technological applications. This is referred to as weakly magnetised plasma.

## 1.3 The importance of free electrons

The energetic electrons produced in low pressure electrical discharges are responsible for driving many processes: ionisation through electron impact, heavy particle electronic (de)excitation, plasma diffusion, and plasma chemistry. Consequently, knowledge of the

[2]DC diode discharges are usually operated in the abnormal glow regime to achieve commercially viable deposition rates [7, p. 559], where $V_d \sim 2 - 5$ kV and $J_i \gtrsim 1$ mA·cm$^{-2}$.

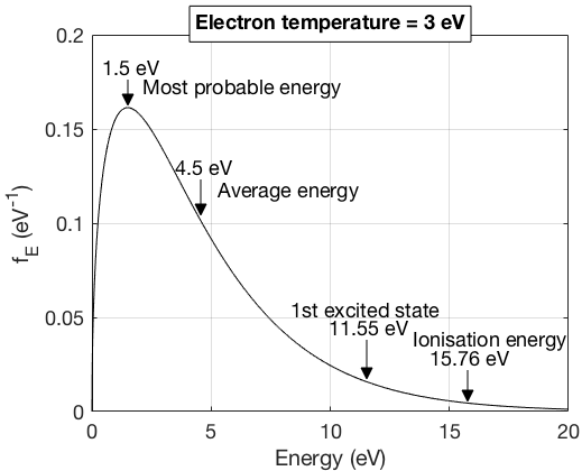


Figure 1.2: Electron energy probability distribution function for $T_e = 3$ eV with the first excitation and ionisation energy of argon gas labelled.

electron properties is essential for any discharge physics investigation. The electron energy distribution function (EEDF) is an important parameter to measure because it contains information about the relative abundance of each electron energy in the plasma and the total electron density is found by integrating over all energies. The EEDF of an electron population in thermodynamic equilibrium is given by the Maxwellian energy distribution, which is characterised by $n_e$ and $T_e$ [7, p. 36]. Elastic collisions (kinetic energy is conserved) between electrons are responsible for thermalising the energy input by the applied electric field, and so this drives the EEDF towards a Maxwellian shape.

The main energy loss mechanism for the EEDF is inelastic collisions (kinetic energy is not conserved) with heavier species because the transfer of kinetic energy during elastic collisions is inefficient due to the large mass difference. The energy threshold for inelastic collisions, however, is relatively high compared to the average electron energy in a low temperature plasma. This is demonstrated by figure 1.2, which shows a Maxwellian EEDF for the case of $T_e = 3$ eV, with the inelastic collision energy threshold (11.55 eV) and ionisation energy (15.76 eV) of argon gas - a typical inert background gas used for plasma processing - labelled. Therefore, collisions between electrons and heavier species result in more efficient energy loss from the high-energy tail of the EEDF.

To summarise, the shape of the EEDF describes the balance of electron heating, thermalisation and energy loss. A Maxwellian EEDF is expected when the electron-electron

collision frequency dominates over the electron power absorption and loss timescales.

## 1.4 Electron diagnostics

A frequently employed electron diagnostic for low temperature plasmas is the single Langmuir probe, where a small metal electrode is inserted into the plasma and the current is monitored as the probe voltage is swept. The experimental procedure is relatively straightforward and the resultant current-voltage characteristic contains localised information about several electron plasma parameters (e.g. $n_e$, $n_i$, $T_e$, and EEDF). The main limitations are that the probe is intrusive and data interpretation is difficult, especially in magnetised plasma conditions.

Spectroscopic techniques are non-intrusive options for electron property measurements. The most simple technique is optical emission spectroscopy (OES), which measures the intensity and shape of line emission from excited heavy species in the plasma. However to extract $n_e$ and $T_e$, an elaborate collisional-radiative model describing electronic transitions may be required. Furthermore, OES is a line-of-sight measurement so the diagnostic suffers from poor spatial resolution unless tomographic techniques, such as Abel inversion [14], are implemented.

Microwave interferometry can be used to determine $n_e$. The underlying principle is that the phase shift of an electromagnetic wave after passing through a plasma is dependent on $n_e$. The main advantages of the technique are that it is non-intrusive and data interpretation is reasonably straightforward. The disadvantages are that it is a line-of-sight measurement, like OES, so only a line-integrated electron density is determined; and the experimental setup is more complicated and expensive than that required for probe and OES measurements.

Laser Thomson scattering is the elastic scattering of laser radiation from free electrons in the plasma. In the incoherent regime, the scattering spectrum is proportional to the electron velocity distribution function; therefore, a Thomson scattering spectrum has the advantage of simple data interpretation which is independent of the plasma conditions (e.g. gas pressure and magnetic field strength). In addition, the measurement is localised and non-intrusive. The main disadvantages are that a complicated and expensive experimental system is required, and weak scattering signals must be detected for measurements in a typical discharge plasma.

## 1.5 Scope of this thesis

The aims of the two main research topics are discussed separately below.

### 1.5.1 Comparison of Langmuir probe and laser Thomson scattering for electron plasma property measurements in magnetron discharges

Magnetised Langmuir probe theory is notoriously difficult; consequently, a complete theory has never been developed despite the wide spread use of weakly magnetised technological plasma sources. The aim of this research was to assess the reliability of a cylindrical Langmuir probe for measurements of $n_e$, $T_e$ and EEDF using unmagnetised probe theories in weakly magnetised plasma. The plasma source for the experiments was a planar magnetron operated using separate DC and HiPIMS power supplies in order to access a wide range of plasma conditions: $0.1 \leqslant T_e[\mathrm{eV}] \leqslant 5.9$, $4 \times 10^{16} \leqslant n_e[\mathrm{m}^{-3}] \leqslant 7 \times 10^{19}$, in addition to, a magnetic field strength of $1 \lesssim B[\mathrm{mT}] \leqslant 33$ and an argon gas pressure of $0.47 - 2.53$ Pa.

A laser incoherent Thomson scattering system was designed and installed to act as the reference diagnostic for the study. This diagnostic was chosen over OES and microwave interferometry because laser Thomson scattering allows determination of both electron temperature and electron density, it has good spatial resolution, and it has simple data interpretation which is independent of the magnetic field strength.

It should be emphasised that the focus of the research in this section was comparing the results obtained using the diagnostics, rather than investigating the magnetron discharge physics.

### 1.5.2 Investigation of electron dynamics in HiPIMS discharges using laser Thomson scattering and optical emission spectroscopy

A high instantaneous discharge power is generated during high power impulse magnetron sputtering (HiPIMS) through the application of short DC pulses to the cathode at a low repetition frequency. This produces a dense plasma that is able to ionise a large fraction of the sputtered atoms, in contrast to DC magnetron operation. Consequently, a significant fraction of the deposition flux is ionised and this leads to improved film properties [15]. A detailed understanding of electron dynamics throughout the discharge are essential for optimising the deposition process; however, relatively few experimental studies have

investigated the strongly magnetised cathode region within the last closed magnetic flux surface boundary due to the non-compatibility of standard laboratory diagnostics. The aim of the research in this section was to provide a comprehensive overview of the electron dynamics by performing laser Thomson scattering measurements at various spatial locations, including inside and outside of the last closed flux surface boundary, for a variety of non-reactive HiPIMS discharge conditions. In addition, optical emission spectroscopy measurements were performed to provide information about the plasma composition, and hence electron-heavy species interactions.

## 1.6 Thesis outline

The outline of this thesis is as follows: chapter 2 contains a review of the relevant background literature, which includes Langmuir probe operation in magnetised plasma, laser Thomson scattering applied to low temperature plasma sources, and DC magnetron and HiPIMS physics; chapter 3 summarises the theories that were implemented to extract plasma density, electron temperature and EEDF from experimental data acquired via Langmuir probe and laser Thomson scattering measurements; chapter 4 is concerned with the experimental setup and diagnostic operation, including the procedures for data acquisition and analysis; chapter 5 contains the results from the comparison of electron plasma property measurements made by Langmuir probe and laser Thomson scattering in HiPIMS discharges; the results in chapter 6 extend the diagnostic comparison study to the lower-density DC magnetron mode; chapter 7 details the results from the investigation of electron dynamics in HiPIMS discharges using a combination of laser Thomson scattering and optical emission spectroscopy; and finally, a summary of the research presented in this thesis, conclusions, future work suggestions and outlook are given in chapter 8.

# Chapter 2

# Review of background

The goal of this chapter is to motivate the two main research aims of this thesis and to situate the research within the wider context of the literature. The literature review is split into three sections: Langmuir probe operation and difficulties in magnetised plasmas, incoherent laser Thomson scattering applied to low temperature plasmas, and magnetron physics including the DC and high power impulse magnetron sputtering (HiPIMS) modes.

## 2.1 Langmuir probe

This section of the literature review is organised as follows: (1) a basic introduction to Langmuir probe physics; (2) previous comparison studies of electron property measurements made by probes and non-intrusive diagnostics in non-magnetised discharges; and finally, (3) the difficulties of probe operation in magnetised plasma and previous experimental work in this regime.

### 2.1.1 Basics

Langmuir probe operation is a relativity simple experimental technique with a long history of use since the foundations of probe theory were developed by Irving Langmuir in the 1920's [16, 17]. The most common design for a single Langmuir probe is a small metal electrode, known as the probe tip (cylindrical, planar or spherical geometry in order of prevalence), inserted into the plasma using an electrically isolated probe stem, and the current drawn by the tip is recorded as the applied voltage is swept with respect to the

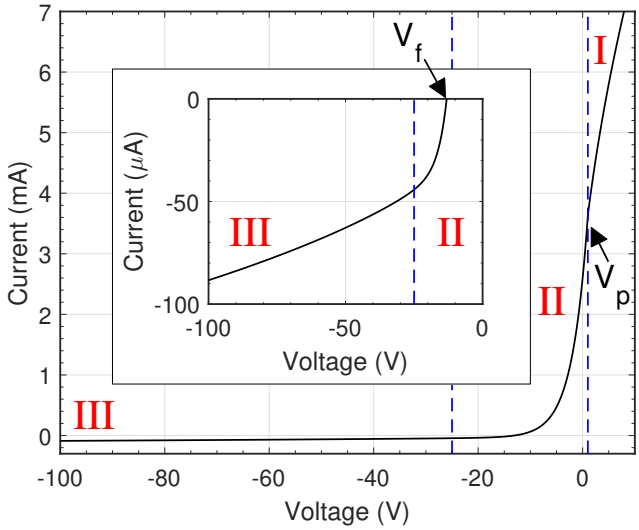


Figure 2.1: Example of a theoretical Langmuir probe current-voltage characteristic. Three regions on the curve are highlighted: (I) electron saturation, (II) electron retardation and (III) ion saturation. The insert shows a zoomed view of the ion saturation region.

electric potential of the conducting vacuum chamber. The space-charge layer, or electrostatic sheath, surrounding the tip during the voltage sweep varies in terms of spatial extent, electric field strength and electric field polarity. Consequently, the sheath impedance, and hence the probe current, varies significantly. An example of a theoretical current-voltage ($IV$) curve is shown in figure 2.1. By convention a positive current corresponds to electron collection and a negative current for ion collection. The curve is split into three sections and these are denoted as (I) electron saturation, (II) electron retardation and (III) ion saturation. A qualitative description of the three regions is given below with respect to the information they contain about the plasma parameters. The quantitative details of the probe theories employed in this research are given in section 3.1.

**I. Electron saturation ($V \geqslant V_p$)**

The electron saturation current is obtained when the applied probe bias is positive with respect to the electric potential of the plasma ($V_p$). Electrons entering the sheath surrounding the probe tip are accelerated towards the probe while ions are repelled. The probe current is dominated by the electron contribution because ions move at much slower

speeds due to their greater mass. Furthermore, in low temperature plasmas, the ion population is approximately at room temperature so most of the ions do not reach the probe when it is biased above $V - V_p \gtrsim 0.1$ V. The increase of the electron current with probe voltage is due to sheath expansion effects. A theory can be employed to calculate electron density ($n_e$) from this region, but caution must be taken not to significantly perturb the plasma by depleting it of electrons [18, p. 183][19, p. 91][20]. In addition, the large electron current can heat the probe tip leading to thermionic emission. This heating, however, is useful for probe tip cleaning by evaporating contaminants from the surface in between measurements.

The plasma potential is identified by the inflection point of the characteristic (known as the 'knee'). At this potential there is no sheath surrounding the probe tip, so the probe collects the sum of the electron and ion thermal currents. Ideally there will be a distinct knee feature, but in practice, the knee can become rounded by plasma potential oscillations and magnetic field effects [21], which introduces uncertainty in the plasma potential measurement. The current collected at the plasma potential is dominated by the electron contribution, as explained above, and can be used to calculate electron density, given that the electron temperature ($T_e$) is known. This procedure is referred to as the knee method.

**II. Electron retardation** ($V_f \lesssim V < V_p$)

For $V < V_p$, the electron collection is retarded and ions are attracted to the probe. As the magnitude of the probe bias increases, a larger fraction of the electron population does not reach the probe. For the case of a Maxwellian electron energy distribution function (EEDF) the electron current decay is exponential, with a slower decay for a higher electron temperature. Eventually the electron and ion currents are equal in magnitude at a specific voltage called the floating potential ($V_f$). At $V < V_f$, only the high energy tail of the EEDF is sampled, and so the probe current becomes dominated by the ion contribution. The electron retardation region can be used to calculate $T_e$ and the EEDF.

**III. Ion saturation** ($V_p - V \gg k_B T_e/e$)

The much smaller ion current dominates the characteristic when a strongly negative potential is applied because the majority of the electron population is unable to reach the surface of the probe. The magnitude of the ion current increases as the probe bias becomes increasingly negative due to sheath expansion effects. The ion saturation current can be

used to calculate ion density ($n_i$), and hence electron density through quasineutrality. Often this is the preferred method of calculating the plasma density because drawing a net ion current is less perturbing compared to the electron current collected near (and beyond) the plasma potential [18, p. 183][19, p. 91]; moreover, ions are less affected by magnetic fields. However, a disadvantage is that collisions with the background gas are more frequent for ions, and so a complicated collisional model may be required [21, 22].

The two main approaches for interpreting the ion saturation region from cylindrical probe measurements in low pressure conditions are to either assume that the ions transverse the probe sheath radially by following the electric field lines, or alternatively, consider the effects of ion orbital motion, which acts to impede collection. The solution to the collisionless radial motion problem with the ion temperature set to zero ($T_i = 0$) was given by Allen, Boyd and Reynolds (ABR) in 1957 for a spherical probe [23], and was extended to cylindrical geometry in 1965 by Chen [24]. On the other hand, the numerical calculations by Laframboise in 1966 [25] remains the most sophisticated orbital motion theory for collisionless conditions to date. The collisionless radial and orbital motion theories predict similar ion currents (for a given density) when the probe operates in the thin sheath regime; defined as $r_p/\lambda_D \gg 1$. In this limit, ions are collected by the probe before significant orbital motion occurs due to the short spatial extent of the sheath relative to the probe radius. Furthermore, the effect of ion collisions in the probe sheath are less important because the ion mean free path is longer relative to the spatial extent of the sheath. In the thick sheath regime, $r_p/\lambda_D < 3$, Laframboise theory tends to the orbital motion limited (OML) theory [17], which predicts a smaller ion current than ABR-Chen theory.

Langmuir probe usage is generally restricted to low density and low temperature plasmas, or short time periods in more hostile environments, to avoid rapid erosion and thermionic emission. In addition to electrical discharges, other examples of probe diagnosis include, weakly magnetised space plasmas where the satellite body acts as the reference electrode for the voltage sweep [26] and the edge region of magnetic confinement fusion devices [27]. Clearly there are a wide range of possible plasma conditions in which probes can operate, and so specialised theories, which are sometimes complicated, have been developed since there is no complete theory. The choice of probe theory depends on many parameters/factors [18, 19], for example: $T_e$ and $T_i$; plasma density; neutral gas density; magnetic field strength ($B$), the $B$-field orientation with respect to the probe, and the cross-magnetic field transport rate; Debye length; plasma flow rate and direction with

respect to the probe; and the probe tip geometry and dimensions. Unfortunately some of these parameters are unknown *a priori* to the probe analysis, unless another diagnostic or simulation is employed, so it can be difficult to select the most appropriate theory.

Despite the problematic interpretation of probe data and the intrusive nature of the measurement, they remain a popular diagnostic because their operation is straightforward, the measurement (in theory) is localised, and they are relatively inexpensive to construct.

### 2.1.2 Comparison with non-intrusive diagnostics in non-magnetised discharges

This section reviews previous diagnostic comparison studies in non-magnetised discharges, involving a Langmuir probe and a non-intrusive diagnostic, for electron property measurements. Most of these investigations have either used microwave interferometry or laser Thomson scattering as the reference diagnostic for assessing the accuracy of the probe determined parameters. The results from these studies are discussed separately below. Details of the particular probe theories employed to calculate electron density are not given because they usually have good agreement with one another, but the choice of ion collection theory is important so these are stated. Moreover, unless stated, the probe was not in the plasma during the measurements by the non-intrusive diagnostic.

#### 2.1.2.1 Microwave interferometry

In general, the agreement between microwave interferometry and Langmuir probe for plasma density measurements is good (e.g. within a factor of $\sim 2$ [28–31]) when the mean free path of the electrons and ions is long compared to the probe sheath thickness. When this condition was not satisfied for ions, Sudit *et al.* [32] found that the ion density from OML theory was up to an order of magnitude greater than both the microwave interferometry measurement and the electron density inferred from the probe. This was attributed to destruction of ion orbital motion in the probe sheath by collisions, and hence inducing radial motion. The ABR-Chen theory for ion collection had better agreement with the electron density determined by the probe. When measurements were performed in a denser region of the plasma, the ion density using Laframboise theory had excellent agreement with the probe determined electron density because the probe sheath thickness, relative to the ion mean free path, was reduced. Similar results were reported by Shih and Levi [33], where they found good agreement between Laframboise theory and

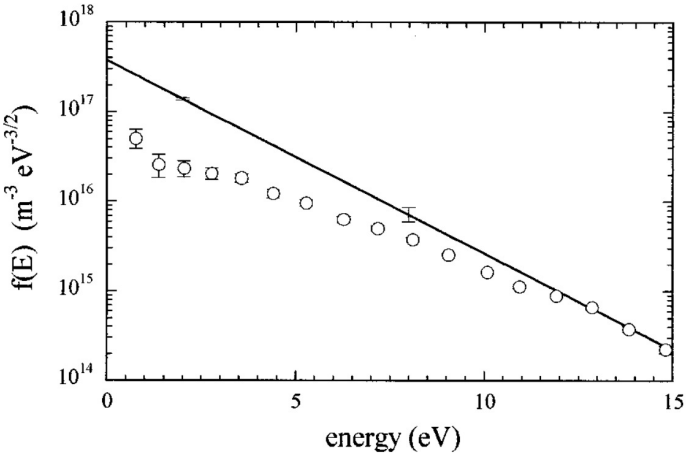


Figure 2.2: Comparison of the EEDF obtained using laser Thomson scattering (line) and Langmuir probe (open circles) in an ICP with 2.67 Pa of argon gas and 500 W RF power. Reproduced from Bowden *et al.* [35].

microwave interferometry only when the probe was operating outside of the thick sheath OML regime. In contrast, Overzet and Hopkins [34] found that the microwave interferometry measurements were up to an order of magnitude greater than the electron and ion densities obtained by the probe using Laframboise theory, when the ion mean free path was smaller than the probe radius. The probe was speculated to be significantly perturbing the plasma.

#### 2.1.2.2 Laser Thomson scattering

There have been several comparison studies using laser Thomson scattering in inductively coupled plasma (ICP) sources [35–37]. This type of low pressure discharge produces a high plasma density ($n_e \sim 10^{17} - 10^{18}$ m$^{-3}$), which implies long electron and ion mean free paths for collisions with neutrals relative to the probe sheath thickness. In general, the electron densities determined via laser Thomson scattering were larger than the values calculated from the probe measurements by a factor of $\leqslant 2$, and the effective electron temperature results were similar or the probe returned temperature values slightly higher ($\sim 25\%$ higher in Noguchi *et al.* [37]). The EEDF measurements, however, were significantly different; an example from the study by Bowden *et al.* [35] is shown in figure 2.2. The Thomson scattering spectrum was consistent with a Maxwellian EEDF (indicated by a straight line on these axes), whereas the probe determined EEDF was non-Maxwellian with a significant

depletion of low energy electrons. Furthermore, laser Thomson scattering measurements performed with a probe inserted into the plasma [35] found that the presence of the probe reduced the electron density inferred from laser Thomson scattering by a factor of $\sim 2$, but the shape of the EEDF was unaltered. For these experiments, the detection volume was located 15 mm from the probe tip; therefore, the probe sheath did not overlap with the Thomson scattering measurement position. It should be noted that the electric bias of the probe tip was not explicitly stated in the paper (e.g. the probe tip could have been floating or a voltage ramp applied); however, measurements were also performed when only a probe stem was inserted (i.e. no probe tip). The electron density reduction in both cases was similar, which implies that the plasma perturbation due to the probe stem was significant.

### 2.1.3 Probe operation in magnetised plasma

This part of the review is concerned with Langmuir probe measurements in magnetised plasma. Firstly, a general introduction about the effect of a magnetic field on charged particle transport is presented; followed by the qualitative effect on the probe $IV$ characteristic and the resultant errors for determining plasma parameters using unmagnetised theories; next, the main mechanisms included in the incomplete magnetised probe theories are summarised with the aim of explaining why the unmagnetised theories become erroneous; and finally, relevant experimental investigations, including diagnostic comparison studies, are reviewed.

#### 2.1.3.1 Charge transport in a magnetic field

Magnetic fields are used to increase the confinement time of charged particles before being lost to the chamber walls. This is advantageous for low pressure ignition of discharges and increasing the plasma density. A magnetic field produces a force on a charged particle that is always perpendicular to its velocity, so no work is done. The net result in a uniform magnetic field is gyroscopic motion, where the particle undergoes circular motion in the cross-magnetic field plane and motion parallel to the field is unaffected. The gyroradius is given by:

$$r_{g,\star} = \frac{m v_{\perp}}{qB}, \tag{2.1}$$

where $m$ is the particle mass, $v_\perp$ is the component of velocity perpendicular to the magnetic field, $q$ is electric charge, $B$ is the magnetic field strength and $\star = e(i)$ for electrons (ions). A particle is considered magnetised when its gyroradius is small relative to the dimensions of the overall plasma.

At $B = 10$ mT, a typical magnetic field strength in processing plasmas, the gyroradius of a 15.76 eV electron (equal to the argon gas ionisation energy - an inert gas commonly used for plasma processing) is $r_{g,e} \sim 1$ mm so the electron is well confined perpendicular to the magnetic field. In contrast, a room temperature argon ion has a gyroradius of $r_{g,i} \sim 15$ mm, so the ion is more weakly confined. The ion population, however, is effectively at the electron temperature due to ambipolar diffusion parallel to the magnetic field [7, p. 90]: an electric field develops to ensure electrons and ions diffuse at the same rate to maintain quasineutrality. When this is taken into account, the ion gyroradius becomes $r_{g,i} \sim 100$ mm assuming $T_e = 1$ eV, and so the ions are not well confined. This regime is referred to as weakly magnetised plasma.

To first order, the influence of a magnetic field on probe measurements depends on the size of the gyroradius relative to the probe collection length scales: $r_{g,\star}/r_p$ and $r_{g,\star}/\lambda_D$, where the parameters are much greater than unity in the limit of $B \to 0$. It is common for researchers to justify that unmagnetised probe theory is valid when these parameters are greater than unity (e.g. [38–40]), but this approach does not consider the global plasma perturbation caused by the probe. The main difficulty of magnetised probe theory is modelling cross-magnetic field transport, which is necessary for calculating the plasma equilibrium when the probe is inserted and drawing current from the plasma. Often the classical model of cross-magnetic field diffusion [7, p. 149], based on a random-walk collisional process, is inapplicable due to anomalous transport mechanisms. An example is the DC magnetron discharge, where the electron cross-magnetic field transport rate was inferred to be significantly faster than the prediction of classical diffusion [41, 42]. Moreover, it is difficult to model ambipolar diffusion in magnetised plasma because it is dependent on the size and geometry of the vacuum chamber [5, p. 161]: quasineutrality can be maintained by non-ambipolar diffusion perpendicular to the magnetic field by a slight adjustment of the electron and ion fluxes parallel to the magnetic field [43]. In low temperature, weakly magnetised plasma there is a larger disparity for the fluxes of 'free' electrons and ions parallel to the magnetic field compared to across the magnetic field. In general, there is always an ambipolar electric field parallel to the magnetic field.

#### 2.1.3.2 Effect on current-voltage characteristic

The transport anisotropy induced by the magnetic field has the effect of reducing the current collected by the probe. This is demonstrated by the reduction of the electron to ion saturation current ratio on the probe $IV$ characteristic [27, 44] because electrons are 'more' magnetised than ions. This leads to electron density underestimation when using unmagnetised theory and, if operating in the strong field regime ($r_{g,i}/r_p \lesssim 1$), the ion density as well.

Another problem is depletion of the low energy part of the EEDF determined by the probe, which corresponds to a greater reduction of electron current in the vicinity of the plasma potential compared to the floating potential region of the $IV$ characteristic [45]. Therefore, the probe determined EEDF will appear non-Maxwellian when the actual EEDF is Maxwellian, which makes it difficult to assign an electron temperature to the characteristic. In general, the electron temperature inferred from the probe is overestimated [46].

A final point is that the magnetic field causes rounding of the knee feature on the probe characteristic which makes it difficult to identify the plasma potential [21]. Accurate plasma potential measurements are required for several reasons: the plasma potential defines the zero energy point of the EEDF (explained in section 3.1.3.3), and so an error in the value of the plasma potential is most significant for the low energy region of the EEDF; calculating electron density using the knee method; and $V_p$ is a parameter required for several ion collection theories (see section 3.1.4). Anyhow, a distinct knee feature might not be representative of the plasma potential without the probe inserted because the probe can significantly drain the magnetic flux tubes intersecting it, and thereby perturb the plasma potential.

#### 2.1.3.3 Magnetised probe theory

A complete probe theory for magnetised plasma has never been formulated because of the difficulty of modelling cross-magnetic field transport. Nevertheless several magnetised probe theories, but for specific discharge conditions (e.g. thin or thick probe sheath), have been developed. Furthermore, some of these theories cannot be implemented without an estimation of the cross-magnetic field transport rate. In this section, several of these theories are discussed with the aim of explaining the main observations reported in section 2.1.3.2; namely, electron current reduction and electron temperature overestimation.

**Electron current reduction**

The theoretical foundation of a cylindrical probe inserted into a magnetised plasma was developed by Laframboise and Rubinstein [47] for the thick sheath limit ($r_p/\lambda_D \rightarrow 0$) and collisionless conditions. Their results are displayed graphically with the theoretical current plotted as functions of the probe potential, angle between the probe tip axis and magnetic field ($\theta$), and $r_{g,e}/r_p$. The reduction of the knee current at the plasma potential was minimised when $\theta = \pi/2$ rad and $r_{g,e}/r_p \rightarrow \infty$. It is, therefore, recommended to use a probe with a small radius in magnetised plasma. At $\theta = \pi/2$ rad and $r_{g,e}/r_p \rightarrow 0$, the knee current was reduced by a factor of $2\pi r_p l_p/(4r_p l_p)$ compared to unmagnetised conditions. This reduction factor is also derived by the analytical model of Usoltceva *et al.* [48], and it shows that the probe only collects current using its surface area projected in the direction of the magnetic field for strong fields. Electron density underestimation will occur unless one takes into account the smaller effective collection area. Furthermore, the effective collection area of the probe is a function of probe potential because the high energy electrons of the EEDF are less confined by the magnetic field so they are collected over a larger surface area [48].

Bohm [49] and Stangeby [50] have modelled the thin sheath and strong magnetic field regime for planar geometry. They hypothesise that there is a long disturbance length, or current tube, extending parallel to the magnetic field from the probe surface with a small cross-sectional area during net electron collection. This is necessary for balancing the electron drain to the probe by slow cross-magnetic field transport, given that ionisation processes are assumed negligible inside the current tube. In this case, the probe does not provide a localised measurement because it is somewhat averaged over the disturbance length scale. They predict that electrons experience significant collisional drag with heavier species in the current tube; consequently, electric fields establish to facilitate electron transport to the probe and ions are repelled. The ion density is reduced at the edge of the probe sheath, hence the electron density is also reduced through quasineutrality, and this leads to a reduction in the collected electron current. To implement the model, the parallel and cross-magnetic field transport rates of electrons are required.

An important effect for limiting the electron current is the return sheath impedance ($Z_{r,sheath}$). In unmagnetised plasma, the return electrode (e.g. the chamber walls) of the probe circuit does not influence the probe $IV$ characteristic because the return current is collected over a large surface area (lowering $Z_{r,sheath}$), so only the conditions at the 'active' probe are important. Günther *et al.* [51] considered the situation where the narrow

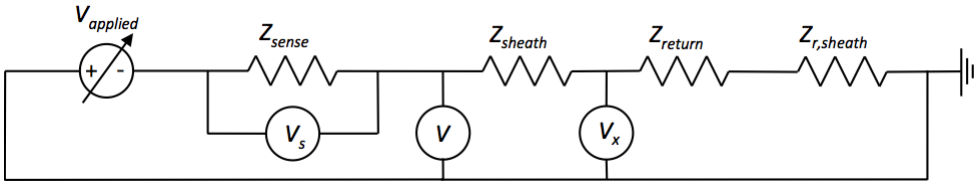


Figure 2.3: Simple model for a single Langmuir probe in a DC plasma. The voltage drop ($V_s$) across the sense resistor ($Z_{sense}$) is small so that the probe bias ($V$) is approximately equal to the applied bias ($V_{applied}$). In unmagnetised plasma, the return current path impedance ($Z_{return}$) and the return electrode sheath impedance ($Z_{r,return}$) are small so that the potential at the probe sheath edge ($V_x$) is equal to the plasma potential ($V_p$), which is set to ground potential (0 V) in this model. Modified from [52].

current tube of the probe intersects the return electrode before reaching its natural length scale. In this case, the ion current to the return electrode limits the electron collection by the probe, and the $IV$ characteristic resembles a measurement from an asymmetric double probe in unmagnetised plasma. Consequently, the electron retardation region appears non-exponential for a Maxwellian EEDF. To predict the reduction of the electron current, one needs to model the current paths of both the electrons and ions, which requires knowledge of their parallel and cross-magnetic field transport rates.

**Electron temperature overestimation**

Electron temperature overestimation occurs because the potential difference across the probe sheath is overestimated in magnetised plasma; hence, the width of the electron retardation region on the $IV$ characteristic is overestimated. Figure 2.3 shows a simple model of a Langmuir probe measurement circuit [52]: $Z_{sheath}$ is the probe sheath impedance; $Z_{return}$ is the return current path impedance; $Z_{r,sheath}$ is the return electrode sheath impedance; $V_x$ is the voltage at the edge of the probe sheath; $V_{applied} < 0$ is the applied probe bias with $V_p \equiv 0$ V (ground potential); $Z_{sense}$ is the sense resistor used to calculate current by measuring the small voltage drop $V_s$; and $V \approx V_{applied}$ is the probe tip bias. In a magnetised plasma, the voltage $V_x$ will be shifted from $V_p$ because of a significant voltage drop across $Z_{return}$ and $Z_{r,sheath}$ [52]. As a result, the magnitude of the potential barrier for electron collection is overestimated unless the variation in $V_x$ is modelled or measured.

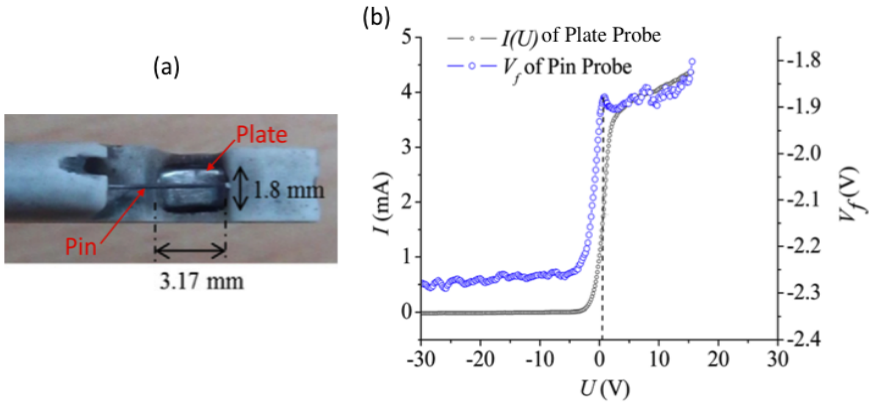


Figure 2.4: (a) The pin-plate probe and (b) the pin floating potential during a plate probe voltage scan. Reproduced from Binwal *et al.* [53].

#### 2.1.3.4 Experimental investigations

Pin-plate probe experiments have been performed to measure the electric potential perturbation at the sheath edge ($V_x$) induced by a Langmuir probe in the DITE tokamak [52, 54] and in a linear plasma device ($B = 11 - 30$ mT) [53]. An image of the pin-plate probe used by Binwal *et al.* [53] is shown in figure 2.4(a). The pin probe is positioned in front of the larger plate probe by a few millimetres to ensure that it is located outside of the plate sheath but approximately the same local plasma is sampled. In addition, the two probes are electrically isolated so that they can be biased independently. Figure 2.4(b) is data from the study by Binwal *et al.* [53], which shows the floating potential of the pin probe during a plate probe $IV$ scan. There was a $\sim 0.5$ V increase in the pin floating potential during the plate voltage sweep, with the sharpest $V_f$ gradient occurring when the plate was biased above the floating potential. A similar trend is reported for the DITE experiments but with a pin floating potential shift of the order of tens of volts. In these investigations, the change in the pin floating potential was interpreted as being a direct indication of the plasma potential shift at the plate sheath edge due to significant return impedances when the plate draws a net electron current.

These experiments show that the electron temperature from a single Langmuir probe should be calculated from the region $V < V_f$ because the inferred plasma potential shift was small here. Moreover, this is sampling the high energy tail of the EEDF, which is 'less' magnetised compared to the bulk. This conclusion is consistent with Langmuir

probe measurements by Tagle *et al.* [46] using the JET tokamak. The electron temperature calculated from the $IV$ characteristic increased as the voltage upper bound for data analysis increased, with the voltage lower bound held constant at $V < V_f$. A constant electron temperature was obtained only when the fit region was restricted to $V < V_f$. The approach of only analysing the tail of the EEDF has also been utilised for electron temperature measurements in magnetised low temperature plasma sources [55, 56]. However, the technique is erroneous when the EEDF is non-Maxwellian because no information is acquired about the low energy part of the EEDF.

The magnitude of the electron density error in the weak magnetic field regime using unmagnetised theory was investigated by Passoth *et al.* [45] (and a preliminary study by Kudrna *et al.* [57]) for the range $B = 10 - 50$ mT using a cylindrical magnetron ($n_e \sim 10^{15} - 10^{17}$ m$^{-3}$) with a noble gas pressure of 1.5 Pa (separate plasmas generated using Ar, Kr and Xe). During the study, the cylindrical probe tip axis was aligned perpendicular to the magnetic field [47], and the ion density determined by the Langmuir probe, using a radial-motion theory, was used to assess the electron density error with the assumption of unmagnetised ions ($r_{g,i}/r_p \gg 1$). For a $r_p = 50$ $\mu$m probe, the agreement between the ion density and electron density was within $\sim 20\%$ up to $B = 40$ mT, beyond which, the electron density was systematically underestimated. However when using a $r_p = 20$ $\mu$m probe, there was still reasonable agreement at $B = 50$ mT, which demonstrated that the relative effect of electron magnetisation was reduced for a thinner probe, as predicted by Laframboise and Rubinstein [47]. A criticism of the study is that a non-intrusive, probe independent method of measuring plasma density was not employed. This is required for drawing reliable conclusions because the choice of ion collection theory is not straightforward when operating with the gas pressure in the range $\sim 0.5 - 10$ Pa because a small number of ion-neutral collisions in the probe sheath can strongly impact the collected ion current [21, 22, 58]. In addition, a non-intrusive diagnostic would allow assessment of the plasma perturbation induced by probe insertion.

#### 2.1.3.5 Comparison with non-intrusive diagnostics in magnetised, low temperature discharges

There have been several previous comparison studies of Langmuir probe and a non-intrusive diagnostic for electron property measurements in magnetised, low temperature discharges. The results obtained using microwave interferometry and laser Thomson scattering are

discussed separately below. Unless stated, the probe was not in the plasma during the measurements by the non-intrusive diagnostic.

**Microwave interferometry**

Brown *et al.* [59] have compared microwave interferometry and Langmuir probe measurements of plasma density using a linear plasma device in the strong magnetic field regime (115-385 mT with $r_{g,i}/r_p$ of the order of unity). Laframboise theory was implemented to calculate the ion density with the probe operating in the thick sheath regime ($0.4 < r_p/\lambda_D < 4$). The ion density was a factor of 1.3-4 lower than the microwave interferometry results, with the magnitude of the plasma density underestimation increasing as probe radius and/or magnetic field strength increase. The agreement between the diagnostics improved when the projected probe area parallel to the magnetic field, rather than the physical area, was used. However, the physical interpretation of this approach is not clear because the effects of orbital motion in Laframboise theory are important in the thick sheath regime, which implicitly assumes that the probe collects ions over its entire surface area.

**Laser Thomson scattering**

Diagnostic comparison studies using laser Thomson scattering have been performed in a magnetised DC arc discharge ($B$ = 20 mT) [60] and in an electron cyclotron resonance discharge (ECR [$B$ = 940 mT]) [61]. The plasma density agreement was good in both investigations (within $\sim$ 20%). The experiment using the arc discharge calculated both ion and electron densities using the Langmuir probe, whereas the ECR discharge only calculated an ion density using the probe. Moreover, the general trend in both cases was for the probe to overestimate the electron temperature by up to a factor of $\sim$ 2. In another investigation Maurmann *et al.* [62] compared the diagnostics in the magnetic null region of a magnetic multipole source. There was good agreement for $n_e$, $T_e$ and EEDF measurements. It should be noted that these comparison studies were for a limited range of discharge conditions, including a constant magnetic field strength in each study.

Laser Thomson scattering measurements were performed with a probe inserted into the ECR discharge to investigate the perturbing effect of the probe [61]. The probe tip was positioned 30 mm from the detection volume; this was the closest possible distance without disturbing the laser Thomson scattering system. The electric bias of the probe tip was not explicitly stated in the paper. The presence of the probe had the following

effects on the laser Thomson scattering results: a reduction in electron density by $20-40\%$; an increase in electron temperature by $20-40\%$; and the EEDF changed from a Maxwellian distribution to a non-Maxwellian distribution for certain discharge conditions. Note that the probe perturbation study using an ICP [35], discussed in section 2.1.2.2, did not observe a change in the shape of the laser Thomson scattering determined EEDF when the probe was inserted, only an electron density reduction. These observations suggest that a probe inserted into a magnetised plasma is more perturbing compared to an unmagnetised plasma; however, it is difficult to draw conclusions when comparing results from different types of discharges.

### 2.1.4 Summary

This section has given a brief introduction to Langmuir probe physics, with the main focus being probe operation in magnetised plasma. The use of unmagnetised probe theories to interpret data from magnetised plasma leads to electron density underestimation, electron temperature overestimation, distortion of the EEDF, and there is difficulty locating the plasma potential on the probe current-voltage characteristic. A magnetised probe theory needs to model the plasma equilibrium obtained when the probe draws current from the plasma, and for cylindrical geometry, it also needs to model the interaction between the charged particle's orbital motion and the magnetic field within the probe sheath. The main limitation for the development of accurate magnetised probe theories is modelling cross-magnetic field transport. It is dependent on classical transport such as diffusion and drifts, and anomalous transport unique to each discharge.

Since no complete magnetised probe theory has been developed, it is instructive to assess the limitations of unmagnetised probe theory. Experimental investigations of Langmuir probes in magnetised plasma have concluded that electron temperature should be calculated from the high energy tail of the EEDF because these electrons are 'less' magnetised due to their larger gyroradius compared to the bulk. This approach is problematic, however, when the EEDF is non-Maxwellian. In terms of diagnostic comparison studies, the use of Langmuir probes for plasma density measurements in the strong magnetic field regime has been systematically investigated by comparing with microwave interferometry measurements [59]. For the weak magnetic field regime, however, a detailed comparison study of plasma density and electron temperature measurements using a non-intrusive diagnostic has not been performed yet. The aim of the research presented in chapters 5 and

6 of this thesis is to assess the reliability of a Langmuir probe for electron plasma property measurements in weakly magnetised plasma by comparing the results obtained from the probe with incoherent laser Thomson scattering measurements.

## 2.2 Incoherent laser Thomson scattering

In this research, laser Thomson scattering was used to both benchmark results obtained using the Langmuir probe and to investigate magnetron physics. Comprehensive reviews on the theory and application of the technique to high and low temperature plasmas are given by references [63–65] and [63, 66–70], respectively. The aim of this section is to review the aspects of the technique that are most relevant to this research. This includes (1) a brief explanation of the physical basis of Thomson scattering in the incoherent regime and the development of the technique for measurements in low temperature plasmas; (2) the various signals measured during an experiment; (3) the signal-to-noise ratio of an experimental Thomson scattering spectrum; and (4) the equipment requirements for a low temperature experiment. It should be noted that the focus of this section is on practical details rather than background theory. The latter is given in section 3.2.

### 2.2.1 Introduction

Thomson scattering is the process of electromagnetic radiation scattering from a free charged particle - for example an electron - as described by classical electromagnetism. It is the low-photon-energy limit of Compton scattering, whereby the change in the photon energy and electron energy due to the scattering event is negligible [64]; hence, it is an elastic process where only the direction of the incident photon changes. When the electron is moving relative to the radiation source, the frequency of the scattered light is Doppler shifted, and hence, the Thomson scattering spectrum from multiple electrons is related to the electron velocity distribution function (EVDF). In the incoherent scattering regime, the phase of the scattered radiation from each electron is uncorrelated; consequently, the scattering spectrum is proportional to the EVDF in one-dimension, with the direction of sensitivity determined by the scattering geometry. Furthermore, the total scattering intensity is proportional to the electron density.

An early demonstration of the usefulness of the incoherent laser Thomson scattering technique was in 1969 when the high performance of the T-3 tokamak was unambiguously

confirmed by electron temperature and electron density measurements [71]. The recently developed ruby laser, capable of producing a high power pulse (4 J with a pulse-width of 25 ns) but at a low repetition rate ($\ll 1$ Hz), was the radiation source for the experiment. A high power laser was necessary because of the small Thomson scattering cross-section. The main advantages of the laser Thomson scattering technique are that the interpretation of the scattering spectrum is straightforward, high spatial and temporal resolutions, and the method is non-intrusive. Following this success, laser Thomson scattering became a wide spread diagnostic for the nuclear fusion community, and still today, provides the benchmark for electron property measurements in modern tokamaks and stellarators (e.g. [72]). The combination of a high plasma density in these devices ($n_e > 10^{19}$ m$^{-3}$) and a high power laser allows one to obtain a strong scattering signal from a single laser pulse. This is advantageous for diagnosing non-steady state conditions and for resolving transient phenomena by firing several lasers in quick succession.

Initial attempts to apply laser Thomson scattering to low temperature plasmas occurred in the late 1970's using the ruby laser [68]. These studies were restricted to discharges that produced an electron density similar to fusion devices, which were, in general, high pressure discharges, such as the impulse-arc discharge [73]. In the mid-1980's there was increased interest in understanding electron behaviour in low pressure discharges in order to optimise the plasma processing of semiconductor materials. However, the electron density determined by probes in such devices was $n_e \lesssim 10^{16}$ m$^{-3}$ and this was significantly below the detection limit of the laser Thomson scattering technique; in addition, the low plasma density was limiting the plasma processing performance. Later in the decade, the low pressure electron cyclotron resonance (ECR) discharge was developed which produced a density of $n_e \sim 10^{18}$ m$^{-3}$, and this led to a new generation of low pressure, high density plasma sources (e.g. ICP, helicon and helicon resonator [7, p. 18]). The first publication of laser Thomson scattering applied to one of these devices was in 1991 using an ECR discharge and a ruby laser [74]. The scattering spectrum was accumulated from 10 laser shots per wavelength measurement, but there were large error bars for the electron temperature and electron density measurements. This was a result of the relatively large 'shot noise' associated with the detection of photons, which arises due to the weak signal at the detector and the quantised nature of light (discussed further in section 4.3.1.3). It was recognised that to significantly improve the signal-to-noise ratio either the laser power needed to increase (from 0.2 J per pulse) and/or the scattering signal needed to be averaged over a greater number of pulses.

In general 'small' technological plasma sources are more susceptible to laser induced plasma perturbation compared to fusion plasmas, so the data accumulation method is favoured for lowering the Thomson scattering detection limit. This takes advantage of the stable nature of many plasma discharges and there is also the option of triggering the laser in phase with any cyclic process, but the technique is unable to resolve transient phenomena. The signal-to-noise ratio of the total number of Thomson scattering photons detected during an experiment depends on the intrinsic shot noise associated with the mean number of Thomson scattering ($N_T$) and plasma emission ($N_E$) photons [70]:

$$\mathrm{SNR}_{total} = \frac{N_T}{(N_T + 2N_E)^{1/2}}. \tag{2.2}$$

It is assumed that the detector does not introduce any additional sources of noise. The factor of two in equation 2.2 is due to the plasma emission spectrum contributing twice to the shot noise [66, p. 60]; this is discussed in section 2.2.2. The value of $N_E$ needs to be minimised in order to optimise the signal-to-noise ratio. This is achieved by using a moderately powered pulsed-laser (100's mJ and $\sim$ 10 ns width per pulse) with a high repetition rate ($\geqslant$ 10 Hz) and a gated photon detector, rather than using a continuous laser delivering the same average power with the photon detector continually active. The commercialisation of such pulsed lasers, like the Nd:YAG type, led to a breakthrough in the application of laser Thomson scattering to low temperature, low pressure discharges in the 1990's [75]. To date Thomson scattering has been used to study a variety of low temperature discharges (see the review by Muraoka and Kono [68]) and the detection limit has been lowered to of the order of $n_e \sim 10^{15}$ m$^{-3}$ using a photon counting technique [76].

### 2.2.2 The total spectrum

The total spectrum measured in a real experiment consists of several different components. It is convenient to explain the different components using an example from this research; such a spectrum, acquired using an argon plasma, is shown in figure 2.5(a). There are four components for a monotonic background gas:

- Thomson scattering: as described above, this contribution is laser scattering from free electrons in the plasma. The $1/e$ full width of a spectrum with $T_e = 1$ eV is $\sim 3$ nm. For a typical low temperature Thomson scattering experiment, the number of Thomson scattering photons detected per pulse is only $\sim 10^{-17} \cdot n_e[\mathrm{m}^{-3}]$ [68] due to

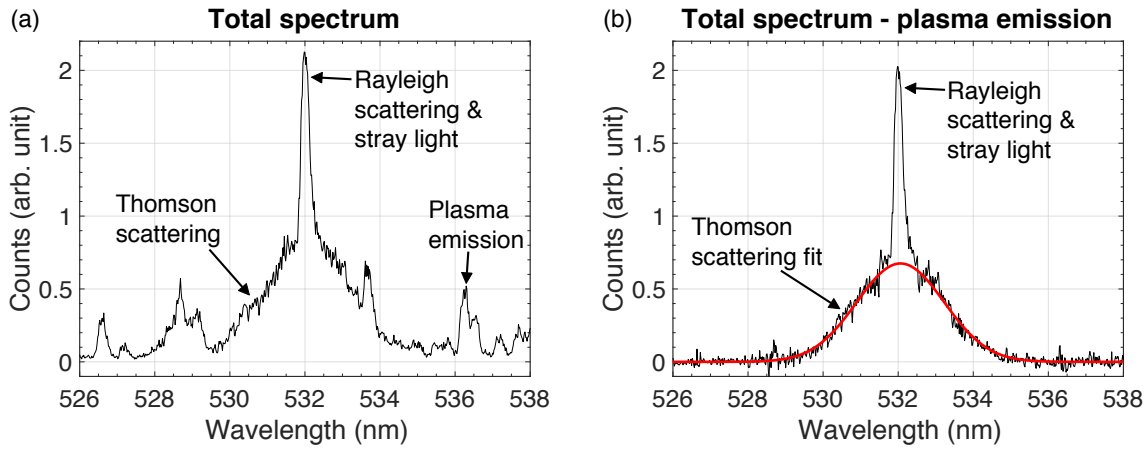


Figure 2.5: (a) An example of the total spectrum acquired during a laser Thomson scattering experiment from this research using an argon plasma. It includes the following components: Rayleigh scattering, stray laser light, plasma emission and Thomson scattering. (b) The plasma emission spectrum subtracted from the total spectrum reveals the wings of the Thomson scattering spectrum.

the small scattering cross-section. Clearly the Thomson scattering signal intensity is weak below $n_e < 10^{19}$ m$^{-3}$, and so the data accumulation method is required.

- Rayleigh scattering: this arises from the incoherent elastic scattering of laser radiation from electrons bound to atoms and ions. The $1/e$ full width of a Rayleigh scattering spectrum, due to the Doppler broadening effect, from room temperature argon gas is $\sim 2$ pm. This is insignificant compared to that of the electrons due to the relatively slow speed of the heavy particles, and it is below the spectral resolution of a typical laser Thomson scattering system. Consequently, other sources of line broadening are important for the measured Rayleigh scattering spectrum, such as, the convolution between the laser linewidth and the instrumental function of the detection system.

- Stray laser light: a small fraction of the intense laser radiation is dispersed as it passes through the optical system, most notably at the chamber entry/exit windows. This stray laser light gets reflected inside the vacuum chamber and subsequently passes through the detection system. As described above, the Doppler broadening effect for the Rayleigh scattering spectrum is insignificant; therefore, the stray laser light and Rayleigh scattering spectra directly overlap. In general, the stray laser light intensity

dominates the Rayleigh scattering signal at low gas pressure (< 10 Pa). Moreover, the stray laser light intensity can be large relative to the Thomson scattering signal because there are an extremely large number of laser photons entering the chamber per pulse, which is of the order of $10^{17} - 10^{18}$ photons, and Thomson scattering has an inherently small cross-section. It should be noted that the example spectrum in figure 2.5(a) is from a high density plasma ($n_e > 10^{19}$ m$^{-3}$). For a less dense plasma, the Thomson scattering signal intensity is reduced, and therefore the relative contribution of stray laser light would increase.

- Plasma emission: the laser wavelength should be chosen to avoid any strong line emission, but a continuum across all wavelengths cannot be avoided. Consequently, the plasma emission spectrum must be subtracted from the total spectrum to obtain the Thomson scattering spectrum. The plasma emission spectrum is a major contributor to noise on the measured Thomson scattering spectrum.

Figure 2.5(b) shows the total spectrum with the plasma emission spectrum subtracted. The central region of the spectrum is contaminated by the Rayleigh scattering and stray light signals but the wings of the Thomson scattering spectrum are unaffected. A Gaussian fit to these wings was applied, which implies a one-dimensional Maxwellian EVDF. The procedures for calculating electron temperature and electron density are explained in section 3.2.3.

### 2.2.3 Spectral signal-to-noise ratio

The signal-to-noise ratio defined in equation 2.2 is based on the total number of photons collected; however, in order to resolve the entire Thomson scattering spectrum, a good signal-to-noise ratio is required at each wavelength [70]. In the incoherent regime, the Thomson scattering spectrum is proportional to the EVDF in one-dimension with the laser wavelength ($\lambda_i$) corresponding to the zero velocity point on the EVDF. For the case of a Maxwellian EVDF, the Thomson scattering spectrum is a Gaussian curve, and so the strength of the scattering signal decreases as the wavelength shift ($\Delta\lambda = \lambda - \lambda_i$) from the laser wavelength increases. This is demonstrated by figure 2.6(a), which shows the population density fraction, or equivalently the fraction of Thomson scattering photons, for a Maxwellian EVDF with $T_e$ =0.5 eV or 5 eV as a function of $\Delta\lambda^2$. Given that the plasma emission signal overlaps with the entirety of the Thomson scattering spectrum and

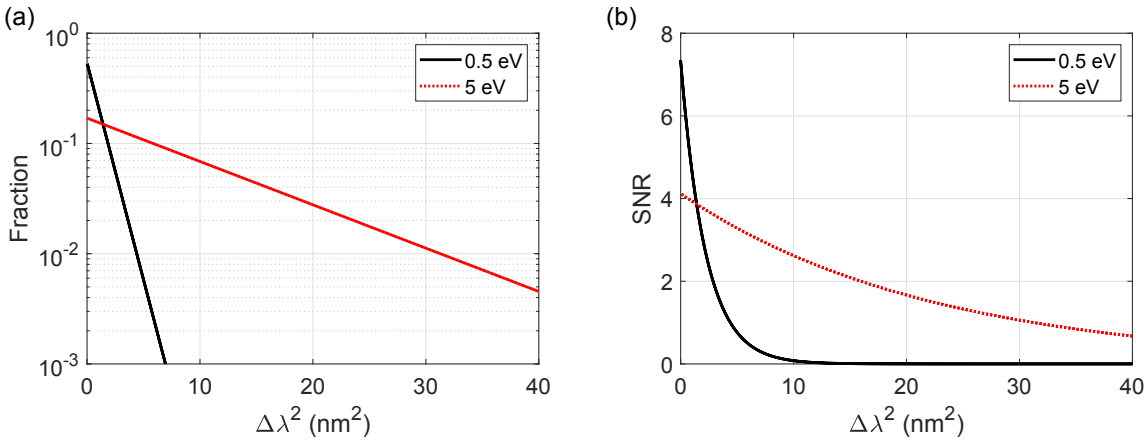


Figure 2.6: (a) Electron population density or Thomson scattering photon number fraction as a function of wavelength for Maxwellian EVDFs with $T_e = 0.5$ eV and 5 eV. (b) The corresponding spectral signal-to-noise ratios based purely on Thomson scattering shot noise with $\text{SNR}_{total} = 10$.

photon shot noise is more important for low photon numbers, it is clear that the signal-to-noise ratio will degrade as $\Delta\lambda^2$ increases. This is demonstrated by figure 2.6(b) which shows the spectral signal-to-noise ratio based purely on Thomson scattering shot noise - the plasma emission was neglected ($N_E = 0$) - with $\text{SNR}_{total} = 10$. The distribution with the lower electron temperature has a greater peak signal-to-noise ratio, but its curve decays faster. In order to resolve the wings of the EVDF with $T_e = 0.5$ eV, a significant increase in $\text{SNR}_{total}$ is necessary, which experimentally requires more laser pulse averaging.

### 2.2.4 Equipment requirements

As previously mentioned, laser Thomson scattering was initially developed for fusion devices such as the tokamak. The single-pulsed nature of the tokamak requires one to maximise the Thomson scattering signal from a single laser shot. This section considers the system adaptations that are required for measurements of low temperature, low density plasma sources using the data accumulation method. A schematic of such a Thomson scattering system is shown in figure 2.7. The important components are discussed below:

- Laser: the Nd:YAG laser operated at the second harmonic wavelength (532 nm) is commonly employed for the data accumulation method due to its high repetition rate, moderate energy per pulse and photon detectors, which have low noise generation

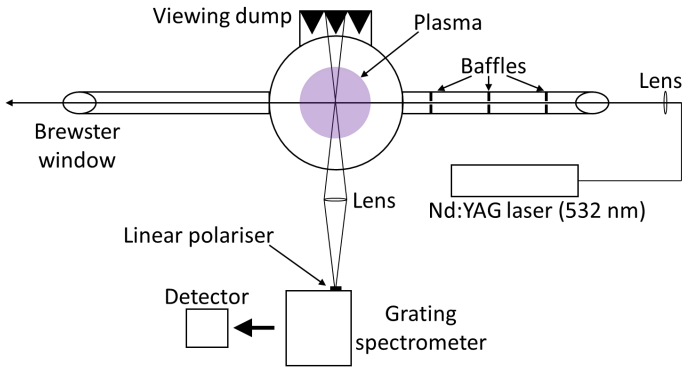


Figure 2.7: Thomson scattering system for low temperature and low density plasma sources [70].

over a period of several minutes (e.g. low dark current), are readily available. Many Thomson scattering systems designed for tokamaks use the Nd:YAG laser at the fundamental frequency (1064 nm) because, in general, photon detectors have a higher quantum efficiency (QE) at this wavelength but at the cost of increased dark current. For example, the generation 3 intensified charge-coupled device (iCCD) camera used in this research has QE = 0.41 at 532 nm, whereas an avalanche photodiode (APD) can have QE $\gtrsim$ 0.8 at 1064 nm [63, p. 42]. In addition, converting the laser to the second harmonic reduces its output power.

- Scattered light collection: most experiments collect the scattered light at $\theta = \pi/2$ rad with respect to the laser beam for ease of optical access and to maximise spatial resolution. In addition, it is efficient to couple the scattered light collected by a lens directly to the spectrometer, rather than through a fibre cable. Both of these design configurations are more difficult to implement in tokamaks, but not impossible [77], due to restricted optical access. Another option is to have the laser entry and detection optics located at the same access port with $\theta = \pi$ rad scattering. In this case, the spatial resolution is determined by the laser pulse-width and detector response time. This technique is called LIDAR (light detection and ranging) and has been applied to large sized tokamaks [78].

- Spectrometer and detector: grating spectrometers are used for low temperature plasma experiments. The options are to either use a monochromator/polychromator with discrete wavelengths exiting the spectrometer, and the photons are detected

using single channel detectors (e.g. photomultipliers [68]); or a spectrometer paired with an iCCD camera detector to simultaneously record a continuous spatial and spectral profile. Often stray laser light redistribution is an issue, so either a double-monochromator or triple-grating spectrometer are employed, with the latter having a mask to attenuate the laser wavelength. A novel approach implemented in 2018 by Vincent *et al.* [79] was to use a Bragg grating notch filter to attenuate the laser wavelength region, in conjunction with a single spectrometer and iCCD camera. The use of a single stage spectrometer results in higher signal transmission. In addition, a linear polariser can be placed in front of the spectrometer to increase the ratio of $N_T/N_E$ because the Thomson scattering photons are linearly polarised (when the laser radiation is linearly polarised), unlike the plasma emission. For fusion devices, filter polychromators and APD's are favoured due to higher transmission and quantum efficiency. Stray laser light is less of an issue because both the scattering signal intensity and the electron Doppler broadening effect are greater. The disadvantage of these systems is that the exit wavelengths are not flexible once installed.

- Reducing stray laser light: this is a critical issue for low temperature, low density systems. The majority of the stray laser light originates from the laser light being dispersed as the beam enters/exits through Brewster windows. A series of apertures (or 'baffles') in the pipe, which the Brewster window attaches to, and a viewing dump placed in the field of view of the collection lens reduces the amount of stray laser light entering the spectrometer. In addition, a linear polariser attenuates the (partly polarised) stray laser light by approximately 25-50% [66, p. 124].

### 2.2.5 Summary

Laser Thomson scattering can be used to determine the electron density, electron temperature and EVDF of a plasma. The main advantages of the diagnostic are that data interpretation is straightforward and independent of the magnetic field strength; high spatial resolution; high temporal resolution for cyclic processes; and the method is non-intrusive. The disadvantages are that it is insensitive to the tail of the EVDF, and a complicated and expensive experimental setup is required. In addition, a difficulty unique to the magnetron setup in this research is that the integration time for measurements is limited because sputter deposition onto the viewing window during magnetron operation reduces the window transmission. A long data accumulation time is favourable to improve the signal-to-noise

ratio.

## 2.3 Review of DC magnetron and HiPIMS physics

A planar magnetron was the plasma source for the experiments reported in this thesis. General reviews about conventional magnetron operation and HiPIMS can be found in references [3, 10] and [15, 80, 81], respectively. This section reviews the aspects of the literature that are most relevant to this research. It is organised as follows: (1) a description of the fundamental processes occurring in sputtering devices; (2) a review of DC magnetron operation; and finally, (3) there is a review of HiPIMS physics, which includes previous electron plasma property measurements.

### 2.3.1 Fundamental processes of sputtering devices

#### 2.3.1.1 Sputtering

Sputtering is the ejection of atoms from a surface due to bombardment by energetic particles. The sputtering yield is defined as the number of sputtered atoms released per incident particle and is dependent on the target material, the type of particle, the particle energy ($E_i$), and the angle of incidence [12]. For the case of plasma sputtering, ions bombard a cathode-target with an energy dependent on the potential difference across the cathode sheath and the chamber pressure. An application of plasma sputtering is physical vapour deposition using low pressure discharges, where the vaporised target material is condensed onto a substrate to form a thin film ($< 1$ $\mu$m) or thick coating ($> 1$ $\mu$m). Typical ion bombardment energies at the target are $E_i = 0.2 - 1.0$ keV.

When $E_i < 1$ keV, the sputtering process is modelled as a series of binary-collision cascades in the target, involving collisions between the incident ion and target atoms, and collisions between target atoms. The energy distribution function of the sputtered atoms is given by Thompson theory [84]. The most energetic distribution is obtained when the masses of the incident ion and target material are equal [82]. For this reason, argon is commonly used as the background gas for non-reactive deposition because it has a similar mass to materials of technological interest and it is less expensive compared to the other noble gases.

Figure 2.8 shows example Thompson distributions for the case of normal-incidence argon ions with energies of $E_i = 300$ eV and 800 eV and a tungsten target (relevant to

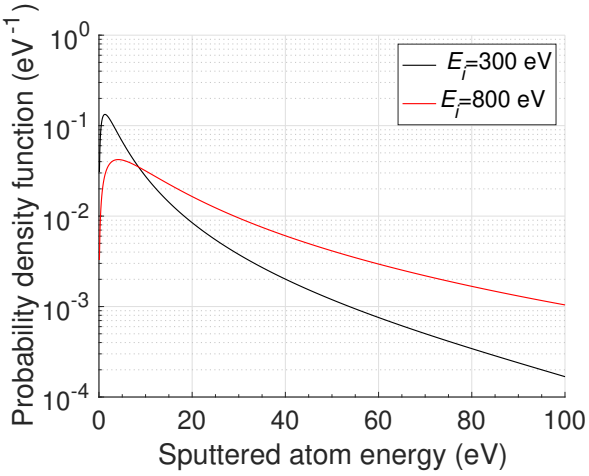


Figure 2.8: Thompson probability density distributions for a tungsten target with argon ion bombardment energies of 300 eV and 800 eV. Curves were produced using the analytical expressions given in reference [82] and the surface binding energy of tungsten was estimated to be 8.7 eV [83].

the research presented in this thesis). The most probable sputtered atom energy is several electronvolts, which greatly exceeds room temperature, and the distribution becomes more energetic as the kinetic energy of the incident ion increases. The production of energetic sputtered atoms, which have a high surface mobility at the substrate, is one of the main advantages of plasma sputtering compared to other deposition techniques (e.g. thermal evaporation) because it results in smoother and denser films [12, p. 55]. Other advantages of plasma sputtering are that it can readily deposit films from high boiling point materials and the stoichiometry of the target material at the substrate is conserved when depositing compounds [12, p. 55].

#### 2.3.1.2 Ion bombardment of the substrate

Ion bombardment on the growing film can increase the surface mobility of adatoms and break grain structures [85, 86]. This prevents a columnar growth morphology and ensures a dense high-quality film without having to significantly raise the substrate temperature. This is obviously beneficial for thermal sensitive substrates. Furthermore, the ion interaction with the film is highly localised in terms of both spatial and temporal extent; thus, the film modification cannot be entirely replicated by substrate heating. In modern sput-

tering devices, the ion energy can be controlled independently of the discharge conditions (e.g. pressure and electrode voltages) by biasing the substrate. The optimal ion energy is dependent on the film and the composition of the ion flux; it can be up to of the order of $E_i \sim 100$ eV [87].

It should be pointed out that ion bombardment can be detrimental to the film properties if the ion energies are too high. In this case, the tendency is to produce films with high compressive stress [88] and even resputtering of the film can occur.

#### 2.3.1.3 Secondary electron emission

Secondary electrons generated at the target surface play an important role in sustaining the discharge because they have enough kinetic energy, after acceleration by the electric field of the target sheath, to directly ionise background gas atoms. In addition, thermalisation of the secondary electrons will raise the electron temperature of the bulk plasma; hence, this will increase the number of electrons that can participate in inelastic processes. The dominant mechanism for secondary electron emission in low pressure, low temperature plasma is ionic Auger emission [89]. Singularly charged argon ions satisfy the requirement for Auger emission but most metals require at least doubly charged ions [90].

### 2.3.2 Magnetron sputtering

Magnetron sputtering is an important technology for the production of high-quality thin films and coatings via physical vapour deposition. The simplest configuration, patented by Chapin in 1979 [3], consists of a set of ferromagnets positioned behind a planar cathode-target with the chamber walls and/or a grounded target shield as the anode. Common target geometries for academic and industrial applications are circular and rectangular. The substrate, which is usually positioned upstream from the target along the centre axis, is biased independently of the electrodes. The magnetic field configuration causes electrons to undergo a closed $\mathbf{E} \times \mathbf{B}$ electron-drift close to the target surface, which produces a Hall current that can be several times greater than the discharge current [42], while the ions are unmagnetised. The confinement of electrons increases the likelihood of electron impact ionisation collisions before they are lost to the anode. This allows ignition of the discharge at both lower pressure and absolute target voltage compared to a discharge without magnetic confinement. The net result is a higher deposition rate, a higher deposition rate per unit power, and a more energetic flux of sputtered particles at the substrate.

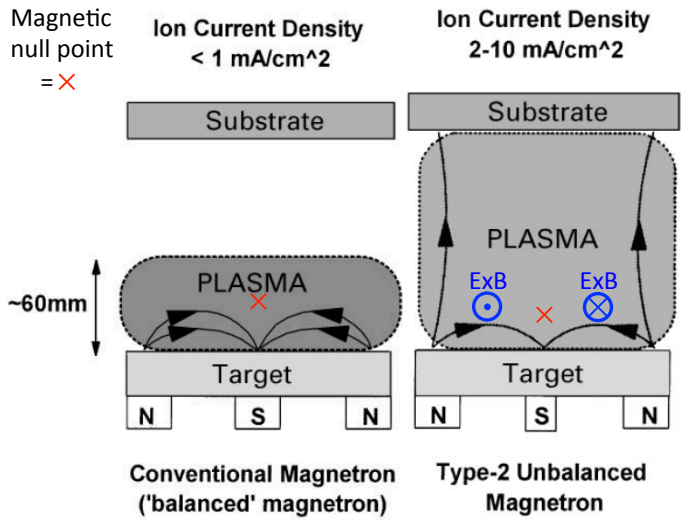


Figure 2.9: Cross-sections of balanced and type-2 unbalanced planar magnetrons. Both configurations have an $\mathbf{E} \times \mathbf{B}$ drift in the same direction - it is demonstrated only for the unbalanced option. The type-2 unbalanced configuration has more magnetic field lines extending from the target to a typical substrate position, resulting in a greater ion flux at the substrate, compared to the balanced magnetron. Modified from Kelly and Arnell [10].

#### 2.3.2.1 Balanced and unbalanced magnetic field configurations

Figure 2.9 shows a cross-section schematic of the two standard magnetic field configurations used for planar magnetron discharges: 'balanced' and 'unbalanced' [91]. A circular geometry for the target is assumed in the discussion below. The difference between the designs is that the magnetic field strength of the inner and outer magnets are equal in the balanced configuration, whereas the strength of the outer magnets are increased relative to the inner magnets in the 'type-2' unbalanced configuration.[1] The general features of both types of magnetron are described below, following this, the impact of unbalancing the magnets is discussed.

Common features of both designs are the two lobes of closed flux surfaces close to the target, and a magnetic field strength minimum ($< 1$ mT) located above the closed flux surfaces and along the centre axis, known as the 'magnetic null'. The typical magnetic field strength within a lobe is $B \sim 10 - 100$ mT. Electrons gyrate about the closed field lines

[1] A type-1 unbalanced magnetron has the strength of the inner magnets increased relative to the outer magnets.

and are reflected by the electric field in the sheath as they approach the target; this leads to a 'bouncing' motion parallel to the magnetic field lines. As aforementioned, electrons experience an $\mathbf{E} \times \mathbf{B}$ drift, and this is caused by the radial component of the magnetic field and the electric field perpendicular to the target surface. The drift direction is the same for both types of magnetron in figure 2.9 but it is indicated only for the unbalanced option. Moreover, the magnetic field is azimuthally symmetric so that the $\mathbf{E} \times \mathbf{B}$ drift is closed in the azimuth direction. This forms a magnetic trap, which produces the most intense ionisation and highest plasma density in the discharge. Consequently, there is enhanced localised erosion of the target following the $\mathbf{E} \times \mathbf{B}$ direction at the position on the target surface where the magnetic field is predominately in the radial direction; this is known as the 'racetrack'. In general, target utilisation is $< 30\%$ [3] so alternative configurations have been developed to make magnetron deposition more economical. An example is the rotating cylindrical magnetron, where target utilisation can approach 90% [3].

As discussed in section 2.3.1.2, ion bombardment on the film during the deposition is beneficial but this requires an appreciable ion density, and hence electron density through quasineutrality, close to the substrate. The effect of increasing the strength of the outer magnets relative to the inner magnets, as in the type-2 unbalanced configuration, is to increase the number of open field lines extending from the target region to the substrate position. In both the balanced and unbalanced configurations, electrons are required to cross magnetic field lines to escape the magnetic trap, but in the unbalanced configuration they are guided towards the substrate by the magnetic field once they have passed the closed flux surfaces. In addition, the magnetic null point is usually located closer to the target for the unbalanced configuration so that electrons do not have to travel as far to escape the magnetic trap. The net result is an increased ion current at the substrate for the unbalanced configuration whilst a good sputter rate at the target is maintained. For conventional DC magnetron operation, the ionisation fraction of the sputtered atom density is $\lesssim 0.1\%$ [15]; therefore, the ion flux to the substrate is dominated by background gas ions.

The type-1 unbalanced configuration, where the strength of the inner magnets are increased relative to the outer magnets, is not commonly used because the open field lines extend to the chamber walls at the side, rather than directly above the target to a typical substrate position [10]. The net result is a lower ion current at the substrate compared to the balanced configuration.

#### 2.3.2.2 DC magnetron electron plasma property measurements

Electron plasma property measurements in DC magnetron discharges are commonly performed using Langmuir probes, despite the difficulty of interpreting probe data from magnetised plasma. The results from previous studies show that both effective electron temperature and electron density increase as the target is approached [38, 92], and they both have a maximum above the racetrack in the magnetic trap [38]. Towards the substrate position, radial gradients of both effective electron temperature and electron density are reduced because electron transport is more isotropic due to the lower magnetic field strength in this region [38].

In general, the EEDF is Maxwellian in the magnetic trap and bi-Maxwellian outside of this region [38, 42, 93, 94]. Typical electron temperatures are $T_e \lesssim 1$ eV for the cold population and $T_e \sim 5$ eV for the warm component. The warm population density dominates close to the target, and the cold population dominates outside of the magnetic trap region. The total electron density in the magnetic trap is $n_e \lesssim 10^{17}$ m$^{-3}$.

The formation of a bi-Maxwellian EEDF is related to the electric potential barrier between the sheath boundaries of the target and the anode/substrate [93, 94]. Low energy electrons do not have enough kinetic energy to be collected by the anode/substrate, and so they are trapped in the bulk plasma. Seo *et al.* [94] found that when the electric potential barrier was increased, by biasing a substrate, a bi-Maxwellian EEDF transitioned to a Maxwellian distribution because the warm population of electrons also became trapped, and there was sufficient time for thermalisation.

#### 2.3.2.3 Alternatives to DC operation

A DC power supply can be used with any electrically conducting target material, but difficulties arise when depositing an insulating film by reactive sputtering [10]. In this process, sputtered atoms from the target chemically react with a carefully controlled atmosphere before being deposited onto the substrate (e.g. alumina coatings [95]). The main issue is that the anode and non-racetrack region of the target are also coated by the insulating film. This leads to a time-varying discharge impedance and arcing on the target surface, which ultimately produces defects in the film. Radio-frequency, pulsed DC discharges and dual magnetron systems are employed to overcome these issues [10].

A seminal paper was published in 1999 by Kouznetsov *et al.* [96] that demonstrated the potential of the magnetron as an ionised physical vapour deposition source without

the application of a secondary discharge in the region between the magnetic trap and substrate (e.g. [97]). A highly negative voltage pulse with a peak of -1600 V was applied to a copper target, producing a peak instantaneous power of 2.8 kW·cm$^{-2}$. The dense plasma generated during the on-time of the pulse caused a large fraction of the sputtered atoms to become ionised (up to 70%), which is advantageous for film deposition. However, a short pulse-width ($\sim$ 100 $\mu$s) and low repetition rate (50 Hz) were required to avoid damaging the target and/or the magnets. This technique is referred to as high power impulse magnetron sputtering (HiPIMS) and is discussed in the next section.

### 2.3.3 High power impulse magnetron sputtering

HiPIMS is characterised by a highly negative voltage pulse applied to the target, typically with an amplitude between $0.5 - 2$ kV, in the frequency range of $10 - 1000$ Hz with a duty cycle of $\lesssim 1\%$. During the pulse, a high instantaneous power density is achieved, typically $0.5 - 10$ kW·cm$^{-2}$ (normalised by the entire target surface area), resulting in a plasma density of the order of $n_e \sim 10^{19}$ m$^{-3}$ in the magnetic trap region [98]. These values are orders of magnitude greater than the characteristics of DC magnetron sputtering, namely, $\sim 10$ W·cm$^{-2}$ and $n_e \leqslant 10^{17}$ m$^{-3}$, but the average power is comparable. During HiPIMS, a large fraction of the sputtered atom density is ionised - up to 90% was reported by Bohlmark *et al.* using a titanium target [99] - resulting in a metal-ion rich plasma; therefore, the process enters the ionised physical vapour deposition (IPVD) regime [80]. An advantage of HiPIMS is that any magnetron rig can be converted into an IPVD source by simply changing the power supply.

This section is organised as follows: the main advantages of IPVD are explained; important processes in HiPIMS discharges are reviewed; and previous electron plasma property measurements are reviewed. It should be noted that the focus is non-reactive HiPIMS discharges using metal targets.

#### 2.3.3.1 Ionised physical vapour deposition

IPVD occurs when a significant fraction of the deposition flux is ionised. This regime has the following advantages: the energy and directionality of the film forming ions can be controlled by biasing the substrate, in contrast to line of sight deposition using neutrals where the energy of the sputtered atoms is strongly dependent on the discharge operating conditions (e.g. target voltage and pressure); the high instantaneous deposition rate and

energy per deposited particle, due to the pulsed nature of HiPIMS, leads to a supersaturation of mobile adatoms on the film surface; and momentum transfer to the film surface is most efficient when the masses of the incident ions and film atoms are equal. Consequently, HiPIMS produces films with superior properties compared to DC magnetron operation [15], namely: improved film density, smoothness and hardness [100, 101]; the ability to produce uniform coatings when using three-dimensional substrates [102], including high aspect ratio trenches for semiconductor manufacturing; and a greater control over film phase [103]. In addition, the implantation of metal ions into the substrate using HiPIMS, prior to the deposition process, improves film adhesion [104]. This is achieved by negatively biasing the substrate (with respect to the chamber walls) with an amplitude of $\sim 0.4 - 1$ kV.

#### 2.3.3.2 Discharge physics

The HiPIMS discharge is initially dominated by processes associated with the background gas, but as the electron density and sputtering rate increase, the plasma becomes metal-rich. This transition strongly influences the discharge physics. In this section, the important processes occurring in the discharge are reviewed. The dynamic evolution of electron plasma properties is discussed separately in section 2.3.3.3.

**Metal ionisation**

A time-dependent global model by Gudmundsson [105], exploring the plasma parameters and the ionisation mechanisms during HiPIMS, found that electron impact ionisation is the dominant process for metal ionisation during the pulse-on time. A high ionisation fraction of metal atoms is achieved because there is a high electron density in the target vicinity; moreover, metals, in general, have low first ionisation energies (compared to argon). The ionisation fraction of the metal flux to a substrate is in the range of $10 - 80\%$ for HiPIMS [106]. During the pulse-off time, heavy particle ionisation mechanisms (e.g. Penning ionisation [97] and charge exchange [105]) become important as both the electron temperature and electron density decrease; however, the overall probability of metal ionisation decreases. Similarly in the DC magnetron, there is a low probability that a sputtered atom will undergo an ionising collision with an electron or an excited/ionised gas atom due to the relatively low electron density in the discharge. The ionisation fraction of the metal flux to a substrate is in the range of a few percent for DC magnetron operation [80].

**Gas rarefaction, self-sputtering and gas recycling**

The initial phase of the HiPIMS discharge is dominated by background gas sputtering and a high plasma density is generated via a positive feedback loop: ions of the background gas are incident upon the target and cause secondary electron emission (as discussed in section 2.3.1.3); sheath energisation through secondary electrons, and Ohmic heating [107, 108] in the target presheath, causes the plasma density in the magnetic trap to increase via electron impact ionisation; this, in turn, increases both the ion flux to the target and the number of electrons available for Ohmic heating, and so on. A competing effect, however, is the reduction of the gas density in front of the target due to gas heating caused by collisions with the energetic sputtered atoms leaving the target. This process is known as 'gas rarefaction' and it reduces the number of background gas atoms available for ionisation. Gas rarefaction has been observed during DC magnetron operation [109], but the effect is more extreme for HiPIMS because HiPIMS discharges have a greater instantaneous sputter rate and a more energetic distribution of sputtered atoms (e.g. figure 2.8). In addition, background gas atoms are depleted by intense ionisation in the magnetic trap [110].

During the pulse, the sputtered atoms replace the background gas in the magnetic trap region to some extent due to the combination of a high sputtering rate and a reduction of background gas density, as described above. The transition to a metal-rich plasma has been observed by optical [111] and particle [112] spectrometries. The sputtered atoms, therefore, play an important role in both the deposition process and sustaining the discharge.

Electron impact ionisation of the sputtered atoms is highly probable in the target vicinity and a fraction of those that become ionised are attracted back to the target by the electric field of the presheath, rather than travelling to the substrate. The sputtering of the target by ions of the same element is known as 'self-sputtering'. This is speculated to be one of the main reasons why the deposition rate of HiPIMS is lower than DC magnetron sputtering at the same average power [15, 100]. The back attraction rate of sputtered ions is dependent on the magnetic field configuration [113] and the pulse duration [114]. Background gas recycling is another factor that will influence the deposition rate [115]. In this process, the gas atoms which have been implanted into the target are outgassed from the surface, become re-ionised and then contribute to the sputtering process again, including secondary electron emission. Background gas recycling can be an important source of sputtering, especially for low self-sputtering yield elements (e.g. graphite [115]).

With regards to the generation of electron-ion pairs to sustain the discharge, the metal atoms in the plasma are more readily ionised than background gas atoms via electron

impact ionisation, but the secondary electron emission yield is dependent on the species incident upon the target. At least doubly charged metal ions or singularly charged argon ions are required to bombard the target to generate secondary electrons via Auger emission [90]. Multiply charged metal ions have been detected in HiPIMS discharges [90, 112, 116]; nevertheless, global models [107, 108] predict that Ohmic heating is dominant over sheath energisation in HiPIMS discharges.

Therefore, the evolution of the discharge current beyond the initial background gas dominant phase is dependent on the interaction between gas rarefaction, gas recycling, self-sputtering and Ohmic heating. A runaway reaction, which generates a discharge current exceeding 1 $A{\cdot}cm^{-2}$ (normalised by the entire area of the target), is usually observed for at least part of the pulse-on period, even for target materials with low self-sputtering yields [115].

**Spokes**

Localised zones of enhanced plasma emission intensity and ionisation have been observed in the target presheath, above the racetrack region, for certain discharge conditions during both DC magnetron operation and HiPIMS [117]. These structures are called 'spokes', and they rotate in the $\mathbf{E} \times \mathbf{B}$ direction during HiPIMS with speeds of several $km{\cdot}s^{-1}$. A recent review of the topic is given by Hecimovic [118]. The azimuthal electric fields generated inside of spokes are theorised to play an important role in the sputtered ion dynamics because of the following experimental observations: the ion energy distribution function of the sputtered metal contains an additional high-energy peak when spokes are present [119]; and spokes are associated with anomalous cross-magnetic field transport of electrons [120], which in turn, modifies the ion transport. For example, spokes enhance the deposition rate of HiPIMS by counteracting the return effect of sputtered ions to the target [121].

The theory of spokes is still an active area of research because it is difficult to obtain reliable measurements of the plasma parameters inside a spoke. The use of electric probes has been restricted to measurements at the perimeter of the spoke for several reasons: a high thermal load inside the spoke; perturbation of the spoke by the intrusive probe; and difficulty interpreting probe data from magnetised plasma close to the target. Details of the probe studies for electron property measurements are given in section 2.3.3.3. Emissive probes have been employed for electric potential measurements and found a potential maximum in the region of the spoke. Studies using optical emission spectroscopy have investigated the spoke movement and propagation speed; however, extracting further quantitative

information from this non-invasive technique requires a complicated collisional-radiative model.

#### 2.3.3.3 Electron plasma property measurements

A detailed understanding of the electron dynamics during HiPIMS is important because electron impact ionisation is the main mechanism for ionising metal atoms, and ambipolar electric fields, driven by the electron mobility parallel to the magnetic field lines, guide metal ions to the substrate in the type-2 unbalanced configuration. In this section, previous electron plasma property measurements in HiPIMS discharges are reviewed.

**Langmuir probes**

Intrusive Langmuir probes have been the most commonly used diagnostic for electron plasma property measurements in HiPIMS discharges, with their usage generally restricted to the region outside of the last closed flux boundary to avoid perturbing the main ionisation region, and the thermal load on the probe is reduced. Moreover, data interpretation is simpler far from the target because electrons are less magnetised.

The plasma density at a typical substrate position ($\sim$ 10 cm from the target) is of the order of $n_e \sim 10^{18}$ m$^{-3}$ during the pulse on-time, with a maximum occurring above the racetrack [123]. Typically there are two peaks in a temporal profile of plasma density for a pulse-width of $\sim$ 100 $\mu$s. A subset of the results from the study by Poolcharuansin and Bradley [122] are shown in figure 2.10: the target voltage and discharge current waveforms are shown in (a) and the plasma density determined by the probe is shown in (b). In this example, both of the peaks in the plasma density profile are located during the pulse-on time [122]; although in other studies, there was a peak during the pulse-on period and the other was a few hundred microseconds after pulse termination [39, 123, 124]. The first peak is theorised to consist primarily of argon ions, which are produced during the initial stages of the pulse-on time, and the second peak is due to the slow drift of 'heavy' metal ions to the probe position [39, 122, 124, 125]. Alternatively, Alami *et al.* [123] suggest that the second peak is due to an ion acoustic wave reflecting off the chamber walls. Another important observation is the slow decay of the plasma density after pulse termination because the substrate will continue to receive ion bombardment in the afterglow, and the remnant plasma provides a seed of electrons for the next pulse. Poolcharuansin and Bradley [122] observed a two-fold exponential decay of plasma density characterised by time constants

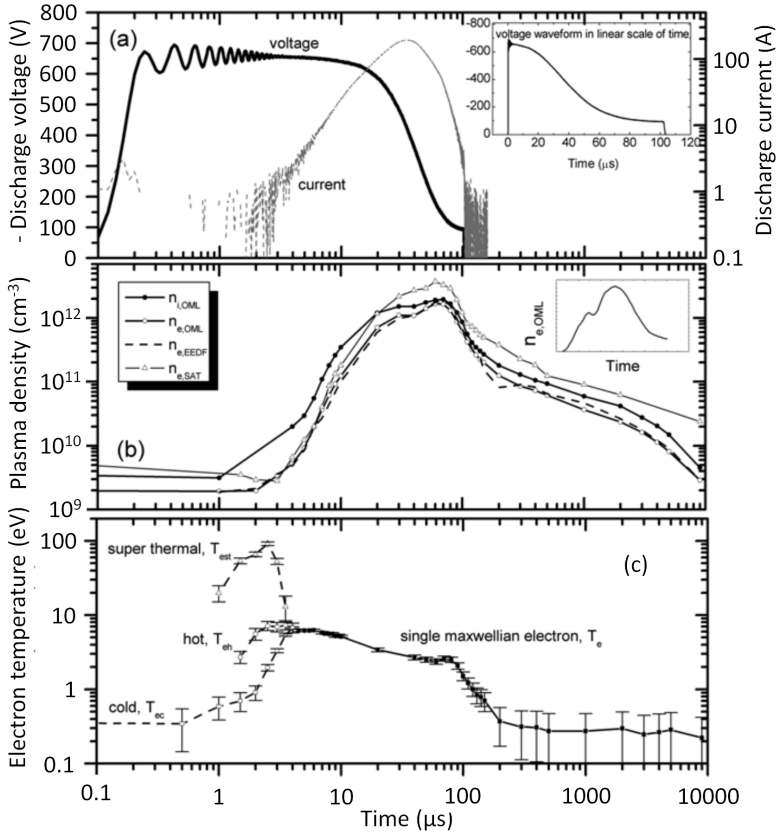


Figure 2.10: Results taken from Poolcharuansin and Bradley [122]. The target material was titanium, the peak power density was 500 W·cm$^{-2}$, the argon gas pressure was 0.5 Pa, and the measurements were performed at a typical substrate position. Plotted are the (a) discharge voltage and current waveforms; (b) the plasma density waveforms using various probe theories (see the original paper for details); (c) the electron temperature waveform, where several different components are labelled. The inserts in the figures shows the data on linear, rather than semi-logarithmic, axes.

of $\sim$ 35 $\mu$s followed by $\sim$ 3.5 ms. The plasma density at the start of the subsequent pulse was $n_e \gtrsim 10^{15}$ m$^{-3}$ for a pulse repetition rate of 100 Hz. The slow decay rate of both background gas and metal ions has also been observed by mass spectrometry [116]. In addition, De Poucques *et al.* [126] concluded, from laser absorption spectroscopy and Langmuir probe measurements in the afterglow, that the decays of metal ion density and electron density are consistent with ambipolar diffusion, and the metal atom decay obeys

classical diffusion.

High energy electrons have been detected at the start of the pulse-on time and these produce extremely negative floating potentials (hundreds of volts below ground potential) [122, 127–129]. For example, Poolcharuansin and Bradley [122] observed three groups of electrons during the first 4 $\mu$s of the pulse: super-thermal ($T_e \leqslant 100$ eV), hot ($T_e \leqslant 7$ eV) and cold ($T_e < 1$ eV). The temporal evolution of these components is shown in figure 2.10(c). The origin of the super-thermal electrons is theorised to be from stochastic electron heating as the cathode sheath expands in the presence of a strong magnetic field [122, 130]. Later during the pulse-on time, there are reports of Maxwellian [122, 131] and non-Maxwellian [39, 124, 127] EEDFs. Regardless, the effective electron temperature, of the order of 1 eV, decreases as the pulse progresses due to inelastic collisions with the increasing density of metal species. Moreover, a minimum in electron temperature was observed above the racetrack where the sputtering rate is highest [123]. At pulse termination, Poolcharuansin and Bradley [122] observed a two-fold exponential decay of electron temperature; the time constants were $\sim 30 - 160$ $\mu$s followed by $\sim 90 - 750$ $\mu$s.

Despite the concerns of perturbing the main ionisation region of the discharge, there are reports of Langmuir probe measurements within the last closed flux surface boundary. Bohlmark *et al.* [98] and Sigurjónsson [132] have both used a single Langmuir probe and the Druyvesteyn method [133][18, p. 80] to obtain spatio-temporal resolved measurements of electron density. The maximum electron density, of the order of $n_e \sim 10^{19}$ m$^{-3}$, was in the magnetic trap region of the discharge. Neither study provided temporal profiles of effective electron temperature within the last closed flux surface boundary. However, Sigurjónsson [132] reports spatially resolved measurements of effective electron temperature within the last closed flux surface boundary at a fixed measurement time during the pulse-on period: $T_e$ was several electronvolts; $T_e$ was independent of radial position; and the axial dependence of $T_e$ was dependent on the background gas pressure.

Lockwood-Estrin *et al.* [134] have reported time-resolved triple probe measurements at the last closed flux surface boundary above the racetrack during a spokes investigation. They measured a peak plasma density of $n_e = 2{\times}10^{19}$ m$^{-3}$ and a peak electron temperature of $T_e = 3.9$ eV for a discharge with a power density of 0.75 kW·cm$^{-2}$. The modulation of the electron plasma properties due to spokes was $\sim 50\%$. The disadvantages of the triple probe method are having to assume a Maxwellian EEDF to analysis the data and

the effective ion mass must be estimated.[2]

An alternative approach is to flush-mount electric probes in the target surface to avoid perturbing the discharge [135]. These probes act as part of the target, but the current to each probe is individually measured which enables the detection of spokes propagation. This method, again, requires knowledge of the effective ion mass. In addition, it requires an estimate of electron temperature since this is not measured. Nevertheless, Hecimovic *et al.* [135] used this approach to measure a peak plasma density of $n_e = 9 \times 10^{19}$ m$^{-3}$ at a discharge power density of $\sim 1.75$ kW·cm$^{-2}$. The plasma density oscillation due to spokes was $\sim 30\%$.

**Non-intrusive diagnostics**

The first reliable measurement of plasma density within the magnetic trap using a non-intrusive diagnostic was reported in 2018 using THz time domain spectroscopy [136]. The main principle of the technique is similar to microwave interferometry, except the phase shift from multiple frequencies is measured, rather than just a single frequency; consequently, the THz diagnostic has better noise resistance. Meier *et al.* [136] have used the technique to measure a line averaged plasma density of $n_e = 10^{18} - 10^{19}$ m$^{-3}$ during discharges with current densities of $1 - 4$ A·cm$^{-2}$ (up to $\sim 2$ kW·cm$^{-2}$). The THz beam was aligned parallel to the target surface, passed through the target centre axis, and the beam diameter (1.5 cm) was comparable to the distance between the magnetic null and the target surface. Therefore, the peak electron density above the racetrack was not resolved. Other disadvantages of their setup are that it has a relatively high detection limit of $n_e \sim 10^{18}$ m$^{-3}$ so afterglow measurements are limited, and a stable plasma is required over the 3 hour integration time per set of discharge conditions.

The first publications of incoherent laser Thomson scattering applied to HiPIMS discharges were in March [137] and April [2] 2019. Tsikata *et al.* [137] demonstrated the utility of the technique by measuring temporal profiles of electron temperature and electron density for a single set of discharge conditions (0.9 A·cm$^{-2}$, 0.45 kW·cm$^{-2}$, 60 $\mu$s pulse-width, 100 Hz, and 1 Pa of argon gas; titanium target) at a single location within the magnetic trap (detection volume dimensions: 0.3 mm diameter and 1.5 mm length). The electron density followed the discharge current profile closely during the pulse-on time with a maximum density of $n_e = 1.7 \times 10^{18}$ m$^{-3}$, and the electron temperature peaked at $T_e = 12$ eV almost instantaneously at the start of the pulse before saturating at $T_e = 3$

[2]This is not required for a single Langmuir probe if one analyses only electron current data.

eV during the current plateau. The afterglow measurements were restricted to 10 $\mu$s after pulse termination; both $T_e$ and $n_e$ decayed. Details of the other publication [2] are given in chapter 5 of this thesis: a comparison of Langmuir probe and laser Thomson scattering for plasma density and electron temperature measurements in HiPIMS discharges.

**Modelling and simulations**

Zero-dimensional kinetic models, most notably the ionisation region model (IRM) [138], have been implemented to investigate HiPIMS physics, including [108]: gas rarefaction and refill; reactive and non-reactive discharges; the effect of magnetic field strength; electron heating mechanisms (Ohmic heating and sheath energisation); the ionisation fraction of sputtered atoms; and the role of self-sputtering. The IRM predicts an electron density of the order of $n_e \sim 10^{19}$ m$^{-3}$ and two electron populations are assumed: bulk electrons and hot secondary electrons after sheath acceleration. To apply the model, theoretical discharge current and voltage waveforms are fit to experimental data using the following fitting parameters: the electric potential drop across the ionisation region; the probability of ion back attraction to the target; and the probability of a secondary electron being recaptured by the target. The basic assumptions of the model have been validated by comparing its results with tunable diode-laser absorption spectroscopy measurements of the argon atom metastable density [139]. There have been, however, no comparisons with experimental electron plasma property measurements.

The disadvantages of the IRM are that the electric potential profile is not self-consistently calculated and a three-dimensional treatment is required for investigating spokes. An alternative self-consistent approach is the use of particle in cell (PIC) simulations branched with a Monte Carlo method to describe the kinetics of the particles [140, 141]. Unfortunately, due to the high computational costs/complexity, simulations have, so far, been restricted to two-dimensions, a temporal length of $\leqslant 9$ $\mu$s (including pulse-on and afterglow), and the simulations do not consider metal in the plasma. A recent simulation [141] calculated an EEDF - an average from inside and outside of the last closed flux surface boundary - which had three components at the start of the pulse, which is similar to that shown in figure 2.10(c) for a substrate position [122]. Later, the EEDF transitioned to a bi-Maxwellian distribution (the low energy population out of the three components disappeared) with the electron temperatures tending to a similar value ($T_e < 10$ eV) as the discharge current plateaued. Furthermore, the electron density reached a maximum value of the order $n_e \sim 10^{18}$ m$^{-3}$ in the magnetic trap. The results of PIC codes can be used

as input parameters for *a posteriori* simulations. For example, Minea *et al.* [140] used a simulation to calculate the metal ionisation fraction, with the self-consistent plasma density results from a PIC code as an input. It is assumed that the results of the PIC code are not affected by the addition of test particles in the subsequent simulation.

### 2.3.4 Summary

High power impulse magnetron sputtering (HiPIMS) is a novel ionised physical vapour deposition technique in which high metal ionisation fractions are obtained through the creation of a dense pulsed-plasma. There is better control of the film growth, compared to line of sight deposition using neutrals as in DC magnetron sputtering, because the energy and directionality of the deposition flux is controlled by biasing the substrate. There have been extensive investigations into the physics of HiPIMS discharges, with the ultimate aim of understanding the creation and transport of metal ions from the target to the substrate, in order to optimise the deposition process. The most developed numerical model is the zero-dimensional ionisation region model, which is a flexible tool; but ultimately, a dimensional treatment is required because localised ionisation zones (spokes), propagating in the $\mathbf{E} \times \mathbf{B}$ direction, play an important role in the ion dynamics. Due to the high computational costs/complexity, two-dimensional particle in cell simulations are still under development.

Extensive Langmuir probe measurements have been performed to investigate the electron dynamics at a typical substrate position. In 2018, THz spectroscopy was implemented to provide the first reliable non-intrusive measurement of plasma density in the magnetic trap [136], although the density determined was line averaged. Following this, laser Thomson scattering was employed to obtain the temporal evolution of the electron velocity distribution function (EVDF) at a single localised position in the magnetic trap for a single set of discharge conditions [137]. In addition, a comparison study of electron plasma property measurements made by Langmuir probes and laser Thomson scattering in HiPIMS discharges was performed [2]; these results are reported in chapter 5. The next step is to investigate the dependence of the EVDF on discharge conditions and spatial location throughout the discharge; these results are reported in chapter 7.

# Chapter 3

# Diagnostic theory

This chapter provides a summary of the theories implemented for each diagnostic to extract plasma density, electron temperature and electron energy distribution function (EEDF) from the experimental data. The Langmuir probe is considered first, followed by laser Thomson scattering.

## 3.1 Langmuir probe

This section is organised as follows: (1) method for locating the plasma potential; (2) general expression for current collected by a cylindrical probe; (3) collection of electrons under a repulsive bias to determine electron density, electron temperature and EEDF; and (4) collection of ions under an attractive bias to determine ion density. Standard theories were employed and so complete derivations have been omitted, rather the key physics is discussed. The reader is referred to the following sources for a comprehensive review, including derivations, of probe theories: Swift and Schwar [18], Chung *et al.* [19], Pfau and Tichý [142], and Schott [143].

### 3.1.1 Plasma potential

The plasma potential ($V_p$) is the transition voltage between polarity reversal of the electric field in the probe sheath. When the probe is biased at $V_p$, there is no sheath around the probe tip. Therefore, the thermal fluxes of electrons and ions are collected, of which the electron contribution dominates. The transition from repulsive to attractive electron collection produces an inflection point on the probe characteristic. In this research, the

inflection point, and hence $V_p$, was located from the maximum in the first derivative of the probe characteristic.

### 3.1.2 General expression for current collected by a cylindrical probe

It is worthwhile documenting the general expression for the current collected by a cylindrical probe because it can be used to derive equations for both attractive and repulsive probe biases [142, p. 180]:

$$I = 2\pi r_s l_p q n \int_{\phi_1}^{\phi_2} \int_{-\infty}^{+\infty} \int_{v_{xy1}}^{v_{xy2}} |\mathbf{e_r} \cdot \mathbf{v}| \cdot f_{\mathbf{v}}(v_{xy}, v_z) \cdot v_{xy} dv_{xy} dv_z d\phi. \tag{3.1}$$

The reader is referred to figure 3.1 for the system geometry. Terms are defined as follows: $\mathbf{e}_\star$ is a unit vector in the $\star$ direction; $\mathbf{v} = \mathbf{v}_{xy} + \mathbf{v}_z$ is the particle velocity comprised of a component in the radial plane of the probe axis ($\mathbf{v}_{xy}$) and an axial component ($\mathbf{v}_z$), where $v_{xy}$ and $v_z$ denote their respective speeds; $\phi$ is the azimuth angle measured anticlockwise from the radial unit vector ($\mathbf{e_r}$) to the vector $\mathbf{v}_{xy}$; $q$ is the electric charge of the particle; $l_p$ and $r_p$ are the length and radius of the probe, respectively; $n$ is the particle number density; and $f_{\mathbf{v}}(v_{xy}, v_z)$ is an axis-symmetric velocity probability distribution function in three-dimensions at the probe sheath boundary, which has a radius of $r_s$. Note that:

$$\int_0^{2\pi} \int_{-\infty}^{+\infty} \int_0^{+\infty} f_{\mathbf{v}}(v_{xy}, v_z) \cdot v_{xy} dv_{xy} dv_z d\phi = 1. \tag{3.2}$$

The current collected during attractive and repulsive biases is calculated by adjusting the limits of equation 3.1 in order to integrate over different regions of the particle's velocity probability distribution function. There are several assumptions: the plasma bulk and probe sheath have a distinct boundary at a radial distance $r_s$ from the probe axis (no presheath); the sheath has a smooth monotonic potential profile; $l_p \gg r_s - r_p$ so that the collection of particles is independent of $v_z$ (integration limits in equation 3.1 show that all values of $v_z$ are allowed); transport in the probe sheath is collisionless; there are no sinks or sources of particles in the probe sheath; current collected by the ends of the probe is negligible ($l_p \gg r_p$); and the current passing through the probe sheath boundary is equal to the current collected by the probe.

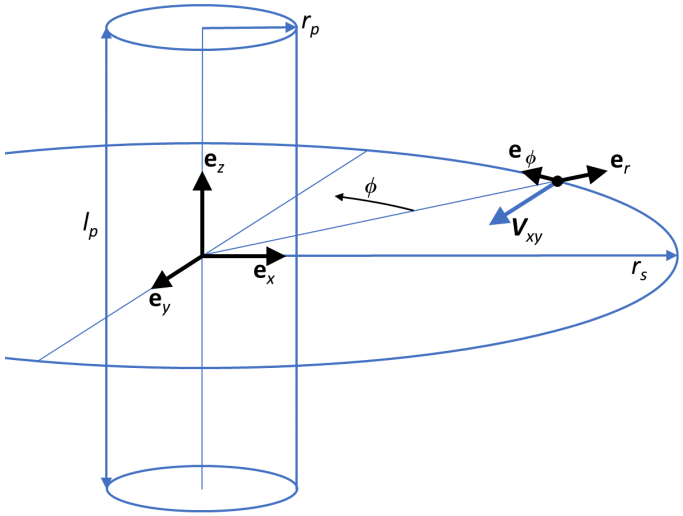


Figure 3.1: Coordinate system for cylindrical probe theory. Terms are defined in the text. Note that the axial component of velocity is not shown.

### 3.1.3 Collection of electrons under a repulsive bias

Repulsive electron current is considered in this section ($V - V_p < 0$) because the ion current can only be experimentally discriminated from the electron current for attractive ion collection.

#### 3.1.3.1 Maxwellian EEDF

The integration limits for equation 3.1 are calculated using conservation of energy and angular momentum, which leads to [144]:

$$I_e = 2en_eA_p \int_{\sqrt{\frac{2e(V_p-V)}{m_e}}}^{\infty} \left(1 - \frac{2e(V_p - V)}{m_e v_{xy}^2}\right)^{1/2} v_{xy}^2 f_{v_{xy}}(v_{xy}) dv_{xy}, \tag{3.3}$$

where $A_p = 2\pi r_p l_p$ is the probe surface area and $m_e$ is the electron mass. Counter-intuitively the electron charge is taken as $q = +e$ by convention, rather than as $q = -e$, so that the electron current collected by the probe has a positive polarity. The term $f_{v_{xy}}$ is the projection of the velocity probability distribution in the $\mathbf{e}_x\mathbf{e}_y$ plane:

$$f_{v_{xy}}(v_{xy}) \equiv \int_{-\infty}^{+\infty} f_{\mathbf{v}}(v_{xy}, v_z) dv_z. \tag{3.4}$$

The electron current to the probe is calculated by substituting a two-dimensional velocity probability distribution into equation 3.3 and integrating. If one assumes a Maxwellian distribution:

$$f_{v_{xy}} = \frac{1}{\hat{v}^2\pi}\exp\left[-\left(\frac{v_{xy}}{\hat{v}}\right)^2\right], \tag{3.5}$$

where $\hat{v} = (2k_BT_e/m_e)^{1/2}$, then the electron current collected by the probe is:

$$I_e(V) = \underbrace{\frac{A_p e n_e}{4}\left(\frac{8k_BT_e}{\pi m_e}\right)^{1/2}}_{I_{es}}\exp\left(\frac{e(V-V_p)}{k_BT_e}\right) = I_{es}\exp\left(\frac{e(V-V_p)}{k_BT_e}\right). \tag{3.6}$$

The electron saturation current, $I_{es}$, is the thermal electron current to the probe at the plasma potential when there is no sheath. The expression can be rearranged to give the electron density:

$$n_e = \frac{4I_{es}}{eA_p}\left(\frac{\pi m_e}{8k_BT_e}\right)^{1/2}. \tag{3.7}$$

This is known as the 'knee' method. The electron temperature can be calculated from equation 3.6:

$$k_BT_e = e\left(\frac{d(\ln I_e)}{dV}\right)^{-1}. \tag{3.8}$$

This implies that a plot of $\ln I_e$ against $V$ is linear for a Maxwellian EVDF (or equivalently EEDF) for $V - V_p < 0$.

#### 3.1.3.2 Bi-Maxwellian EEDF

A bi-Maxwellian EVDF is indicated by two distinct gradients in the $\ln I_e$ against $V$ plot; an example is shown in figure 3.2. In this case the electron current to the probe is:

$$I_e = I_c\exp\left(\frac{e(V-V_p)}{k_BT_c}\right) + I_w\exp\left(\frac{e(V-V_p)}{k_BT_w}\right), \tag{3.9}$$

where $I_c$ and $I_w$ are the saturation currents of the cold and warm populations, respectively; $T_c$ and $T_w$ are the cold and warm electron temperatures, respectively. In the limit $T_w > T_c$ and $V \ll V_p$, equation 3.9 can be approximated as:

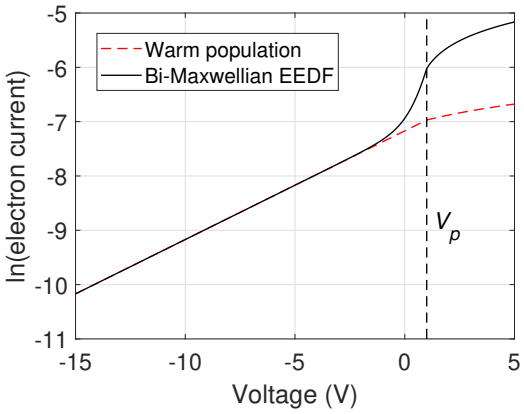


Figure 3.2: Natural logarithm of electron current against voltage for a theoretical bi-Maxwellian EEDF with properties [$n_c = 5 \times 10^{16}$ m$^{-3}$, $T_c = 0.5$ eV and $n_w = 1 \times 10^{16}$ m$^{-3}$, $T_w = 5$ eV] and a single Maxwellian EEDF with properties [$n_e = 1 \times 10^{16}$ m$^{-3}$, $T_e = 5$ eV].

$$\ln I_e \approx \frac{e(V - V_p)}{k_B T_w} + \ln(I_w). \tag{3.10}$$

Equation 3.10 is fit to the measured $\ln I_e$ against $V$ data in the region $V \ll V_p$ to obtain $T_w$ and $I_w$. The electron density of the warm component ($n_w$) is calculated using equation 3.7. Next, the warm component is subtracted from the total current to leave only the cold component:

$$\ln\left[I_e - I_w \exp\left(\frac{e(V - V_p)}{k_B T_w}\right)\right] = \frac{e(V - V_p)}{k_B T_c} + \ln(I_c). \tag{3.11}$$

Equation 3.11 is fit to the cold component to obtain $T_c$ and $I_c$, and the corresponding electron density ($n_c$) is calculated using equation 3.7.

An effective electron temperature ($T_{eff}$) can be defined based on the average energy of a three-dimensional bi-Maxwellian probability energy distribution ($f_{Ep}$):

$$< E >= \int_0^\infty E f_{E_p} dE = \frac{3k_B(f_c T_c + f_w T_w)}{2} = \frac{3k_B T_{eff}}{2}, \tag{3.12}$$

where $f_c$ and $f_w$ give the fraction of the components to the total number density. Thus:

$$k_B T_{eff} = k_B \left( \frac{n_c T_c + n_w T_w}{n_c + n_w} \right) = k_B \left( \frac{I_c T_c^{1/2} + I_w T_w^{1/2}}{I_c T_c^{-1/2} + I_w T_w^{-1/2}} \right). \tag{3.13}$$

#### 3.1.3.3 Non-Maxwellian EEDF

The Druyvesteyn formula [133][18, p. 80] calculates the EEDF of an isotropic plasma for a cylindrical (or any non-concave) probe in three-dimensions:

$$f_E^D(E) = \frac{4}{A_p e^2} \left( \frac{m_e E}{2e^2} \right)^{1/2} \cdot \frac{d^2 I_e}{dV^2}, \tag{3.14}$$

where energy is $E = e(V_p - V)$ in units of joules. This method has applicability when the EEDF appears non-Maxwellian. Integration of the EEDF gives the electron density:

$$n_e = \int_0^\infty f_E^D(E) dE, \tag{3.15}$$

and the average energy of the distribution defines an effective electron temperature:

$$< E >= \int_0^\infty E f_E^D(E) dE / n_e = \frac{3 k_B T_{eff}}{2}. \tag{3.16}$$

The Druyvesteyn EEDF will always yield the correct electron density when integrated over all electron energies even if the plasma is completely anisotropic [144], but the shape of the inferred EEDF is correct only when the plasma is isotropic. It should be highlighted that the theoretical expression for the electron current, which has to be differentiated twice, is given by equation 3.3 [144]. The electron current is independent of the component of velocity parallel to the probe axis ($v_z$), and so it is not possible to sample the entire velocity distribution from a single cylindrical probe orientation.

### 3.1.4 Collection of ions under an attractive bias

In general, attractive theories are applied to ion collection rather than electron collection because net ion current collection is less perturbing; hence, the discussion in this section focuses on singularly charged ions and $V - V_p < 0$.

Two groups of ions are collected by the probe. In order to explain this, it is insightful to consider the constraint on the values of $\phi$ allowed at the probe sheath edge for an ion to be collected by the probe. Conservation of energy and angular momentum leads to [142,

p. 181]:

$$\sin^2\phi(v_{xy}, V) \leqslant \underbrace{\left(\frac{r_p}{r_s}\right)^2 \cdot \left(1 + \frac{2e(V_p - V)}{m_i v_{xy}^2}\right)}_{A_v}, \tag{3.17}$$

where $m_i$ is the ion mass. This expression shows that only certain ion velocities at the sheath edge, characterised by $v_{xy}$ and $\phi$, can result in collection by the probe for a given probe potential and relative sheath thickness ($r_p/r_s$). This is a consequence of ion angular momentum inhibiting collection by the probe (explained in section 3.1.4.2). The extremities of the inequality correspond to the case of grazing ion incidence on the probe surface for each value of $v_{xy}$. The two groups of ions are defined based on the value of $v_{xy}$ relative to a critical speed given by the condition $A_v = 1$ [142, p. 183][143, p. 678]:

$$v^\star \equiv \left(\frac{2e(V_p - V)}{m_i(r_s^2/r_p^2 - 1)}\right)^{1/2}. \tag{3.18}$$

Ions with $v_{xy} \leqslant v^\star$ will automatically satisfy equation 3.17 because $A_v \geqslant 1$ (note the sinusoidal function) so they will definitely be collected by the probe once they pass the sheath radius, regardless of their $\phi$ value at the sheath edge. The ion collection is 'sheath limited' in this case. When $v_{xy} > v^\star$, equation 3.17 can only be satisfied for ions with certain values of $\phi$ at the sheath edge. These ions are 'orbit limited'.

#### 3.1.4.1 Thick sheath limit

In the thick sheath limit ($r_s - r_p \gg r_p$), the critical speed from equation 3.18 is reduced; hence, the sheath limited current is negligible and the collected current is 'orbital motion limited' (OML). The current collected by the probe is calculated using equation 3.1 with the integration limits given by equation 3.17 and ($v_{xy1} = v^\star \to 0$, $v_{xy2} = \infty$), with electric charge taken as $q = -e$ by convention. For the case of a Maxwellian velocity probability distribution function (equation 3.5) one obtains [143, p. 680]:

$$I_i = -A_p n_i e \left(\frac{k_B T_i}{2\pi m_i}\right)^{1/2} \frac{2}{\sqrt{\pi}} \left(1 - \frac{e(V - V_p)}{k_B T_i}\right)^{1/2}. \tag{3.19}$$

This expression was first derived in 1926 by Mott-Smith and Langmuir [17]. Applying the limit $T_i \to 0$ removes the ion temperature dependence in equation 3.19:

$$\lim_{T_i \to 0} I_i = -\frac{A_p n_i}{\pi} \left( \frac{2e^3 (V_p - V)}{m_i} \right)^{1/2}. \tag{3.20}$$

The plasma density is determined using the gradient ($G$) from a plot of $I_i$ against $(V_p - V)^{1/2}$:

$$n_i = \frac{-G\pi}{A_p} \left( \frac{m_i}{2e^3} \right)^{1/2}. \tag{3.21}$$

#### 3.1.4.2 Numerical solutions

The discussion up to now, in section 3.1, has not considered the exact form of the electric potential profile in the probe sheath: a monotonic function was assumed for both attractive and repulsive biases. Potential barriers in the probe sheath, however, can reduce the particle flux to the probe during attractive collection. This effect is not important for repulsive collection [25], and so the formulae given in section 3.1.3 are accurate. The formation of a potential barrier is demonstrated by considering the energy of an ion during attractive collection:

$$E = e(V(r) - V_p) + \frac{m_i (v_r^2 + v_\phi^2)}{2}, \tag{3.22}$$

and its angular momentum:

$$L = m_i r v_\phi, \tag{3.23}$$

where $v_r \equiv v_{xy} \cos\phi$ and $v_\phi \equiv v_{xy} \sin\phi$ are the radial and azimuthal speeds at a radius $r$ from the probe axis respectively, and $V \to V_p$ as $r \to \infty$. Combining the two equations gives:

$$E - \underbrace{\left( e(V(r) - V_p) + \frac{L^2}{2m_i r^2} \right)}_{U(r)} = \frac{m_i v_r^2}{2}, \tag{3.24}$$

where $U(r)$ is an effective potential energy barrier with an attractive electric potential term (negative polarity) and a repulsive contribution from angular momentum (positive polarity). Particles can only be collected if $E - U(r) \geqslant 0$ for all $r \geqslant r_p$, otherwise $v_r$ is imaginary at some point during the orbit. Local maxima in $U(r)$ can occur depending on $L$

and the electric potential profile $V(r)$ [25], and their presence will reduce the number of ions collected by the probe. The correct approach for calculating the probe current, therefore, is to solve the Poisson equation in order to determine self-consistent spatial profiles of electric potential, electron density and ion density. These calculations are difficult because all possible trajectories have to be considered, including orbits that are only deflected by the probe potential and not collected because they still contribute to the space potential.

A simplified model was proposed by Allen, Boyds and Reynolds (ABR) in 1957 [23] to calculate the electric potential around a spherical probe for the limiting case of zero ion temperature ($T_i = 0$). The theory assumes that the motion of ions from infinity to the probe surface is purely radial and collisionless. The results show that potential barriers do not form for these conditions, and so all ions are eventually collected by the probe. ABR theory was extended to cylindrical probes by Chen [24]. The first solution for finite $T_i$ was given by Bernstein and Rabinowitz in 1959 for the case of a monoenergetic ion energy distribution and collisionless conditions [145]. They considered the full range of possible ion orbits and the subsequent formation of potential barriers. Laframboise extended the theory to include a Maxwellian ion velocity distribution in 1966 [25] and this is still state-of-the-art today. The OML theory, detailed in section 3.1.4.1, is an excellent approximation of Laframboise theory when $r_p/\lambda_D < 3$ [146], where $\lambda_D$ is the Debye length, because the effect of potential barriers is negligible in this regime.

As $T_i \to 0$, one might expect the ABR-Chen and Laframboise theories to agree, but this is true only for spherical probes and not cylindrical probes [19, p. 16]. The disagreement arises because different ion currents are calculated, in cylindrical geometry, for an isotropic angular momentum distribution at infinity (Laframboise's approach) compared to zero angular momentum at infinity (ABR-Chen's approach). Laframboise theory is the correct approach because, in reality, ions will acquire a distribution of angular momentum through scattering processes far from the probe even if they are travelling at relatively slow speeds. ABR-Chen theory predicts a larger ion current for a given plasma density compared to Laframboise theory in the limit of $T_i \to 0$ because orbital motion and potential barriers reduce the collected current. Nevertheless, ABR-Chen theory has found applicability when collisions in the probe sheath destroy orbital motion and induce radial motion [21, 22, 58].

Analytical fits to the numerical solutions of the ABR-Chen and Laframboise theories have been performed by other researchers so that the theories can be readily applied to experimental data. Details of the parameterisations used in this research are given below.

**Parameterisation of ABR-Chen theory**

The solution to the ABR-Chen equation has been parameterised by Klagge [57, 147]. The ion current collected by the probe is:

$$I_i[\mathrm{A}] = -I_{norm} \cdot i_{ABR} = -I_{norm} \cdot a(\eta_p/b)^c, \tag{3.25}$$

where,

$$I_{norm} = r_p n_i l_p e \left( \frac{2\pi e T_e[\mathrm{eV}]}{m_i} \right)^{1/2}, \tag{3.26}$$

$$\eta_p = \frac{V_p - V}{T_e[\mathrm{eV}]}, \tag{3.27}$$

$$\xi_p = r_p/\lambda_D, \tag{3.28}$$

$$\begin{aligned} a &= 0.04 + (\xi_p + 0.6)^{0.05}, \\ b &= 0.09[\exp(-1/\xi_p) + 0.08], \\ c &= (\xi_p + 3.1)^{-0.6}. \end{aligned} \tag{3.29}$$

**Parameterisation of Laframboise theory**

The extensive numerical calculations by Laframboise have been parameterised by Chen for the case of $T_i = 0$ [146]. The correction to Laframboise theory for finite ion temperatures when $T_i < 0.1$ eV is negligible [25]. The assumption of room temperature ions ($T_i < 0.1$ eV) is common in discharge plasmas. Chen gives the ion current collected by the probe as:

$$I_i[\mathrm{A}] = -I_{norm} \cdot i_{Laf} = -I_{norm} \cdot \left( \frac{1}{\left[ A(\xi_p) \eta_p^{B(\xi_p)} \right]^4} + \frac{1}{\left[ C(\xi_p) \eta_p^{D(\xi_p)} \right]^4} \right)^{-1/4}, \tag{3.30}$$

where the coefficients are,

$$\begin{aligned} A &= a + \left( \frac{1}{b\xi_p^c} - \frac{1}{d\ln(\xi_p/f)} \right)^{-1}, \\ B, D &= a + b\xi_p^c \exp(-d\xi_p^f), \\ C &= a + b\xi_p^{-c}, \end{aligned} \tag{3.31}$$

| | $a$ | $b$ | $c$ | $d$ | $f$ |
|---|---|---|---|---|---|
| $A$ | 1.12 | 0.00034 | 6.87 | 0.145 | 110 |
| $B$ | 0.50 | 0.008 | 1.50 | 0.180 | 0.80 |
| $C$ | 1.07 | 0.95 | 1.01 | — | — |
| $D$ | 0.05 | 1.54 | 0.30 | 1.135 | 0.370 |

Table 3.1: Coefficients for calculating $ABCD(\xi_p)$ for Laframboise theory (reproduced from Chen [146]).

and $a, b, c, d$ are given in table 3.1.

## 3.2 Laser Thomson scattering

In this research, laser Thomson scattering measurements were performed in the incoherent regime using a specific scattering geometry. The aim of this section is to explain both the relevant theoretical background to the technique and how to extract electron properties from a measured spectrum. This section is organised as follows: (1) single electron scattering to explain the fundamental principles of Thomson scattering, including the scattering geometry; (2) incoherent scattering from multiple electrons; and finally, (3) interpretation of the scattering spectrum to obtain electron density and electron temperature.

### 3.2.1 Single electron Scattering

Thomson scattering is the elastic scattering of electromagnetic waves from free electrons in the plasma as described by classical electromagnetism. Consider a linearly polarised electromagnetic wave from a laser propagating along the $\mathbf{e}_i$ unit vector direction towards an electron. The electric field at time $t$ and position $\mathbf{x}$ is:

$$\mathbf{E}_i = \mathbf{E}_0 \exp[i(\mathbf{k}_i \cdot \mathbf{x} - \omega_i t)], \tag{3.32}$$

where $\mathbf{E}_0 = E_0 \mathbf{e}_0$ is the amplitude vector with magnitude $E_0$ in the $\mathbf{e}_0$ unit vector direction, $\omega_i$ is angular frequency, $\lambda_i = 2\pi c/\omega_i$ is wavelength, $c$ is the speed of light, and $\mathbf{k}_i = k_i \mathbf{e}_i = 2\pi \mathbf{e}_i/\lambda_i$ is wavevector. These quantities are measured in the laboratory frame of reference. Due to the electron motion relative to the laboratory, there are two Doppler shifts associated with the Thomson scattering process. These are demonstrated by figure 3.3. The first Doppler shift is the angular frequency of the incident wave measured in the

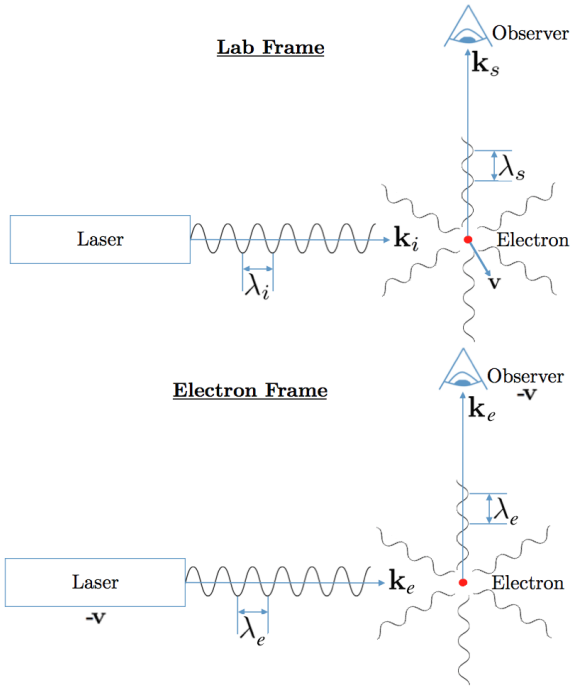


Figure 3.3: An electron is moving at velocity $\mathbf{v}$ relative to the laboratory frame, and so the laser frequency in the electron rest frame is doppler shifted. In addition, the frequency of the radiation emitted by the electron is Doppler shifted relative to an observer in the laboratory frame. Terms are defined in the text.

electron rest frame [66, p. 10]:

$$\omega_e = \omega_i - \mathbf{k}_i \cdot \mathbf{v}, \tag{3.33}$$

where $\mathbf{v}$ is the electron velocity. The magnetic field component of the incident electromagnetic wave can be neglected during the scattering event when the electron motion is non-relativistic [64]. The electron oscillates in the direction of the incident electric field (i.e. $\mathbf{E}_0$) resulting in the emission of electric-dipole radiation of angular frequency $\omega_e$ as measured in the electron rest frame. The corresponding wavevector of the scattered radiation originating from the electron's position is $\mathbf{k}_e = k_e \mathbf{e}_s = 2\pi \mathbf{e}_s / \lambda_e$, where $\mathbf{e}_s$ is the scattering unit vector pointing in the direction of an observer and $\lambda_e = 2\pi c / \omega_e$.

The second Doppler shift is the angular frequency of the electron-emitted radiation that is measured in the laboratory frame [66, p. 10]:

$$\omega_s = \omega_e + \mathbf{k}_s \cdot \mathbf{v}, \tag{3.34}$$

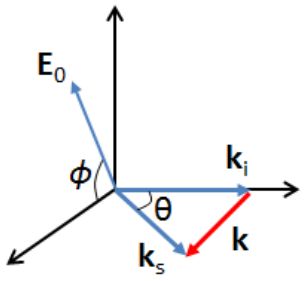


Figure 3.4: The geometry of the incident and scattered wavevectors with respect to the laser polarisation. The electron is located at the origin.

where $\mathbf{k}_s = k_s\mathbf{e}_s = 2\pi\mathbf{e}_s/\lambda_s$ is the scattered wavevector originating from the electron's position measured in the laboratory frame by an observer, $\lambda_s = 2\pi c/\omega_s$ is the wavelength measured by the observer, and the electron velocity has remained constant during the scattering process.

By defining the following vector (see figure 3.4):

$$\mathbf{k} \equiv \mathbf{k}_s - \mathbf{k}_i, \tag{3.35}$$

the change in the angular frequency of the laser due to the scattering process is:

$$\omega_s - \omega_i = \mathbf{k} \cdot \mathbf{v} = kv_k, \tag{3.36}$$

where $v_k$ is the component of the electron velocity in the $\mathbf{k}$ direction, and the magnitude of the $\mathbf{k}$ vector is:

$$k = |\mathbf{k}| \approx 2k_i \sin(\theta/2), \tag{3.37}$$

using $\lambda_i \approx \lambda_s$ for $v_k \ll c$ and $\sin^2(\theta/2) = (1-\cos\theta)/2$. Therefore, the frequency shift of the scattered light is dependent on both the wavelength of the incident wave and a one-dimensional component of the electron's total velocity with the geometry of the scattering system determining the direction of sensitivity (i.e. $\mathbf{k}$). Equation 3.36 can also be written in terms of a wavelength shift ($\Delta\lambda = \lambda_s - \lambda_i$), which is a more common laboratory unit:

$$\Delta\lambda \approx \frac{-\lambda_i^2 k v_k}{2\pi c}. \tag{3.38}$$

Next, one will consider the differential cross-section for Thomson scattering because

the radiated power is not uniformly distributed in space [66, p. 15]:

$$\frac{d\sigma_T}{d\Omega} = r_c^2(1 - \sin^2\theta\cos^2\phi), \tag{3.39}$$

where $r_c = 2.818 \times 10^{-15}$ m is the classical electron radius, $\theta$ is the angle between $\mathbf{k}_i$ and $\mathbf{k}_s$, and $\phi$ is the angle between the electric field polarisation of the laser and the scattering plane; see figure 3.4 for angle definitions. The maximum power radiated, which is proportional to the differential cross-section, occurs when $\mathbf{k}$ is perpendicular to $\mathbf{E}_0$ ($\phi = \pi/2, 3\pi/2$ rad and/or $\theta = 0, \pi$ rad; note that $\theta = 0$ rad corresponds to $\mathbf{k} \approx 0$), and there is no scattered radiation along the length of the dipole axis ($\phi = 0, \pi$ rad and $\theta = \pi/2, 3\pi/2$ rad).

Finally, one will consider the polarisation of the scattered light. It is assumed that the scattered radiation is detected in the far field (see figure 3.5). The electric field amplitude vector of the scattered wave is [66, p. 14]:

$$\mathbf{E}_{s0} = E_{s0}[\mathbf{e}_s \times (\mathbf{e}_s \times \mathbf{e}_0)], \tag{3.40}$$

where $E_{s0}$ is the magnitude, and definitions for the unit vectors, $\mathbf{e}_0$ and $\mathbf{e}_s$, can be found in the immediate text following equations 3.32 and 3.34, respectively. The polarisation state is linear, which allows one to use a linear polariser at the entrance of a spectrometer to attenuate unpolarised noise signals (e.g. plasma emission) whilst allowing the Thomson scattering signal to pass. Most Thomson scattering experiments have $\phi = \pi/2$ rad to maximise the differential cross-section; thereby, the polarisation axis of the incident and scattered waves are parallel to one another.

### 3.2.2 Coherent and incoherent scattering from multiple electrons

When there are multiple electrons participating in Thomson scattering, the total electric field is given by the superposition of the individual waves. The electric field of a scattered wave, produced from a single electron, at the observer's position in the far field at time $t$ is [66, pp. 14, 15]:

$$\mathbf{E}_s = \mathbf{E}_{s0}\exp\Big[i\big(k_s r_o - \omega_s t - \mathbf{k}\cdot\mathbf{r}_e(t=0)\big)\Big], \tag{3.41}$$

where $r_o$ is the radial distance from the coordinate system origin to the observer's position and $\mathbf{r}_e(t=0)$ is the radial distance vector from the system origin to the electron's position

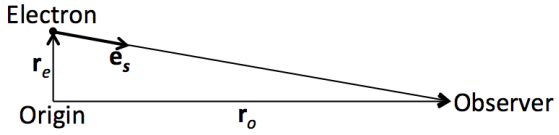


Figure 3.5: The electron ($\mathbf{r}_e$) and observer ($\mathbf{r}_o$) position vectors, and the scattering unit vector $\mathbf{e}_s$. The origin is located so that the radiation is detected in the far field: $|\mathbf{r}_e| = r_e \ll |\mathbf{r}_o| = r_o$.

at the start of the scattering event[1]; see figure 3.5. Each scattered wave has the same amplitude, but there are different values of $\lambda_s$ and $\mathbf{r}_e(t=0)$. The Poynting vector at the observer's position at time $t$ from multiple electrons is:

$$\mathbf{S}[\mathrm{W{\cdot}m^{-2}}] = c\epsilon_0 \sum_i^N \mathbf{E}_{s,i} \times \left(\mathbf{e}_s \times \sum_j^N \mathbf{E}_{s,j}\right) = \left(c\epsilon_0 \sum_i^N \mathbf{E}_{s,i} \cdot \sum_j^N \mathbf{E}_{s,j}\right)\mathbf{e}_s, \tag{3.42}$$

where $N$ is the number of electrons in the detection volume, the subscripts $i$ and $j$ refer to the scattered wave from each electron, and $\epsilon_0$ is the permitivity of free space. The magnitude of the time-averaged Poynting vector can be written as two separate contributions [64]:

$$|\langle \mathbf{S} \rangle| = \underbrace{N|\langle \mathbf{S}_{single} \rangle|}_{\text{incoherent term}} + \underbrace{c\epsilon_0 \left\langle \sum_i^N \mathbf{E}_{s,i} \cdot \sum_{j \neq i}^N \mathbf{E}_{s,j} \right\rangle}_{\text{coherent term}}, \tag{3.43}$$

where $|\langle \mathbf{S}_{single} \rangle| = c\epsilon_0 E_{s0}^2/2$ is the average power flux produced from a single radiating electron with its scattered electric field given by equations 3.40 and 3.41. The incoherent term is simply the sum of the contributions from each electron; whereas the coherent term is dependent on the phase difference between the scattered waves.

The phase difference of two scattered waves of wavelength $\lambda_s$ depends on the initial position of the electrons (equation 3.41), which are separated by a distance of the order of millimetres in a typical experimental setup for a low temperature plasma source. If one considers an electron at the initial position $\mathbf{r}_e(t=0) + \Delta\mathbf{r}_e$, then the condition for constructive interference with a scattering electron at the initial position $\mathbf{r}_e(t=0)$, with both electrons radiating at wavelength $\lambda_s$ in the laboratory frame, is:

[1]The observer receives the radiation at a later time due to the speed of light being finite.

$$\mathbf{k} \cdot (\mathbf{r}_e(t=0) + \Delta\mathbf{r}_e) - \mathbf{k} \cdot \mathbf{r}_e(t=0) = k\Delta r_{ek} = 2\pi n, \tag{3.44}$$

with integer $n$ and $\Delta r_{ek}$ is the initial position offset projected along $\mathbf{k}$. It is, therefore, convenient to write the spatial separation along $\mathbf{k}$ between two electrons as $(2\pi n/k) + x$, where $x < 2\pi/k$, and $2\pi/k$ is the scale length over which coherence effects are probed [67].

Returning to equation 3.43, the coherent term will equal zero when the distribution of $x$ values from $N$ electrons is random. The shortest correlation length scale in a plasma is the Debye length [64], which determines the radius of the electron cloud surrounding positive ions. When the condition $2\pi/k \ll \lambda_D$ is satisfied, the scattering experiment will resolve the 'random' positions of electrons within a small volume element of the Debye sphere; hence, the coherent term is zero, and one operates in the incoherent regime. In contrast, electron positions are correlated over the length scale $2\pi/k \geqslant \lambda_D$ through electron density fluctuations caused by, for example, ion acoustic waves and/or the plasma frequency; therefore, one operates in the coherent regime in this case.

The influence of coherent effects is usually described by the Salpeter parameter [68]:

$$\alpha \equiv \frac{1}{k\lambda_D}, \tag{3.45}$$

where $\alpha \ll 1$ for the incoherent regime. An upper limit for this thesis is $\alpha \sim 0.08$ for the case of $n_e = 10^{20}$ m$^{-3}$ and $T_e = 1$ eV, with $\theta = \pi/2$ rad and $\lambda_i = 532$ nm. Van de Sande [66, p. 31] has shown that for $\alpha = 0.3$ and $T_e = 1$ eV, electron density is underestimated by 7% and electron temperature is overestimated by 21% when coherence effects are neglected. Therefore, the incoherent scattering approximation is valid in this research.

### 3.2.3 Interpretation of an incoherent scattering spectrum

In this section an expression for an incoherent scattering spectrum in terms of experimental units - counts and wavelength - and the electron velocity distribution function (EVDF) is derived. Following on from this, expressions for electron density, electron temperature and drift velocity are derived.

The discussion in section 2.2.1 highlights that shot noise can be significant when laser Thomson scattering is applied to low temperature plasma sources. This is a quantum phenomenon, and so the preferred unit in section 3.2.3 is photon number as opposed to scattered power. In the incoherent regime, the total number of photons detected is the

average number of photons scattered per electron multiplied by the number of electrons in the detection volume: this corresponds to the incoherent term in equation 3.43. Consider a pulsed laser of wavelength $\lambda_i$, an average power of $P_i$, and a pulse repetition rate of $\nu_l$; a collection solid angle of $\Delta\Omega$; a detection volume of length $L$; and an integration time of $t_T$, then the total number of Thomson scattering photons collected for an ideal system is:

$$N_{Ti} = \nu_l t_T N_l n_e L \frac{d\sigma_T}{d\Omega} \Delta\Omega, \tag{3.46}$$

where the number of laser photons entering the detection volume per pulse is $N_l = \lambda_i P_i/(hc\nu_l)$. It is assumed that the plasma is optically thin so that each photon is scattered a maximum of once.

One will now consider the shape of the scattering spectrum. The wavelength shift of a scattered photon is proportional to $v_k$ (equation 3.38). Consequently, the probability distribution for the wavelength of the scattered photon ($S_\lambda$) is directly related to the electron velocity probability distribution function in the **k** direction ($f_k$):

$$S_\lambda(\lambda_s)d\lambda_s = f_k \frac{dv_k}{d\lambda_s} d\lambda_s \approx \frac{-c}{2\lambda_i \sin(\theta/2)} \cdot f_k(\lambda_s)d\lambda_s, \tag{3.47}$$

where $S_\lambda(\lambda')d\lambda_s$ is the probability that the scattered photon has wavelength $\lambda'$ within the range $d\lambda_s$, and equations 3.37 and 3.38 have been used to relate $v_k$ and $\lambda_s$:

$$v_k(\lambda_s) = \frac{2\pi c}{k}\left(\frac{1}{\lambda_s} - \frac{1}{\lambda_i}\right) \approx \frac{-c\Delta\lambda}{2\lambda_i \sin(\theta/2)}. \tag{3.48}$$

The total scattering intensity recorded by the detector is proportional to $N_{Ti}$ and the shape of the spectrum is given by equation 3.47. The expression for an ideal incoherent Thomson scattering spectrum in terms of photon number and wavelength is:

$$f_{N\lambda}(\lambda_s)d\lambda_s = N_{Ti} S(\lambda_s)d\lambda_s = N_{Ti} \cdot \frac{-c}{2\lambda_i \sin(\theta/2)} \cdot f_k(\lambda_s)d\lambda_s. \tag{3.49}$$

Note that $f_{N\lambda}(\lambda_s)$ is proportional to the EVDF, defined as $n_e f_k(v_k)$. Integration of equation 3.49 across all wavelengths gives:

$$\int_0^{+\infty} f_{N\lambda}(\lambda_s)\lambda_s = N_{Ti}. \tag{3.50}$$

For a real experiment, however, the number of photons detected is $< N_{Ti}$ because of non-

ideal optical components and the quantum efficiency of the detector is less than unity. Moreover, integrating a measured spectrum gives a unit of counts·nm rather than photon number. These considerations are incorporated into the factor $C_0$ so that the spectrum equation in units of counts and wavelength is:

$$f_{c\lambda}(\lambda_s)d\lambda_s = C_0 N_{Ti} \cdot \frac{-c}{2\lambda_i \sin(\theta/2)} \cdot f_k(\lambda_s)d\lambda_s. \tag{3.51}$$

The term $C_0$ is defined by the ratio of the measured integrated spectrum ($N_{Tc}$) in units of counts·nm to the number of Thomson scattering photons collected for an ideal system:

$$C_0 \equiv \frac{\int_0^{+\infty} f_{c\lambda}(\lambda_s)\lambda_s}{\int_0^{+\infty} f_{N\lambda}(\lambda_s)\lambda_s} = \frac{N_{Tc}}{N_{Ti}}. \tag{3.52}$$

#### 3.2.3.1 Electron density

Using equations 3.46 and 3.52 an expression for electron density is:

$$n_e = \frac{N_{Tc}}{C_0 \nu_l L \Delta\Omega \cdot t_T N_l \frac{d\sigma_T}{d\Omega}}. \tag{3.53}$$

For this research, the term $C_0 \nu_l L \Delta\Omega$ was calculated via Rayleigh scattering of room temperature argon gas, $t_T$ was selected by the experimentalist, $N_l$ was measured using a laser power meter, and the differential cross-section is given by equation 3.39 ($\phi = \theta = \pi/2$ rad); hence, absolute electron densities were determined.

**Rayleigh scattering calibration**

Rayleigh scattering is the elastic scattering of electromagnetic radiation from electrons bound to heavy species, such as atoms, ions and molecules. The Doppler broadening effect is less for a Rayleigh scattering spectrum compared to a Thomson scattering spectrum because heavy species move at slow speeds relative to free electrons. The incoherent Rayleigh scattering spectrum in terms of counts and wavelength is analogous to equation 3.51, which was derived for Thomson scattering:

$$f_{R\lambda}(\lambda_s)d\lambda_s = C_0 N_{Ri} \cdot \frac{-c}{2\lambda_i \sin(\theta/2)} \cdot f_{Rk}(\lambda_s)d\lambda_s, \tag{3.54}$$

where $f_{Rk}(\lambda_s)$ is the one-dimensional velocity probability distribution of the heavy species in the direction of $\mathbf{k}$. The total number of Rayleigh scattering photons for an ideal system

when considering scattering from a gas of density $n_g$ and integration time $t_R$ is:

$$N_{Ri} = \nu_l t_R N_{Rl} n_g L \frac{d\sigma_R}{d\Omega} \Delta\Omega, \tag{3.55}$$

where $N_{Rl}$ is the number of laser photons per pulse and $d\sigma_R/d\Omega$ is the Rayleigh scattering differential cross section: for ground-state argon this is equal to $d\sigma_R/d\Omega = 5.4 \times 10^{-32}$ $\mathrm{m^2{\cdot}sr^{-1}}$ with $\theta = \phi = \pi/2$ rad [66, p. 20].

The calibration procedure was to measure the total Rayleigh scattering signal ($C_0 N_{Ri}$) from room temperature argon gas as a function of gas pressure. The gas density $n_g$ was calculated using the ideal gas law and $N_{Rl}$ was measured using a laser power meter (note $N_{Rl} \approx N_l$ was selected). The gradient of a linear plot of $C_0 N_{Ri}$ against $n_g$ was used to calculate $C_0 \nu_l L \Delta\Omega$.

#### 3.2.3.2 Electron temperature and drift velocity

This section details how electron temperature is calculated when the EVDF is Maxwellian or bi-Maxwellian, including the presence of a drift velocity. This was the case for all of the measurements reported in this thesis. Details of how to interpret a non-Maxwellian EVDF are given in reference [66, p. 26].

**Maxwellian EVDF**

The one-dimensional probability velocity distribution function for a Maxwellian distribution is a Gaussian curve:

$$f_k = \frac{1}{\hat{v}\pi^{1/2}} \exp\left[ -\left( \frac{v_k}{\hat{v}} \right)^2 \right] = \frac{1}{\hat{v}\pi^{1/2}} \exp\left[ -\left( \frac{-\Delta\lambda c}{2\lambda_i \sin(\theta/2)\hat{v}} \right)^2 \right], \tag{3.56}$$

where $\hat{v} = (2k_B T_e/m_e)^{1/2}$ is the most probable electron energy and $\Delta\lambda = \lambda_s - \lambda_i$. The scattering spectrum (equation 3.51) will also have a Gaussian shape because the spectrum is proportional to $f_k$. The half $1/e$ width of the measured scattering spectrum is at $\Delta\lambda = \Delta\lambda_{1/e} = \lambda_{1/e} - \lambda_i$:

$$\frac{1}{e} = \frac{f_{c\lambda}(\lambda_s = \lambda_{1/e})}{f_{c\lambda}(\lambda_s = \lambda_i)} = \exp\left[ -\left( \frac{-\Delta\lambda_{1/e} c}{2\lambda_i \sin(\theta/2)\hat{v}} \right)^2 \right]. \tag{3.57}$$

Rearranging for electron temperature gives:

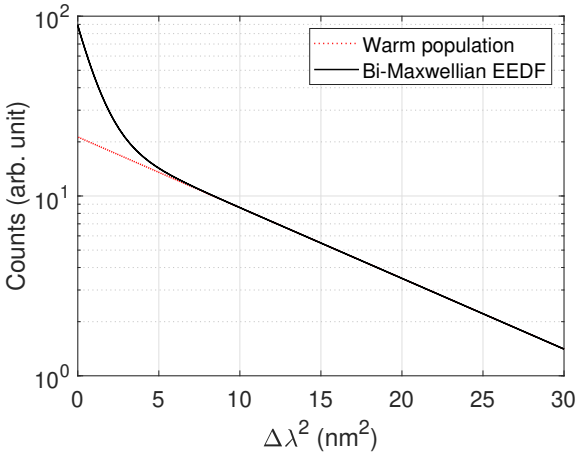


Figure 3.6: Theoretical Thomson scattering spectrum for the case of a bi-Maxwellian EVDF with properties ($T_c = 0.5$ eV, $f_c = 0.5$) and ($T_w = 5$ eV, $f_w = 0.5$)

$$k_B T_e = \frac{m_e c^2}{8\sin^2(\theta/2)} \left( \frac{\Delta\lambda_{1/e}}{\lambda_i} \right)^2. \tag{3.58}$$

Moreover, the area under a measured spectrum is:

$$N_{Tc} = A\Delta\lambda_{1/e}\pi^{1/2}, \tag{3.59}$$

where $A$ is the amplitude of the Gaussian.

**Bi-Maxwellian EVDF**

A one-dimensional bi-Maxwellian electron velocity probability distribution function has the form:

$$f_k = \frac{f_c}{\hat{v}_c \pi^{1/2}} \exp\left[ - \left( \frac{v_k}{\hat{v}_c} \right)^2 \right] + \frac{f_w}{\hat{v}_w \pi^{1/2}} \exp\left[ - \left( \frac{v_k}{\hat{v}_w} \right)^2 \right], \tag{3.60}$$

where $f_c$ and $f_w$ are the fractions of the total electron density that each electron population contributes ($f_c + f_w = 1$), $\hat{v}_c = (2k_B T_c/m_e)^{1/2}$ and $\hat{v}_w = (2k_B T_w/m_e)^{1/2}$. An example theoretical spectrum is shown in figure 3.6; a Gaussian curve appears linear on these axes. The electron temperature of each population is calculated using equation 3.58.

**Drift velocity**

For the case of a Maxwellian EVDF, the measured spectrum has the general form:

$$f_{c\lambda}(\lambda_s) = A\exp\left[-\left(\frac{\lambda_s - \lambda_d}{\Delta\lambda_{1/e}}\right)^2\right], \tag{3.61}$$

where $A$, $\lambda_d$ and $\Delta\lambda_{1/e}$ are fitting coefficients. A drift velocity is present when $\lambda_d \neq \lambda_i$. The drift velocity is calculated using equation 3.38:

$$v_d = \frac{2\pi c(\lambda_i - \lambda_d)}{\lambda_i^2 k}. \tag{3.62}$$

The EVDF for a Maxwellian or bi-Maxwellian distribution with a drift velocity ($v_d$) has $v_k \rightarrow v_k - v_d$ in equations 3.56 and 3.60, respectively.

# Chapter 4

# Experimental setup

In this chapter the experimental apparatus and procedures for Langmuir probe and laser Thomson scattering measurements in DC magnetron and HiPIMS discharges are detailed. The first section describes the magnetron sputtering source; the second section is about the Langmuir probe system; and the final section is concerned with laser Thomson scattering.

## 4.1 Magnetron sputtering system

This section is split into three parts: (1) a general description of the vacuum system; (2) measurements of the magnetron's magnetic field configuration; and (3) a description of the power supplies used.

### 4.1.1 Vacuum system

A schematic of the experimental apparatus is shown in figure 4.1. A VTech 150 series unbalanced magnetron (supplied by GENCOA Ltd) equipped with a 150 mm diameter planar tungsten target (purity $> 99.95\%$) was mounted vertically above the vacuum chamber. The perimeter of the target was surrounded by a ground shield which was positioned $\sim 5$ mm above its surface. The chamber was pumped down to a base pressure of $\sim 1.5 \times 10^{-3}$ Pa, as measured by an inverted magnetron gauge (G2 [Edwards AIM-X]), using a turbomolecular pump (Pfeiffer TMU071P) backed by a rotary pump (1 [Edwards RV3]). The height of the target surface was adjustable with respect to the diagnostic alignment. Argon gas ($> 99.99\%$ purity) was fed into the vacuum chamber using a mass flow controller (MFC [MKS 1179A]) and the argon pressure was monitored using a capacitance manometer of

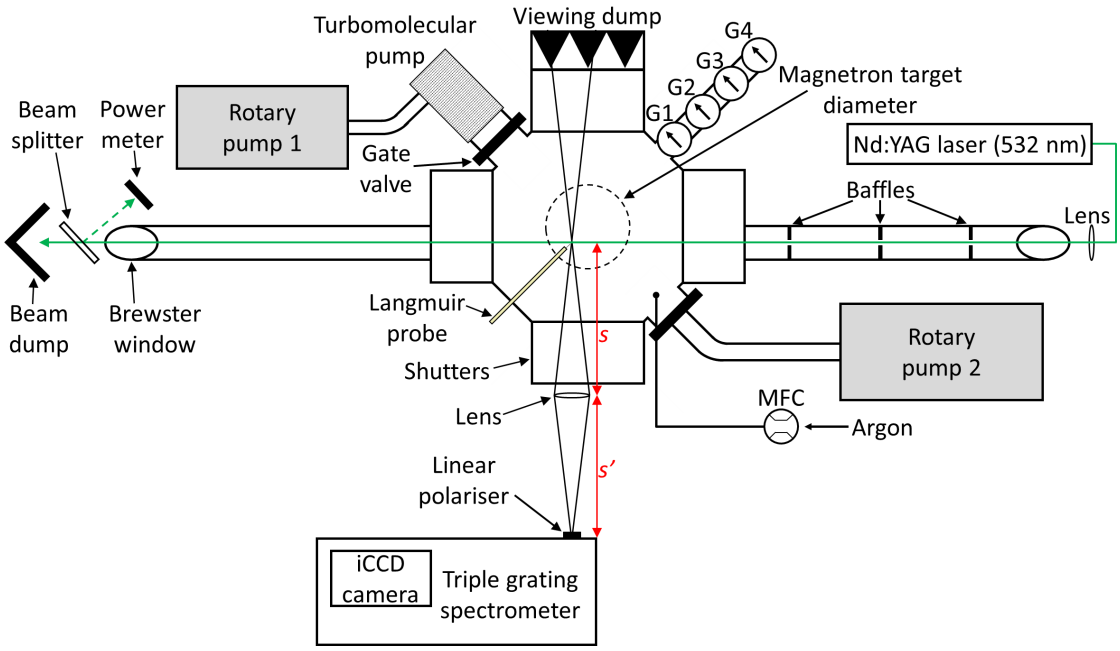


Figure 4.1: Schematic of the experimental apparatus for laser Thomson scattering and Langmuir probe measurements. The function of each component is described in the text. The following abbreviations have been used: mass flow controller (MFC); intensified charge-coupled device (iCCD); pressure gauge (G1-G4); object distance ($s$); and image distance ($s'$).

range $1.33\times10^{-3}-1.33\times10^{1}$ Pa (G4 [MKS Baratron 627]). Another capacitance manometer, of range $1.33\times10^{0}-1.33\times10^{4}$ Pa (G3 [MKS Baratron 626]), and rotary pump (2 [Edwards E2M40]) were installed on the chamber for use during the Rayleigh scattering calibration procedure (practical details given in section 4.3.2). In addition, an active Pirani gauge (G1 [Edwards APG100-XM]) was installed for monitoring the chamber pressure from atmospheric pressure down to $1\times10^{-2}$ Pa.

### 4.1.2 Magnetron magnetic field

The magnetic field configuration of the unbalanced magnetron in the radial-height ($r-z$) plane is shown in figure 4.2. The magnitude and direction of the magnetic field were measured using a digital Gauss meter with its axial probe (Hirst GM04) mounted on a two-dimensional rail. The main 'racetrack' erosion is at ($r\approx48$ mm, $z=0$ mm), which

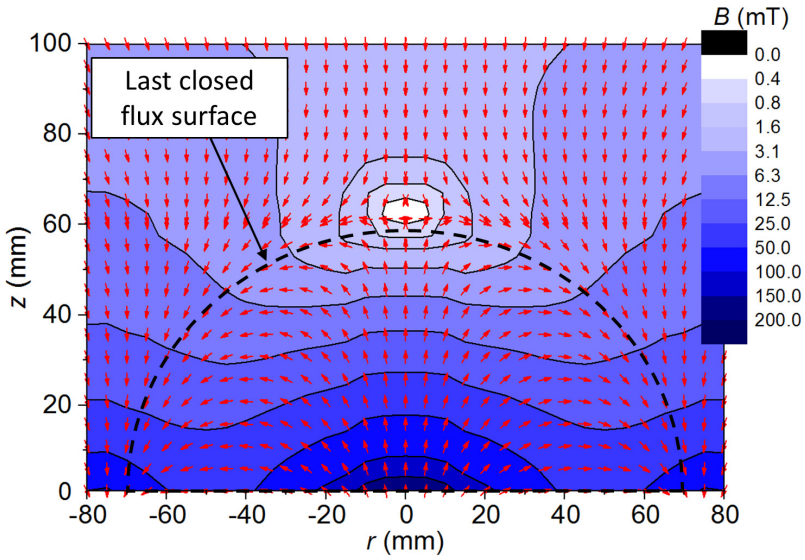


Figure 4.2: The measured magnetic field configuration of the magnetron in the radial-height ($r - z$) plane. The origin of the system corresponds to the centre of the target surface. The last closed flux surface is highlighted and the magnetic null is located at ($r = 0$ mm, $z = 61$ mm). For reference, the main racetrack erosion is at ($r \approx 48$ mm, $z = 0$ mm).

corresponds to the position where the magnetic field is radial on the target surface, and the magnetic null is located at ($r = 0$ mm, $z = 61$ mm). In section 4.3.4, the Langmuir probe and laser Thomson scattering measurement positions are described and illustrated using schematic diagrams for clarity. The reader should refer to figure 4.2 for a detailed view of the magnetic field configuration.

### 4.1.3 Power supplies

For DC magnetron operation, a Pinnacle Plus power supply (Advanced Energy Industries, Inc.) was used.

The HiPIMS power supply was a Sinex 3 unit (Chemfilt Ionsputtering AB Ltd.). The target voltage $V_d(t)$ was measured using a $\times 100$ voltage probe (Tektronix P5100) and the discharge current $I_d(t)$ was measured using a Pearson current monitor (model 110A). The outputs were displayed on an oscilloscope (Tektronix DPO3034) and then transferred to a personal computer for analysis. A code written in MATLAB calculated time-average

power and the peak power density at the target, which was normalised by the area of the entire target in units of W·cm$^{-2}$. These quantities, in addition to the chamber pressure, were used to characterise the discharges. Note that the calculated power densities are lower bounds because, in reality, the discharge current is localised above the racetrack region.

The instantaneous discharge power is:

$$P(t) = I_d(t)V_d(t), \tag{4.1}$$

and the time-average power is:

$$P_{ave} = \int_0^w I_d(t)V_d(t)f dt, \tag{4.2}$$

where $w$ and $f$ are the HiPIMS pulse-width and frequency, respectively.

## 4.2 Langmuir probe system

This section is split into three parts: (1) a description of the Langmuir probe used in the experiments; (2) the data acquisition systems for DC magnetron and HiPIMS measurements; and (3) the procedure for implementing both the electron and ion collection theories which were described in section 3.1.

### 4.2.1 Probe construction

A schematic of the Langmuir probe is shown in figure 4.3. Tungsten wire with purity 99.95% and radius $r_p$ was fed through alumina ceramic tubing, which had an outer diameter (OD) of 2 mm (C3), and was exposed to the plasma to form the probe tip. Another ceramic of OD=1 mm (C4) was coaxially inserted into C3 and recessed by $\sim$ 2.5 mm from the plasma facing end. This ensured that the tungsten wire did not make contact with the sputter coated region of C3, otherwise there would be a significant increase in the surface area for charge collection, leading to increased plasma perturbation and erroneous calculation of plasma parameters. Figure 4.3(a) shows the two tip configurations: 'L' shaped and 'straight'. For the 'L' shaped probe, the length of the probe ($l_p$) was taken as the length perpendicular to the axis of the ceramic. The length parallel to the ceramic axis ($\sim$ 0.25 mm) was neglected during the data analysis.

The same probe stem was used for all measurements (figure 4.3(b)), but several probe

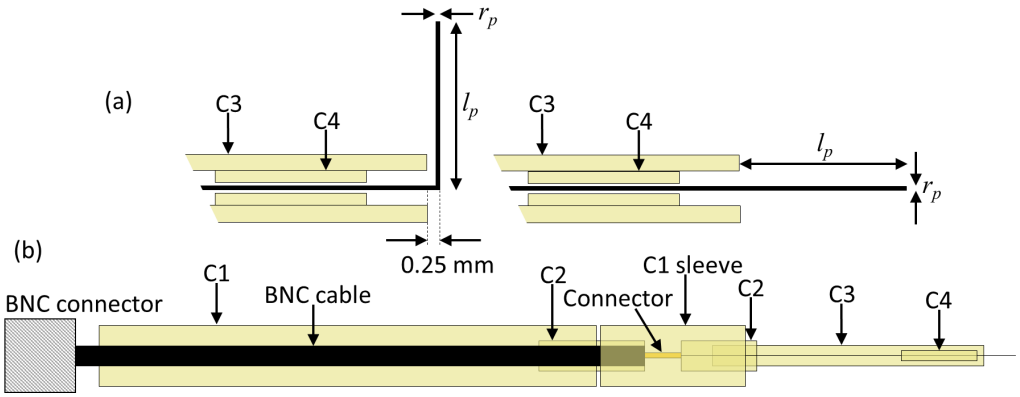


Figure 4.3: (a) Langmuir probe tip configurations: 'L' shaped and a 'straight' probe. The probe tip length and radius are $l_p$ and $r_p$, respectively. (b) The Langmuir probe stem with the various alumina ceramic tubes labelled (outer diameter/inner diameter): C1 (6/4 mm), C2 (3/2.1 mm), C3 (2/1.2 mm) and C4 (1/0.5 mm).

tips were used; their dimensions ($r_p$ and $l_p$) are given when relevant. The stem consisted of a BNC cable inserted into an OD=6 mm ceramic tube (C1). The ground shield in the BNC cable provides shielding from electromagnetic interference. The probe was connected to the data acquisition system by a BNC connector. At the plasma facing end, the BNC cable was terminated by a male D-sub connector, which protruded out the end of an OD=3 mm ceramic tube (C2). Vacuum seals were formed between C1 and C2, and the male connector and C2 using vacuum epoxy resin. Furthermore, there was a vacuum seal between C1 and the chamber flange using an O-ring. The probe tip was attached to the male connector by soldering the tungsten wire to a female D-sub connector, which was encased by ceramic (C2). A sleeve of ceramic C1 was placed over the D-sub connection to prevent exposure to the plasma.

### 4.2.2 Data acquisition

The probe stem was inserted radially into the vacuum chamber as demonstrated by figure 4.1. A schematic of the Langmuir probe circuit is shown in figure 4.4. The voltage applied to the probe was measured using a $\times 10$ voltage probe (Tektronix P6139A) at the base of the probe stem and the current in the circuit was determined by measuring the voltage drop across a sense resistor ($Z_{sense}$) using a precision difference amplifier (AD8479). The

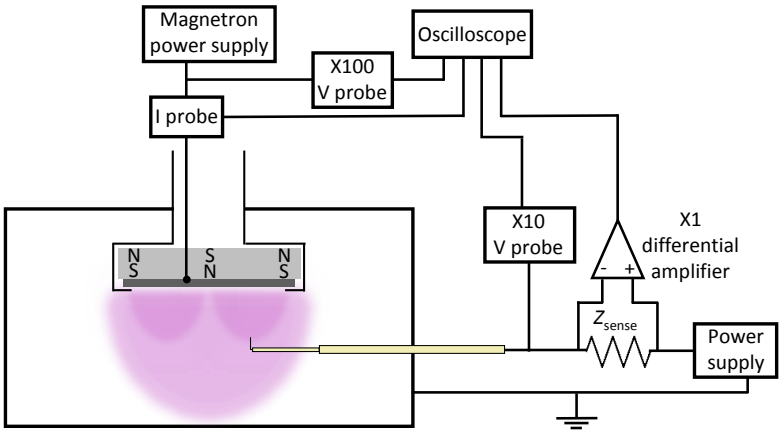


Figure 4.4: The Langmuir probe data acquisition system. For measurements during DC plasma conditions, the probe power supply outputs a voltage ramp, whereas during HiP-IMS, the probe power supply outputs a constant voltage. The probe voltage is measured using a $\times 10$ voltage probe and the current is determined by measuring the voltage drop across a sense resistor ($Z_{sense}$). The oscilloscope triggering settings are explained in the text.

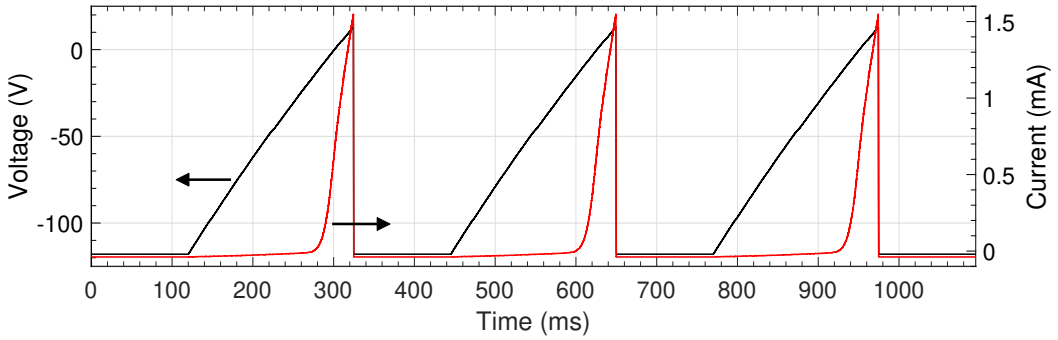


Figure 4.5: Experimental data from this research demonstrating the voltage waveform applied to the probe and the corresponding probe current during DC magnetron operation.

value of $Z_{sense}$, the voltage waveform applied to the probe, and the oscilloscope (Tektronix DPO3034) triggering settings were dependent on the mode of magnetron operation.

To generate a probe $IV$ characteristic during DC magnetron operation, a sawtooth voltage waveform was applied to the probe and the resultant output from the differential amplifier was recorded. The maximum current of the probe power supply was 25 mA and

the value of the sense resistor was $Z_{sense} = 68.3\ \Omega$. The waveforms were averaged over $\geq 50$ cycles using the oscilloscope, which was triggered by the sawtooth voltage waveform, and the data was transferred to a personal computer for analysis. Typical probe current-voltage waveforms are demonstrated using experimental data from this research in figure 4.5. The experimental details for these measurements are not important, rather, these waveforms are displayed for illustrative purposes only. The $IV$ characteristics were constructed using MATLAB software, with resolutions of $\sim 0.02$ V and $\lesssim 0.1\ \mu$A, by replacing the time axis of the probe current waveforms with the corresponding probe voltage. Measurements were routinely compared to check for increased probe surface area due to sputter coating.

The peak-to-peak voltage and DC offset of the sawtooth waveform were adjusted to limit the electron saturation current to the probe whilst acquiring the full ion saturation region (up to -120 V). The total period of the waveform was 325 ms with a duty cycle of 63%. During the off-time in the period, the probe potential was held constant at $-120$ V for ion bombardment cleaning. In addition, the probe was cleaned by biasing the probe into the electron saturation region so that the tungsten wire glowed before a set of measurements.

To acquire time-resolved probe measurements for HiPIMS, a DC power supply was manually varied instead of the sawtooth waveform. The maximum current of the probe

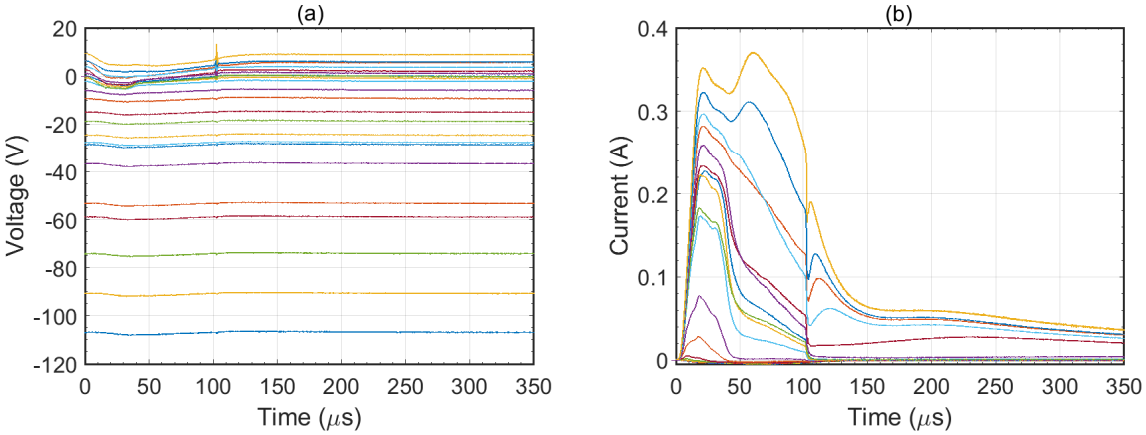


Figure 4.6: A DC voltage was applied to the probe during HiPIMS and manually varied to generate the data for the $IV$ characteristic. The oscilloscope was triggered by the target voltage waveform. Experimental data from this research demonstrating typical probe voltage and probe current waveforms are shown in (a) and (b), respectively.

power supply was 5 A. In this case, the oscilloscope was triggered by the discharge voltage waveform, and the probe current-voltage waveforms were averaged over 128 cycles before being recorded. Experimental data from this research to demonstrate the typical (a) probe voltage and (b) probe current waveforms are shown in figure 4.6. The voltage step was reduced when the probe bias was $V \gtrsim V_f$ so that the net electron region on the $IV$ characteristic was captured with greater resolution compared to the net ion region. Note that some of the data has not been plotted for clarity: each voltage sweep had $> 100$ points with a resolution of $\sim 0.2-0.75$ V for net electron collection. The range of the sense resistor was $Z_{sense} = 1.5 - 500\ \Omega$ depending on the discharge conditions and whether collecting net ion or electron current. An analysis code using MATLAB software constructed time-resolved $IV$ curves by averaging the data over $\sim 0.1\ \mu$s.

### 4.2.3 Procedure for calculating electron current and ion density

The probe theories discussed in section 3.1.3 for electron collection require the electron current rather than, as measured by the Langmuir probe, the total probe current. The electron current was calculated by subtracting a fit to the ion current region from the total probe current. The Laframboise and ABR-Chen parameterisations of the ion current (section 3.1.4.2) require $T_e$, $V_p$, $n_i$ and the probe tip dimensions to generate theoretical curves in units of ampere. An iterative approach was required because $T_e$ is calculated after the ion current fit.

The procedure was to apply an initial fit to the ion current using the following function: $f(V) = [A(V_p - V)^{1/2} + B(V_p - V)]$, where $A, B$ are fitting coefficients; the fit was applied to the region $V < V_f - 20$ V. An electron temperature (or an effective electron temperature) was then calculated; this is denoted as $T_{e1}$. Next, theoretical curves generated using Laframboise theory and ABR-Chen theory were fit to the ion current using $T_{e1}$ by minimising the sum of squared residuals with $n_i$ as the fitting parameter. Typical fits to the ion current region are shown in figure 4.7 for (a) low and (b) high plasma density. These ion current fits were used to calculate another electron temperature, denoted as $T_{e2}$; note a separate temperature is generated for each ion collection theory. Next, another fit to the ion current was performed using $T_{e2}$, and the resultant electron temperature and ion density are denoted as $T_{e3}$ and $n_{if}$, respectively. The agreement between $T_{e2}$ and $T_{e3}$ was generally within $\sim 1\%$; therefore, $n_{if}$ was taken as the final ion density. Note that all of the quantities reported in this thesis that are dependent on electron current were

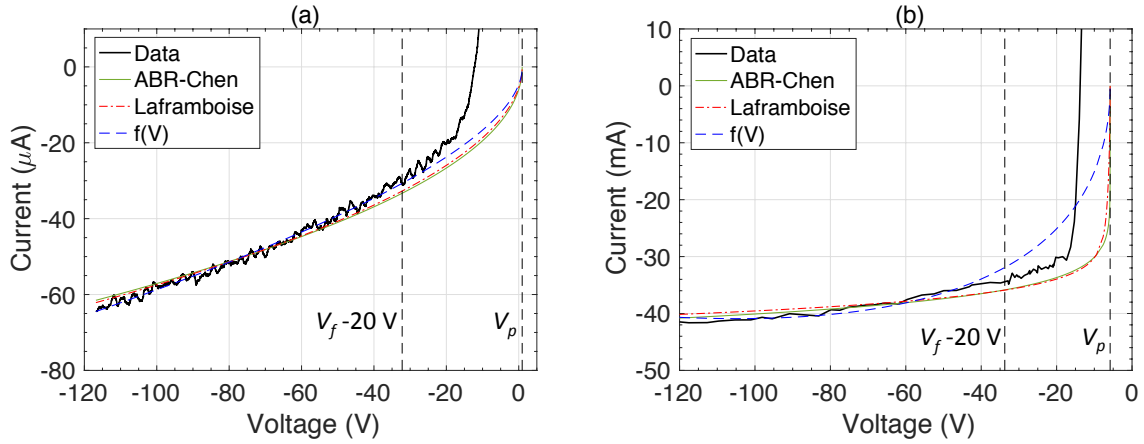


Figure 4.7: Typical fits to the region $V < V_f - 20$ V by the ABR-Chen ((a) $n_i = 3.61 \times 10^{15}$ m$^{-3}$ and (b) $8.11 \times 10^{19}$ m$^{-3}$) and Laframboise theories ((a) $n_i = 3.09 \times 10^{16}$ m$^{-3}$ and (b) $1.21 \times 10^{20}$ m$^{-3}$) and $f(V) = [A(V_p - V)^{1/2} + B(V_p - V)]$. The electron temperature is (a) 2.62 eV and (b) 1.45 eV, and the probe dimensions were $r_p = 50$ $\mu$m and $l_p = 5.5$ mm.

calculated using the ion current fit from Laframboise theory. For comparison, the electron temperature calculated using ABR-Chen theory was within $\sim 2\%$ of the value calculated using Laframboise theory.

## 4.3 Laser Thomson scattering system

This section is split into several parts: (1) equipment, including the triple-grating spectrometer, laser triggering for time-resolved measurements, sources of noise; (2) the data acquisition procedure; (3) the analysis procedure; (4) the detection volume locations and the position of the collection lens; and (5) the effects of plasma perturbation are considered.

### 4.3.1 Equipment

A schematic plan view of the laser Thomson scattering apparatus is shown in figure 4.1; the chamber was designed to reduce the amount of stray laser light reaching the detector. The radiation source for the experiments was a Nd:YAG laser operated at the second-harmonic wavelength (532 nm). The laser supplied $\lesssim 240$ mJ per pulse, as measured by a laser power meter (Gentec-EO SOLO2) in a calibrated beam splitter configuration positioned after the laser had exited the chamber. The laser had a pulse duration of $t_l = 5$ ns, a beam

divergence of 0.5 mrad and a 10 Hz repetition rate. The laser was focused by a 1 m focal length lens so that the beam diameter was $\sim 0.25$ mm at the measurement location. The beam path was in the plane of the target surface and the laser electric field was linearly polarised in the direction perpendicular to this plane. Two different laser alignments within the target surface plane were used. This is explained in section 4.3.4.

The scattered light was collected by a lens ($d = 75$ mm diameter, $f = 200$ mm focal length) positioned at $\pi/2$ rad with respect to both the laser propagation and polarisation axes in order to maximise the Thomson scattering differential cross-section (equation 3.39). The exposure of the viewing window to the plasma was regulated by mechanical shutters so that the window was only being coated by sputter deposition during a measurement. In addition, a piece of inexpensive soda glass was placed in front of the main viewing window so that only the soda glass needed to be replaced when the transmission became too low. The direction of the vector $\mathbf{k}$ with respect to the magnetron magnetic field is described in section 4.3.4. An image of the detection volume was presented to the entrance slit (0.30 mm $\times$ 6 mm) of a triple-grating spectrometer (TGS [Horiba T64000]), with the slit length aligned parallel to the laser propagation axis. The spectrometer was configured in the double-subtractive configuration to attenuate the wavelength region 531.5-532.5 nm using a mask for removal of the stray laser light and Rayleigh scattering signals. Consequently, only the wings of the Thomson scattering spectra were fit during data analysis. The advantages of using a TGS and its operating principle are explained in section 4.3.1.1.

An intensified charge-coupled device (iCCD) camera (Andor iStar DH320T-18U-A3) recorded the spectra in two-dimensions: 1024 pixels along a wavelength axis and 255 pixels along a spatial axis. The final grating in the TGS determined the spectral range recorded by the camera. All three of the TGS gratings had 1800 grooves per mm, which produced a spectral range of 522.94-541.05 nm on the CCD. The wavelength range covered by the camera intensifier, however, was 526.37-537.71 nm. The signal on the CCD array was integrated over the data acquisition period so that the array was only readout once per spectrum. During the acquisition, both the photocathode and the voltage applied to the microchannel plate (MCP) of the camera intensifier were gated by a trigger signal from the laser Q-switch. The photocathode was open for $\Delta t_{PC} = 7.5$ ns per laser pulse with the MCP voltage applied $\sim 100$ ns earlier to allow time for settling. Furthermore, the gain of the MCP was maximised to improve the signal-to-noise ratio. The choice of camera settings are explained in section 4.3.1.3.

#### 4.3.1.1 Triple-grating spectrometer

A triple-grating spectrometer (TGS) was used in this research because they have excellent stray light rejection. The key feature of a TGS, in the double-subtractive configuration, is a notch filter to attenuate a narrow region of the spectrum. This is achieved by inserting a mask between the first and second spectrometers. The notch filter is centred on the laser wavelength in a laser Thomson scattering experiment. In this section, the problems caused by having a large stray laser light signal are discussed and the operating principle of the TGS is explained.

**Camera saturation by stray laser light**

The maximum amount of charge that each pixel in the CCD can store between readouts is referred to as the saturation level. In order to prevent damage to the camera, the signal intensity should be kept below the saturation level by adjusting the camera settings (e.g. intensifier gain and integration time between readouts). In a laser Thomson scattering experiment, a high intensifier gain and a long data integration time are both favourable for improving the signal-to-noise ratio. The limiting factor for saturation is the spectral component with the largest amplitude.

The different spectral components measured during a laser Thomson scattering experiment are explained in section 2.2.2. The signal with the largest amplitude is the superposition of stray laser light and Rayleigh scattering spectra. Both of these components have a narrow spectral width compared to the Thomson scattering spectrum, and they are centred on the laser wavelength. Moreover, the intensity of the stray laser light is usually greater than the Rayleigh scattering component in low pressure discharges.

In this research, the stray laser light intensity, when the laser alignment with respect to the baffles (apertures) in the laser entry pipe was optimised, was equivalent to the Rayleigh scattering intensity from $\sim 2.7$ Pa of room temperature argon gas. At a typical laser pulse energy of 240 mJ, it would take $\sim$ 1200 laser pulses for CCD pixels to saturate if only stray laser photons were being collected with the camera settings configured for a Thomson scattering experiment (see section 4.3.1.3 for details about the camera settings). For DC magnetron conditions, the integration period for Thomson scattering measurements was 3000-9000 laser pulses for an adequate signal-to-noise ratio. Attenuation of the spectrum about the laser wavelength region was required, given the additional contribution of Rayleigh scattering and the possibility of laser misalignment which would significantly

increase the stray laser light intensity. This attenuation was provided by the TGS notch filter in this research; or alternatively, a single grating spectrometer with a mask inserted before the iCCD camera could have been used. The main advantage of the TGS is that it has better stray laser light rejection performance.

Another method to avoid saturating the camera, without the use of a notch filter, is to perform several consecutive measurements, each with a relatively short integration time, and then add them together. The signal-to-noise ratio of this approach, however, is lower than the notch filter method because noise is added to the total spectrum each time the CCD is readout. This is known as readout noise. Other sources of noise during a laser Thomson scattering experiment are discussed in section 4.3.1.3.

**Redistribution of stray laser light**

The uniform illumination of a spectrometer entrance slit by a monochromatic light source will produce a peak with a finite spectral width. This is referred to as the instrumental function of the detection system $I_I(\lambda)$. Contributions to the instrumental function include the entrance slit width of the spectrometer ($w$), aberrations caused by non-ideal optical elements, and signal diffusion in the iCCD camera. Another source of line broadening for all laser dependent signals is the laser linewidth $I_{LW}(\lambda)$. A measured Rayleigh scattering spectrum $f_{R\lambda}(\lambda)$ can be mathematically expressed as a convolution of the Doppler broadening effect $I_{DB}(\lambda)$, the instrumental function and the laser linewidth:

$$f_{R\lambda}(\lambda) = A_R \cdot I_{DB}(\lambda) * I_I(\lambda) * I_{LW}(\lambda) \approx A_R \cdot I_I(\lambda), \tag{4.3}$$

where $A_R$ is an amplitude scaling factor. The instrumental function was the dominant factor for determining the width of a Rayleigh scattering spectrum in this research; this is demonstrated by considering the spectral width of the individual components. The full-width-half-maximum (FWHM) of $f_{R\lambda}(\lambda)$ was $\approx 220$ pm when $w = 0.3$ mm; FWHM $\approx 1.5$ pm for $I_{DB}(\lambda)$; and FWHM $\approx$ 40 pm for $I_{LW}(\lambda)$ (stated by the laser manufacturer). Assuming Gaussian profiles, the FWHM of $I_I(\lambda)$ is calculated to be $\approx 216$ pm. In addition, a measured stray laser light spectrum is given by equation 4.3 but with a different amplitude scaling factor.

Figure 4.8 shows a measured Rayleigh scattering spectrum, which is effectively the instrumental function of the detection system as explained above. The instrumental function was normalised to satisfy:

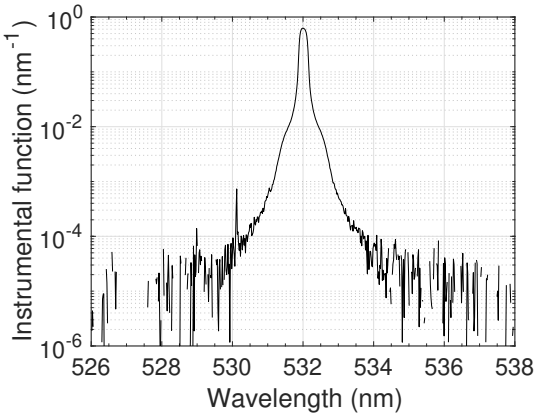


Figure 4.8: The instrumental function of the detection system used in this research. The first, second and third slit widths of the triple-grating spectrometer were 0.30 mm, 20 mm and 0.42 mm, respectively.

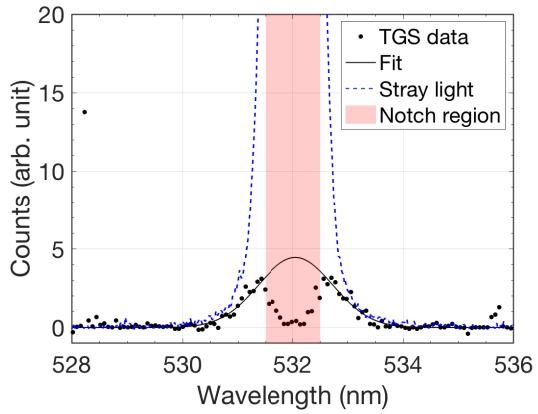


Figure 4.9: Comparison of a Thomson scattering spectrum ($n_e = 4.1 \times 10^{16}$ m$^{-3}$ and $T_e = 0.4$ eV) obtained using the triple-grating spectrometer and the simulated stray laser light signal that would be present if the mask was not inserted. The region attenuated by the notch filter is highlighted. The integration period was 4800 laser pulses. The first, second and third slit widths of the triple-grating spectrometer were 0.30 mm, 20 mm and 0.42 mm, respectively.

$$\int_0^\infty I_I(\lambda)d\lambda = 1, \tag{4.4}$$

so that the probability of a photon of wavelength 532 nm being assigned a wavelength $\lambda'$ on the iCCD camera, within the range $d\lambda$, is $I_I(\lambda')d\lambda$. It is problematic when significant numbers of stray laser photons are redistributed so that they overlap with the wings of the Thomson scattering spectrum.

Figure 4.9 shows a comparison of a Thomson scattering spectrum ($n_e = 4.1 \times 10^{16}$ m$^{-3}$ and $T_e = 0.4$ eV) obtained using the TGS from 4800 laser pulses and the simulated stray laser light spectrum that would be present if the mask was not inserted inside the TGS. The measured Thomson scattering spectrum would be dominated by the stray laser light spectrum without the mask in place. The insertion of the mask has two effects: attenuation of the region $531.5 - 532.5$ nm and improved stray laser light rejection across the spectrum.

**Operating principle**

A schematic of the TGS in the double-subtractive configuration is shown in figure 4.10. Light enters the spectrometer through the first slit (S1, width= 0.3 mm) and is collimated onto the first grating (G1). Eventually, the dispersed light exits the first spectrometer by passing through the second slit (S2). The width of S2 (20 mm) is much greater than S1 to account for the light dispersion and a mask is placed at the centre of the slit to remove the wavelength region $531.5 - 532.5$ nm.

Due to redistribution of stray laser light in the first spectrometer, a small percentage of the 532 nm photons are able to avoid the mask and pass through S2. If the iCCD camera was placed immediately after S2 then the stray laser light spectrum would be similar to the one shown in figure 4.9 but with the notch filter region attenuated[1]. The measured Thomson scattering spectrum at this point would, therefore, be dominated by the wings of the stray laser light spectrum.

The arrangement of the second spectrometer in the TGS is mirrored with respect to the first spectrometer in order to cancel the light dispersion. This is known as the double-subtractive configuration. The dispersed light minus the central region of the spectrum is recombined at the second grating (G2) and exits the second spectrometer by passing through the third slit (S3). The width of slit S3 (0.42 mm) is slightly larger than S1 to

[1]The stray laser light profile in figure 4.9 was produced using the instrumental function of all three spectrometers combined. The redistribution of stray laser light by the first spectrometer requires the instrumental function of the first spectrometer only.

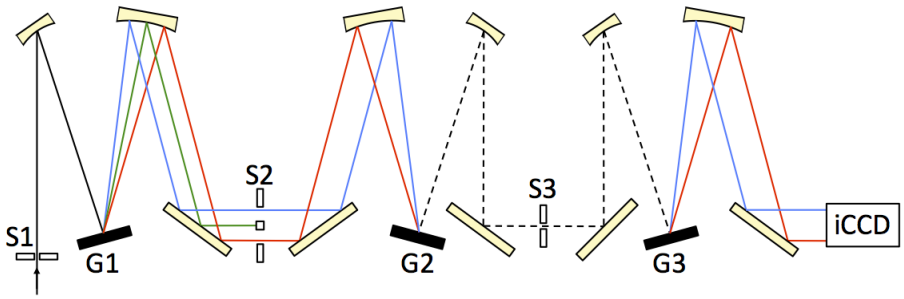


Figure 4.10: Schematic of the triple-grating spectrometer with the three slits (S) and three gratings (G) labelled. Slit S2 has a mask to remove the wavelength region 531.5 to 532.5 nm.

account for misalignment, but the slit width is kept small. This is to reduce the probability that a 532 nm photon is redistributed by the second spectrometer such that it is able to pass through S3. Note that without redistribution by the second spectrometer, a 532 nm photon would hit the wall beside S3 because its position on G2 would be incorrect[2]. Furthermore, the small slit width reduces the amount of background light entering the third spectrometer from the previous spectrometers. Background light is produced from the scattering of light, including contributions from all of the diffraction orders, off optical components inside a spectrometer. This produces a fairly homogeneous signal over the entire surface of the CCD, and hence appears as a wavelength-independent background signal.

The third spectrometer with grating G3 is used to disperse the light onto the iCCD camera for analysis. A 532 nm photon entering this spectrometer would have passed S3 at approximately the correct spatial position for its wavelength. In order for this photon to interfere with the Thomson scattering measurement, the third spectrometer would need to redistribute the photon to the region outside of $531.5 - 532.5$ nm.

To summarise, the TGS has excellent stray laser light rejection because the probability of redistributing a 532 nm photon so that it is able to pass through each exit slit, with the mask inserted, and then be registered outside of the region $531.5 - 532.5$ nm on the iCCD camera is very small. The disadvantages of the TGS are its sensitivity to misalignment, optical/mechanical complexity and a reduction in overall signal intensity compared to a single-grating spectrometer because the TGS has more optical components.

[2]Strictly speaking this is true only when the width of slits S1 and S3 are equal.

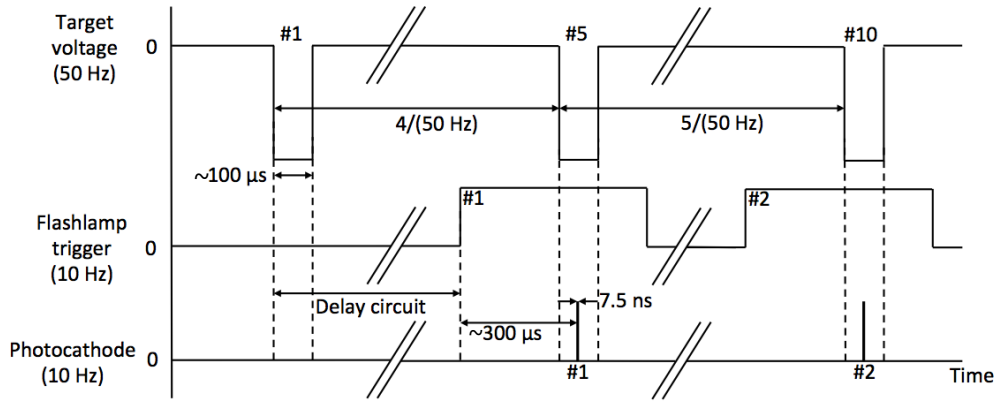


Figure 4.11: Timing diagram of the target voltage waveform during HiPIMS, the input trigger to the laser flashlamps and the photocathode activation period to collect the scattered photons.

#### 4.3.1.2 Time-resolved HiPIMS measurements

To acquire time-resolved Thomson scattering measurement during HiPIMS, a constant phase relationship between the activation of the laser Q-switch and the target voltage waveform was required. Since the laser Q-switch was internally triggered by a signal synchronised with the flashlamp 'fire' order, the task was to externally trigger the laser flashlamps with a signal in phase with the target waveform. A simple solution would be to externally trigger the HiPIMS power supply using a signal generator, which could also be used to derive an input trigger for the laser flashlamps. However, the Sinex 3 power supply did not accept a trigger input, so this could not be done. Instead, the flashlamp trigger was derived from the target voltage waveform (master clock). A block diagram of the circuit used to derive the flashlamp trigger signal is shown in appendix A. The laser flashlamp trigger had to remain $10 \pm 8\%$ Hz, so the frequency of the master clock signal was divided by 5 because the HiPIMS repetition rate was set to 50 Hz in the experiments. The iCCD camera was triggered by a signal, which was a synchronised precursor to the activation of the Q-switch, sent from the laser.

A timing diagram of the target voltage pulse, the flashlamp input trigger and the photocathode activation of the iCCD camera is shown in figure 4.11. The triggering signal derived from the first target voltage pulse causes laser radiation to be injected into the plasma, and the photocathode to open, during the fifth target voltage pulse. The next

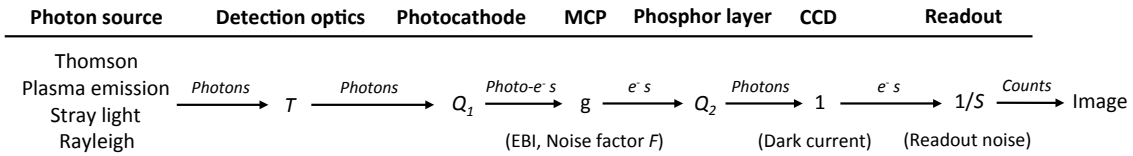


Figure 4.12: The path of photons from various sources through the detection system. The total number of counts corresponding to a specific signal is found by multiplying the number of photons at the source by the various factors ($TQ_1gQ_2/S$); terms are defined in the text. In addition, the various noise sources originating from inside the iCCD camera are labelled.

trigger is derived from the sixth target voltage pulse and the process repeats. A delay in the laser flashlamp triggering signal was used to shift the temporal position of laser pulse/photocathode activation with respect to the target voltage waveform. The temporal resolution of the system was $\sim 5$ $\mu$s. This was limited by the jitter in the target voltage waveform.

#### 4.3.1.3 Sources of noise

In this section, the origin of noise in a Thomson scattering spectrum is discussed by considering the path of photons from within the vacuum chamber to charge being readout from the CCD. This path is illustrated by figure 4.12 and the properties of the photon detection system are summarised in table 4.1. There are three main sources of noise in an iCCD image: statistical noise on the Thomson scattering and plasma emission signals, intensifier noise and CCD noise. Discussed below are the settings of the iCCD camera to optimise the signal-to-noise ratio.

Thomson scattering photons pass through the optical system with transmission $T \sim 0.05$ and are incident upon the photocathode of the iCCD camera, which has a quantum efficiency of $Q_1 = 0.41$. The number of Thomson scattering photons reaching the photocathode per laser pulse is of the order of $\sim 10^{-17} \cdot n_e[\mathrm{m}^{-3}]$ [68]. Consequently, for a typical low pressure discharge, there are relatively large fluctuations in the number of photoelectrons generated per pulse due to the probabilistic nature of the quantised scattering event. This process is known as shot noise and is modelled by the Poisson distribution. Therefore, the mean number of photoelectrons generated from $N_p$ laser pulses is $\lambda_{TS}^2 \equiv TQ_1N_p\hat{N}_{Ti}$ and the standard deviation is $\lambda_{TS}$; where the number of Thomson scattering photons collected

| Parameter | Symbol | Value | Units |
|---|---|---|---|
| Laser pulse-width | $t_l$ | 5 | ns |
| Laser beam-width | $b_w$ | $\sim 0.25$ | mm |
| TGS entrance slit length | $l_s$ | 6 | mm |
| TGS entrance slit width | $w$ | 0.3 | mm |
| Image magnification | $m$ | -1.82 | — |
| Detection volume length | $L = l_s/m$ | 3.3 | mm |
| Detection volume width | $w/m$ | 0.17 | mm |
| Optics transmission | $T$ | $\sim 0.05$ | — |
| Collection solid angle | $\Delta\Omega$ | 0.046 | sr |
| Photocathode gate width | $\Delta t_{PC}$ | 7.5 | ns |
| Photocathode QE | $Q_1$ | 0.41 | — |
| Combined phosphor and CCD QE | $Q_2$ | $\gtrsim 0.9$ | (estimated) |
| Photoelectron effective gain | $gQ_2$ | 1299 | CCD $e^-$/Photocathode $e^-$ |
| Min photoelectron effective gain | $g_0Q_2$ | 1.65 | CCD $e^-$/Photocathode $e^-$ |
| MCP gate width | $\Delta t_{MCP}$ | 107.5 | ns |
| MCP noise factor | $F$ | $\sim 1.6$ | — |
| Readout sensitivity | $S$ | 3.4 | CCD $e^-$/Count |

Table 4.1: Parameters for the photon detection system. The TGS entrance slit and detection volume dimensions are explained in section 4.3.4.2.

per pulse for an ideal system is $\hat{N}_{Ti} = N_{Ti}/N_p$ and $N_{Ti}$ is given by equation 3.46.

Next, the photoelectrons are accelerated to the MCP by an electric field, where the electron current and the shot noise are amplified by gain $g$. The amplification process, however, is described by a distribution function, and so an additional source of noise is introduced. The total noise after the MCP is the shot noise entering it multiplied by $Fg$, where the MCP noise factor was stated by the manufacturer as $F \sim 1.6$. The relative standard deviation, or equivalently the reciprocal of the signal-to-noise ratio, due to shot noise on the Thomson scattering signal is:

$$\frac{1}{\mathrm{SNR}_{TS}} = \frac{gF\lambda_{TS}}{g\lambda_{TS}^2}. \tag{4.5}$$

This amplified shot noise is also present on the plasma emission signal because only a small number of plasma emission photons are collected per pulse due to the short photocathode activation time ($\Delta t_{PC} = 7.5$ ns). The relative standard deviation, or equivalently the reciprocal of the signal-to-noise ratio, due to shot noise on the plasma emission signal is:

$$\frac{1}{\mathrm{SNR}_{PE}} = \frac{gF\lambda_{PE}}{g\lambda_{TS}^2}, \tag{4.6}$$

where $\lambda_{PE} \equiv (TQ_1N_p\hat{N}_E)^{1/2}$ is the photoelectron shot noise due to plasma emission, and $\hat{N}_E$ is the number of plasma emission photons collected per laser pulse for an ideal system.

The final stages in the camera are to convert the electrons into photons by a phosphor layer, and these are guided to the CCD chip to produce electron-hole pairs; the total quantum efficiency is $Q_2 \gtrsim 0.9$. The shot noise produced from this process is negligible because the high gain of the MCP ($gQ_2 = 1299$) ensures that there are a large number of electrons in the CCD per photoelectron generated.

The main noise contribution from the intensifier is the amplification of thermally generated photoelectrons by the MCP. This is known as the effective background illumination (EBI) and can be minimised by gating the MCP voltage (width $\Delta t_{MCP} = 107.5$ ns) with the laser pulse so that the dark current is only amplified for a short fraction of the total camera exposure time. The effective gain of the MCP when no voltage is applied is $g_0Q_2 = 1.65$. Other sources of noise include dark current within the CCD and the readout noise during the conversion of charge in each pixel to counts with a sensitivity of $S = 3.4$ electrons per count. The CCD noise contribution is minor if a high intensifier gain is used, the CCD is kept at a low temperature (243 K in this research), and the CCD array is readout once per spectrum by integrating over the data acquisition period. Note that each measurement of a Thomson scattering spectrum requires measuring two spectra/images: the first spectrum is the image acquired with the laser on and plasma on, and the second spectrum is the image acquired with the laser off and plasma on.

To summarise, the dominant noise contributions to the measured Thomson scattering spectrum are the Thomson scattering and plasma emission shot noise when the gain of the intensifier is high, both the MCP voltage and photocathode are gated with the laser pulse, and the CCD is cooled and readout once per spectrum. The total signal-to-noise ratio can, therefore, be calculated by summing the relative standard deviation of the Thomson scattering and plasma emission shot noise contributions in quadrature [66, p. 58]:

$$\mathrm{SNR}_{total} \approx \left(\frac{1}{\mathrm{SNR}_{TS}^2} + \frac{2}{\mathrm{SNR}_{PE}^2}\right)^{-1/2} = \frac{\hat{N}_{Ti}}{F} \cdot \left(\frac{N_pTQ_1}{\hat{N}_{Ti} + 2\hat{N}_E}\right)^{1/2}. \tag{4.7}$$

The factor of two arises from the plasma emission noise contributing to both spectra per measurement. For typical DC plasma conditions with $n_e = 10^{17}$ m$^{-3}$, $N_p = 6000$, an

energy per laser pulse of 240 mJ, assuming $\approx 68\%$ of the laser photons pass through the detection volume (justified in section 4.3.4.2), and assuming $\hat{N}_E < \hat{N}_{Ti}/2$, one obtains $\mathrm{SNR}_{total} > 36$. This calculation, however, does not take into account the loss of photons due to attenuation by the notch filter nor the stability of the plasma (e.g. $T_e$ and $n_e$) during a measurement.

The signal-to-noise ratio can be improved further by using a photon counting technique. Photon counting involves comparing the signal in a pixel to an externally set threshold and a count is only registered when this threshold is exceeded. The high gain of the intensifier enables differentiation between a true signal and noise generated inside the camera. In theory, the spectra acquired are not affected by the gain error; therefore, one would set $F = 1$ in equation 4.7 and the signal-to-noise ratio improves by a factor of $\sim 1.6$. The disadvantage of photon counting is that each pixel can only detect a maximum of one photon (or count), and so multiple readouts of the CCD are required per measurement. This results in a significantly longer data acquisition time compared to simple integration, where the CCD is readout once per measurement. Photon counting was not implemented in this research because it was important to minimise the data acquisition time due to the window transmission decreasing during plasma sputtering.

### 4.3.2 Data acquisition

The first step of the measurement procedure was to record an image with both the laser and plasma on, and the TGS mask inserted. This image contained both the Thomson scattering and plasma emission signals, and was accumulated from $3000 - 9000$ laser pulses during DC magnetron operation and $100 - 600$ pulses during HiPIMS. Moreover, the mean laser power was measured during the data acquisition period. Immediately after recording the first image, the laser was turned off and an image of the plasma emission was recorded using the same acquisition time as the first image.

The next step was to subtract the second image from the first image. An example of the resultant image is shown in figure 4.13. A Thomson scattering spectrum was generated by summing over all of the counts in the spatial direction within the intensifier region (indicated by the white box) of the image. This corresponds to averaging over $\sim 3.3$ mm (explained in section 4.3.4.2). The pixel to wavelength conversion was given by the dispersion relation (nm/mm) in the TGS manual. This was experimentally verified using a line emission light source. The wavelength axis was averaged over 4 pixels, resulting in a

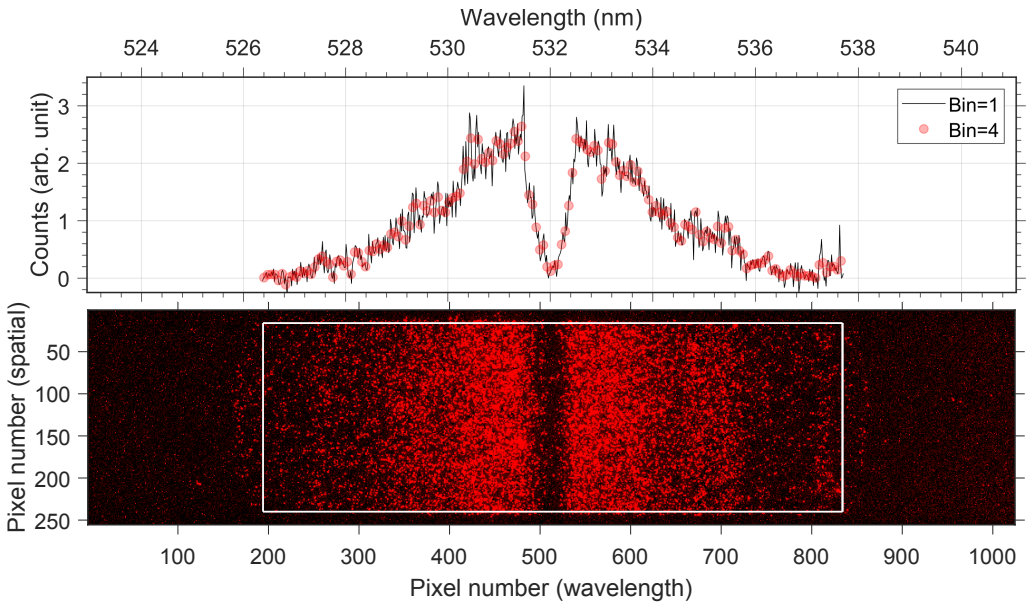


Figure 4.13: The iCCD camera image after subtracting the plasma emission background image from the image recorded with the laser and plasma on. The Thomson scattering spectrum in the top figure was obtained by summing the CCD counts in the spatial direction. The white box in the bottom figure indicates the intensifier region - data outside of this region was discarded. Also shown is a comparison of the spectrum obtained after binning 4 wavelength pixels during data analysis compared to the raw signal (bin = 1).

resolution of $\sim 0.071$ nm, during the data analysis. This reduced the noise in the measured Thomson scattering spectra as demonstrated by the spectrum shown in figure 4.13. Note that the resolution of the camera intensifier was $\sim 1.15$ pixels, or equivalently $\sim 0.02$ nm.

The influence of the stray laser light and Rayleigh scattering signals on the Thomson scattering measurements was assessed by performing a measurement with the laser on, the mask inserted and argon gas in the chamber without a plasma. No signal was observed, which confirmed that stray laser light redistribution was not an issue.

The Rayleigh scattering calibration procedure for determining absolute electron densities was performed after each Thomson scattering measurement. The mask inside the TGS was removed for this. The theoretical details are given in section 3.2.3.1: Rayleigh scattering intensity was measured for various argon gas pressures at a constant laser power. A Rayleigh scattering spectrum was acquired by subtracting an image of the stray laser light

(chamber at base pressure and laser on) from the image obtained with the laser on and gas in the chamber (plasma off), and then the resultant image was processed to produce a spectrum by following the same procedure as for Thomson scattering, as described above, but the wavelength pixels were not averaged. Each Rayleigh scattering spectrum was numerically integrated to calculate the scattering intensity for a given pressure. The range of gas pressure ($50 - 1000$ Pa) used for the calibration ensured that the Rayleigh scattering signal dominated the stray laser light signal. Frequent calibration was required because the transmission of the collection window decreased during magnetron operation due to film growth. The rate of change of the window transmission was minimised by using a high mass element (tungsten) for the magnetron target. The electron density overestimation, as a result of performing the Rayleigh scattering calibration with a lower window transmission compared to the start of the Thomson scattering measurement, was limited to $< 10\%$ by adjusting the data acquisition time for the Thomson scattering measurements.

The range of argon gas pressure used during the Rayleigh scattering calibration necessitated that the gate valve to the turbomolecular pump was closed. After the Rayleigh scattering measurements were complete, the chamber was pumped down by rotary pump 2 (see figure 4.1) so that the gate valve to the turbomolecular pump could be reopened. The two gate valves were never both open simultaneously.

### 4.3.3 Analysis procedure

In theory, the average electron energy and the electron density of the electron velocity distribution function (EVDF) can be numerically calculated from a incoherent Thomson scattering spectrum without having to apply a model to the data. In this research, however, the measured Thomson scattering spectra were attenuated over a spectral range of $531.5 - 532.5$ nm, which corresponds to a densely populated region of the EVDF, due to the TGS notch filter. It was, therefore, necessary to apply a fit to the uncontaminated experimental data in order to model the attenuated region, and hence obtain electron properties that were representative of the bulk population. The fit applied was either a Gaussian or a double-Gaussian curve which corresponds to a single or bi-Maxwellian EVDF, respectively. The electron temperature detection limit of the TGS can be estimated by setting $\lambda_{1/e} = 0.5$ nm (the half width of the TGS notch filter) in equation 3.58; this gives $T_e = 0.11$ eV.

The double-Gaussian curve will always fit the data best, in terms of minimising the sum of squared residuals (SSR), because there are more fitting parameters. Moreover, higher

order Gaussian functions will return an even better fit. The approach in this research was, therefore, to always accept the simplest model which provides an adequate fit to the data. Two criteria were defined, for when to accept the double-Gaussian fit over the Gaussian fit, to ensure that the data was analysed consistently:

1. The value of SSR from the Guassian fit exceeds the SSR value from the double-Gaussian fit by a factor of 1.15.

2. The $1/e$ amplitudes of the two Gaussians in the double-Gaussian fit both exceed 500 counts.

The first criterion is an arbitrary threshold of when the double-Gaussian fit is significantly better than the Gaussian fit. The second criterion ensures that both of the Gaussian's in the double-Gaussian fit are above the noise level of the detector. The shapes of the Thomson scattering spectra in the experiments did not suggest that higher order Gaussian functions were required. It should be emphasised that the exact values chosen for the above criteria do not impact the conclusions of this research.

#### 4.3.3.1 Deconvolution of the Thomson scattering spectrum and the instrumental function

An experimentally determined Thomson scattering spectrum is a convolution of the Doppler broadening effect due to the electron motion and the instrumental function of the detection system (see equation 4.3 and the subsequent discussion in that section). Consequently, a measured Thomson scattering spectrum will have a greater spectral width than that based on just Doppler broadening alone; hence, the electron temperature will be overestimated unless the two components are deconvolved. Assuming a Gaussian curve for the instrumental function, the temperature overestimation is $\sim 5\%$ at $T_e = 0.15$ eV, and the error is reduced for higher electron temperatures. The lower limit of electron temperature measured in this research was $\gtrsim 0.1$ eV, so a deconvolution procedure was implemented to improve the accuracy of the results. This procedure was applied to all of the measured Thomson scattering spectra for completeness.

The deconvolution procedure was to numerically convolve a Gaussian function with the (non-Gaussian) instrumental function, and then this was fitted to the experimental Thomson scattering spectrum. The deconvolved electron properties were calculated from the Gaussian function. The instrumental function was taken as the Rayleigh scattering

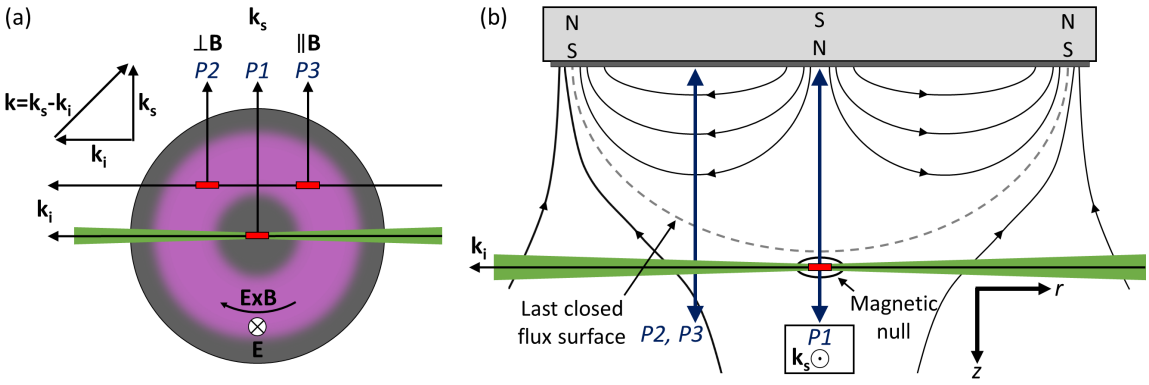


Figure 4.14: (a) The orientation of the two laser beam paths with respect to the target diameter and the location of the detection volumes (closed rectangles), which are labelled as $P1, P2, P3$. The detection volume locations in the $r-z$ plane of the magnetron are shown in (b). Note that the magnetron was mounted vertically above the vacuum chamber.

spectrum corresponding to the highest gas pressure used during the absolute electron density calibration. It should be emphasised that the experimental data was not deconvolved - only the fit to the data was. An attempt to deconvolve the experimental data using the convolution theorem was unsuccessful because it required dividing a function by the Fourier transform of the instrumental function which contains zeros.

### 4.3.4 Measurement positions

#### 4.3.4.1 Location of the detection volumes

There were two different laser alignments, both of which had the laser propagation direction in the target surface plane. The beam paths with respect to the target surface are shown in figure 4.14(a). The first alignment passed through the target diameter and the second alignment ran parallel to this but with a perpendicular separation distance of 29 mm.

Measurements were performed at three different detection volume locations; these are indicated by the closed rectangles in figure 4.14(a) and are labelled as $P1, P2, P3$. For each detection volume location, the collection lens and TGS were positioned at $\pi/2$ rad with respect to the laser propagation direction. Consequently, the direction of the vector $\mathbf{k}$=$\mathbf{k}_s$-$\mathbf{k}_i$ was constant, but its orientation with respect to the local magnetic field varied. Note that the arrangement of the apparatus in figure 4.1 was for the $P2$ configuration.

The positions of the detection volumes in the $r-z$ of the magnetron are shown in figure

4.14(b). Detection volume $P1$ was located along the centre line of the magnetron ($r = 0$ mm), whereas $P2$ and $P3$ were located at the radial position $r = 41$ mm. The azimuth angles of $P2$ and $P3$ were $3\pi/4$ rad and $\pi/4$ rad, respectively (measured anticlockwise from laser entry through the centre of the chamber in figure 4.14(a)). The magnetic field direction at $r = 41$ mm, within the last closed flux surface boundary, was approximately radial. Consequently, $\mathbf{k}$ was aligned perpendicular to the magnetic field at $P2$ and parallel to the magnetic field at $P3$. It should be noted that the main racetrack erosion was located at ($r = 48$ mm, $z = 0$ mm) and that the $r$ value corresponding to a purely radial magnetic field was dependent on $z$, as shown by figure 4.2. The height variation of measurements was $z = 10 - 70$ mm, which was achieved by moving the magnetron mount with the diagnostic alignment fixed. Measurements closer to the target were limited by the ground shield surrounding the magnetron which protruded 5 mm above the target surface.

#### 4.3.4.2 Location of the collection lens

An important consideration is the distance of the lens from the detection volume ($s$) because this determines the solid angle for collection ($\Delta\Omega$), the solid angle of the light cone entering the TGS ($\Delta\Omega_{\mathrm{TGS}}$), and the image magnification ($m$) at the entrance of the TGS. The relationship between $s$ and the distance of the lens from the TGS ($s'$) is given by the following equation:

$$\frac{1}{f} = \frac{1}{s} + \frac{1}{s'}, \tag{4.8}$$

where $f = 200$ mm is the focal length of the lens. These lengths are indicated in figure 4.1. The image magnification is given by:

$$m = -\frac{s'}{s} = -\frac{f}{s - f}. \tag{4.9}$$

The total number of Thomson scattering photons collected for an ideal system ($N_{Ti}$) is given by equation 3.46. The following substitutions into this equation can be made: the detection volume length is $L = l_s/m$, where $l_s = 6$ mm is the length of the entrance slit; the solid angle for collection is $\Delta\Omega \approx \pi d^2/(4s^2)$, where $d = 75$ mm is the lens diameter; and the number of photons in the detection volume per pulse is $N_l \approx N_l' w/(b_w m)$, where $N_l'$ is the total number of laser photons per pulse, $b_w \sim 0.25$ mm is the laser beam waist, and $w$ is the width of the TGS entrance slit. The latter was set to $w = 0.30$ mm as a

compromise between signal intensity and spectral resolution. Using equations 3.46 and 4.9, one finds:

$$N_{Ti} = \nu_l t_T n_e \frac{d\sigma_T}{d\Omega} \cdot \frac{\pi N_l' w l_s d^2}{4 b_w f^2} \cdot \underbrace{\frac{(s-f)^2}{s^2}}_{x_s(s)}, \tag{4.10}$$

where $x_s(s)$ is proportional to the number of Thomson scattering photons collected in the experiment. Figure 4.15 shows $x_s$ plotted as a function of $s$. It is advantageous to maximise $x_s$, but limitations include: the maximum acceptance solid angle of the TGS ($\Delta\Omega_{\mathrm{TGS}} = 0.014$ sr or equivalently $f/\# = 7.5$), $w/m$ cannot exceed the laser beam waist of $b_w \sim 0.25$ mm, and the closest possible approach of the lens to the detection volume is $s \approx 250$ mm due to physical constraints. The figure shows that the optimal value of $s$ was 310 mm for maximising the Thomson scattering signal and satisfying the above conditions. Therefore, the dimensions of a detection volume with $s = 310$ mm, $s' = 564$ mm, $m = -1.82$, $l_s = 6$ mm, $w = 0.3$ mm and $b_w \sim 0.25$ mm, are $\approx (l_s/m)\times(w/m)\times b_w = 3.3 \times 0.17 \times 0.25$ mm$^3$. The FWHM of the instrumental function was $\approx 0.22$ nm.

### 4.3.5 Plasma perturbation by laser

Laser Thomson scattering can be considered a non-invasive technique for electron property measurements when two conditions are satisfied: (i) the number of electrons in the detection volume is significantly greater than the number of photoelectrons generated by the laser radiation per pulse, and (ii) electron heating by the electric field of the laser radiation is negligible. These two considerations are discussed separately below.

#### 4.3.5.1 Photoionisation

Direct photoionisation of ground state argon is a multi-photon process since the energy per photon is 2.33 eV at $\lambda_i = 532$ nm and the first ionisation energy is 15.76 eV [148]. Direct photoionisation is only possible from excited states with energy $\geqslant (15.76 - 2.33)$ eV, and these states are not expected to be densely populated because they are not metastable. For a non-resonant process, the multi-photoionisation rate is proportional to the photon flux raised to the power equal to the number of photons involved in the transition [149], and so varying the laser power will have a significant impact on the number of photoelectrons generated. If the total electron density is independent of laser power, then the contribution

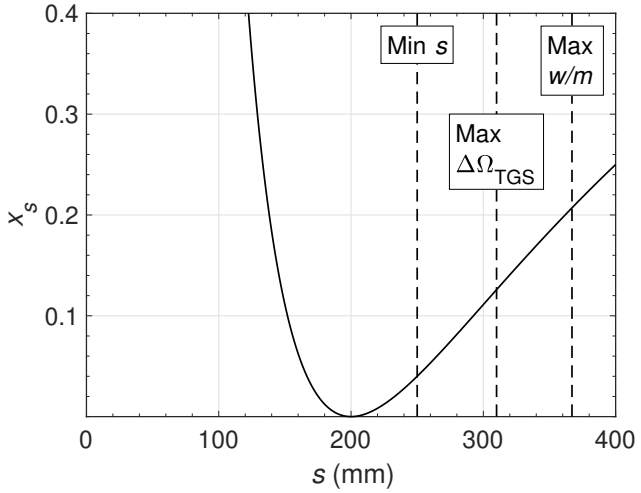


Figure 4.15: The function $x_s$ is proportional to the number of Thomson scattering photons collected during an experiment. Highlighted are the values of $s$ that correspond to the closest possible approach of the collection lens to the collection window; maximum acceptance solid angle of the TGS ($\Delta\Omega_{\mathrm{TGS}} = 0.014$ sr); and when $w/m$ is equal to the beam waist ($b_w \sim 0.25$ mm).

of photoelectrons must be negligible. This was found to be true for all measurements when the laser power was varied by a factor of 2.

#### 4.3.5.2 Laser heating

Kunze states that inverse bremsstrahlung radiation[3] is the dominant process by which absorbed laser radiation is given to free electrons [150, p. 589]. A formula for the upper limit for the relative increase in electron temperature is [150, p. 589]:

$$\frac{\Delta T_e}{T_e} = 5.26 \times 10^{-11} \cdot \frac{n_e Z^2 \lambda_i^3 I_0}{T_e[\mathrm{eV}]^{3/2}} \left(1 - \exp\left(\frac{-hc}{\lambda_i T_e[\mathrm{eV}]}\right)\right), \tag{4.11}$$

where $Z$ is ion charge in units of electron charge and $I_0$ is the laser intensity in units of J·m$^{-2}$. The formula assumes $t_{ee} < t_l < t_{ie}$, where $t_{ee}$ is the electron-electron collision time, $t_l$ is the laser pulse-width, and $t_{ie}$ is the ion-electron collision time. Therefore, the formula gives an upper limit to the change in electron temperature because the electrons have

[3] An electron absorbs a photon in the presence of an ion to conserve momentum.

enough time during the laser pulse to thermalise the energy gained amongst themselves but not to transfer any to the ions. The formula also assumes that the plasma absorption coefficient is not altered by the laser beam. This criterion is satisfied when the maximum kinetic energy gained by an electron in the laser electric field is much less than the photon energy [150, p. 590]. Solving the electron equation of motion in the presence of an electric field with a field strength of $E_0 \sin(\omega_i t)$ gives the electron velocity amplitude as $eE_0/(m_e\omega_i)$, where $\omega_i = 2\pi c/\lambda_i$. Therefore, the criterion is:

$$\frac{e^2 E_0^2}{2m_e\omega_i^2} \ll \frac{hc}{\lambda_i} = 2.33 \text{ eV}. \tag{4.12}$$

In this research, each laser pulse had $\sim$ 240 mJ of energy, a pulse-width of $t_l = 5$ ns, and a beam diameter in the scattering volume of $b_w \sim 0.25$ mm. This results in an intensity of $\sim 10^{15}$ W·m$^{-2}$. Setting the time average magnitude of the Poynting vector $\langle S \rangle$ to the laser intensity allows calculation of the electric field amplitude using:

$$E_0 = \left( \frac{2\langle S \rangle}{\epsilon_0 c} \right)^{1/2}. \tag{4.13}$$

The left hand side of equation 4.12 is equal to 5 meV, which is significantly lower than the energy of a $\lambda_i = 532$ nm photon (2.33 eV); hence, the plasma absorption coefficient can be assumed constant. Substituting $n_e = 10^{20}$ m$^{-3}$, $T_e = 1$ eV and $Z = 1$ into equation 4.11 gives $\Delta T_e/T_e = 0.004$; therefore, laser heating is negligible, and the effect is reduced for a less dense plasma.

# Chapter 5

# Comparison of Langmuir probe and laser Thomson scattering for plasma density and electron temperature measurements in HiPIMS discharges[1]

## 5.1 Introduction

High power impulse magnetron sputtering (HiPIMS) is a novel ionised physical vapour deposition (IPVD) technique [80] in which high metal ionisation fractions ($\sim$ 70% in Kouznetsov *et al.* [96]) are obtained through the creation of a dense plasma ($n_e \sim 10^{19}$ $\mathrm{m}^{-3}$). This necessitates high target power densities ($0.5 - 10$ kW·cm$^{-2}$) and these are generated using short high-voltage pulses (width $\sim 10 - 100$ $\mu$s) with low duty cycle ($\lesssim 1\%$) to prevent target melting. The main advantages of HiPIMS for the deposition of thin films are discussed in section 2.3.3.1. The key point is that the energy and directionality of the sputtered ions can be controlled by biasing the substrate, in contrast to line of sight deposition using sputtered neutrals as in conventional DC magnetron operation. This results

[1]The research presented in this chapter has been published in a peer-reviewed journal [2]. Additional results and discussion are included in this chapter.

in HiPIMS producing films with superior properties (e.g. denser, harder and smoother) [100, 101].

Electrons perform a closed $\mathbf{E} \times \mathbf{B}$ drift inside the last closed flux surface boundary of the magnetron, which confines electrons and produces a dense plasma. This magnetic trap region produces the most intense ionisation in the discharge, predominately through the process of electron impact ionisation [105]. Moreover, in the unbalanced magnetron configuration [91, section 2.3.2.1], sputtered ions are guided from the magnetic trap region towards the substrate by ambipolar diffusion parallel to open magnetic field lines. This process is driven by the high mobility of electrons parallel to the magnetic field. A detailed understanding of the electron dynamics inside the magnetic trap and at the substrate are, therefore, required in order to optimise the deposition process. The most fundamental electron plasma properties for any physics investigation are electron density ($n_e$) and electron temperature ($T_e$). A detailed review of electron plasma property measurements in HiPIMS discharges is given in section 2.3.3.3; this is summarised below.

Unfortunately HiPIMS poses a difficult environment for diagnostic operation due to the high sputter flux, the relative abundance of species has a dynamic evolution, electron density between pulses spans several orders of magnitude and at least an order of magnitude for electron temperature, and the plasma is spatially inhomogeneous. These effects are most pronounced inside the last closed flux surface boundary. Non-intrusive diagnostics are obviously desirable and examples of such techniques applied to HiPIMS include optical emission spectroscopy [99, 111, 125] and THz time-domain spectroscopy [136]. The former can be implemented with relative ease to give time-resolved information about the abundance of excited species, but it is challenging to extract quantitative information about electron plasma properties because a complicated collisional-radiative model describing electronic transitions is required. The latter is a novel technique for measuring electron density, but the setup in Meier *et al.* [136] had a relatively high detection limit ($n_e > 10^{18}$ $\mathrm{m}^{-3}$), so measurements during the pulse-off time were limited, and a long integration time (3 hours) was necessary. A drawback of both methods is that the measurements are line integrated. Another non-intrusive technique, which was recently implemented, is incoherent laser Thomson scattering [137]. This diagnostic provides a localised measurement with simple data interpretation; however, a complex, expensive experimental setup is required which is available in only a few laboratories.

Electrostatic probes are an alternative approach to electron plasma property measurements in HiPIMS discharges. Probe measurements are simple to undertake, but data

interpretation is difficult when a magnetic field is present, as discussed in section 2.1.3, and the relative abundance of ionic species is required for calculating ion density ($n_i$). Previous studies have used target inserts to detect localised ionisation zones (spokes) and obtain the ion density at the edge of the target sheath [135]. Moreover, intrusive Langmuir probes are typically used outside of the magnetic trap for measurements of $n_i$, $n_e$, $T_e$ and the electron energy distribution function (EEDF) [39, 122–125, 127–129, 131]. There have been few Langmuir probe studies within the last closed flux surface boundary [98, 132, 134] because the presence of the probe stem and current drainage to the probe tip are expected to significantly perturb the main ionisation region. In addition, data interpretation is simpler far from the target because unmagnetised electron collection by the probe is more valid, and the concern over probe lifetime, due to excessive sputter deposition and melting, is alleviated.

In this chapter, the first comparison of electron temperature and electron density measurements in HiPIMS discharges made by Langmuir probe and incoherent laser Thomson scattering is reported. The interpretation of an incoherent Thomson scattering spectrum is unambiguous and unaffected by magnetic fields, and so reliable electron plasma properties are obtained with excellent spatial and temporal resolutions. The aim of this research was to determine whether a Langmuir probe can provide reliable time-resolved measurements of electron temperature and electron density in HiPIMS discharges, including in the magnetic trap.

This chapter is organised as follows: section 5.2 contains a description of the discharge conditions, the data interpretation methods for each diagnostic and an estimation of the measurement uncertainties. The results are presented in section 5.3 and are discussed in section 5.4. Section 5.5 is the conclusion. It should be emphasised that the aim of this research is a comparison of the two diagnostic techniques rather than investigating the discharge physics, and the content of this chapter reflects this.

## 5.2 Experimental setup

The experimental setup and the procedures, including data acquisition and analysis, for Langmuir probe and laser Thomson scattering measurements in HiPIMS discharges are described in chapter 4. Furthermore, the relevant background theory for interpretation of the experimental data from each diagnostic is presented in chapter 3. The specific details related to this investigation are described below.

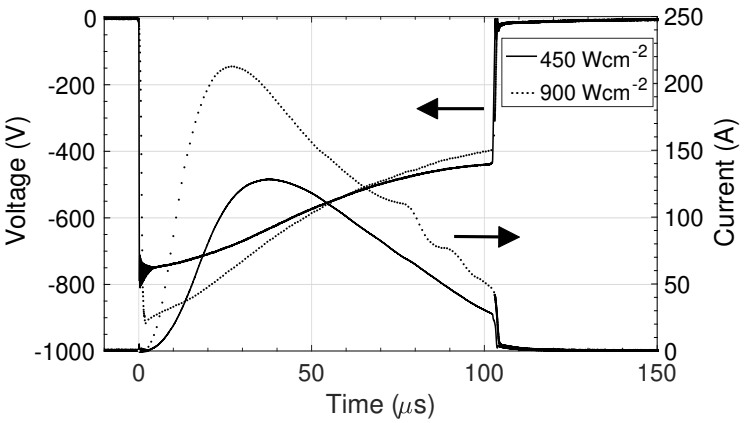


Figure 5.1: Current-voltage-time waveforms for the two discharge conditions: peak power densities of 450 W·cm$^{-2}$ and 900 W·cm$^{-2}$ with a pulse-width of 100 $\mu$s, a pulse repetition rate of 50 Hz and 1.6 Pa of argon gas.

### 5.2.1 Magnetron sputtering system

Two different voltage waveforms were applied to the tungsten target with 1.6 Pa of argon gas in the chamber. Figure 5.1 shows the current-voltage-time waveforms and these produced peak power densities of $450 \pm 25$ W·cm$^{-2}$ and $900 \pm 25$ W·cm$^{-2}$ (normalised by the entire area of the target). The pulse-width and repetition rate were 100 $\mu$s and 50 Hz, respectively. The measurement times reported in this chapter are with respect to the start of the target voltage pulse ($t = 0$ $\mu$s). In addition, measurements were performed at 0.8 Pa, but the conclusions from these results were similar to the higher pressure case, so only the results from the 1.6 Pa discharges are presented in this chapter.

The measurement positions in the study were the magnetic null point ($r = 0$ mm, $z = 61$ mm, $P1$) and at a single location in the magnetic trap ($r = 41$ mm, $z = 10$ mm, $P2$). The magnetic field strength at these positions were $B \lesssim 1$ mT and $B = 33$ mT, respectively. The terms $P1$ and $P2$ refer to the scattering geometry as explained in section 4.3.4. A detailed view of the magnetic field configuration is shown in figure 4.2.

### 5.2.2 Laser Thomson scattering system

The laser Thomson scattering system was operated in the incoherent regime; consequently, the scattering spectrum was proportional to the one-dimensional electron velocity distribu-

tion function (EVDF). The measurements performed in the $P2$ configuration were sensitive to the component of the EVDF that was perpendicular to the magnetic field in the target surface plane. For the $P1$ measurements, the EVDF component was in an arbitrary direction in the target surface plane. The Thomson scattering signal was accumulated from 100 to 600 laser pulses depending on the electron density and the opacity of the light collection window.

### 5.2.3 Langmuir probe system

#### 5.2.3.1 Apparatus

The Langmuir probe tip consisted of tungsten wire of radius $r_p = 50$ $\mu$m and was 'L' shaped. There was $\sim 0.25$ mm length parallel to the probe stem and $l_p = 5.5$ mm length perpendicular to it. The probe stem was inserted radially into the vacuum chamber so that the $l_p = 5.5$ mm length was parallel to the target surface-normal. In this orientation, the (approximately) radial magnetic field at the $P2$ measurement position was parallel to the probe tip surface-normal, which reduces the effect of electron magnetisation on the measured probe current-voltage ($IV$) characteristic [47].

A concern during HiPIMS measurements is that the rapidly changing target voltage can induce large displacement currents in the probe sheath. The plasma, however, acts to shield the target potential so that the temporal variation of the space potential is smaller in the plasma bulk as opposed to within the target sheath. Probe data is reported for $t \geqslant 10$ $\mu$s to avoid the large transient in plasma potential as the (initially) low density plasma responds to the voltage pulse applied to the target. During the pulse-on time, the rate of change of the plasma potential measured by the probe was of the order 1 V/$\mu$s. The displacement current in the probe circuit is given by [151]:

$$i_d = C_s \frac{\mathrm{d}V_p}{dt}, \tag{5.1}$$

where the sheath capacitance ($C_s$) is approximately [151]:

$$C_s \approx \frac{0.5\epsilon_0(2\pi r_p l_p)}{\lambda_D}, \tag{5.2}$$

$\epsilon_0$ is the permitivity of free space and $\lambda_D$ is the Debye length. An upper limit for $i_d$ in this study is found by using $\lambda_D = 1$ $\mu$m, which gives $i_d < 8$ $\mu$A. This is far smaller than the magnitude of the ion current collected by the probe, of the order 1 mA, during the

pulse-on period.

The plasma potential was approximately constant in the pulse-off period once the target potential had dropped to ground potential. Measurements are reported before and after this transient period (note that the voltage pulse terminates a few microseconds after $t = 100$ $\mu$s in figure 5.1). Therefore, the displacement current through the probe sheath can be neglected.

Another concern is the voltage induced in the probe circuit by the time-varying discharge current. This effect was minimised by ground shielding both the magnetron power supply cable and the probe circuitry. The significance of the induced voltage in the probe circuit for current measurements was assessed by retracting the Langmuir probe towards the insertion flange so that the tip was no longer exposed to the plasma. The measured current was lower, by a factor of the order of 100, than the ion current collected when the probe was at a measurement position. This effect was, therefore, deemed negligible.

#### 5.2.3.2 Probe theory

The following plasma parameters were determined using the Langmuir probe (theory given in section 3.1): plasma potential, floating potential, electron density and electron temperature assuming a Maxwellian EVDF, and ion density using both Laframboise and ABR-Chen theories. A smooth first derivative of the $IV$ characteristic, for locating the plasma potential, was obtained by applying a second order Savitzky-Golay filter [152] with a window length of $\sim 2$ V to the $IV$ characteristic prior to differentiating. The filter preserved the shape of the raw $IV$ characteristic; nevertheless, the other probe analyses were performed on the unsmoothed characteristic.

The calculation of ion density requires knowledge of the effective ion mass in the discharge, but the ionic composition during the experiments was an unknown mixture of argon and tungsten ions. Ion density was calculated assuming that the ions collected by the probe were purely singularly charged argon ions. This approach will underestimate the ion density because a greater effective ion mass would impede collection, resulting in a lower ion current for a given density. The ion densities calculated using the mass of a singularly charged tungsten ion (not displayed) were a factor of 2-3 times larger. Note that multiply charged ions were neglected.

The probe theories implemented assume collisionless collection by the probe. The validity of this assumption is assessed by comparing the mean free path of electrons and

ions to the probe radius and the Debye length [19, p. 2]. The mean free path of an electron (subscript: $me$) or ion (subscript: $mi$) is calculated using:

$$\lambda_{me,mi} = \frac{1}{\sigma n}, \tag{5.3}$$

where $\sigma$ is the cross-section for a two-particle collision between an electron or ion and another species which has a number density of $n$. Experimental cross-sections for collisions between an electron or ion with an argon atom can be found in the literature [153, 154]. The Coulomb collision cross-section can be estimated by the cumulative $\pi/2$ rad deflection cross-section [7, p. 58]:

$$\sigma = \frac{8}{\pi}\left(\frac{e^2}{4\pi\epsilon_0 W_R}\right)^2 \ln\left(2\lambda_D \cdot \frac{4\pi\epsilon_0 W_R}{e^2}\right), \tag{5.4}$$

where $e$ is electron charge, $W_R$ is the kinetic energy in the centre of mass frame:

$$W_R = \frac{m_1 m_2 v_R^2}{2(m_1 + m_2)}, \tag{5.5}$$

$v_R$ is the magnitude of the relative velocity vector between particles 1 and 2, and $m$ denotes mass.

The peak cross-section for an electron and an argon atom collision is $\sigma = 2.3 \times 10^{-19}$ m$^2$ between electron energies 0.12-20 eV [153], which gives $\lambda_{me}/r_p = 375$ at 1.6 Pa of argon gas (assuming at 500 K) and $\lambda_{me}/\lambda_D > 1180$ using $\lambda_D < 10$ $\mu$m. The cross-section for a Coulomb collision between an electron and an argon ion (similar to electron-electron collisions) is estimated using $W_R \approx 3k_B T_e/2$ (see appendix B; $k_B$ is the Boltzmann constant), which gives $\lambda_{me}/r_p = 21 - 2890$ and $\lambda_{me}/\lambda_D = 461 - 16000$. Note that the electron temperature and electron density determined by laser Thomson scattering were used in these calculations. The assumption of collisionless electron collection is justified given the long electron mean free path relative to the probe collection length scales.

The cross-section for a momentum exchange collision between an argon ion and an argon atom at an ion temperature of $T_i = 500$ K is $\sigma = 1.5 \times 10^{-18}$ m$^2$ [154], which gives $\lambda_{mi}/r_p = 58$ at 1.6 Pa of argon gas and $\lambda_{mi}/\lambda_D > 288$ using $\lambda_D < 10$ $\mu$m. The cross-section for a Coulomb collision between two argon ions (dominates ion-electron collisions) is estimated using $W_R \approx 3k_B T_i/2$ (see appendix B), which gives $\lambda_{mi}/r_p = 0.05 - 9$ and $\lambda_{mi}/\lambda_D = 2 - 83$. Since the probe collection length scales and the ion mean free path are

similar in magnitude, the probe operates in the weakly collisional regime. This is discussed further in section 5.4.2.

### 5.2.4 Measurement uncertainties

This section considers the magnitude of the experimental error in the measurements of plasma density and electron temperature made by each diagnostic in order to determine the accuracy of the diagnostic comparison.

Gating of the camera photocathode and intensifier by the laser pulse, setting a high gain, and reading the CCD once per spectrum ensured that the main source of noise in a Thomson scattering spectrum were the fluctuations in the overlapping plasma emission spectrum rather than noise generated inside the iCCD camera. The quality of the Gaussian function fit to a Thomson scattering spectrum was affected by this noise level. Other sources of error include the intrinsic shot noise on the Thomson scattering spectrum, plasma drift during the integration time, measuring the laser power, measuring the chamber pressure during the Rayleigh scattering calibration, and the systematic electron density overestimation as a result of the window transmission being lower during the Rayleigh scattering calibration compared to the start of the Thomson scattering measurement. An estimate for the combined effect of the factors described above, except for the systematic window transmission error, was found by calculating the standard deviation of the plasma parameters from multiple measurements. The mean of the relative standard deviation for electron density and electron temperature measurements were both $\sim 5\%$. Taking into account a 10% upper limit for the systematic overestimation of electron density from the Rayleigh scattering calibration, a general upper limit for the electron density error was $\sim 15\%$.

The main sources of error for the Langmuir probe measurements were measuring the probe surface area; and noise on the $IV$ characteristic, resulting in curve fitting errors, originating from plasma fluctuations and the probe circuitry. The combined effect of the error sources was estimated by performing repeat measurements using different probes which had similar lengths and equal radii. The mean of the relative standard deviation for the electron density, electron temperature and ion density measurements during the pulse-on time were $\sim 20\%$, $\sim 10\%$ and $\sim 10\%$, respectively. The larger uncertainty for electron density stems from locating the plasma potential because only this data point on the $IV$ characteristic was used in the calculation, in conjunction with $T_e$, as opposed to

| Figure | Position | Peak power ($\mathrm{W{\cdot}cm^{-2}}$) | $r_{g,e}/r_p$ | $r_{g,e}/\lambda_D$ |
|---|---|---|---|---|
| 5.5 | Magnetic null, $P1$ | 450 | 29-106 | 333-1046 |
| 5.7 | Magnetic trap, $P2$ | 450 | 1.0-3.4 | 10-85 |
| 5.8 | Magnetic trap, $P2$ | 900 | 1.1-3.5 | 18-114 |

Table 5.1: Summary of the electron magnetisation parameters at different measurement positions and discharge power densities. Gyroradius was approximated by assuming that the gyration kinetic energy is 2/3 of the total three-dimensional kinetic energy. The total electron kinetic energy and Debye length were calculated using the laser Thomson scattering results.

fitting multiple data points. The pulse-off time measurements were noisier because the sense resistor value was limited by the maximum current during the pulse-on time; this was more extreme for the measurements in the magnetic trap because there was a greater range of plasma density during a cycle. A boxcar method of data acquisition would solve this problem. The mean of the relative standard deviation for the electron density, electron temperature and ion density measurements during the pulse-off time were $\sim 30\%$, $\sim 20\%$ and $\sim 30\%$, respectively.

The discussion above indicates that results from the two methods can be considered consistent if the values are within $\sim 10-25\%$ of each other during the pulse-on time, and $\sim 20-35\%$ during the pulse-off time; lower (upper) bounds correspond to $T_e$ ($n_e$) measurements. In section 5.3, when direct comparisons are made, the errors for those specific conditions are used.

## 5.3 Results

The results section is split into two parts based on the location of the measurements: the magnetic null point and a position in the magnetic trap region. Table 5.1 summarises the measurement position, the peak discharge power density and the electron magnetisation parameters. The electron magnetisation parameters relate the electron gyroradius to the probe radius ($r_{g,e}/r_p$) and the length scale of the probe sheath ($r_{g,e}/\lambda_D$). The parameters tend to zero in the limit of strong $B$-field. The collection of ions was not expected to be significantly affected by the magnetic field because $r_{g,i}/r_p > 88$ and $r_{g,i}/\lambda_D > 596$.

Error bars, representing the standard deviation of repeated measurements, are plotted for all of the probe measurements and some of the laser Thomson scattering measurements.

For the latter, often the size of an error bar was comparable to the marker size in the figures. It should be noted that the error bars do not take into account any systematic electron density overestimation from performing the Rayleigh scattering calibration after the Thomson scattering measurement; the systematic error was $< 10\%$. The probe was not inside the vacuum chamber during the laser Thomson scattering measurements.

It should be noted that any drift velocity identified by the laser Thomson scattering measurements was at least an order of magnitude smaller than the root mean square speed associated with the thermal motion of the electrons. The probe data was analysed assuming zero drift velocity.

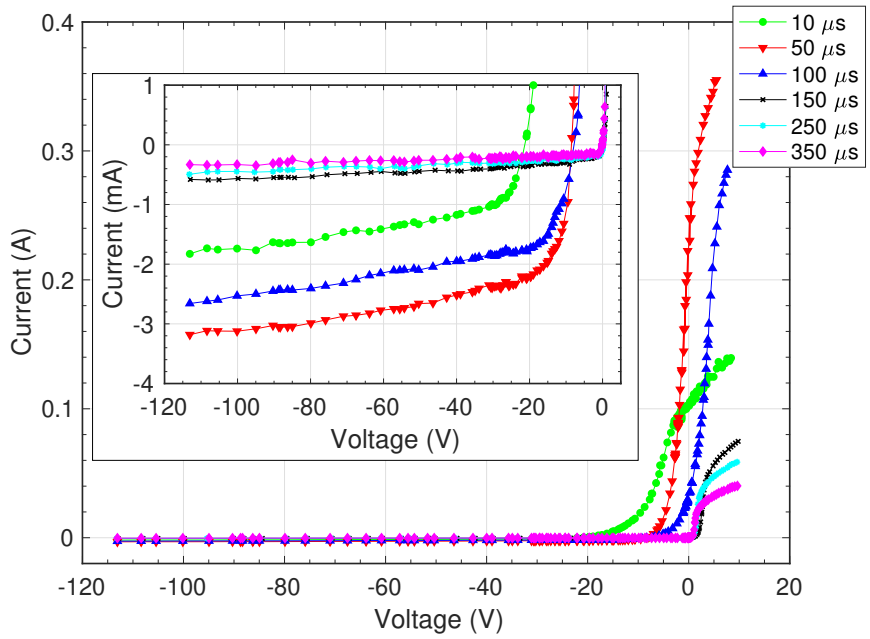


Figure 5.2: Evolution of the Langmuir probe $IV$ characteristics at the magnetic null point ($r = 0$ mm, $z = 61$ mm, $P1$) for a peak target power density of 450 W·cm$^{-2}$, a pulse repetition rate of 50 Hz, a pulse-width of 100 $\mu$s and 1.6 Pa of argon gas. Insert shows a zoomed view of the net ion current region. The time of the measurement with respect to the start of the target voltage pulse is indicated in the legend.

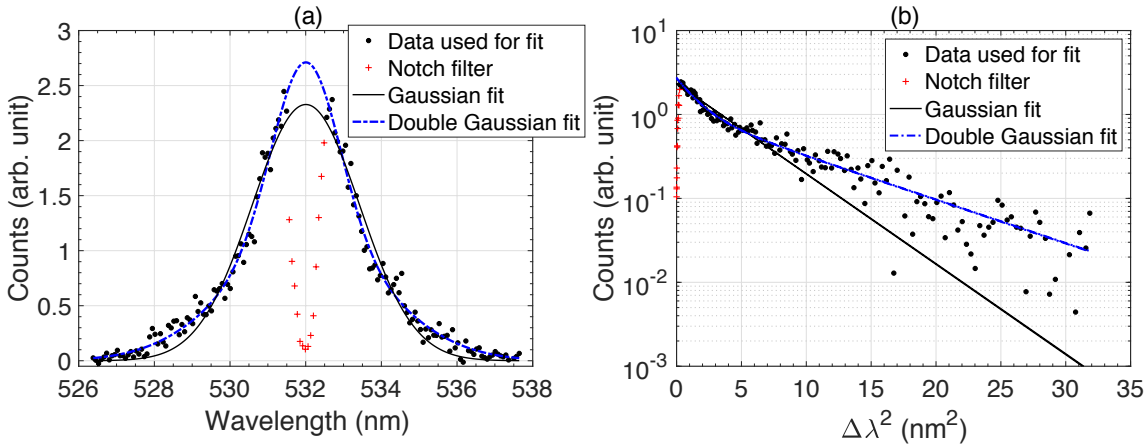


Figure 5.3: Comparison of a Gaussian and double-Gaussian fit (assumes a Maxwellian or bi-Maxwellian EVDF, respectively) to the Thomson scattering data at the magnetic null point ($r = 0$ mm, $z = 61$ mm, $P1$) at $t = 10$ $\mu$s for a peak target power density of 450 W·cm$^{-2}$, a pulse repetition rate of 50 Hz, a pulse-width of 100 $\mu$s and 1.6 Pa of argon gas. A Maxwellian EVDF appears linear on the axes in (b) when the drift velocity of the distribution is zero; where $\Delta\lambda = \lambda - \lambda_i$ ($\lambda$ is the wavelength axis and $\lambda_i = 532$ nm is the laser wavelength).

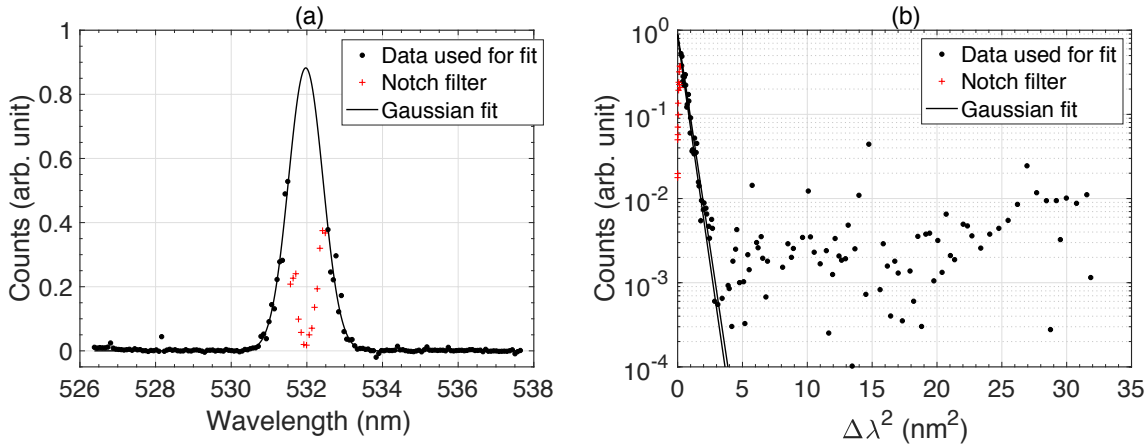


Figure 5.4: Same conditions as figure 5.3 but at $t = 350$ $\mu$s. The centre of the Gaussian fit was at 531.96 nm; hence, two fit lines appear in (b).

### 5.3.1 Negligible $B$-field

This section details the results at the magnetic null point for a peak discharge power density of 450 W·cm$^{-2}$. The magnetic field strength is negligible at this measurement position. Figure 5.2 shows a selection of $IV$ curves from the Langmuir probe. The time indicated in the figure is referenced to the start of the target voltage pulse. It is clear from the variation of both magnitude and curve shape that the plasma parameters have a dynamic evolution, which is ideal for a diagnostic comparison study.

Two extreme Thomson scattering spectra, in terms of shape, for these discharge conditions are shown in figures 5.3 and 5.4. The measurement times were $t = 10$ $\mu$s and $t = 350$ $\mu$s, respectively. The experimental data is shown by scatter points, with the black filled circles indicating the data used for the fit and the red '+' symbols indicating the data attenuated by the notch filter in the triple-grating spectrometer. A double-Gaussian fit was most appropriate for the spectrum in figure 5.3, which implies a bi-Maxwellian EVDF. The electron temperature and electron density of the two populations were $T_{c,T} = 0.8 \pm 0.2$ eV and $n_{c,T} = (6.7 \pm 1.9) \times 10^{17}$ m$^{-3}$ for the cold group, and $T_{w,T} = 3.7 \pm 0.5$ eV and $n_{w,T} = (1.0 \pm 0.2) \times 10^{18}$ m$^{-3}$ for the warm group. A single Gaussian fit was appropriate in figure 5.4, implying a Maxwellian EVDF, returning $T_e = 0.2 \pm 0.01$ eV and $n_e = (5.4 \pm 0.1) \times 10^{17}$ m$^{-3}$.

Figure 5.5(a) shows the electron temperature from both diagnostics as a function of time from the start of the voltage pulse. The Thomson scattering spectra were consistent with Maxwellian EVDFs, except at $t = 10$ $\mu$s, when a bi-Maxwellian EVDF was most appropriate, as discussed above. The probe measurements were consistent with a Maxwellian EVDF throughout and had excellent agreement with the results obtained using laser Thomson scattering during the pulse-on period, except the cold population of electrons at $t = 10$ $\mu$s was not detected. During the pulse-off period, the electron temperature determined by the probe was systematically a factor of $\sim 1.5$ greater than the Thomson scattering results, which approximately corresponds to the lower limit of the probe error bars. There were larger error bars for the probe results during this period because lower electron temperatures had fewer data points in the electron retardation region of the $IV$ characteristic for curve fitting.

The corresponding total plasma density from both diagnostics as a function of time is shown in figure 5.5(b). The three densities obtained by analysing the probe characteristic were the electron density using the knee method ($n_{e,P}$), and the ion densities ($n_{i,P}$)

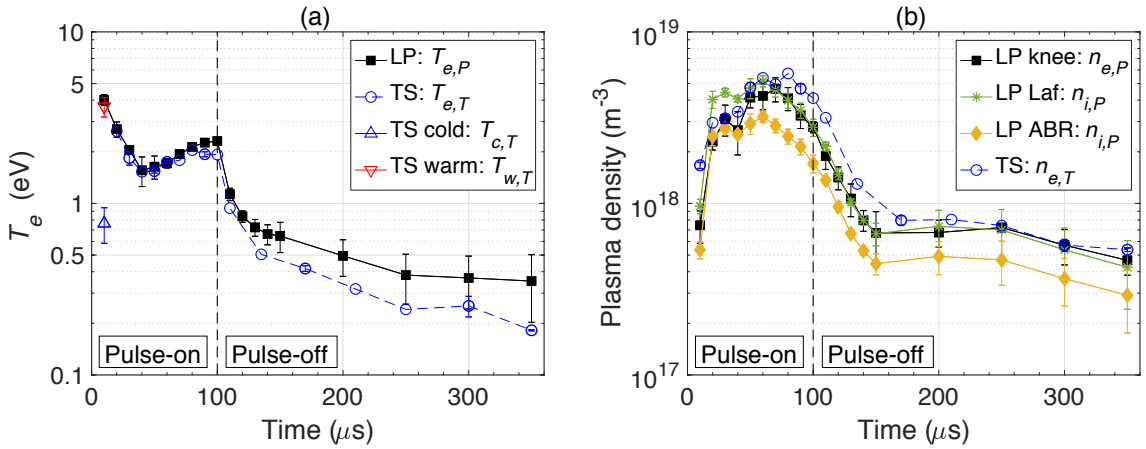


Figure 5.5: Temporal profile of (a) electron temperature and (b) plasma density measured by Langmuir probe and laser Thomson scattering during HiPIMS at the magnetic null point ($r = 0$ mm, $z = 61$ mm, $P1$). The data analysis methods are indicated in the legend. The target voltage had a pulse-width of 100 $\mu s$, a repetition rate of 50 Hz, a peak power density of 450 W·cm$^{-2}$ and the argon gas pressure was 1.6 Pa.

from Laframboise theory and ABR-Chen theory. The probe generally underestimated the plasma density, but all of the probe theories were within a factor of $\sim 2.5$ of the values obtained using laser Thomson scattering. The best agreement (within a factor of $\sim 1.5$) with the results of Thomson scattering were both the ion density calculated using Laframboise theory and the electron density determined using the knee method.

### 5.3.2 Weak $B$-field

The results reported in this section are from measurements in the magnetic trap, where electron magnetisation is important, at peak power densities of 450 W·cm$^{-2}$ and 900 W·cm$^{-2}$. The Thomson scattering spectra were consistent with Maxwellian EVDFs. The probe determined EVDFs, however, were non-Maxwellian which suggests that the collection of electron current by the probe is distorted by the magnetic field. Non-Maxwellian EVDFs are indicated by a non-linear region on a plot of natural logarithm of electron current against voltage for $V \leqslant V_p$. An example is shown in figure 5.6 for the 450 W·cm$^{-2}$ case at $t = 30$ $\mu$s. To calculate an effective electron temperature from the probe data (and this is also used to calculate an electron density using the knee method), the technique discussed in section 2.1.3.4 for probe operation in magnetised plasma was implemented: only

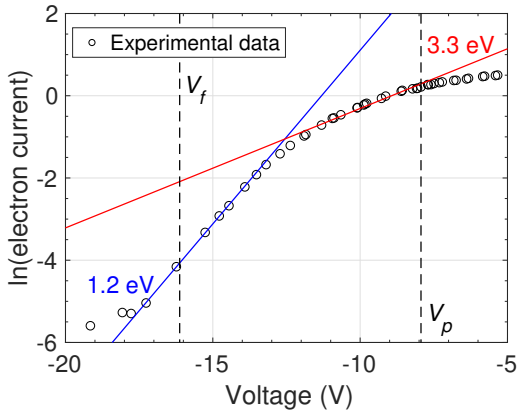


Figure 5.6: Natural logarithm of electron current against voltage. The measurement was performed at $t = 30$ $\mu$s and in the magnetic trap ($r = 41$ mm, $z = 10$ mm, $P2$). A linear line on these axes for $V \leqslant V_p$ corresponds to a Maxwellian EVDF. Separate electron temperatures were calculated from the gradient of the curve in the vicinity of the plasma potential and floating potential. The target voltage had a pulse-width of 100 $\mu s$, a repetition rate of 50 Hz, a peak power density of 450 W·cm$^{-2}$ and the argon gas pressure was 1.6 Pa.

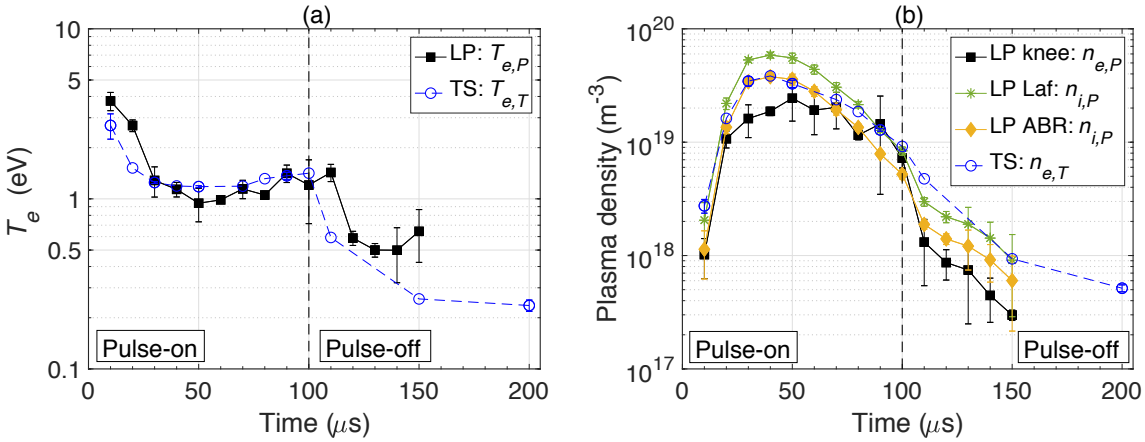


Figure 5.7: Temporal profile of (a) electron temperature and (b) plasma density measured by Langmuir probe and laser Thomson scattering during HiPIMS in the magnetic trap ($r = 41$ mm, $z = 10$ mm, $P2$). The data analysis methods are indicated in the legend. The target voltage had a pulse-width of 100 $\mu s$, a repetition rate of 50 Hz, a peak power density of 450 W·cm$^{-2}$ and the argon gas pressure was 1.6 Pa.

the floating potential region of the characteristic was included in the data fit. The effective electron temperature from the floating potential region was a factor of $\sim 3$ lower than the value obtained in the vicinity of the plasma potential. The Druyvesteyn method (explained in section 3.1.3.3) was not implemented because this calculates an effective electron temperature using the entire electron energy distribution function, including the falsely depleted highly-magnetised low energy region, leading to electron temperature overestimation.

Figure 5.7(a) shows the electron temperature from both diagnostics as a function of time from the start of the voltage pulse for a peak power density of 450 W·cm$^{-2}$. The temporal range of the probe results are limited to $t = 150$ $\mu$s due to the afterglow $IV$ characteristics being noisy. The results from the diagnostics had good agreement during the pulse-on period. In the pulse-off period, the probe overestimated the electron temperature by a factor of $\sim 2.5$ at $t = 150$ $\mu$s.

The corresponding plasma density results are shown in figure 5.7(b). During the pulse-on time, the electron density determined by the Langmuir probe was up to a factor of $\sim 2$ lower than the laser Thomson scattering results. In the pulse-off period, the underestimation of electron density by the Langmuir probe was a factor of $\sim 3$. With respect to the ion collection theories, ABR-Chen theory had excellent agreement with the laser Thomson

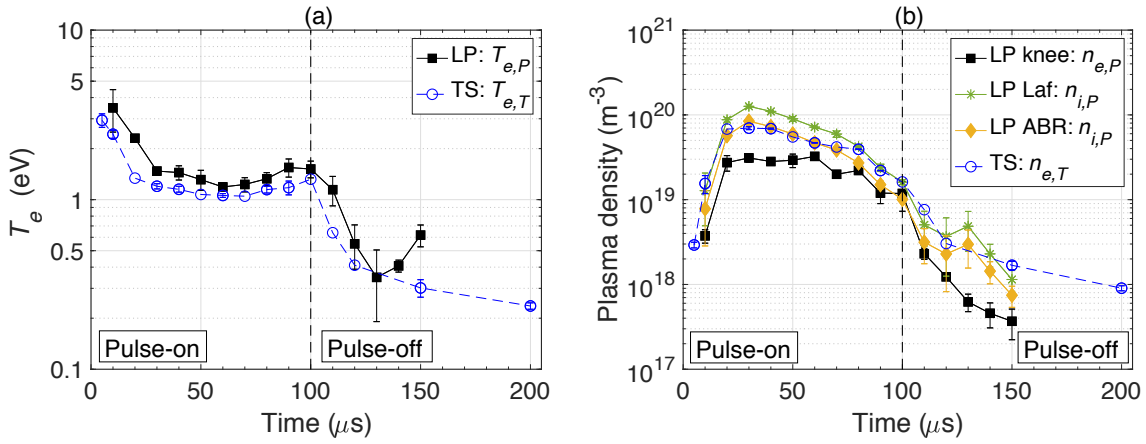


Figure 5.8: Temporal profile of (a) electron temperature and (b) plasma density measured by Langmuir probe and laser Thomson scattering during HiPIMS in the magnetic trap ($r = 41$ mm, $z = 10$ mm, $P2$). The data analysis methods are indicated in the legend. The target voltage had a pulse-width of 100 $\mu s$, a repetition rate of 50 Hz, a peak power density of 900 W·cm$^{-2}$ and the argon gas pressure was 1.6 Pa.

scattering results when $n_e \gtrsim 3 \times 10^{19}$ m$^{-3}$; and for these conditions, Laframboise theory overestimated the plasma density by a factor of $\sim 1.5$. At a lower plasma density, however, Laframboise theory was the most accurate.

Similar trends are shown in figure 5.8 for a peak discharge power density of 900 W·cm$^{-2}$. The maximum electron density measured by laser Thomson scattering ($(7.0 \pm 0.3) \times 10^{19}$ m$^{-3}$) was approximately double the maximum electron density measured in the magnetic trap for the 450 W·cm$^{-2}$ discharge. The systematic electron density underestimation by the probe is more pronounced at the higher discharge power density: the electron density from the knee method was within a factor of $\sim 2.5$ of the laser Thomson scattering results during the pulse-on time.

## 5.4 Discussion

The results show that Langmuir probe measurements can give reasonable estimates of electron temperature and plasma density in HiPIMS discharges. There are, however, several aspects of the results that warrant further discussion: (1) why did the probe not detect the warm population of electrons at the start of the HiPIMS pulse at the magnetic null point? (2) Why was ABR-Chen theory the most accurate ion collection theory above $n_e \gtrsim 3 \times 10^{19}$ m$^{-3}$ ? (3) Can the electron density underestimation by the Langmuir probe be accounted for by magnetised probe theory? These topics are discussed separately below.

### 5.4.1 The sensitivity of Langmuir probe measurements to cold and warm electron populations

Based on the electron properties of the bi-Maxwellian EVDF detected by laser Thomson scattering at the magnetic null point at $t = 10$ $\mu$s, one can construct a theoretical electron current against voltage curve to compare with the experimental data from the Langmuir probe. This is shown in figure 5.9; a linear line on these axes for $V \leqslant V_p$ indicates a Maxwellian EVDF. The electron current expected from the warm population alone is also plotted. The two theoretical curves only deviate noticeably for $V_p - 2 < V \leqslant V_p$, which corresponds to the low energy region of the EVDF; nonetheless, the increase in electron current in this region due to the cold population appears small on these axes. This is despite the electron density of the two populations being of the same order of magnitude.

The experimental electron current appears slightly depleted in the region close to $V_p$

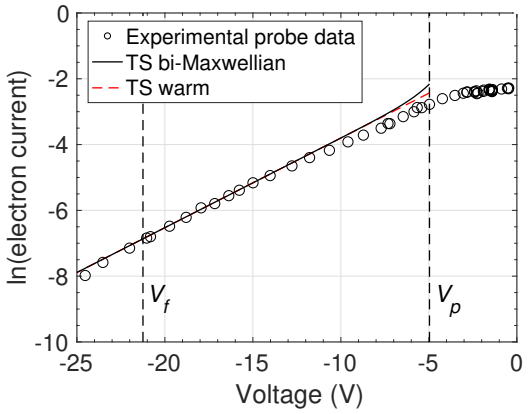


Figure 5.9: Natural logarithm of electron current against voltage. Plotted are experimental data from the probe and theoretical curves calculated from the properties of the bi-Maxwellian EVDF determined from laser Thomson scattering (an example spectrum is shown in figure 5.3). The measurements were performed at the magnetic null point ($r = 0$ mm, $z = 61$ mm, $P1$) at $t = 10$ $\mu$s for a peak target power density of 450 W·cm$^{-2}$, a pulse repetition rate of 50 Hz, a pulse-width of 100 $\mu$s and 1.6 Pa of argon gas.

compared to the theoretical curves; hence, the probe did not detect the cold population of electrons. A similar effect, but more extreme, was observed in a previous Langmuir probe and laser Thomson scattering comparison study using an inductively coupled plasma [35, section 2.1.2.2]. Bowden *et al.* [35] concluded that either the probe measured perturbed plasma due to the presence of the probe or the data interpretation was incorrect. Considering the former, the perturbing effect of the probe is due to the floating probe stem being in the plasma and/or the probe tip collecting a net current. The probe draws a relatively large electron current from the plasma when the low energy region of the EEDF is sampled, which could cause a reduction of the local plasma density [18, p. 183][19, p. 91][20]. This effect might be exacerbated by the fact that electrons have to diffuse across the magnetic field from within the last closed flux surface boundary to reach the magnetic null point in order to replenish the electrons drained by the probe, given that the magnetic trap is the main ionisation region in the discharge. In addition, one would expect the cross-magnetic field transport of low energy electrons to be more restricted due to their smaller gyroradii.

### 5.4.2 Choice of ion collection theory

The collisionless radial motion theory by ABR-Chen always predicts a larger ion current to the probe for a given plasma density compared to the collisionless orbital motion theory by Laframboise in the limit of $T_i \to 0$ (see section 3.1.4.2 for further discussion). ABR-Chen theory will, therefore, always return a lower ion density. It has been extensively reported in the literature that ABR-Chen theory has applicability when a small number of collisions in the probe sheath destroy orbital motion and induce radial motion [21, 22, 58]. One can speculate that this effect is responsible for the observation that the ion density calculated using ABR-Chen theory had better agreement with the laser Thomson scattering results above $n_e \gtrsim 3 \times 10^{19}$ m$^{-3}$ compared to Laframboise theory. The high plasma density reduces the Coulomb mean free path and it becomes similar in magnitude to the probe sheath thickness as shown by the calculations in section 5.2.3.2. Moreover, the strong sputtering wind in front of the target reduces the mean free path of the ions further. Nevertheless, the agreement between the ABR-Chen and Laframboise theories for ion density measurements was always within a factor of $\sim 1.5$. This is a result of orbital motion effects being reduced in dense plasmas with thin probe sheathes; therefore, both theories predict a similar ion current. For all of the plasma conditions investigated, both of the theories had reasonable agreement with the results of laser Thomson scattering (within a factor of $\sim 2.5$).

Underestimation of the effective ion temperature is another effect that would lead to ion density overestimation using Laframboise theory. Room temperature ions were assumed in this research, but Laframboise computed the theoretical ion current for various ratios of $T_i/T_e$ [25]. An increase in the effective ion temperature would increase the current collected by the probe for a given ion density. Mass spectrometry measurements [116] have shown that the singularly-charged metal ion population in a HiPIMS discharge has an average energy of the order of electronvolts. Moreover, collisions between metal species and argon results in an enhancement of the argon ion energy distribution tail. It should be highlighted that the ABR-Chen theory is for cold ions only ($T_i = 0$).

To summarise, the various factors leading to ion density overestimation using Laframboise theory: a weakly collisional probe sheath and underestimation of the effective ion temperature. Factors common to both ABR-Chen and Laframboise theories: underestimation of the effective ion mass favours ion density underestimation, and the tendency is to underestimate the probe surface area due to the design of the 'L' shape probe leading

to ion density overestimation. A future experiment could use a mass spectrometer to determine the effective ion mass and the effective ion temperature to assess the accuracy of the ion collection theories in more detail.

### 5.4.3 Electron magnetisation

It is important to point out that different components of the EVDF were sampled, for determining electron temperature, by the probe and laser Thomson scattering diagnostics. The former is sensitive to the EVDF in the two-dimensional plane of the probe tip surface-normal (see equation 3.3), which corresponded to the plane spanned by the target-surface in these experiments; whereas, the laser Thomson scattering measurements in the magnetic trap were sensitive to the direction perpendicular to the magnetic field in the target-surface plane. In the magnetic trap, the laser Thomson scattering measurements were consistent with a Maxwellian EVDF, but the probe measurements appeared non-Maxwellian. A possibility is that the non-Maxwellian EVDFs determined by the probe are due to non-Maxwellian EVDFs in the direction parallel to the magnetic field, rather than distortion of the $IV$ characteristic caused by the magnetic field. Although, if this was true, one would still expect the electron densities determined by the diagnostics to be consistent with one another. The electron density determined by the knee method (see equation 3.7) was lower than the laser Thomson scattering results; therefore, the effective electron temperature measurement by the probe is overestimated and/or the electron saturation current is underestimated. Since the electron temperature calculated from the floating potential region is a lower bound for the probe characteristic, one can conclude that the electron saturation current is reduced by the magnetic field and this will also distort the shape of the probe determined EVDF.

The effect of the magnetic field on the electron plasma property measurements made by the Langmuir probe was mitigated by two techniques: orientating the probe tip axis perpendicular to the magnetic field and analysing only the floating potential region for calculating electron temperature. The net result at $B = 33$ mT during the pulse-on time was an electron density underestimation relative to laser Thomson scattering by a factor up to $\sim 2.5$, and similar electron temperature measurements were obtained. This justifies the use of triple probes in HiPIMS plasma with similar magnetic field strengths to this study [134] because the triple probe only samples the high energy tail of the EVDF. However, the discrepancy in electron density cannot be explained by the magnetised probe theories

of Laframboise and Rubinstein [47] or Usoltceva *et al.* [48] (see section 2.1.3.3). The theoretical reduction of the electron saturation current, and hence electron density (given a correct electron temperature), by these theories is a factor of $\sim 1.17$ when $r_{g,e}/r_p = 1$ (as in this study). Moreover, the largest possible theoretical reduction is a factor of $\pi/2 = 1.57$ in the limit of a strong magnetic field ($r_{g,e}/r_p, r_{g,e}/\lambda_D \to 0$). Nevertheless, the probe was successful in providing a reasonable indication of the electron plasma properties in HiPIMS discharges, which suggests that the intrusive probe did not significantly perturb the plasma.

A limitation of the method used to interpret the electron current data of the probe is that it will fail if the EVDF of the plasma is non-Maxwellian because the effective electron temperature from the floating potential region will not be representative of the overall distribution. In addition, the accuracy of the probe measurements in the pulse-off period degrades because the average energy of an electron decreases, resulting in smaller gyroradii and enhanced impedance for collection by the probe.

## 5.5 Conclusion

The research presented in this chapter is the first comparison of electron plasma property measurements made by Langmuir probe and laser Thomson scattering in HiPIMS discharges. Measurements were performed at the magnetic null, where the magnetic field strength is negligible ($B \lesssim 1$ mT), and at a single position within the magnetic trap, where the magnetic field strength is significant for electron magnetisation ($B = 33$ mT). Laser Thomson scattering was chosen as the reference diagnostic because it is a non-intrusive technique, it provides absolute electron density measurements, and its data interpretation is independent of magnetic field strength and orientation.

At the magnetic null, the electron velocity distribution functions (EVDFs) determined from both diagnostics were, in general, consistent with Maxwellian distributions. During the pulse-on and pulse-off periods, the electron temperature agreement was good and the probe underestimated the electron density, compared to laser Thomson scattering, by up to a factor of $\sim 1.5$. In contrast, the EVDF agreement in the magnetic trap was poor: the Thomson scattering spectra were consistent with Maxwellian distributions, whereas the probe determined EVDFs were distorted by the magnetic field and they appeared non-Maxwellian. An electron temperature was calculated from the probe measurements, which was used to calculate electron density, by analysing only the floating potential region of the probe current-voltage characteristic. This method samples the high energy tail of

the EVDF, which is less affected by the magnetic field. During the pulse-on time, the electron temperature agreement was reasonable and the Langmuir probe underestimated the electron density by up to a factor of $\sim 2.5$. During the pulse-off period, the accuracy of the probe determined parameters degraded because the effects of electron magnetisation increase as electron temperature decreases.

To conclude, the reasonable agreement during the pulse-on time demonstrates that the Langmuir probe did not significantly perturb the discharge; therefore, probes are suitable for measurements of general electron characteristics in HiPIMS discharges, including in the magnetic trap region. This is a significant outcome because the Langmuir probe is a standard diagnostic for low temperature plasmas, but their usage in the magnetic trap region has, so far, been restricted. This was mainly due to the difficulty of interpreting probe data from a highly magnetised region of the discharge and concerns over plasma perturbation.

It should be noted that the perturbing effect of a Langmuir probe on highly transient phenomena, such as spokes, was not investigated because the diagnostics in the study were used to calculated time-averaged electron plasma properties. In addition, the accuracy of the Langmuir probe for calculating ion density needs to be investigated further because the ion collection theories are dependent on quantities that were not measured in this investigation: the relative abundance of ionic species in the plasma and the ion energy distribution function.

# Chapter 6

# Comparison of Langmuir probe and laser Thomson scattering for electron plasma property measurements in DC magnetron discharges[1]

## 6.1 Introduction

Electrons are the driving force of many physical and chemical processes in low temperature plasma sources. Knowledge of the electron energy distribution function (EEDF) is essential for any discharge physics investigation because it determines the types of interactions a heavy species can have with an electron (e.g. elastic and inelastic collisions) and the frequency at which they occur. For the case of a Maxwellian distribution of electrons, the EEDF is characterised by electron temperature ($T_e$) and electron density ($n_e$). For many conditions/discharges, however, the EEDF is non-Maxwellian, and so its shape must be measured.

Langmuir probes are routinely used for electron plasma property measurements in both Maxwellian and non-Maxwellian [155] plasmas. The current-voltage ($IV$) characteristic

[1]The research presented in this chapter has been published in a peer-reviewed journal [1].

from a single Langmuir probe is relatively simple to measure; moreover, it contains a wealth of localised information, which can be used to calculate several plasma parameters by implementing a suitable probe theory [18, 19, 143]: $n_e$, $T_e$, EEDF, ion density ($n_i$), plasma potential ($V_p$) and floating potential ($V_f$). The main limitations are that the probe is intrusive and a probe theory is selected based on the plasma properties *a priori* to the data analysis.

As discussed in section 2.1.3, one of the most challenging operating regimes of the Langmuir probe is in magnetised plasma because it is difficult to model the transport anisotropy caused by the magnetic field impeding cross-field transport [18, p. 267]. Furthermore, the probe has a longer disturbance length scale compared to operation in an unmagnetised plasma because the charge collected by the probe is replenished at a slower rate [49]. In these conditions, the probe current is reduced and is dependent on several parameters: the probe tip size with respect to the ion and electron gyroradii ($r_{g,i}, r_{g,e}$ for ions and electrons, respectively) [45, 47] and Debye length ($\lambda_D$); the probe tip orientation with respect to the $B$-field [47, 48]; chamber size/geometry [43]; collisionality [18, p. 267]; plasma instabilities; and the applied voltage with respect to $V_p$. Some of these factors are unique to each discharge and a complete probe theory has never been developed. An experimentalist, therefore, often has to use unmagnetised probe theories. The resultant errors from this approach are discussed in section 2.1.3.2: uncertainty locating $V_p$ due to rounding of the $IV$ curve knee [21]; distortion of the measured EEDF, especially the low energy part [45]; plasma density underestimation [45, 57, 59]; and $T_e$ overestimation [46].

Technological plasma sources generally use weak magnetic fields ($B < 100$ mT), as a result, electrons are the only magnetised species in the plasma. Experimental effort is required to demonstrate the error caused by using unmagnetised electron probe theories in these conditions in order to understand the limitations of the diagnostic. Previous studies have used the probe determined $n_i$ as the benchmark to compare with $n_e$ [45, 57, section 2.1.3.4], despite the ion current collected by the probe being strongly influenced by collisions with the background gas [21, 22, 58]. Therefore, the choice of probe theory for calculating $n_i$ is crucial, and so the benchmark density cannot be considered reliable. In addition, the accuracy of $T_e$ measurements using a probe in weakly magnetised conditions remains to be verified. A probe comparison study using an accurate independent diagnostic is required.

This chapter presents a comparison of the Langmuir probe and incoherent laser Thomson scattering diagnostics in weakly magnetised plasma in order to assess the accuracy

of the Langmuir probe for electron plasma property measurements ($n_e$, $T_e$ and EEDF). The advantages of using laser Thomson scattering as the reference diagnostic are that it has simple data interpretation, which is independent of magnetic field strength, because the shape of the scattering spectrum is proportional to the electron velocity distribution function (EVDF) in the incoherent regime [67, section 3.2.3]; the calibration procedure for absolute electron density values is straightforward; it is non-intrusive; and it has good spatial resolution. Other non-intrusive diagnostics, such as microwave interferometry [156] and optical emission spectroscopy [157], are unable to provide the same unambiguous measurements of localised $n_e$, $T_e$ and EEDF. The disadvantages of laser Thomson scattering are that a complex, expensive experimental setup is required and the measurements are insensitive to the tail of the EVDF. Previous comparison studies of Langmuir probes and laser Thomson scattering, detailed in sections 2.1.2.2 and 2.1.3.5, found relatively good agreement [35–37, 60–62], but there has not been a detailed study in weakly magnetised conditions.

A planar-circular unbalanced magnetron was the plasma source for this investigation. A preliminary comparison study using high power impulse magnetron sputtering (HiPIMS) discharges, detailed in chapter 5 [2], found good agreement between the diagnostics for electron density and electron temperature measurements up to $B = 33$ mT. The aim of the research presented in chapter 6 was to extend the comparison study to the lower-density DC magnetron mode and determine the plasma conditions for which unmagnetised Langmuir probe theory gives a reasonable indication of electron plasma properties.

Section 6.2 contains a description of the experimental apparatus, which includes the discharge conditions, the data interpretation methods used to extract plasma parameters, and an estimation of the measurement uncertainties. The results are presented in section 6.3 and a discussion comparing the diagnostics follows in section 6.4. Section 6.5 is the conclusion. It should be emphasised that the aim of this research was to compare the results from the diagnostics rather than investigate the discharge physics, and the content of this chapter reflects this.

## 6.2 Experimental setup

The experimental setup and the procedures, including data acquisition and analysis, for Langmuir probe and laser Thomson scattering measurements in DC magnetron discharges are described in chapter 4. Furthermore, the relevant background theory for interpretation

of the experimental data from each diagnostic is presented in chapter 3. The specific details related to this investigation are described below.

### 6.2.1 Magnetron sputtering system

The range of discharge parameters used in this study were $0.47 - 2.53$ Pa of argon gas and $15 - 125$ W of DC power. The measurement positions were the magnetic null point ($r = 0$ mm, $z = 61$ mm, $P1$), where $B \lesssim 1$ mT; and in the magnetic trap region ($r = 41$ mm, $z = 10 - 50$ mm, $P2$ and $P3$), where $B = 5 - 33$ mT, with $B$ increasing as the target surface is approached ($z$ decreasing). The terms $P1, P2$ and $P3$ refer to the geometry of the scattering system as explained in section 4.3.4. A detailed view of the magnetic field configuration is shown in figure 4.2.

### 6.2.2 Laser Thomson scattering system

The laser Thomson scattering diagnostic was operated in the incoherent regime; consequently, the scattering spectrum was proportional to the EVDF in one-dimension. The measurements performed in the $P2$ and $P3$ configurations were sensitive to the component of the EVDF that was perpendicular and parallel to the magnetic field in the target surface plane, respectively. For the $P1$ measurements, the EVDF component was in an arbitrary direction in the target surface plane. The Thomson scattering signal was accumulated from 3000 to 9000 laser pulses depending on the electron density and the opacity of the light collection window.

### 6.2.3 Langmuir probe system

#### 6.2.3.1 Apparatus

The probe tip used for the measurements at the magnetic null point ($P1$) was orientated parallel to the probe stem with a length of $l_p = 5.5$ mm. This is referred to as a 'straight' probe. The tips used in regions $P2$ and $P3$ were 'L' shaped with $\sim 0.25$ mm length parallel to the probe stem, which was neglected during analysis, and $l_p = 5$ mm length parallel to the target surface-normal. The 'L' probe was orientated so that the local magnetic field direction was approximately parallel to its surface-normal in order to reduce the effects of electron magnetisation [47]. The probe tip radius was $r_p = 50$ $\mu$m for both the 'straight' and 'L' probes. Several other probe tip dimensions $(r_p, l_p)$ were used in this study to

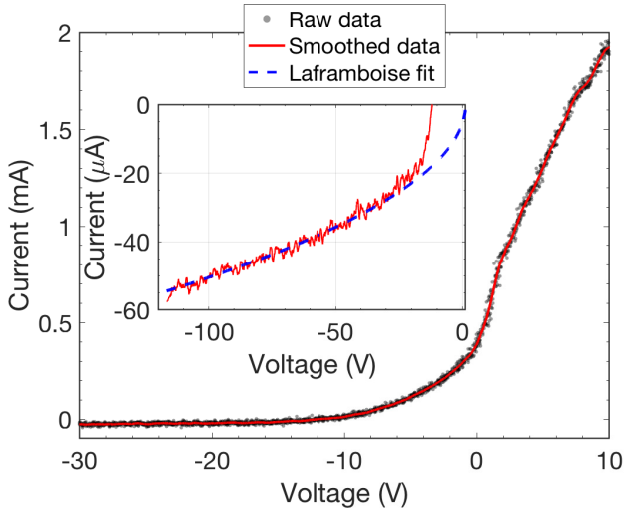


Figure 6.1: Langmuir probe current-voltage characteristic measured at the magnetic null point ($r = 0$ mm, $z = 61$ mm, $P1$) for discharge conditions of 100 W DC and 1.6 Pa of argon gas. Plotted are the raw probe data and the smoothed characteristic from applying a second order Savitzky-Golay filter with a window length of $\sim 1.5$ V. The insert shows the ion current fit from Laframboise theory.

investigate the effect of probe size on the electron density measurements. This is discussed in section 6.3.3.

#### 6.2.3.2 Probe theory

The following plasma parameters were determined using the Langmuir probe (section 3.1): plasma potential; floating potential; electron density and temperature assuming Maxwellian and bi-Maxwellian EVDFs; the EEDF using the Druyvesteyn method, and the resultant electron density and effective temperature; and ion density using Laframboise theory. Data analysis was performed on the $IV$ characteristic after the raw data had been smoothed by a second order Savitzky-Golay filter [152] with a window length of $\sim 1.5$ V. An example Langmuir probe characteristic is shown in figure 6.1 and the insert shows the fit from Laframboise theory to the ion saturation current region. Ion density was calculated assuming that the ions collected by the probe were purely singularly charged argon ions because the density of tungsten ions in the plasma was expected to be small during DC operation. A smooth second derivative for the Druyvesteyn method was obtained by

applying a second order Savitzky-Golay filter with a window length of $\sim 2.0$ V to the first derivative of electron current with respect to voltage, and then differentiating.

The probe theories implemented assume collisionless collection by the probe. To assess the validity of this assumption, the cross-sections given in section 5.2.3.2 can be used to estimate the electron and ion mean free paths ($\lambda_{me}$ and $\lambda_{mi}$, respectively) during DC magnetron operation, and these can be compared to the probe collection length scales. Consideration of electron and argon atom (at 500 K) collisions gives $\lambda_{me}/r_p = 237 - 1280$ and $\lambda_{me}/\lambda_D > 456 - 2450$ using $\lambda_D < 26$ $\mu$m, where the upper and lower bounds correspond to the extremes of the argon gas pressure. Coulomb collisions between electrons and argon ions (similar mean free path to electron-electron collisions) gives $\lambda_{me}/r_p > 1190$ and $\lambda_{me}/\lambda_D > 4610$. Note that the electron temperature and electron density determined by laser Thomson scattering were used in these calculations. The assumption of collisionless electron collection is justified given the long electron mean free path relative to the probe collection length scales.

The orbital motion of ions in the probe sheath is impeded by collisions when

$$\lambda_{mi} < \lambda_{OML} \equiv r_p \left( \frac{e(V_p - V)}{k_B T_i} \right)^{1/2}, \tag{6.1}$$

where $e$ is electron charge, $k_B$ is the Boltzmann constant, $\lambda_{OML}$ is a parameter derived from orbital motion limited theory [58] valid for ($r_p/\lambda_D < 3$) [146]. Assuming an argon ion temperature of $T_i = 500$ K and $V_p - V = 100$ V, a value of $\lambda_{OML} = 2.4$ mm is obtained for the $r_p = 50$ $\mu$m probe. The mean free path for ion momentum exchange collisions with argon atoms is $\lambda_{mi} = 1.8 - 9.8$ mm for the pressure range used in this study. In addition, the ion mean free path from Coulomb collisions, which is dominated by argon ion-ion collisions, is $\lambda_{mi} \lesssim 1$ mm in the DC plasma conditions. Since $\lambda_{mi}$ and $\lambda_{OML}$ are comparable in magnitude, the probe operates in the weakly collisional regime where ion dynamics are a mixture of orbital and radial motion [21, 22, 58].

Table 6.1 shows a comparison of the lower bounds for the electron and ion collision parameters from this section (DC magnetron conditions) and section 5.2.3.2 (HiPIMS conditions) for an argon gas pressure of 1.6 Pa and probe radius of $r_p = 50$ $\mu$m. It appears that the assumption of collisionless conditions is more valid in the DC mode for both electrons and ions.

| Parameter | HiPIMS | DC |
|---|---|---|
| $\lambda_{me}/r_p$ | 21 | 375 |
| $\lambda_{me}/\lambda_D$ | 461 | 721 |
| $\lambda_{mi}/r_p$ | 0.05 | 11 |
| $\lambda_{mi}/\lambda_D$ | 2 | 26 |

Table 6.1: Comparison of the lower bounds for the electron and ion collision parameters for HiPIMS (chapter 5) and DC magnetron operation (chapter 6) at an argon pressure of 1.6 Pa and a probe radius of $r_p = 50$ $\mu$m.

### 6.2.4 Measurement uncertainties

The general discussion in section 5.2.4 about experimental uncertainties also applies to the measurements in the DC magnetron. In this case, the mean of the relative standard deviation for electron density and electron temperature measurements made by laser Thomson scattering were $\sim 6\%$ and $\sim 8\%$, respectively. Taking into account a 10% upper limit for the systematic overestimation of electron density from the Rayleigh scattering calibration, a general upper limit for the electron density error was $\sim 16\%$.

The mean of the relative standard deviation for the plasma density and electron temperature measurements made by the probe was between $10-15\%$. Therefore, a reasonable upper limit for the general error in the plasma parameters determined by the probe was $\sim 15\%$.

The discussion above indicates that results from the two methods can be considered consistent if the values are within $\sim$ 20% of each other. In section 6.3, when direct comparisons are made, the errors for those specific conditions are used.

## 6.3 Results

The results section is divided into three parts: two describing the measurements from different regions of the plasma (sections 6.3.1 and 6.3.2) and a final section (section 6.3.3) describing the checks that were performed to confirm the reliability of the results from each diagnostic. Table 6.2 summarises the measurement position and the electron magnetisation parameters for sections 6.3.1 and 6.3.2. The collection of ions was not expected to be significantly affected by the magnetic field because $r_{g,i}/r_p > 88$ and $r_{g,i}/\lambda_D > 204$.

Error bars, representing the standard deviation of repeated measurements, are plotted for the laser Thomson scattering measurements. Often the size of an error bar was

| Section | Position | $r_{g,e}/r_p$ | $r_{g,e}/\lambda_D$ |
|---|---|---|---|
| 6.3.1 | Magnetic null, $P1$ | 42-48 | 88-181 |
| 6.3.2 | Magnetic trap, $P2$ | 2-9 | 6-33 |

Table 6.2: Summary of the electron magnetisation parameters at different measurement positions. Gyroradius was approximated by assuming that the gyration kinetic energy is 2/3 of the total three-dimensional kinetic energy. The total electron kinetic energy and Debye length were calculated using the laser Thomson scattering results.

comparable to the marker size in the figures. It should be noted that the error bars do not take into account any systematic electron density overestimation from performing the Rayleigh scattering calibration after the Thomson scattering measurement; the systematic error was $< 10\%$. The repeatability of the probe determined parameters were generally within 15% during DC magnetron operation. Unless explicitly stated, the diagnostics were not operated simultaneously and the probe was not inside the vacuum chamber during the laser scattering measurements.

It should be noted that any drift velocity identified by the laser Thomson scattering measurements was at least an order of magnitude lower than the root mean square speed associated with the thermal motion of the electrons. The probe data was analysed assuming zero drift velocity.

### 6.3.1 Negligible $B$-field

The measurements reported in section 6.3.1 were made at the magnetic null point, where the magnetic field strength is negligible ($B \lesssim 1$ mT). Power and pressure scans were performed: $15 - 125$ W with 1.6 Pa of argon gas and $0.47 - 2.53$ Pa of argon gas at 25 W. Figures 6.2(a) and 6.3(a) show the electron temperature results from both diagnostics for the respective scans. The Thomson scattering spectra were consistent with Maxwellian EVDFs, whereas a bi-Maxwellian EVDF (or equivalently EEDF) was obtained for most of the probe measurements. A typical electron current characteristic consistent with a bi-Maxwellian EEDF is shown in figure 6.4(a). The cold electron temperature measured by the probe had good agreement with the laser Thomson scattering results ($T_e \sim 0.5$ eV). An exception is at 0.47 Pa, where the EEDF determined by the probe was Maxwellian with an electron temperature of $T_{e,P} = 4.8 \pm 0.3$ eV. An example electron current characteristic for these conditions is shown in figure 6.4(b). This result was confirmed by taking repeat

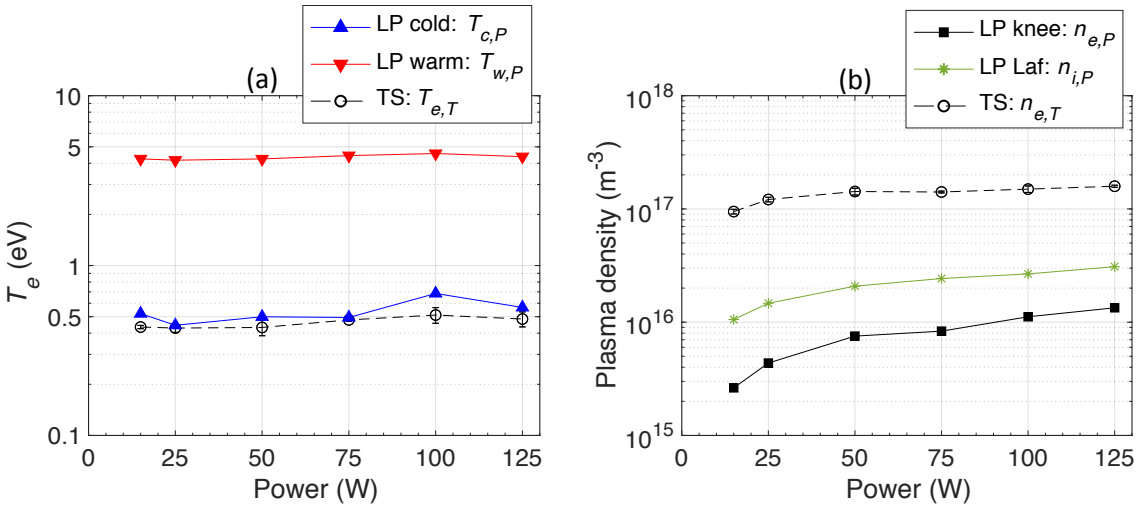


Figure 6.2: Power dependence of (a) electron temperature and (b) plasma density measured by Langmuir probe and laser Thomson scattering during DC magnetron operation. The data analysis methods are indicated in the legend. The argon gas pressure was 1.6 Pa and the measurements were performed at the magnetic null point ($r = 0$ mm, $z = 61$ mm, $P1$).

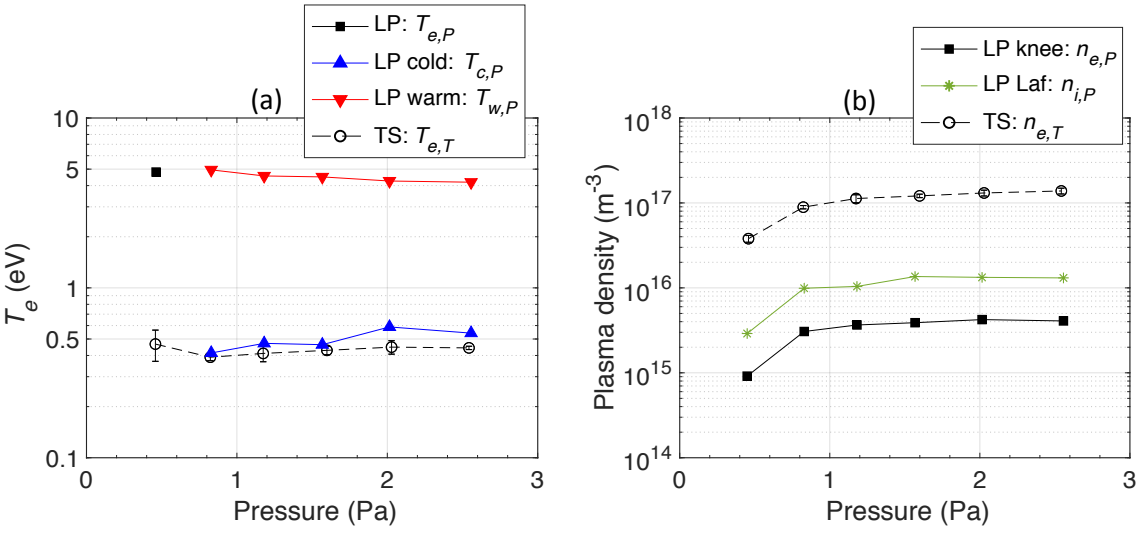


Figure 6.3: Pressure dependence of (a) electron temperature and (b) plasma density measured by Langmuir probe and laser Thomson scattering during DC magnetron operation. The data analysis methods are indicated in the legend. The discharge power was 25 W and the measurements were performed at the magnetic null point ($r = 0$ mm, $z = 61$ mm, $P1$).

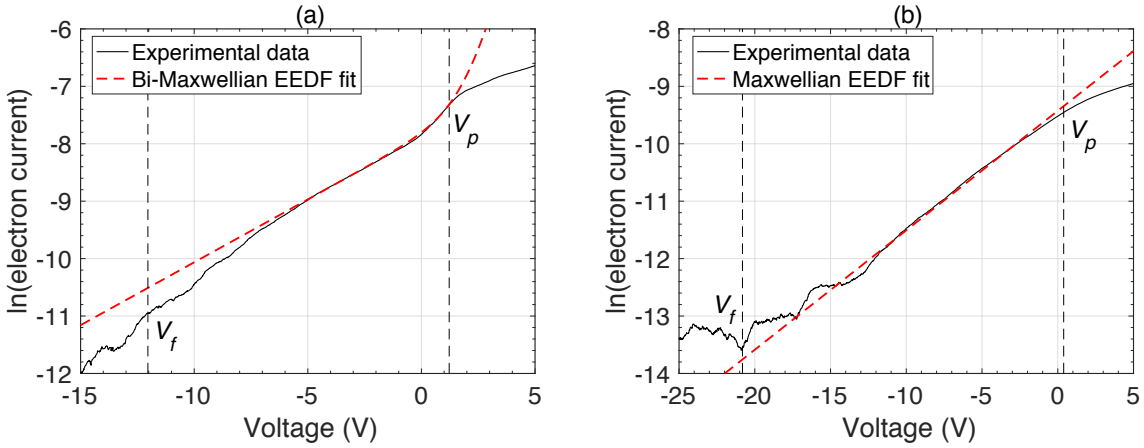


Figure 6.4: (a) Natural logarithm of electron current against voltage at the magnetic null point ($r = 0$ mm, $z = 61$ mm, $P1$) for discharge conditions of 100 W DC and 1.6 Pa of argon gas. The data is consistent with a bi-Maxwellian EEDF. The electron temperature and electron density of the two populations were $T_{c,P} = 0.7 \pm 0.1$ eV and $n_{c,P} = (5.2 \pm 0.5) \times 10^{15}$ m$^{-3}$ for the cold group, and $T_{w,P} = 4.6 \pm 0.2$ eV and $n_{w,P} = (6.0 \pm 0.4) \times 10^{15}$ m$^{-3}$ for the warm group. (b) A probe measurement from the magnetic null point ($r = 0$ mm, $z = 61$ mm, $P1$) for discharge conditions of 25 W DC and 0.47 Pa of argon gas. The data is consistent with a Maxwellian EEDF. The electron properties were $T_{e,P} = 4.8 \pm 0.3$ eV and $n_{e,P} = (9.1 \pm 0.1) \times 10^{14}$ m$^{-3}$.

measurements using a 'straight' probe with dimensions of $r_p = 25$ $\mu$m, $l_p = 10$ mm. The cause of this discrepancy is discussed in section 6.4.1.

The corresponding plasma density results are shown in figures 6.2(b) and 6.3(b). Plotted are the electron density determined from laser Thomson scattering using a Gaussian fit ($n_{e,T}$), and the electron ($n_{e,P}$) and ion ($n_{i,P}$) densities from the Langmuir probe. The results from the two diagnostics have significant quantitative differences: $n_{e,T}$ was systematically above $n_{e,P}$ by an order of magnitude, and $n_{i,P}$ exceeded $n_{e,P}$ by a factor of $\sim 3$. The relative density of the cold and warm electron populations measured by the probe were $\sim 50\%$ (not shown).

### 6.3.2 Weak $B$-field

The measurements reported in section 6.3.2 were made in the magnetic trap region of the discharge, where electron magnetisation is important. The discharge conditions were 100 W and 1.6 Pa of argon gas. Figure 6.5(a) shows the electron temperature results from the

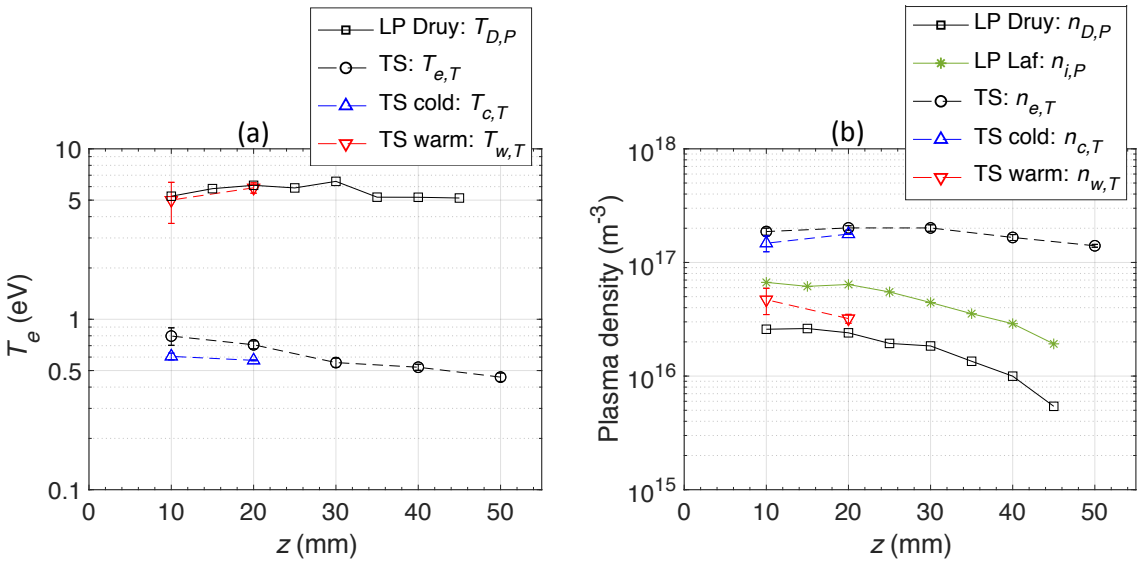


Figure 6.5: (a) Electron temperature and (b) plasma density as a function of axial distance from the target measured by Langmuir probe and laser Thomson scattering during DC magnetron operation. The data analysis methods are indicated in the legend. The discharge power was 100 W, the argon gas pressure was 1.6 Pa and the measurements were performed at ($r = 41$ mm, $z = 10 - 50$ mm, $P2$). The magnetic field strength varied from $B = 5$ mT ($z = 50$ mm) to 33 mT ($z = 10$ mm).

diagnostics as a function of distance from the target surface ($z$) in the $P2$ configuration. The Thomson scattering spectra between $z = 30 - 50$ mm were consistent with Maxwellian EVDFs, characterised by an electron temperature of $T_{e,T} < 1$ eV, but closer to the target there was evidence of an additional warm population of electrons. The criteria for accepting a double-Gaussian fit, detailed in section 4.3.3, were satisfied for some of the measurements at $z = 10$ mm and 20 mm, returning a warm electron temperature of $T_{w,T} \sim 5.5$ eV. Figure 6.6 shows a Thomson scattering spectrum from $z = 10$ mm that is consistent with a bi-Maxwellian EVDF. For comparison, figure 6.7 shows a spectrum from $z = 50$ mm that is consistent with a Maxwellian EVDF. The probe determined EEDFs were non-Maxwellian, and so the Druyvesteyn method was used to calculate an effective electron temperature ($T_{D,P}$), and this had good agreement with $T_{w,T}$.

The corresponding plasma density results are shown in figure 6.5(b). Plotted are $n_{e,T}$; the cold ($n_{c,T}$) and warm ($n_{w,T}$) electron densities determined from laser Thomson scattering using a double-Gaussian fit; the electron density determined from the Druyvesteyn

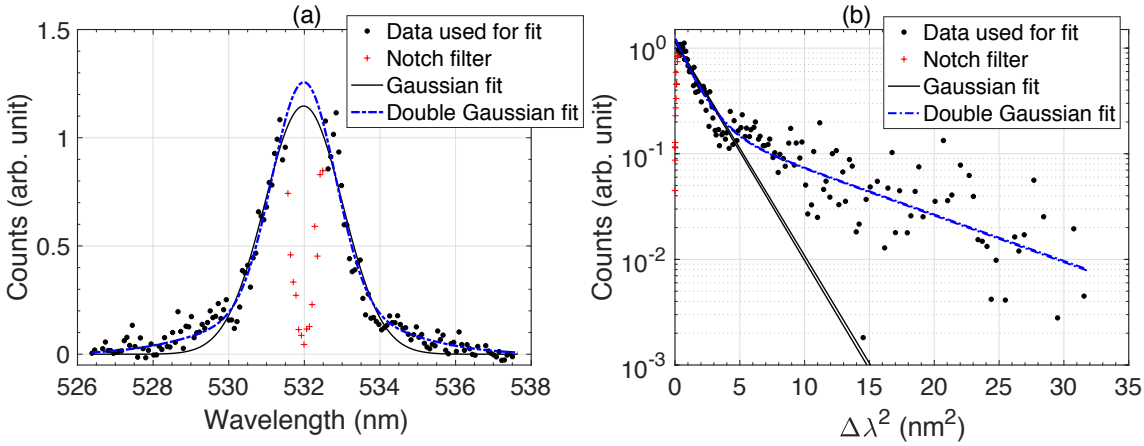


Figure 6.6: Comparison of a Gaussian and double-Gaussian fit (assumes a Maxwellian or bi-Maxwellian EVDF, respectively) to Thomson scattering data in the magnetic trap ($r = 41$ mm, $z = 10$ mm, $P2$) for discharge conditions of 100 W DC and 1.6 Pa of argon gas. A Maxwellian EVDF appears linear on the axes in (b) when the drift velocity of the distribution is zero; where $\Delta\lambda = \lambda - \lambda_i$ ($\lambda$ is the wavelength axis and $\lambda_i = 532$ nm is the laser wavelength). The electron temperature and electron density of the two populations were $T_{c,T} = 0.61 \pm 0.03$ eV and $n_{c,T} = (1.5 \pm 0.2) \times 10^{17}$ m$^{-3}$ for the cold group, and $T_{w,T} = 5.0 \pm 1.4$ eV and $n_{w,T} = (4.7 \pm 1.2) \times 10^{16}$ m$^{-3}$ for the warm group.

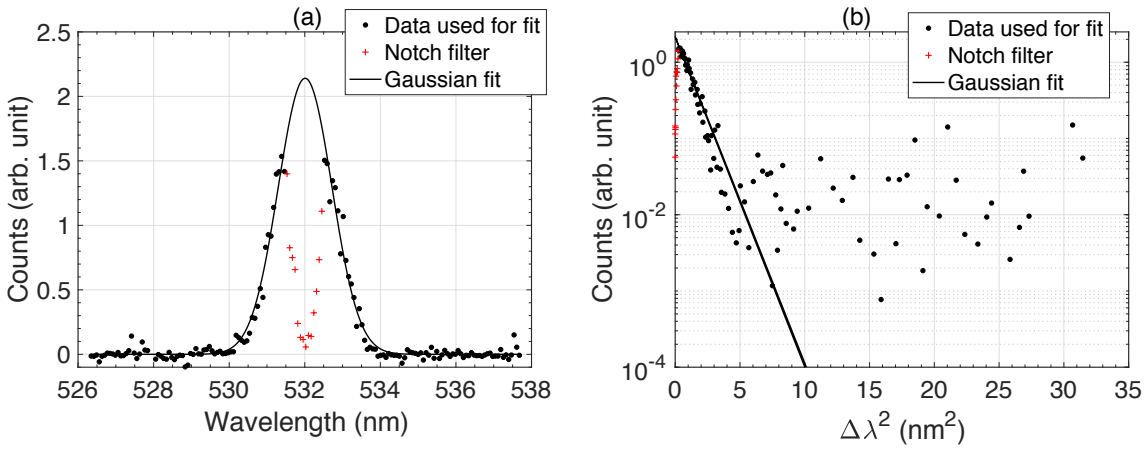


Figure 6.7: Same conditions as figure 6.6 but at ($r = 41$ mm, $z = 50$ mm, $P2$). The electron temperature and electron density were $T_{e,T} = 0.45 \pm 0.03$ eV and $n_{e,T} = (1.40 \pm 0.04) \times 10^{17}$ m$^{-3}$, respectively.

method ($n_{D,P}$); and $n_{i,P}$. The probe determined densities were significantly below $n_{e,T}$ and $n_{c,T}$, but they were comparable to $n_{w,T}$.

It should be noted that the method employed in section 5.3.2 for calculating an effective electron temperature from the floating potential region of the probe characteristic was not appropriate for the DC magnetron because this method is only valid when the plasma has a Maxwellian EEDF: some of the Thomson scattering spectra were consistent with a bi-Maxwellian EVDF when $z \leqslant 20$ mm. Nevertheless, implementation of the method (not shown) reduced the electron temperature by a factor of $\sim 2.2$ and increased the electron density by a factor $\sim 1.8$ compared to the Druyvesteyn method. This lower electron temperature is an intermediate value between the cold and warm populations determined by laser Thomson scattering, and the higher electron density remains significantly below the results of laser Thomson scattering.

As aforementioned in section 6.2.2, the laser Thomson scattering system in the $P2$ configuration was sensitive to the component of the EVDF that was perpendicular to the magnetic field in the target suface plane. Measurements were also performed in the $P3$ configuration ($z = 10 - 50$ mm) in order to measure the component of the EVDF that was parallel to the magnetic field. Similar $n_e$ and $T_e$ were obtained in the $P2$ and $P3$ configurations for discharge conditions of 100 W DC and 1.6 Pa of argon gas, although there was a systematic difference in the drift velocities (not shown). However, the drift velocity was at least an order of magnitude lower than the root mean square speed associated with the thermal motion of the electrons. One can conclude that anisotropy in the target-surface plane was small in these experiments.

### 6.3.3 Diagnostic checks

The results presented in sections 6.3.1-2 show that the plasma density determined by the probe is significantly lower than the laser Thomson scattering measurements of electron density during DC magnetron operation. Section 6.3.3 describes the background reliability checks that were performed to ensure that the data was obtained and analysed correctly.

#### 6.3.3.1 Laser Thomson scattering

To confirm the reliability of the laser Thomson scattering diagnostic checks of laser perturbation, anomalous Mie scattering and the Rayleigh scattering calibration procedure were carried out. Firstly, the laser power was varied from 1.1 W to 2.4 W during sep-

arate Thomson scattering measurements, but the same electron plasma properties were obtained. This gives confidence that photoionisation and plasma heating by the laser is negligible. Secondly, Thomson scattering measurements without the spectrometer notch filter in place were performed to check for Mie scattering from the sputtered tungsten at the laser wavelength. The signal at the laser wavelength decreased by 15% when the plasma was on, compared to when there was just gas in the chamber. These measurements were performed at ($r$ = 41 mm, $z$ = 30 mm, $P2$) with discharge conditions of 50 W and 1.6 Pa of argon gas. This rules out the possibility of misidentifying the Thomson scattering signal from an excessively large Mie scattering signal, and instead indicates gas rarefaction [109]. Finally, the Rayleigh scattering calibration procedure for absolute density measurements was extensively checked and verified by performing the calibration with nitrogen gas, varying the gas pressure range (and data accumulation time), varying the laser power at constant gas pressure, and using a second pressure gauge.

These checks confirmed that the laser Thomson scattering results were reproducible, reliable and accurate.

#### 6.3.3.2 Langmuir probe

The main checks for the Langmuir probe included investigating the influence of electron magnetisation on the collected electron current; the plasma perturbation induced by the presence of the probe stem and biasing the probe tip; and the effect of the floating alumina tube adjacent to the probe tip. These are described below.

A possibility is that the magnetic field was significantly reducing the electron current collected by the probe, even far from the target, which resulted in electron density underestimation. When electron magnetisation is significant, the electron density determined by a probe is strongly dependent on the probe tip radius and its alignment with respect to the magnetic field [47]. Therefore, the measurements reported in section 6.3.2 were repeated using two 'straight' probe tips with their axes aligned approximately parallel to the local magnetic field. Their dimensions were $r_p$ = 50 $\mu$m, $l_p$ = 5 mm and $r_p$ = 125 $\mu$m, $l_p$ = 5.75 mm, respectively. Figure 6.8 shows the electron density calculated using the Druyvesteyn method as a function of distance from the target for these probes and the 'L' probe from section 6.3.2. There was excellent agreement between the three probes at $z$ = 45 mm, where the magnetic field strength is $B$ = 6 mT, but the density profiles diverge as the target is approached. One can conclude from figure 6.8 that the electron density

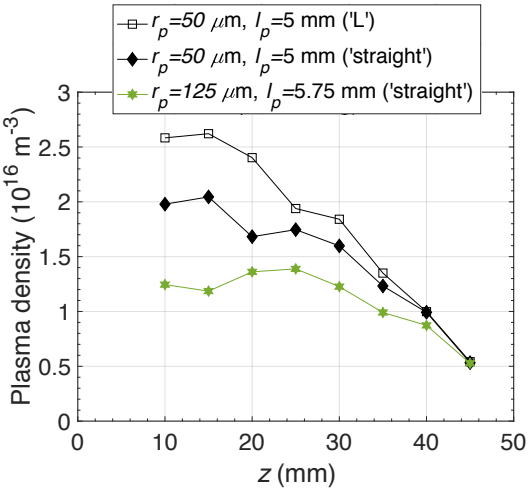


Figure 6.8: Comparison of different probe sizes and orientations for electron density measurements as a function of axial distance from the target in the magnetic trap ($r = 41$ mm, $z = 10 - 45$ mm, $P2$). Electron density was calculated using the Druyvesteyn method. The DC discharge power and argon gas pressure were 100 W and 1.6 Pa, respectively. The magnetic field strength varied from $B = 6$ mT ($z = 45$ mm) to 33 mT ($z = 10$ mm).

underestimation by the probe at the magnetic null, where $B \lesssim 1$ mT, is not caused by an electron magnetisation effect that is dependent on the probe tip radius nor its orientation.

The global plasma perturbation induced by a Langmuir probe was examined by performing laser Thomson scattering measurements with a probe inserted close to the detection volume. An 'L' shaped probe ($r_p = 50$ $\mu$m, $l_p = 6.5$ mm) was radially inserted into the vacuum chamber with its length parallel to the target surface-normal so that its radial presheath was directed towards the detection volume. The closest approach of the probe wire to the detection volume without stray laser light adversely affecting the laser Thomson scattering system was $\sim 13$ mm; the detection volume was positioned outside of the probe sheath. The power scan measurements in section 6.3.1 were repeated using the laser Thomson scattering diagnostic with various probe biases applied (-100 V, $V_f$, $V_p$+ 5 V), but the results were the same as when the probe was not inside the chamber. One can conclude that there was not a significant global perturbation to the discharge caused by the probe stem nor the probe tip bias, but there is the possibility of a significant localised perturbation at a location outside of the detection volume. One can speculate that such a perturbation would be mainly caused by the probe stem because the plasma density was significantly underestimated, relative to the laser Thomson scattering results, using

both electron and ion collection theories (i.e. independent of the probe tip bias), and the electron density underestimation was independent of the probe tip dimensions in regions of low magnetic field strength, as shown by figure 6.8.

Another possibility is that the floating alumina tube adjacent to the probe tip is reducing the collected current by a shadowing effect and/or a sheath interaction effect. To check for this, the measurements in section 6.3.1 were repeated using a longer probe tip whilst maintaining an approximately constant probe surface area. The electron plasma properties measured using a $r_p = 25$ $\mu$m, $l_p = 10$ mm 'straight' probe were in agreement with a $r_p = 50$ $\mu$m, $l_p = 5.5$ mm 'straight' probe to within 20%. Therefore, one can conclude that the alumina tube adjacent to the probe tip did not significantly influence current collection.

Other checks were to vary the time period of the voltage ramp applied to the probe (10-325 ms); repeat the measurements in section 6.3.1 using a 'L' rather than a 'straight' probe; and calculate the ion density using orbital-motion-limited theory (see section 3.1.4.1), which uses the ion current gradient, rather than the parameterisation of Laframboise theory. One can rule out these considerations as being responsible for the diagnostic discrepancy.

## 6.4 Discussion

The results show that the diagnostics gave large quantitative differences for plasma density measurements and the EEDF agreement was poor, even when the magnetic field strength was negligible at the measurement position. The results in chapter 5, however, indicate that the probe provides a reasonable estimate of plasma density and electron temperature during the higher-density HiPIMS mode. The EEDF and plasma density comparisons are discussed separately in further detail below.

### 6.4.1 EEDF comparison

It should be emphasised that the diagnostics measure different components of the EVDF or equivalently EEDF. The laser Thomson scattering diagnostic provides a one-dimensional EVDF, with the direction of sensitivity determined by the scattering geometry; whereas, the electron current collected by the probe, in theory, depends only on the EEDF components in the axis-normal plane of the tungsten wire. The laser Thomson scattering results

in section 6.3.2 show that there was no significant anisotropy of the EEDF caused by the magnetic field in the target-surface plane; therefore, one does not expect anisotropy at the magnetic null where the magnetic field strength is weaker. Henceforth, it is assumed that the plasma is isotropic and this allows a direct comparison of the EEDF measurements once converted into the same spatial dimension; the EEDF measurements presented are three-dimensional.

Before discussing the EEDF measurements it is worth pointing out the limitations of each diagnostic. The maximum electron energy sampled by the laser Thomson scattering system is 14 eV based on the wavelength range measured; however, the signal-to-noise ratio degrades as energy increases. This is a consequence of the electron population density, and hence the laser Thomson scattering signal, decreasing as energy increases. In contrast, a Langmuir probe can measure energies up to $\gtrsim e(V_p - V_f)$, but the diagnostic has the following limitations: plasma potential uncertainty gives the electron energy axis an erroneous offset and this is most significant for the low energy part of the EEDF; the accuracy of the ion subtraction procedure for calculating the electron current ($I_e$) is critical for measuring the distribution tail; and the Druyvesteyn method for non-Maxwellian EEDFs requires the second derivative of the $I_eV$ characteristic and this necessities smoothing of the experimental data. This can lead to an apparent depletion of the low energy region [158].

The influence of the magnetic field on probe measurements at the magnetic null is expected to be small, and therefore, good diagnostic agreement was expected in section 6.3.1. However, the probe determined EEDFs were generally consistent with bi-Maxwellian distributions, whereas the Thomson scattering spectra were consistent with Maxwellian EEDFs. Figure 6.9(a) shows a comparison of EEDF measurements at the magnetic null ($r = 0$, $z = 61$ mm, $P1$) for a DC discharge power of 100 W and an argon pressure of 1.6 Pa. The following are plotted: EEDF obtained from fitting equation 3.9 to the probe $IV$ characteristic; EEDF calculated using the probe Druyvesteyn method; EEDF obtained from the Thomson scattering Gaussian fit; and the laser Thomson scattering detection limit for a bi-Maxwellian EEDF, which has a warm electron temperature equal to the value measured by the probe, and a cold electron population with properties determined from the single Gaussian fit. The low energy part ($< 3.5$ eV) of the probe determined EEDF was significantly depleted compared to the laser Thomson scattering measurement. This is reflected in the different densities determined for each diagnostic. Nevertheless, the shapes of the analytical fits in this region are similar because the electron temperature

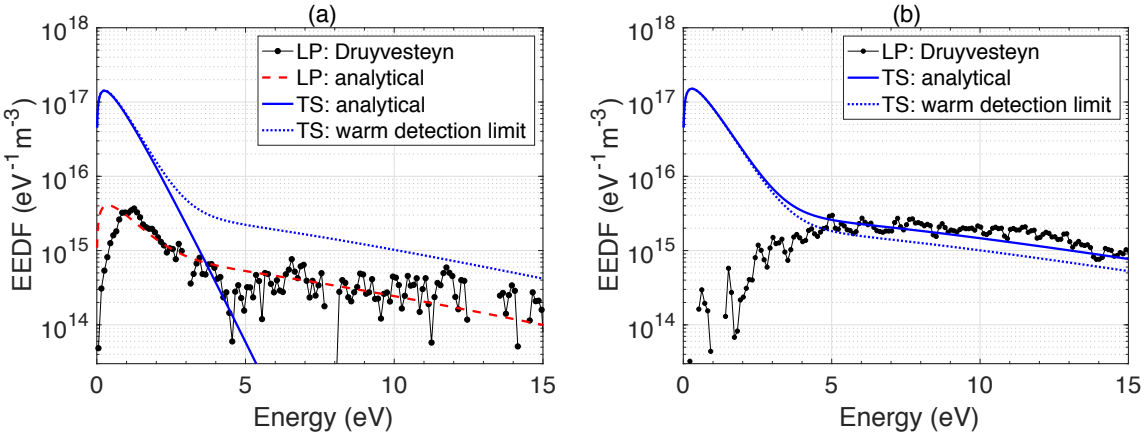


Figure 6.9: Electron energy distribution function measurements made by Langmuir probe and laser Thomson scattering during DC magnetron operation at (a) the magnetic null point ($r = 41$ mm, $z = 61$ mm, $P1$) and (b) the magnetic trap ($r = 41$ mm, $z = 20$ mm, $P2$). The data analysis methods are indicated in the legend. The discharge power and argon gas pressure were 100 W and 1.6 Pa, respectively.

measurement of the cold population made by the Langmuir probe had good agreement (within a factor of 1.3) with the laser Thomson scattering result. The presence of the warm electron population detected by the probe, however, cannot be verified because its density is below the laser Thomson scattering double-Gaussian detection limit; this is the case for all of the DC magnetron measurements at the magnetic null. It should be noted that the detection limit is partly determined by the number of laser pulses during the iCCD camera integration time. The limits calculated for this chapter were based on an integration time which gives an electron density overestimation of $\lesssim 10\%$, due to performing the Rayleigh scattering procedure after the Thomson scattering measurement.

Low energy depletion of the EEDF determined by a Langmuir probe has been reported in a previous probe and laser Thomson scattering comparison study using an inductively coupled plasma (ICP) by Bowden *et al.* [35, section 2.1.2.2]. They found the effect to be more extreme at lower pressure. This is consistent with the observation reported in section 6.3.1, where only the laser Thomson scattering diagnostic detected a cold population of electrons at the lowest argon backing pressure (discharge conditions of 25 W DC and 0.47 Pa). Bowden *et al.* [35] concluded that either the probe measured perturbed plasma due to the presence of the probe or the Druyvesteyn method was not appropriate for measuring the low energy part of the EEDF. One can speculate that the first conclusion is correct

because the apparent depletion mechanism is more severe in the DC magnetron discharge, and this is consistent with the accepted idea that probe measurements in a magnetised plasma are more perturbing compared to an unmagnetised environment [49]. The probe induced perturbation is a result of the floating probe stem being in the plasma and/or the probe tip drawing a net current. As discussed in section 6.3.3.2, one cannot rule out the possibility of a significant plasma perturbation in the vicinity of the probe tip in the DC magnetron caused by the probe stem. Moreover, Bowden *et al.* [35] observed that the total Thomson scattering intensity, hence the electron density, decreased when a probe stem was inserted into the ICP, but the shape of the laser Thomson scattering determined EVDF did not change. Similarly, the presence of a probe in an electron cyclotron resonance discharge [61, section 2.1.3.5] resulted in a reduction of the total Thomson scattering intensity; in addition, the electron temperature of the laser Thomson scattering determined EVDF increased.

The results in sections 6.3.1 and 6.3.2 show that the probe consistently measures an electron temperature or effective temperature with $T_e > 4$ eV. The corresponding electron densities are below the detection limit of the laser Thomson scattering diagnostic except at $z = 10$ mm and 20 mm in the magnetic trap ($r = 41$ mm, $P2$). Figure 6.9(b) compares the EEDFs from the diagnostics at $z = 20$ mm. Plotted are the EEDF calculated using the probe Druyvesteyn method; EEDF obtained from the laser Thomson scattering double-Gaussian fit; and the detection limit of the warm component measured by laser Thomson scattering as part of a double-Gaussian fit. There was good agreement between the diagnostics above 5 eV, but again, the low energy part of the probe EEDF was depleted. The depletion was more severe compared to the measurements at the magnetic null, but this is expected because the magnetic field is stronger ($B = 21$ mT compared to $B \lesssim 1$ mT). The magnetic field impedes electron collection, so this effect is strongest for low energy electrons which have small gyroradii. Note that the speculated probe stem depletion mechanism may still be present in the magnetic trap.

Measurements during HiPIMS at the magnetic null position were reported in chapter 5. The electron plasma property measurements, hence the EEDFs, from the diagnostics were generally consistent with one another. Therefore, significant depletion of low energy electrons, at a measurement position with a negligible magnetic field strength, is not observed by the probe in HiPIMS unlike in the lower-density DC magnetron mode. This is discussed in section 6.4.2 because significant depletion of low energy electrons results in total electron density underestimation.

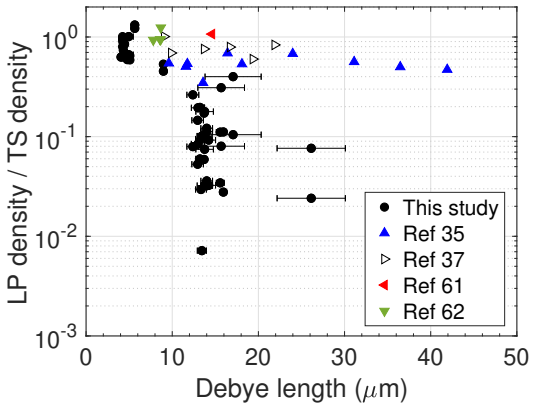


Figure 6.10: Plasma density measured by Langmuir probe normalised by electron density determined from laser Thomson scattering as a function of Debye length (determined from laser Thomson scattering). Plotted are all data from sections 5.3.1, 6.3.1, 6.3.2, and data from the literature [35, 37, 61, 62].

### 6.4.2 Density comparison

In unmagnetised plasma it is common for probe measurements of ion density to exceed the electron density by up to an order of magnitude (e.g. Sudit and Woods [32] and therein) because of both ion-neutral collisional effects [21, 22, 58] and electron depletion as a result of drawing the relatively large electron saturation current from the plasma [18, p. 183][19, p. 91][20]. However, it is surprising that the ion density measured by the probe was significantly lower than the laser Thomson scattering measurement of electron density during DC magnetron operation because the effect of ion magnetisation was expected to be small. Furthermore, as discussed in section 6.2.3.2, the collisionless probe theories implemented are, to the first order, more valid for the DC magnetron mode. In addition, the agreement between the diagnostics for electron density measurements improved as the magnetic field strength increased in the magnetic trap, opposite to what is expected. These anomalous observations suggest that the probe perturbation is significant and dependent on the plasma conditions local to the measurement position.

One would expect the probe perturbation to be reduced in plasmas with small $\lambda_D$ because the spatial extent of the sheath surrounding the floating stem and biased wire is smaller. Figure 6.10 shows that, in this study, the diagnostic density agreement improved as $\lambda_D$ decreased. Plotted are all data from sections 5.3.1 (HiPIMS measurements

at the magnetic null), 6.3.1 and 6.3.2; the graph axes are electron and ion density from the Langmuir probe normalised by the electron density determined from laser Thomson scattering, against the Debye length determined from laser Thomson scattering. In addition, data from several other comparison studies using different types of magnetised [61, 62] and unmagnetised [35, 37] discharges are included in the plot; the plasma density range from these references is $n_e = (1.7 - 34) \times 10^{17}$ m$^{-3}$. The figure shows that it is common for the Langmuir probe to underestimate the plasma density by a factor of $\lesssim 2$, but the underestimation can be over an order of magnitude for the magnetron when $\lambda_D > 10$ $\mu$m, which corresponds to the DC mode. It is clear that the current collected by a probe is strongly influenced by the discharge physics.

The plasma replenishment rate is another important factor for determining the scale of the plasma perturbation induced by a probe. Both the floating probe stem and biased tungsten wire deplete the plasma of charge, which has to be resupplied by ionisation and then transported to the depleted region. The discharge physics of HiPIMS and DC magnetron operation is significantly different and this will affect the replenishment rate. Examples include: electrons gain more energy from sheath acceleration during the on-time of HiPIMS, and so each secondary electron can potentially cause more ionising collisions; HiPIMS discharges have faster electron cross-magnetic field transport than DC discharges [15], and therefore, electrons can more readily escape the main ionisation zone of the discharge; the dense HiPIMS plasma has a high degree of target-metal ionisation; HiPIMS has a greater gas rarefaction effect in front of the target; Coulomb collisions are more important during HiPIMS due to the higher plasma density; and the HiPIMS waveforms in chapter 5 did not reach steady-state.

## 6.5 Conclusion

The aim of the research in this chapter was to assess the reliability of a Langmuir probe for electron plasma property measurements (plasma density, electron temperature and electron energy distribution function (EEDF)) in weakly magnetised plasma, by comparing the results obtained from the probe with laser Thomson scattering measurements. Laser Thomson scattering was chosen as the benchmark diagnostic because it provides absolute electron density measurements, it is insensitive to magnetic field effects, and it is a non-intrusive technique. A magnetron was used as the plasma source due to its ability to operate in different discharge regimes (by changing the power supply) which cover a wide

plasma density range. Details of a comparison study with the magnetron operated in a high-power pulsed-DC mode (HiPIMS) were given in chapter 5. The results presented in this chapter were for the lower-density DC magnetron mode. The novelty of this research is the use of a reliable non-intrusive technique as the benchmark diagnostic. In addition, the accuracy of electron temperature or EEDF measurements made by a Langmuir probe in weakly magnetised plasma had not been, previously, systematically investigated.

Measurements were performed at different locations within the magnetic field configuration of the magnetron: at the magnetic null position where magnetic field effects on the probe measurements should be negligible, and in the magnetic trap region with field strengths of up to $B = 33$ mT. The DC magnetron generated plasma densities of $n_e = (4 - 20) \times 10^{16}$ m$^{-3}$ and the bulk electron temperature was $T_e < 1$ eV. Close to the target, the laser Thomson scattering diagnostic resolved a warm electron population with a temperature of $T_e \sim 5.5$ eV.

The diagnostics are expected to generate similar results in conditions for which unmagnetised probe theory is valid, regardless of the operating regime of the magnetron. However, there was good agreement (within a factor of $\sim 1.5$) for electron density measurements at the magnetic null only for the higher-density HiPIMS mode ($n_e > 10^{18}$ m$^{-3}$). The electron densities determined by laser Thomson scattering during the DC mode were an order of magnitude greater than the plasma density determined from the Langmuir probe, using both electron and ion collection theories, for certain discharge conditions.

The comparison of EEDFs was generally limited to the bulk electrons because laser Thomson scattering is less sensitive to the tail of the distribution. When the conditions for unmagnetised probe theory were satisfied, the probe gave a reliable indication of the bulk electron temperature (within a factor of $\sim 1.5$) during both operating regimes. However, for the DC mode, the population density of the low energy part of the probe EEDF was depleted. This effect was more pronounced for measurements at locations with higher magnetic field strengths.

The reason for the discrepancy in plasma density measurements was investigated by carefully checking for perturbing effects from both diagnostics. The reliability of the laser Thomson scattering system was checked by considering laser intensity effects; investigating enhanced scattering due to other species; and the Rayleigh scattering calibration procedure was verified. The diagnostic was confirmed to be reliable. The reliability of the probe diagnostic was checked by repeating measurements with different probe tip dimensions and orientations in order to assess the plasma perturbation caused by the probe tip and the

shadowing effect of the ceramic stem. These effects were not responsible for the diagnostic discrepancy. Any global effects were checked by the simultaneous measurement of the two diagnostics, but the probe did not show any clear perturbation. However, the distance between the probe and detection volume was limited by stray laser light levels, and so the detection volume may have been positioned outside of the perturbed region.

The conclusion from this study is that the presence of the probe stem in the discharge environment, intruding across the magnetic field lines from the probe port to the measurement position, affects the development of the DC magnetron plasma. This effect is not seen in the HiPIMS case for an unknown reason that may be linked to its shorter Debye length-scale and the discharge physics in this highly transient pulsed regime. While the link between probe presence and perturbation in the DC mode is not clear, elimination of other possible perturbative effects means that this is the only possible conclusion.

The results of this research demonstrate the usefulness of applying the, complicated but unambiguous, laser Thomson scattering technique to discharge plasmas. It is desirable to know the reasons for the reported discrepancies because Langmuir probes are the most commonly used diagnostic in low temperature plasmas for electron plasma property measurements, and therefore understanding their limitations is of paramount importance. It may be the case that the significant discrepancies are due to the specific nature of the magnetron discharge. It has a highly non-uniform magnetic field that changes in direction and intensity across small distances, and this might exacerbate the perturbing effect of any solid object inserted into the environment. Further investigations could include a similar study using a discharge with a more uniform field structure, and in which the density can be varied over a wide range without changing the plasma generation technique.

# Chapter 7

# Investigation of electron dynamics in HiPIMS discharges using laser Thomson scattering and optical emission spectroscopy

## 7.1 Introduction

The research in this chapter focuses on electron dynamics in HiPIMS discharges, which are a type of plasma source used for ionised physical vapour deposition (IPVD) [80]. These sources are characterised by a high ionisation fraction of sputtered (metal) atoms. This results in a significant fraction of metal ions in the deposition flux, which leads to improved film properties. Other important parameters affecting the film growth include the energy distribution function of each of the incident species on the substrate and their associated particle flux [159].

An overview of the discharge physics in HiPIMS is given in section 2.3.3.2. The plasma conditions at the substrate position, and hence the film properties, are ultimately dependent on the complex interaction between several dynamic processes, namely: self-sputtering, gas rarefaction, gas recycling, and large-scale self-organisation into spokes. One approach to understand the discharge physics is through the use of numerical models and simulations. Global zero-dimensional models, most notably the ionisation region

model [138], have been applied to study a range of temporal phenomena in HiPIMS discharges [108]. However, a dimensional treatment is necessary for several reasons: modelling the spatial inhomogeneity of the plasma, for accurately determining the electric potential profile of the discharge, and for investigating the physics of spokes. On the other hand, self-consistent two-dimensional particle in cell simulations are still under development [140, 141]. They have, so far, been limited to a total simulation time of $\leqslant 9$ $\mu$s and they do not consider the sputtering process.

Experimental investigations are essential for validating models and for developing a deeper understanding of the discharge physics outright. A variety of plasma diagnostics have been applied to HiPIMS discharges, including: mass spectrometry [112, 116], optical emission spectroscopy [99, 111, 125], THz time domain spectroscopy [136], laser techniques (e.g. laser-induced fluorescence [160], laser absorption spectroscopy [139] and laser Thomson scattering [2, 137]) and time-resolved Langmuir probe measurements [39, 98, 122–125, 127–129, 131, 132, 134]. A number of these diagnostics can provide measurements of electron temperature and electron density. Accurate spatio-temporal resolved measurements of electron plasma properties are imperative because they provide information about the fundamental processes of the HiPIMS discharge for IPVD: the ionisation rate of metal atoms, which is highest in the magnetic trap region; and the transport of metal ions from the target to the substrate [161].

As discussed in sections 2.3.3.3 and 5.1, experimental measurements of the electron plasma properties in the magnetic trap region poses a difficult challenge. Extensive Langmuir probe measurements have been performed to characterise the electron plasma properties in the region close to the substrate [39, 122–125, 127–129, 131], but there have been few reports of measurements in the magnetic trap [98, 132, 134]. This is mainly due to distortion of the probe current-voltage characteristic by the magnetic field and concerns over plasma perturbation. The first reliable measurements of the temporal evolution of the plasma density in the magnetic trap region for a variety of discharge powers and pressures was reported using THz time domain spectroscopy in 2018 [136]. A plasma density in the range of $n_e = 10^{18} - 10^{19}$ m$^{-3}$ was measured for discharge current densities of $1 - 4$ A·cm$^{-2}$. These measurements, however, were line-of-sight averaged over the entire diameter of the target, and the beam diameter was comparable to the height of the magnetic null point from the target surface. Following this, the incoherent laser Thomson scattering technique was applied to HiPIMS discharges in 2019 by Tsikata *et al.* [137] and Ryan *et al.* [2, chapter 5]. Localised measurements of both electron temperature and electron density in

the magnetic trap were acquired for the first time.

In each of the previous studies, reliable electron plasma property measurements were reported only for a limited spatial region of the discharge. The aim of the research presented in this chapter was to provide a comprehensive overview of the electron dynamics. The approach was to use laser Thomson scattering for measurements of electron temperature and electron density, and optical emission spectroscopy (OES) provided information about excited atomic and ionic states. The combination of these two diagnostics gives an insight into the electron-heavy species interactions occurring in the plasma. Measurements were performed at various spatial locations, including inside and outside of the problematic magnetic trap region, for a variety of non-reactive HiPIMS discharge conditions.

An important point to highlight is that the results of chapter 5 indicate that Langmuir probe measurements, when carefully interpreted and assuming a Maxwellian electron velocity distribution function (EVDF), can provide reasonable estimates of electron temperature and electron density in the magnetic trap region. Laser Thomson scattering, however, was chosen to measure the electron plasma properties for the research presented in chapter 7 because its data interpretation does not enforce the assumption of a Maxwellian EVDF and its measurement accuracy is independent of magnetic field strength.

Another aim of the investigation was to use the laser Thomson scattering system to measure the ratio between the azimuthal and discharge current densities ($J_\phi/J_D$) in the magnetic trap because this provides an indication of the cross-magnetic field transport rate of electrons. Previous studies using intrusive electric and magnetic probes have concluded that this ratio is anomalously low for both HiPIMS ($1.5 < J_\phi/J_D < 12$) [120, 162–164] and DC magnetron operation ($8 < J_\phi/J_D < 30$) [41, 42], which suggests that electrons are crossing the magnetic field lines faster than the prediction of classical theory based on collisions.

This chapter is organised as follows: section 7.2 contains a description of the discharge conditions, the laser Thomson scattering system, and the OES diagnostic. The results of the electron plasma property measurements are presented in section 7.3. This includes investigating the effects of background gas pressure, target voltage pulse-width and spatial location. The results from the $J_\phi/J_D$ measurements are detailed in section 7.4. The conclusion is given in section 7.5.

## 7.2 Experimental setup

The experimental setup and procedure, including data acquisition and analysis, for laser Thomson scattering measurements in HiPIMS discharges are described in sections 4.1 and 4.3. Furthermore, the theory used to interpret the Thomson scattering spectra is presented in section 3.2. The specific details related to this investigation are described below.

### 7.2.1 Magnetron sputtering system

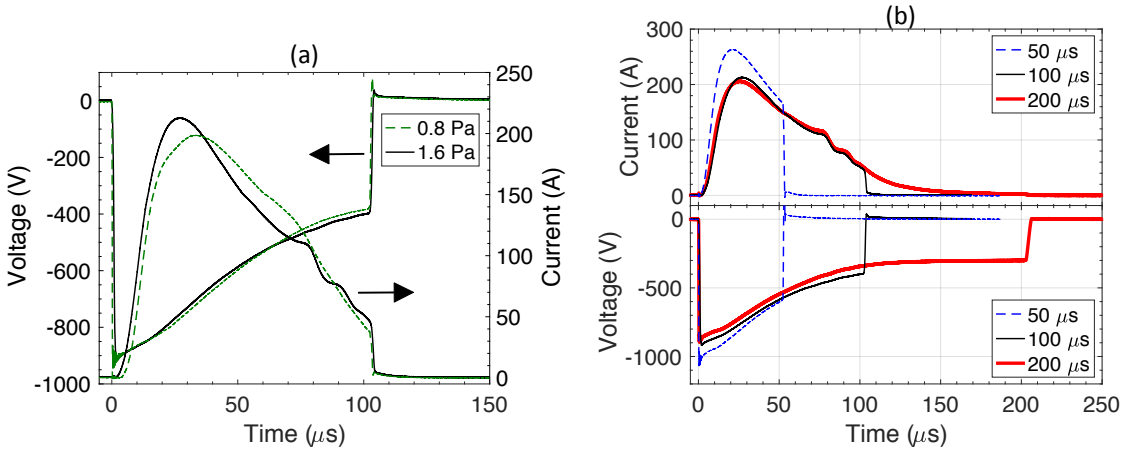


Figure 7.1: Examples of discharge current-voltage-time waveforms. The common operating conditions were an average power of 400 W and a 50 Hz repetition rate. For (a), the pulse-width was 100 $\mu$s with an argon gas pressure of either 0.8 Pa or 1.6 Pa. For (b), the argon gas pressure was 1.6 Pa with a pulse-width of either 50 $\mu$s, 100 $\mu$s or 200 $\mu$s.

For this study, the average power of the discharge and the target pulse repetition rate were fixed at 400 W and 50 Hz, respectively. Figure 7.1(a) shows a comparison of the target voltage and current waveforms at a pulse-width of 100 $\mu$s with an argon gas pressure of either 0.8 Pa or 1.6 Pa; and figure 7.1(b) shows a comparison of pulse-width (50 $\mu$s, 100 $\mu$s or 200 $\mu$s) at a fixed argon pressure of 1.6 Pa. The waveforms corresponding to discharge conditions of 100 $\mu$s pulse-width and 1.6 Pa are plotted in both (a) and (b) to enable a direct comparison. All temporal measurements in this chapter are referenced to the start of the target voltage pulse ($t = 0$ $\mu$s). A noticeable feature of all the discharges is the decay of the target voltage during the pulse-on period, rather than a maintaining a constant value. This will strongly impact the discharge current waveform. It should be pointed out

that this is a limitation of the commercial power supply rather than the discharge physics; nevertheless, the waveforms in figure 7.1 are representative of HiPIMS discharges used for industrial applications [165, p. 27].

### 7.2.2 Laser Thomson scattering system

The laser Thomson scattering diagnostic was operated in the incoherent regime; consequently, the scattering spectrum was proportional to the EVDF in one-dimension. Measurements were performed along the centre axis of the magnetron ($r = 0$ mm, $z = 10 - 70$ mm, $P1$) and in the magnetic trap region ($r = 41$ mm, $z = 10 - 70$ mm, $P2$). In the $P2$ configuration, the EVDF measurement was sensitive to the component that was perpendicular to the magnetic field in the target surface plane, as explained in section 4.3.4. This was important for measuring $J_\phi$ in section 7.4. For the $P1$ measurements, the EVDF component was in an arbitrary direction in the target surface plane. A detailed view of the magnetic field configuration is shown in figure 4.2.

Sputter deposition onto the light collection window during magnetron operation reduces the window transmission. The Rayleigh scattering procedure for determining absolute electron densities was performed after each Thomson scattering measurement. The data accumulation time was adjusted between $10 - 60$ s ($100 - 600$ laser pulses) depending on the discharge conditions so that electron density overestimation, due to performing the Rayleigh scattering measurements with a reduced window transmission, was $< 10\%$. The detection limit of the Thomson scattering system was reached when this data accumulation time produced a Thomson scattering spectrum that was extremely noisy and/or narrow relative to the notch filter region. A longer data accumulation time would improve the signal-to-noise ratio and enable resolution of the EVDF shape; however, the electron density would be significantly overestimated and this approach necessitates frequent changing of the collection window, which is a time consuming process because of having to vent the vacuum chamber.

### 7.2.3 Optical emission spectroscopy

Time-resolved OES measurements were performed to provide information about the species composition of the plasma. This involved measuring the intensity of selected line emission. These measurements utilised the same experimental setup as the laser Thomson scattering system in the $P2$ configuration but with several alterations to improve the spectral and

spatial resolutions. (i) The width of the triple-grating spectrometer (TGS) entrance slit was set to 0.1 mm (rather than 0.3 mm) to improve the spectral resolution of the system, so that there was less overlap between adjacent line emission peaks. The full-width-half-maximum of the instrumental function was $\sim 0.08$ nm. (ii) The wavelength range of the TGS output was adjusted from being centred at 532 nm to the wavelength range of interest for the plasma emission measurements. (iii) The mask inside the TGS for blocking the stray laser light was removed because the laser was not firing during the measurements; moreover, the laser wavelength region was not of interest. (iv) The camera was triggered at 50 Hz, which is the HiPIMS pulse frequency rather than at the laser repetition rate of 10 Hz, with a gate width of 1 $\mu$s. (v) To improve the spatial resolution in the $z$ direction, the collection solid angle of the lens was restricted by a 3 mm diameter aperture placed on the collection window, as demonstrated by figure 7.2.

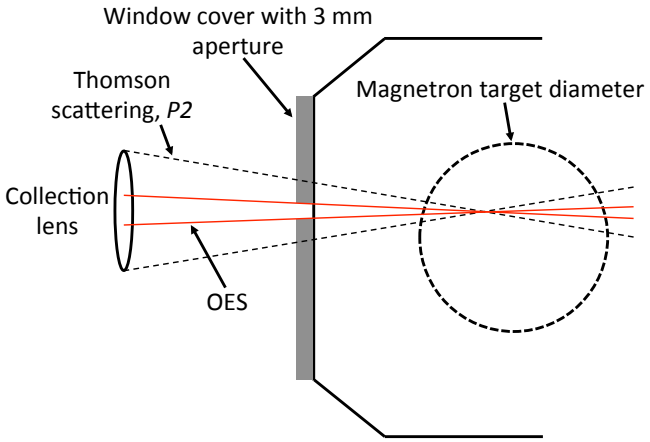


Figure 7.2: Comparison of the collection solid angle for the optical emission spectroscopy and laser Thomson scattering ($P2$ configuration) measurements.

Table 7.1 summarises the line emission investigated from various species: Ar I, Ar II, W I and W II. A large number of emission lines were considered by a series of experiments and also on theoretical grounds. The selected lines were chosen because they have a relatively strong intensity; they have a large Einstein coefficient for spontaneous emission ($A_{ul}$), and therefore, the emission intensity is representative of the instantaneous density of the excited states; and they did not overlap with other significant line emission. Moreover, during the selection process the temporal trends observed for the selected lines were compared with those from other lines of the same species to check for consistency, which gives confidence

| Species | $\lambda$ (nm) | $A_{ul}$ ($10^7$ s$^{-1}$) | $E_l$ (eV) | $E_u$ (eV) | $E_{iz}$ (eV) |
|---|---|---|---|---|---|
| Ar I | 751.47 | 4.5 | 11.83 | 13.48 | 15.76 |
| Ar II | 480.60 | 7.8 | 16.64 | 19.22 | 27.63 |
| W I | 361.75 | 1.1 | 0.37 | 3.79 | 7.86 |
| W II | 361.38 | 1.15 | 1.81 | 5.24 | 16.37 |

Table 7.1: Summary of the line emission investigated for various species in the plasma: $\lambda$ refers to the wavelength of the transition, $A_{ul}$ is the Einstein transition coefficient for spontaneous emission, $E_l$ is the lower energy level, $E_u$ is the upper energy level and $E_{iz}$ is the ionisation energy of the species. This data was taken from the NIST Atomic Spectra Database [148].

that the transitions were correctly identified.

The OES results in this chapter are displayed as relative intensities, where each data point in a temporal profile of line emission intensity is normalised by the maximum intensity measured in that particular temporal scan. The data acquisition time for each time-resolved data point was $10 - 20$ s ($500 - 1000$ HiPIMS pulses). In order to minimise the error caused by the changing window transmission during magnetron sputtering, the measurement procedure was to acquire a complete temporal profile for a particular wavelength, and then the wavelength region of interest was changed, as opposed to varying wavelength with a fixed measurement time. Repeat measurements were performed at the end of each temporal scan to monitor the decrease in the transmission of the collection window; this was limited to $< 15\%$. The line emission intensity was calculated by fitting a Gaussian curve to the peak and then calculating the area under the curve.

The simplistic Corona model [157] was used to interpret the OES data in a qualitative manner. In the model it is assumed that electron excitation in atoms/ions occurs via electron collisions, and emission occurs via spontaneous radiative decay. The line emission intensity ($I$) depends on the electron density; the number density of the atom/ion ground state ($n_0$); and the excitation rate coefficient ($R_{ex}$), which is a function of electron temperature:

$$I \propto n_e n_0 R_{ex}(T_e). \tag{7.1}$$

| Pulse-width ($\mu$s) | Pressure (Pa) | $\tau_{n1}$ ($\mu$s) | $\tau_{n2}$ ($\mu$s) | $\tau_{T1}$ ($\mu$s) | $\tau_{T2}$ ($\mu$s) |
|---|---|---|---|---|---|
| 50 | 1.6 | 15 | 165 | 25 | 270 |
| 100 | 1.6 | 10 | 165 | 20 | 115 |
| 200 | 1.6 | 40 | - | 15 | - |
| 100 | 0.8 | 10 | 45 | 10 | 65 |

Table 7.2: Electron density ($\tau_n$) and electron temperature ($\tau_T$) exponential decay constants during the pulse-off period. The subscripts 1 and 2 refer to the initial and long-term decays, respectively. Measurements were performed at ($r = 41$ mm, $z = 10$ mm, $P2$). The discharge conditions were an average power of 400 W and a 50 Hz repetition rate.

## 7.3 Electron temperature and electron density measurements

This section is split into three parts: section 7.3.1 details the results from measurements at a single spatial location in the magnetic trap using different discharge conditions, section 7.3.2 investigates the spatial dependence of electron plasma properties for a single set of discharge conditions, and section 7.3.3 is concerned with the results from measurements at a typical substrate position using different discharge conditions.

All of the Thomson scattering spectra in this chapter appeared consistent with a Maxwellian EVDF. Error bars, representing the standard deviation of repeated measurements, are shown for some of the laser Thomson scattering measurements. Often the size of an error bar was comparable to the marker size in the figures. It should be noted that the error bars do not take into account any systematic electron density overestimation from performing the Rayleigh scattering calibration after the Thomson scattering measurement; the systematic error was $< 10\%$. A general discussion regarding measurement uncertainties is given in section 5.2.4.

### 7.3.1 Measurements in the magnetic trap

In this section, the results from laser Thomson scattering and OES measurements in the magnetic trap ($r = 41$ mm, $z = 10$ mm, $P2$) are presented. The structure of this section is to compare the general features of the temporal profiles of electron temperature and electron density for different discharge conditions, before examining the individual profiles in detail and correlating them with the OES measurements. The results from the pressure variation and pulse-width variation investigations are presented separately.

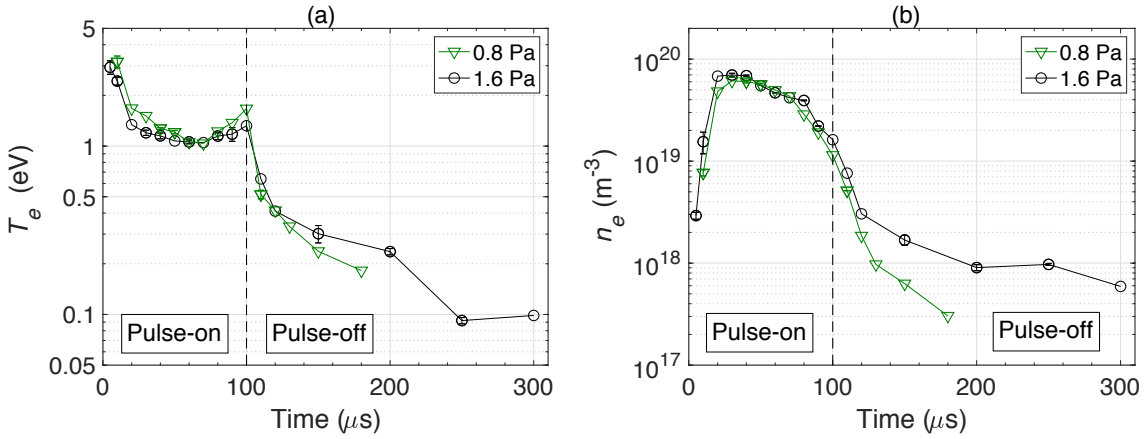


Figure 7.3: Comparison of (a) electron temperature and (b) electron density as a function of time for discharge conditions of 400 W average power, a 50 Hz repetition rate, a pulse-width of 100 $\mu$s and an argon gas pressure of either 0.8 Pa or 1.6 Pa. Measurements were performed at ($r = 41$ mm, $z = 10$ mm, $P2$).

#### 7.3.1.1 Pressure variation

Published values for the ionisation fraction of the metal flux to a substrate are in the range of $10-80\%$ [106]. It is clear that metal atoms still play an important role in the deposition process. The energy of the ions can be controlled by biasing the substrate, but the energy of the metal atoms is determined by the Thompson distribution [84] and their mean free path. Operation at a lower argon background pressure produces a more energetic flux of metal atoms at the substrate due to an increased mean free path for collisions with gas atoms. This tends to produce higher quality films; for example, higher density, reduced grain sizes, and better adhesion between the film and substrate [128, 166]. It is important, however, that low pressure operation still produces a dense plasma in the HiPIMS discharge so that a large fraction of the sputtered vapour is ionised. In this section, the effect of argon gas pressure variation in the magnetic trap region is examined.

Figure 7.3(a) shows a comparison of the temporal profiles of electron temperature in the magnetic trap for argon gas pressures of 0.8 Pa and 1.6 Pa. The corresponding discharge current-voltage waveforms are shown in figure 7.1(a). Similar trends were observed for both pressures: a peak in electron temperature at the start of the pulse, a minimum in electron temperature during the pulse-on time at $t \approx 60-70$ $\mu$s, and a two-fold decay of electron temperature during the pulse-off period ($t > 100$ $\mu$s). In addition, there was a

slightly lower electron temperature at higher pressure during the pulse-on period.

At higher pressure, the mean free path of electrons for collisions with argon neutrals is reduced. Consequently, there is a greater energy loss rate from the high energy tail of the electron energy distribution function (EEDF) through inelastic collisions. After thermalisation of the electron population, the average energy of the EEDF is reduced, and so a lower electron temperature is obtained.

The corresponding electron density measurements are shown in figure 7.3(b). Both profiles closely follow the discharge current variation. The maximum density at 1.6 Pa was $n_e = (7.0 \pm 0.3) \times 10^{19}$ m$^{-3}$, compared to $n_e = (6.1 \pm 0.2) \times 10^{19}$ m$^{-3}$ at 0.8 Pa. This is consistent with a greater peak target power density for the 1.6 Pa discharge: $900 \pm 25$ W·cm$^{-2}$ at 1.6 Pa compared to $835 \pm 25$ W·cm$^{-2}$ at 0.8 Pa. During the pulse-off period, there was a two-fold decay of electron density.

The fitting of exponential functions to the electron temperature and electron density profiles during the pulse-off period gives initial ($\tau_1$) and long-term ($\tau_2$) decay constants. All of the decay constants for the measurements reported in section 7.3.1 are summarised in table 7.2. The uncertainty from the fitting procedure is reflected by rounding to the nearest 5 $\mu$s. It is important to realise that only a small fraction of the afterglow period was recorded: the total afterglow period was 19.9 ms, whereas measurements were performed up to $\sim 0.2$ ms after pulse termination. Therefore, the accuracy of $\tau_2$ for characterising the long-term evolution of the discharge is uncertain, and so no conclusions are drawn from these values in this chapter.

The initial decay of electron temperature is caused by energetic electrons participating in inelastic collisions and/or escaping to surfaces inside the vacuum chamber, since they are able to overcome local ambipolar electric fields and the electric potential barrier of the sheath. The remaining portion of the EEDF loses energy through elastic collisions at a slower rate. The initial decay of electron temperature at 0.8 Pa ($\tau_{T1} = 10$) was faster than at 1.6 Pa ($\tau_{T1} = 20$). This is consistent with reduced neutral drag for high energy electrons escaping to the chamber walls at lower pressure. In addition, the electron temperature is slightly higher at the end of the pulse-on time for the 0.8 Pa discharge. Therefore, a greater fraction of the population is above the energy threshold for inelastic collisions with heavier species, although the electron mean free path for collisions with argon neutrals increases at lower pressure.

The rapid loss of high energy electrons and ambipolar diffusion to the target or chamber walls are responsible for the initial electron density decay. The initial density decay

constants for the two discharges were both $\tau_{n1} = 10$ $\mu$s. A simple one-dimensional diffusion model by Bäcker *et al.* [167] found that collisional effects have a greater influence on the long-term, rather than the initial density decay, with a slower decay predicted at higher pressure. The long-term decay constants in this research ($\tau_{n2} \geqslant 45$) were much greater than the decay constant associated with the discharge current during the pulse-off period ($< 1$ $\mu$s). This highlights that both the pulse-on and pulse-off periods play an important role in the deposition process.

A theoretical value for the timescale of the electron density decay can be estimated by calculating the time required for the plasma to reach the grounded target surface via ambipolar diffusion parallel to the magnetic field [167]:

$$\tau \sim \frac{L_B}{c_s}, \tag{7.2}$$

where $L_B$ is the distance parallel to the magnetic field line from the measurement position to the target surface; $c_s = (k_B T_e/m_i)^{1/2}$ is the ion sound speed, which is characteristic of the ambipolar diffusion speed; $m_i$ is the ion mass; and $k_B$ is the Boltzmann constant. The mass was estimated as the mean of the mass of argon and tungsten because the ionic abundance in the plasma was not measured and the metal content was expected to be significant. The length $L_B = 25$ mm was estimated using the spatial map of the magnetron's magnetic field configuration shown in figure 4.2, and the electron temperature was taken as $T_e = 1.5$ eV to represent the EEDF at pulse termination. Equation 7.2 returns a value of $\tau = 22$ $\mu$s, which has reasonable agreement with the experimentally determined values of $\tau_{n1} = 10$ $\mu$s for both discharges. Therefore, ambipolar diffusion to the target surface is important, as expected. In the model, rapid losses from the high-energy tail of the EEDF were not considered, and so the tendency is for the theoretical values to overestimate the decay timescale.

The electron dynamics in the discharge are strongly dependent on the plasma composition. For this reason, time-resolved OES measurements were performed to provide information about the abundance of atoms and singularly-charged ions from both argon and tungsten. The results from the OES measurements for an argon gas pressure of 1.6 Pa and a pulse-width of 100 $\mu$s are shown in figure 7.4(a). The electron temperature and electron density results for these discharge conditions, shown in figure 7.3, are re-plotted to enable a direct comparison. At the start of the target voltage pulse when $T_e > 2$ eV, there was a maximum in the Ar I emission intensity; there was a relatively strong Ar II

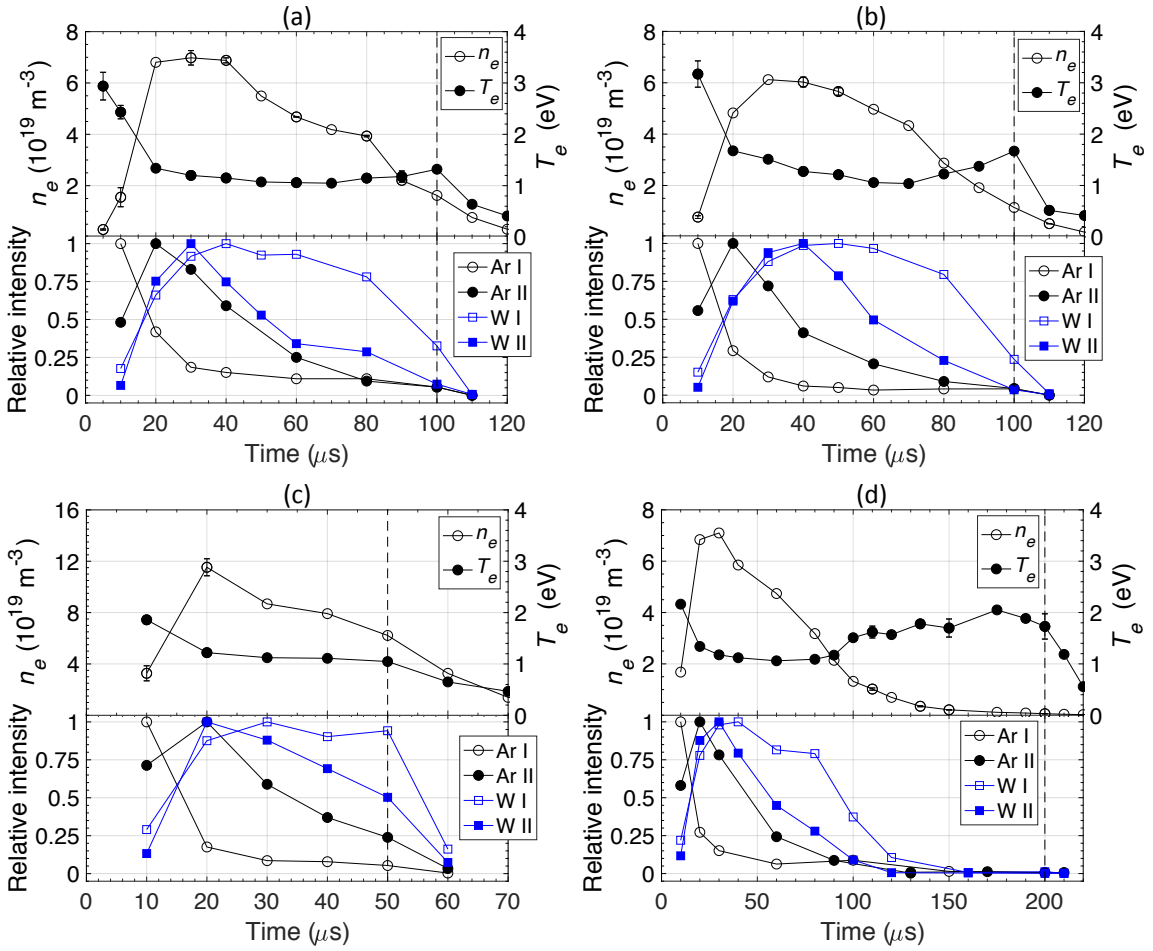


Figure 7.4: Temporal profiles of electron density, electron temperature and intensity of line emission, normalised by the peak number of counts for each line in a profile, from various species in the plasma (Ar I, Ar II, W I, W II). The common discharge conditions were an average power of 400 W and a 50 Hz repetition rate. For the measurements in (a) and (b), the pulse-width was 100 $\mu$s with an argon gas pressure of either 1.6 Pa or 0.8 Pa, respectively. For (c) and (d), the argon gas pressure was 1.6 Pa with a pulse-width of either (c) 50 $\mu$s or (d) 200 $\mu$s, respectively. The dashed lines indicate the end of the target voltage pulse.

signal; and the emission intensity from both tungsten species was relatively low.

A larger fraction of the EEDF is able to excite a tungsten species through an inelastic collision because the upper energy levels of the argon excited states are higher than that of tungsten (table 7.1). Moreover, the average electron energy in the discharge is significantly lower than the upper energy levels of the argon states. These observations indicate that $R_{ex}(T_e)$ is larger for the tungsten species. Given the relatively weak tungsten emission at the start of the pulse, this suggests that the ground state density of both tungsten species is low, and hence, the discharge is initially argon dominated.

Between $10 \leqslant t[\mu\text{s}] \leqslant 30$, the intensity of the Ar I line decreased, the Ar II emission intensity peaked at $t = 20$ $\mu$s, and the emission from both tungsten species increased. These trends are consistent with depletion of argon neutrals through intense ionisation and gas rarefaction [109]. Huo *et al.* [110] investigated the gas rarefaction effect for a HiPIMS discharge with an aluminium target and 1.8 Pa of argon gas using the ionisation region model. They found that the argon gas density was reduced by a factor of two during the pulse-on time, with 70% of the reduction caused by ionisation losses and 30% via the sputter wind kick-out process. In the research presented in this chapter, the contribution of the sputter wind process might be lower due to the larger mass difference between argon and tungsten, and hence inefficient momentum exchange, compared to argon and aluminium.

Another feature during this period is that the electron temperature decreased to $T_e \sim 1.2$ eV as the electron density increased. This is consistent with significant cooling of the EEDF as the density of metal species, which have a significantly lower energy threshold for inelastic collisions compared to argon, increases due to the increasing sputtering rate.

As expected, the peak in the ionic emission intensity from both elements correlates strongly with the maximum in both the discharge current, shown in figure 7.1(a), and electron density. The maximum Ar II signal was at $t = 20$ $\mu$s, while the W II emission peaked later at $t = 30$ $\mu$s. The delay in the maximum signal from W II is a consequence of gas rarefaction and the sputtering rate increasing as electron density increases, so tungsten replaces argon in the target vicinity to some extent after the initial stages of the discharge. Gudmundsson [105] reports that electron impact ionisation is the main mechanism for ionising metal atoms in HiPIMS discharges during the pulse-on time, with smaller contributions from Penning and charge exchange processes.

Beyond $t > 30$ $\mu$s, the electron density decreased as a result of the drop in target voltage and, consequently, discharge power. A future study could investigate the discharge

physics of the metal-rich phase by using a power supply that outputs a constant voltage. Nevertheless, the results of this work are representative of HiPIMS discharges used for industrial applications [165, p. 27]. The drop in electron density causes the rate of inelastic collisions to decrease, which is consistent with the decrease in emission intensity from all species. An exception, however, is the W I emission between $30 \leqslant t[\mu s] \leqslant 60$, when the emission signal was approximately constant. This indicates a significant density of W I in the plasma. The electron temperature began to rise when the W I emission started to decrease after $t > 60$ $\mu$s, which can be interpreted as a reduction of W I density. In the pulse-off period, the intensity of the line emission from all species was weak because both the electron temperature and electron density were relatively low compared to the pulse-on time, and the supply of metal to the plasma through sputtering stopped.

The OES results from a discharge with an argon pressure of 0.8 Pa are shown in figure 7.4(b). The trends were similar to the 1.6 Pa discharge, except the transition to a metal-rich plasma occurred later. For the 0.8 Pa discharge, the peak in W II emission occurred at $t \approx 30 - 40$ $\mu$s compared to $t = 30$ $\mu$s at 1.6 Pa. This correlates well with a longer gas breakdown phase (the period before the discharge current rise during the pulse-on time) and a delayed maximum for both electron density and discharge current for the lower pressure discharge. This is a consequence of a reduced electron impact ionisation rate during the initial stages of the pulse because there are fewer argon neutrals in the chamber at lower pressure.

#### 7.3.1.2 Pulse-width variation

In this section, the effect of varying the HiPIMS pulse-width is investigated. The average discharge power was maintained at 400 W so varying the pulse-width affects the instantaneous discharge power, and hence the electron density. A high electron density is necessary for producing a high ionisation fraction of sputtered atoms.

Figure 7.5(a) shows a comparison of the temporal profiles of electron temperature in the magnetic trap for pulse-widths of 50 $\mu$s, 100 $\mu$s and 200 $\mu$s. The corresponding discharge current-voltage waveforms are shown in figure 7.1(b). The data for the 100 $\mu$s pulse-width discharge is the same as reported in section 7.3.1.1, but it is re-plotted here for ease of comparison. The electron temperature results for the three discharges were similar during the overlapping pulse-on periods. Notable features outside of these periods are that the 50 $\mu$s pulse-width discharge terminated before a rise in electron temperature, unlike the

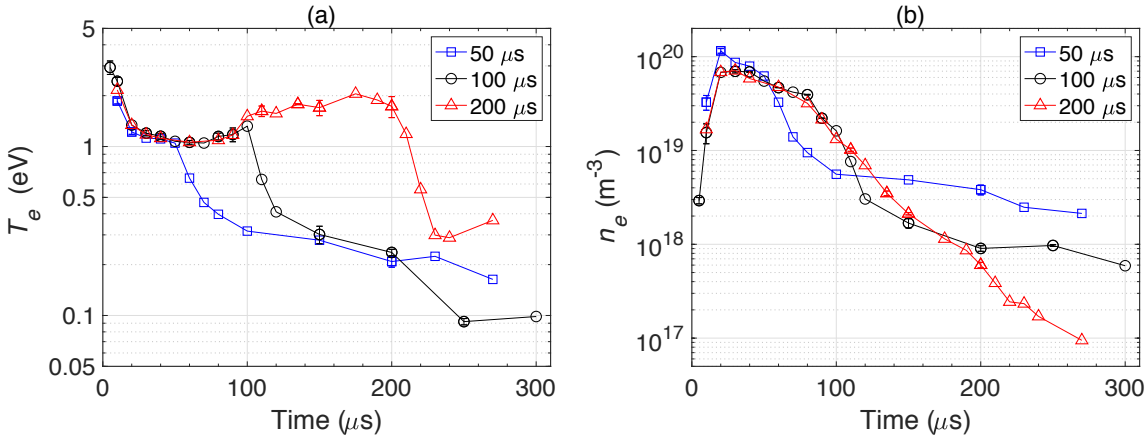


Figure 7.5: Comparison of (a) electron temperature and (b) electron density as a function of time for discharge conditions of 400 W average power, a 50 Hz repetition rate, an argon gas pressure of 1.6 Pa, and a pulse-width of either 50 $\mu$s, 100 $\mu$s or 200 $\mu$s. Measurements were performed at ($r = 41$ mm, $z = 10$ mm, $P2$).

other two discharges; and during the period $100 < t[\mu\text{s}] < 200$ of the 200 $\mu$s pulse-width discharge, the electron temperature increased to $\sim 2$ eV, while the electron temperature decayed for the other discharges which were in their pulse-off phase.

The corresponding electron density profiles are shown in figure 7.5(b). The 50 $\mu$s pulse-width discharge produced a maximum electron density of $n_e = (1.15 \pm 0.07) \times 10^{20}$ m$^{-3}$, whereas the peak values for the other two discharges were similar at $n_e \sim 7 \times 10^{19}$ m$^{-3}$. This is consistent with the hierarchy of peak target power density: $1290 \pm 25$ W·cm$^{-2}$, $900 \pm 25$ W·cm$^{-2}$ and $860 \pm 25$ W·cm$^{-2}$ for the discharges with pulse-widths of 50 $\mu$s, 100 $\mu$s and 200 $\mu$s, respectively. For comparison, the number density of room temperature argon gas at a pressure of 1.6 Pa is $3.9 \times 10^{20}$ m$^{-3}$, so the ratio of maximum electron density to argon gas density is $> 0.30$[1] for the 50 $\mu$s pulse-width discharge.

A basic model [127], based on the discharge voltage ($V_d$) and discharge current ($I_d$), can estimate the maximum electron density of the 50 $\mu$s pulse-width discharge relative to the other two discharges. One assumes that the ionic composition of the plasma is purely singularly charged tungsten and the role of argon is neglected. The number of tungsten atoms, which are sources of electrons, in the plasma is determined by the sputtering rate. The sputtering rate is proportional to $Y_{SS}(V_d)I_d$, where $Y_{SS}(V_d)$ is the self-sputtering

[1]Greater than sign because gas heating will reduce the argon gas density in the HiPIMS discharge.

yield of tungsten. The rate of change of electron density ($\mathrm{d}n_e/\mathrm{d}t$) is proportional to the electron impact ionisation rate, which itself is proportional to the sputtering rate multiplied by the electron density for a constant electron temperature. Since $n_e \propto I_d$, this gives $\mathrm{d}n_e/\mathrm{d}t \propto Y_{SS}(V_d)I_d^2$. For the 50 $\mu$s pulse-width discharge, the maximum discharge current of $I_d \approx 265$ A occurred at $t \approx 20$ $\mu$s when the target voltage was $V_d \approx -850$ V, which gives $Y_{SS} \approx 0.9$ [168]. For the 100 $\mu$s pulse-width discharge, the maximum discharge current of $I_d \approx 215$ A occurred at $t \approx 25$ $\mu$s when the target voltage was $V_d \approx -750$ V, which gives $Y_{SS} \approx 0.75$ [168]. The model predicts that $\mathrm{d}n_e/\mathrm{d}t$ is a factor of $\sim 1.80$ greater for the 50 $\mu$s pulse-width discharge relative to the 100 $\mu$s pulse-width discharge, which has good agreement with the experimentally determined maximum electron density ratio of $1.65 \pm 0.04$.

The exponential decay constants for the pulse-off period of the discharges are summarised in table 7.2 (displayed at the start of section 7.3.1). The 50 $\mu$s and 100 $\mu$s pulse-width discharges had a two-fold decay for both electron density and electron temperature. For the 200 $\mu$s pulse-width discharge, only initial decay constants were measured because, after this period, the electron density fell below the detection limit of the laser Thomson scattering system.

The initial electron temperature decay constants were $\tau_{T1} = 25$ $\mu$s, 20 $\mu$s and 15 $\mu$s for the 50 $\mu$s, 100 $\mu$s and 200 $\mu$s pulse-widths, respectively. A faster initial decay is associated with a higher electron temperature at the end of the pulse-on period. The initial electron density decay constants were $\tau_{n1} = 15$ $\mu$s, 10 $\mu$s and 40 $\mu$s for the 50 $\mu$s, 100 $\mu$s and 200 $\mu$s pulse-widths, respectively. The reason for the slower decay for the 200 $\mu$s pulse-width discharge is not immediately obvious, but it might be related to the lower plasma density, by over an order of magnitude, at the end of the pulse-on time compared to the other discharges.

The OES results are shown in figure 7.4(a,c,d) for the discharges with pulse-widths of 100 $\mu$s, 50 $\mu$s and 200 $\mu$s, respectively. The results for the 100 $\mu$s pulse-width discharge were discussed in section 7.3.1.1. The trends for the 50 $\mu$s and 100 $\mu$s pulse-widths were similar during the overlapping pulse-on period, except for the 50 $\mu$s pulse-width discharge, the peak in the intensity of the W II emission overlapped with the Ar II peak at $t = 20$ $\mu$s, rather than the W II peak occurring at $t = 30$ $\mu$s. This is consistent with the faster rise time and earlier peak in the discharge current for the shorter pulse-width. Furthermore, the electron temperature did not increase during the pulse-on time for the 50 $\mu$s pulse-width discharge because the decaying target voltage was terminated before the transition

to the lower-density mode, where a lower metal density is expected due to the reduced sputtering rate. This is demonstrated by the relative intensity of the W I line, which was 0.95 and 0.3 at the end of the pulse-on time for the 50 $\mu$s and 100 $\mu$s pulse-widths, respectively. A similar trend is observed for the W II line. EEDF cooling due to inelastic collisions with metal species is, therefore, important throughout the pulse-on time of the 50 $\mu$s pulse-width discharge.

The results for the 200 $\mu$s pulse-width discharge followed the same trends as the 100 $\mu$s pulse-width discharge during the overlapping pulse-on period. The two discharges had a similar peak power density because a relatively small amount of energy was deposited into the plasma during $100 < t[\mu s] < 200$ of the 200 $\mu$s pulse-width discharge. During this period for the 200 $\mu$s pulse-width discharge, the electron temperature increased as both the electron density and the line emission intensity of all the species decreased. This is consistent with a reduced sputtering rate at the target due to the decreasing discharge power; hence, the electron temperature rises because the rate of inelastic collisions decreases. Furthermore, weak emission intensity from argon species is expected because of the reduction in electron density compared to the start of the pulse, despite the similar electron temperature.

#### 7.3.1.3 Comparison with other studies

The results from measurements in the magnetic trap show, at the start of the pulse, a rapid increase in electron temperature and a slower increase in plasma density relative to their maximum attained values. This is a typical feature of pulsed plasma sources [169]. Initially, the input power is deposited into a relatively low electron density, and so the electron temperature is high. The electron temperature decreases as the electrons dissipate their energy through inelastic collisions with the background gas; consequently, the electron density increases.

The maximum electron density during the HiPIMS discharges was of the order of $n_e = 10^{19} - 10^{20}$ m$^{-3}$, which is consistent with the prediction of global models [107, 108, 138, 139], and previous measurements made by Langmuir probes [98, 132, 134] and non-intrusive diagnostics [135, 136]. The only other report of laser Thomson scattering applied to HiPIMS discharges is by Tsikata *et al.* [137], where they measured an electron density of the order of $n_e = 10^{18}$ m$^{-3}$ in the magnetic trap. This lower electron density is a result of different discharge conditions including a lower peak target power density.

The peak electron temperature of $T_e \sim 2-3$ eV measured at the start of the pulse in this research is a relatively low value compared to Langmuir probe measurements outside of the magnetic trap region, where $T_e > 10$ eV [122, 127, 128]. Furthermore, Tsikata *et al.* [137] measured $T_e \sim 12$ eV at the initiation of the target voltage pulse. These high energy populations, if present, were not observed in this research for several reasons. (i) The earliest measurement time was $t = 5$ $\mu$s and a high plasma density was already established ($n_e > 10^{18}$ m$^{-3}$). Therefore, significant amounts of electron impact ionisation (an energy loss mechanism) had already occurred. An earlier measurement time might be required; however, note that the measurements were averaged over 5 $\mu$s due to the target voltage jitter (see section 4.3.1.2). (ii) The highest electron temperature measured in this research was $T_e = 3.3$ eV, and the corresponding Thomson scattering spectrum is shown in figure 7.6; the experimental details are described in the caption. In order to measure higher electron temperatures, which have broader Thomson scattering spectra, a greater spectral range needs to be covered by the iCCD camera. This property is determined by the groove density of the third grating inside the TGS. (iii) A significant increase in the data accumulation time is required because, as discussed in section 2.2.3, the signal-to-noise ratio of a Thomson scattering spectrum degrades as $\Delta\lambda^2 = (\lambda - \lambda_i)^2$ increases; where $\lambda$ is the wavelength axis and $\lambda_i = 532$ nm is the laser wavelength.

### 7.3.2 Spatial dependence

The HiPIMS discharge is expected to produce a spatially-inhomogeneous plasma because of the unique magnetic field configuration of the magnetron. In this section, the results from measurements above the racetrack region and along the centre axis are presented. The discharge conditions were an average power of 400 W, a 50 Hz repetition rate, a 100 $\mu$s pulse-width and 1.6 Pa of argon gas.

#### 7.3.2.1 Scan above the racetrack region

An axial scan of laser Thomson scattering measurements was performed from $z = 10 - 70$ mm at a radial position of $r = 41$ mm. This radial position was close to the main racetrack erosion on the target surface at $r \approx 48$ mm. The magnetic field configuration of the magnetron is shown in figure 4.2. The magnetic field direction at $r = 41$ mm was approximately radial for the measurements within the last closed flux surface boundary ($z \lesssim 50$ mm). The scattering geometry was arranged in the $P2$ configuration, which

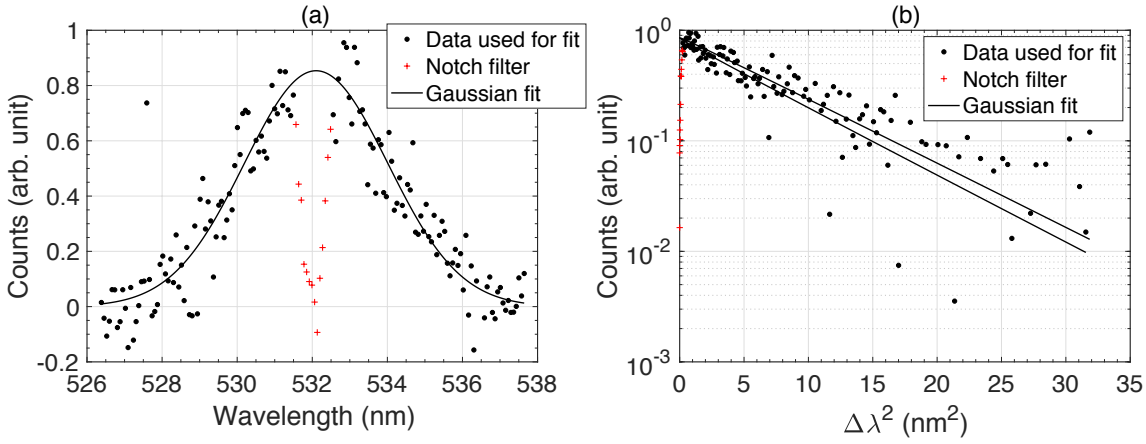


Figure 7.6: Example Thomson scattering spectrum at $t = 10$ $\mu$s for discharge conditions of 400 W average power, a pulse repetition rate of 50 Hz, a pulse-width of 100 $\mu$s and an argon gas pressure of 0.8 Pa. A Maxwellian EVDF appears linear on the axes in (b) when the drift velocity of the distribution is zero; where $\Delta\lambda = \lambda - \lambda_i$ ($\lambda$ is the wavelength axis and $\lambda_i = 532$ nm is the laser wavelength).

measures the component of the EVDF perpendicular to the magnetic field, as explained in section 4.3.4.

The electron temperature profiles are shown in figure 7.7(a). Each spatial position had a peak in electron temperature at the start of the pulse, a minimum in electron temperature around $t \approx 40 - 70$ $\mu$s, and then another peak towards the end of the pulse-on period. During the pulse-off period, there was a two-fold decay of electron temperature at all spatial positions.

The corresponding electron density results are shown in figure 7.7(b). There was a single maximum at each spatial position with the temporal location of the peak delayed at distances farther from the target: the temporal location of the peak shifted from $t = 30-70$ $\mu$s as height increased from $z = 10 - 70$ mm. The speed of propagation was $\sim 1.5$ km$\cdot$s$^{-1}$. Furthermore, the magnitude of the electron density maximum decreased as distance from the target increased: $n_e = (7.0 - 1.0) \times 10^{19}$ m$^{-3}$ as height increased from $z = 10 - 70$ mm. The electron density had a two-fold decay in the pulse-off period at all spatial locations.

These results indicate the diffusion of a dense plasma away from the target. The speed of propagation corresponds to a directional energy of 2.1 eV for tungsten ions. This is the same order of magnitude as the most probable energy of sputtered particles when

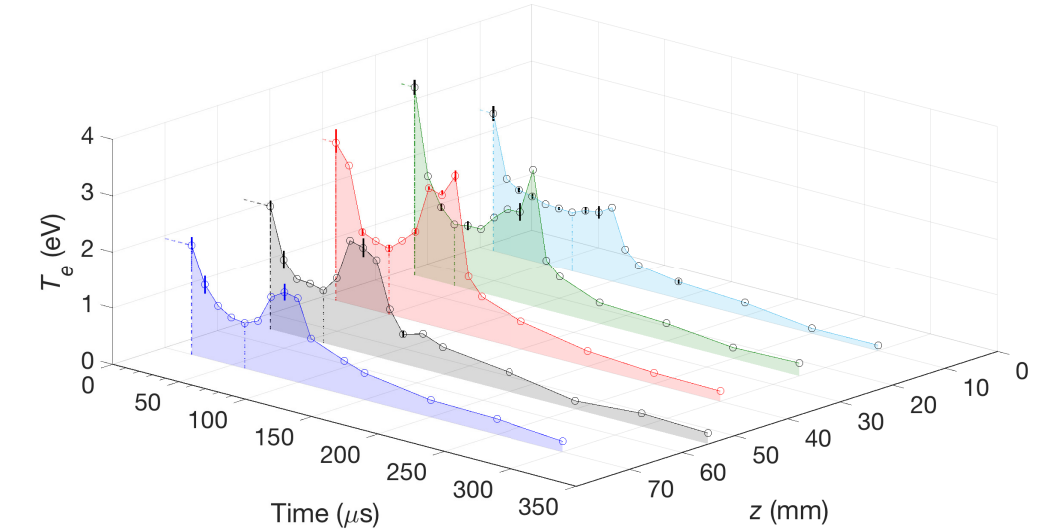


(a)

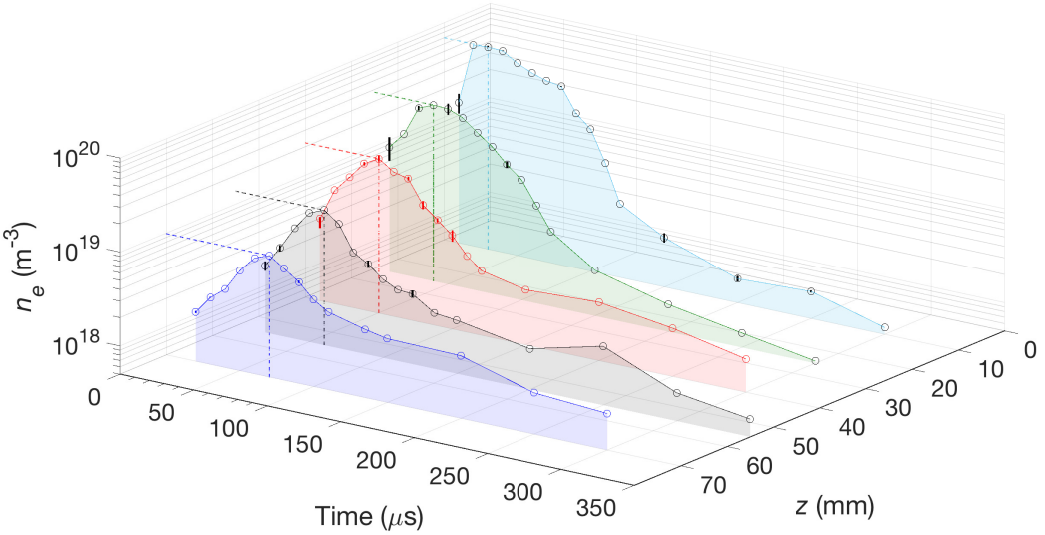


(b)

Figure 7.7: (a) Electron temperature and (b) electron density as a function of distance from the target ($z$). The dashed lines in (a) indicate the maximum and minimum electron temperatures in a profile, while in (b) they indicate the maximum electron density in a profile. Measurements were performed at ($r = 41$ mm, $z = 10-70$ mm, $P2$). The discharge conditions were an average power of 400 W, a 50 Hz repetition rate, a 100 $\mu$s pulse-width and 1.6 Pa of argon gas.

| $z$ (mm) | $\tau_{n1}$ ($\mu$s) | $\tau_{n2}$ ($\mu$s) | $\tau_{T1}$ ($\mu$s) | $\tau_{T2}$ ($\mu$s) |
|---|---|---|---|---|
| 10 | 10 | 165 | 15 | 115 |
| 25 | 20 | 140 | 10 | 260 |
| 40 | 30 | 270 | 15 | 150 |
| 55 | 80 | 245 | 15 | 185 |
| 70 | 80 | 195 | 15 | 175 |

Table 7.3: Electron density ($\tau_n$) and electron temperature ($\tau_T$) exponential decay constants during the pulse-off period. The subscripts 1 and 2 refer to the initial and long-term decays, respectively. Measurements were performed at ($r = 41$ mm, $z = 10 - 70$ mm, $P2$). The discharge conditions were an average power of 400 W, a 50 Hz repetition rate, a 100 $\mu$s pulse-width and 1.6 Pa of argon gas.

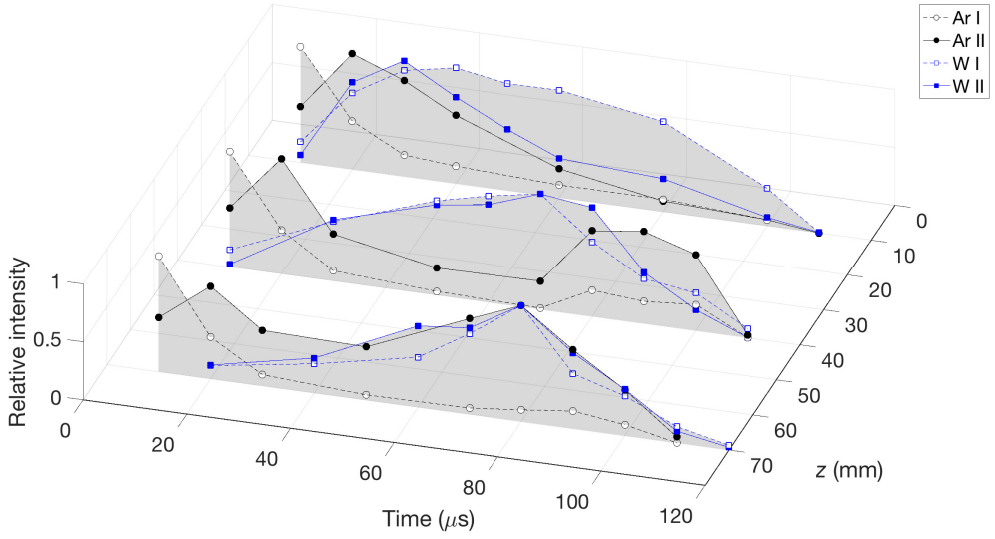


Figure 7.8: Temporal profiles of line emission intensity, normalised by the peak number of counts for each line in a profile, from various species in the plasma (Ar I, Ar II, W I, W II). Measurements were performed at ($r = 41$ mm, $z = 10 - 70$ mm, $P2$). The discharge conditions were an average power of 400 W, a 50 Hz repetition rate, a 100 $\mu$s pulse-width and 1.6 Pa of argon gas.

assuming a Thompson energy distribution [84, e.g. figure 2.8 in this thesis]. Ambipolar electric fields and collisions with argon neutrals will reduce the average sputtered ion energy in the plasma.

The exponential decay constants for both electron temperature and electron density are summarised in table 7.3. The initial decay constant for electron temperature was independent of spatial location, but the initial density decay was slower as the distance to the target increased for measurements inside the last closed flux surface boundary ($z \lesssim 50$ mm). The latter is consistent with a greater distance parallel to the magnetic field from the measurement position to the target surface ($L_B$) as $z$ increases. For example, substituting $L_B = 55$ mm and $T_e = 2.8$ eV into equation 7.2 for the $z = 40$ mm measurement position gives $\tau = 35$ $\mu$s, which has reasonable agreement with the experimentally determined value of $\tau_{n1} = 30$ $\mu$s. A theoretical value of $\tau = 22$ $\mu$s was calculated for the initial density decay at the $z = 10$ mm position in section 7.3.1.1. In addition, the initial density decay times will be influenced by the electron density wave travelling away from the target. This favours a slower plasma density decay farther from the target.

OES measurements were performed at $z = 10$ mm, 40 mm and 70 mm to provide further insight into the plasma dynamics. The results are shown in figure 7.8. The trends for the measurements at $z = 10$ mm were discussed in section 7.3.1.1. The maximum emission intensity from W I and W II occurred later as the distance to the target increased. This is consistent with tungsten travelling outwards from the target. Moreover, the electron density maximum at each position occurred when the electron temperature had a low value relative to the start and end of the pulse-on time, which indicates EEDF cooling due to a high density of metal species. These observations suggest that there is a significant density of metal ions in the spatially-propagating electron density maximum in figure 7.7(b). However, the peak W II signal occurred after the electron density maximum at $z = 40$ mm and 70 mm. This discrepancy can be explained by the fact that the emission intensity is dependent on the electron temperature through the rate coefficient $R_{ex}(T_e)$, and not just on particle densities. The electron temperature increases after an electron density maximum, which increases $R_{ex}(T_e)$. For example, the electron density maximum at $z = 70$ mm occurred at $t = 70$ $\mu$s when $T_e = 0.9$ eV, but the W II emission had a peak intensity at $t = 80$ $\mu$s when $T_e = 1.4$ eV. In addition, the OES measurements are line of sight integrated so the majority of the emission collected was not radiated from inside the detection volume.

At all spatial locations, the intensity of emission from argon species was high at the

start of the discharge pulse ($t \leqslant 20$ $\mu$s). Following this, there was a decrease in the argon emission intensity. However, later during the pulse-on time at $z = 40$ mm and 70 mm, there was a rise in the emission intensity from both Ar I and Ar II, which was not observed at $z = 10$ mm. The rise in the argon emission intensity correlates well with a greater electron temperature increase towards the end of the pulse-on time for $z = 40$ mm and 70 mm, relative to $z = 10$ mm. The rise in the argon emission intensity is due to $R_{ex}(T_e)$ increasing and possibly argon gas refilling the volume. The importance of argon gas refill can be assessed by comparing the length scale of the plasma with the distance travelled by argon gas between the electron density maximum at a certain spatial location, when argon gas depletion is expected to be significant, and the rise in Ar I emission at that position. For example, figure 7.7(b) shows that the electron density maximum at $z = 40$ mm occurred at $t = 50$ $\mu$s and there was a rise in the Ar I emission at $t = 80$ $\mu$s. The distance travelled by 'cool' argon gas of temperature 500 K in 30 $\mu$s is 1.7 cm, which is small compared to the target diameter (15 cm). Therefore, argon gas refill is not expected to be significant during the pulse-on time of the 100 $\mu$s pulse-width discharge in the magnetic trap region, despite the decrease in discharge power.

It can be concluded that the rise in the emission intensity for Ar I and Ar II towards the end of the pulse-on time is due to the increase in electron temperature after the electron density wave has passed through the region. The electron temperature at the end of the pulse-on time ($t = 100$ $\mu$s) was dependent on spatial position. The electron temperature at $t = 100$ $\mu$s had a minimum at $z = 10$ mm, a maximum at $z = 40$ mm and then decreased towards $z = 70$ mm. The peak at $z = 40$ mm represents the balance between a lower metal density farther from the target, which favours a higher electron temperature; but this results in being farther from the main electron heating region [107], which favours a lower electron temperature.

#### 7.3.2.2 Scan along the centre axis

Measurements along the centre line ($r = 0$ mm) were performed at $z = 10$ mm, 40 mm and 70 mm with the scattering geometry aligned in the $P1$ configuration. In this alignment, the direction of sensitivity for the EVDF measurements was arbitrary. The electron temperature results are shown in figure 7.9(a). Similar trends to those above the racetrack region were observed: a peak in electron temperature at the start of the pulse, a minimum during the pulse-on time, a peak towards the end of the pulse-on time, and a two-fold

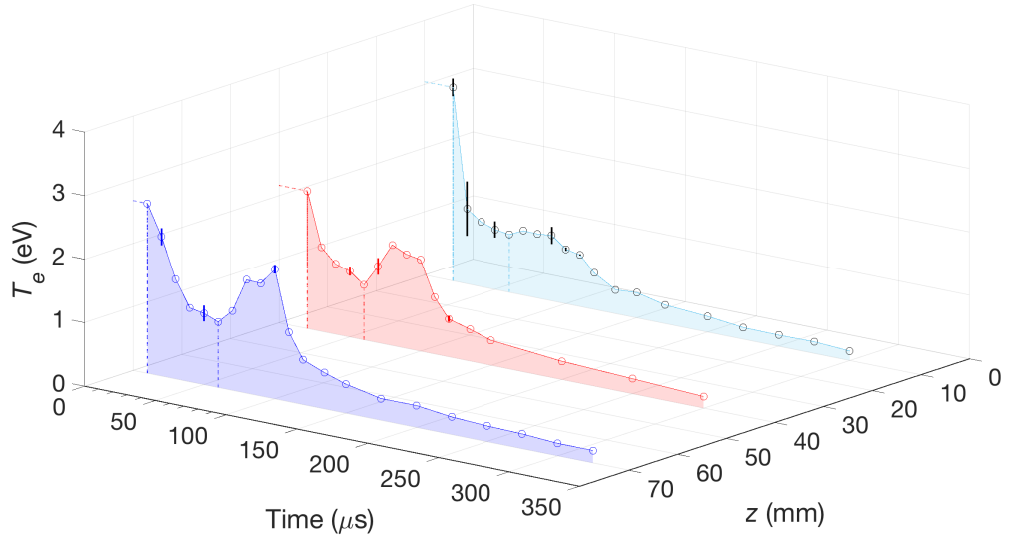


(a)

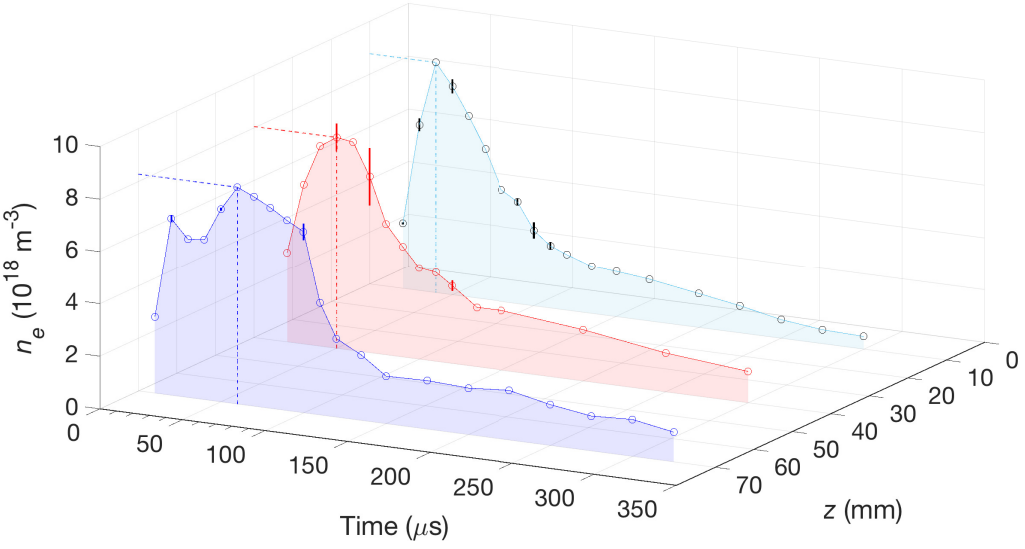


(b)

Figure 7.9: (a) Electron temperature and (b) electron density as a function of distance from the target ($z$). The dashed lines in (a) indicate the maximum and minimum electron temperatures in a profile, while in (b) they indicate the maximum electron density in a profile. Measurements were performed at ($r = 0$ mm, $z = 10$ mm, 40 mm, 70 mm, $P1$). The discharge conditions were an average power of 400 W, a 50 Hz repetition rate, a 100 $\mu$s pulse-width and 1.6 Pa of argon gas.

decay in the pulse-off period.

The electron density results are shown in figure 7.9(b). The maximum electron density at each spatial position was similar ($n_e \sim 8.5 \times 10^{18}$ m$^{-3}$) and the maximum occurred at a later time as $z$ increased: $t = 40 - 60$ $\mu$s as $z = 10 - 70$ mm. The propagation speed was $\sim 3.0$ km·s$^{-1}$. An interesting feature is the double-peak structure during the pulse-on time at $z = 70$ mm. The temporal location of the two peaks were $t = 20$ $\mu$s and 60 $\mu$s, with the later one having a greater electron density. During the pulse-off period, there was a two-fold decay of electron density, except at $z = 10$ mm, where only a single decay was observed.

The results shown in figure 7.9(b) indicate that the plasma constituting the second electron density peak at ($t = 60$ $\mu$s, $r = 0$ mm, $z = 70$ mm, $P1$) originates from the target region because there is evidence for propagation along the centre axis. Hence, this plasma probably contains a significant metal ion density. The origin of the first peak at ($t = 20$ $\mu$s, $r = 0$ mm, $z = 70$ mm, $P1$), however, is more difficult to understand because this initial peak is not observed in the profiles closer to the target. Possible explanations are that (i) the temporal resolution of the measurements was insufficient to observe the propagation of the plasma constituting the first peak. Measurements were attempted at ($t = 10$ $\mu$s, $r = 0$ mm, $z = 10$ mm and 40 mm, $P1$), but the electron density was below the Thomson scattering detection limit. (ii) The drift speed of the plasma significantly decreased at $z = 70$ mm causing an increase in electron density, although this effect did not appear to be significant for the second peak. (iii) The argon plasma generated during the initial stages of the pulse-on time is guided to the centre axis by the magnetic field outside of the last closed flux surface boundary, leading to a maximum along the centre axis at $z \approx 70$ mm. It should be noted that the electron density maxima in figure 7.7(b) occur at $t \geqslant 30$ $\mu$s so the electron density wave above the racetrack cannot be responsible for the first peak at ($t = 20$ $\mu$s, $r = 0$ mm, $z = 70$ mm, $P1$) along the centre axis.

Along the centre line, the magnetic field is directed perpendicular to the target surface. Consequently, electrons can readily stream away from the target and cross the last closed flux surface boundary. Above the racetrack region, however, electrons have to cross the magnetic field to escape the magnetic trap. Therefore, one would expect a greater propagation speed of the plasma along the centre line, which was observed ($\sim 3.0$ km·s$^{-1}$ from figure 7.9(b) compared to $\sim 1.5$ km·s$^{-1}$ from figure 7.7(b)). Another observation is that the maximum electron density was greater above the racetrack region compared to along the centre line. This is expected because electrons are well confined in the magnetic trap,

| $z$ (mm) | $\tau_{n1}$ ($\mu$s) | $\tau_{n2}$ ($\mu$s) | $\tau_{T1}$ ($\mu$s) | $\tau_{T2}$ ($\mu$s) |
|---|---|---|---|---|
| 10 | 115 | - | 40 | 170 |
| 40 | 80 | 245 | 25 | 200 |
| 70 | 25 | 365 | 20 | 215 |

Table 7.4: Electron density ($\tau_n$) and electron temperature ($\tau_T$) exponential decay constants during the pulse-off period. The subscripts 1 and 2 refer to the initial and long-term decays, respectively. Measurements were performed at ($r$ = 0 mm, $z$ = 10 mm, 40 mm, 70 mm, $P1$). The discharge conditions were an average power of 400 W, a 50 Hz repetition rate, a 100 $\mu$s pulse-width and 1.6 Pa of argon gas.

above the racetrack. In addition, the difference in maximum electron density was reduced as the distance from the target increased, which is consistent with a lower magnetic field strength farther from the target, and so the electron motion becomes more isotropic. The diffusion of plasma from above the racetrack to the centre line might explain the broadness of the $z$ = 70 mm profile in figure 7.9(b).

The exponential decay constants for the centre line measurements are detailed in table 7.4. There were faster initial decays for both electron temperature and electron density as the distance from the target increased. The former is consistent with a faster decay when there is a higher electron temperature at the end of the pulse-on time. In contrast, above the racetrack region, a slower initial decay of electron density was observed for positions farther from the target (table 7.3). A possible reason for the difference is that losses to the chamber walls are more important along the centre axis, due to the open magnetic field configuration.

#### 7.3.2.3 Comparison with other studies

Other researchers have reported a double-peak structure in temporal profiles of electron density at a typical substrate position using Langmuir probes [122, 125], similar to the one observed at $z$ = 70 mm in figure 7.9(b); although, some researchers report that the second peak is during the pulse-off period [39, 123, 124], rather than during the pulse-on time. In most of these studies, the ionic composition of the earlier peak was conjectured to be predominately Ar II, and a strong metal contribution for the later peak. This hypothesis was supported by OES measurements [125, 161]. Alternatively, Alami *et al.* [123] attributed the second peak to the reflection of an ion acoustic wave off the chamber walls. The propagation speed of the metal is estimated in some of the Langmuir probe

| Pulse-width ($\mu$s) | Pressure (Pa) | $\tau_{n1}$ ($\mu$s) | $\tau_{n2}$ ($\mu$s) | $\tau_{T1}$ ($\mu$s) | $\tau_{T2}$ ($\mu$s) |
|---|---|---|---|---|---|
| 50 | 1.6 | 80 | 225 | 85 | 350 |
| 100 | 1.6 | 25 | 365 | 20 | 215 |
| 200 | 1.6 | 245 | - | 20 | - |
| 100 | 0.8 | 25 | 860 | 15 | 55 |

Table 7.5: Electron density ($\tau_n$) and electron temperature ($\tau_T$) exponential decay constants during the pulse-off period. The subscripts 1 and 2 refer to the initial and long-term decays, respectively. Measurements were performed at ($r = 0$ mm, $z = 70$ mm, $P1$). The discharge conditions were an average power of 400 W and a 50 Hz repetition rate.

studies by assuming that the temporal delay of the second peak with respect to the first peak is the time required for the metal ions to travel from the target to the measurement position [122, 125]. This gives $\sim 1.75$ km·s$^{-1}$ for this work, which is closer to the speed calculated for above the racetrack region ($\sim 1.5$ km·s$^{-1}$) rather than the centre axis speed ($\sim 3.0$ km·s$^{-1}$). Similar speeds ($\sim 2$ km·s$^{-1}$) were calculated in the Langmuir probe studies at comparable argon gas pressures [122, 125]. One can conclude that this method gives the correct order of magnitude for the metal ion propagation speed.

To the author's knowledge, the only other spatio-temporal surveys of electron density within the last closed flux surface boundary have been by Bohlmark *et al.* [98] and Sigurjónsson [132]. Both of these studies used a Langmuir probe and the Druyvesteyn method (explained in section 3.1.3.3) to interpret the probe data. However, the results in chapter 5 indicate that the Druyvesteyn method is unreliable when electrons are strongly magnetised. Regardless, their results show that the highest electron density is in the magnetic trap region, which is consistent with the results presented in section 7.3.2. Neither of these probe studies report temporal profiles of effective electron temperature within the last closed flux surface boundary.

### 7.3.3 Measurements at a typical substrate position

This section details the results of laser Thomson scattering measurements at a position on the centre axis and outside of the last closed flux surface boundary ($r = 0$ mm, $z = 70$ mm, $P1$). The direction of sensitivity for the EVDF measurements was arbitrary. The trends identified at this measurement position should be representative of those at a typical substrate position, which is usually located after the magnetic null point ($z > 61$ mm in this research). The results obtained from varying the background gas pressure and the target

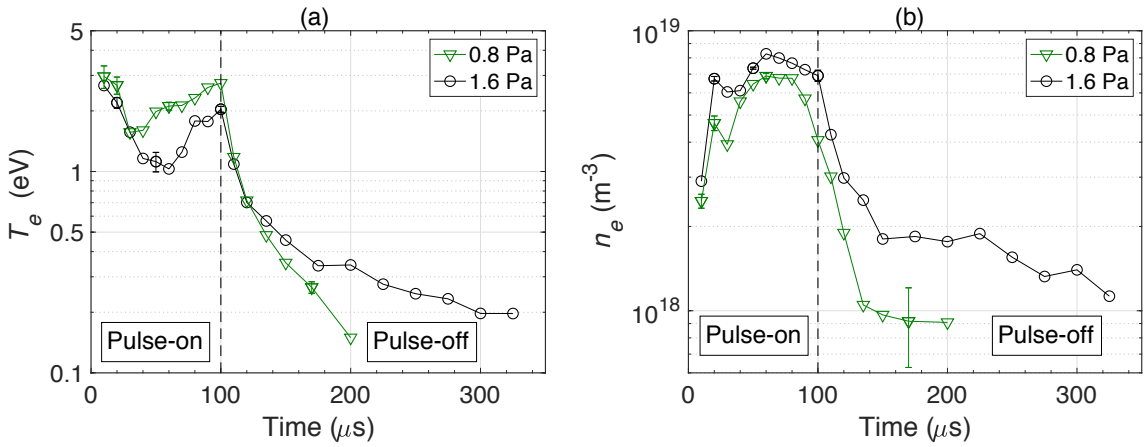


Figure 7.10: Comparison of (a) electron temperature and (b) electron density as a function of time for discharge conditions of 400 W average power, a 50 Hz repetition rate, a pulse-width of 100 $\mu$s and an argon gas pressure of either 0.8 Pa or 1.6 Pa. Measurements were performed at ($r = 0$ mm, $z = 70$ mm, $P1$).

voltage pulse-width are discussed separately. Note that the discharge conditions are the same as those used for the measurements reported in section 7.3.1, where the measurement position was in the magnetic trap.

#### 7.3.3.1 Pressure variation

Figure 7.10(a) shows the electron temperature results for argon gas pressures of 0.8 Pa and 1.6 Pa. The corresponding discharge current-voltage waveforms are shown in figure 7.1(a). The trends in the electron temperature results were similar to those observed in the magnetic trap region, which were presented in figure 7.3(a): a greater electron temperature during the pulse-on time at lower pressure; a peak at the start of the pulse, followed by a minimum, and a rise towards the end of the pulse-on time; and a two-fold decay in the pulse-off period.

The corresponding electron density profiles for the substrate position are shown in figure 7.10(b). The results for the two pressures had similar trends: a narrow peak at $t = 20$ $\mu$s; a larger second peak, which was broader and centred at $t \approx 60$ $\mu$s; and a two-fold decay in the pulse-off period. In addition, there was a greater electron density during the pulse-on time of the higher pressure discharge. The origins of the two maxima in each temporal profile were discussed in sections 7.3.2.2 and 7.3.2.3: the first peak is speculated

to originate from argon ions and the second peak is thought to originate from metal-rich plasma.

The cooling of the EEDF in figure 7.10(a) during the pulse-on time can be attributed to a large number of inelastic collisions with metal species. An anomalous result, however, is that the second electron density peak for the 0.8 Pa discharge in figure 7.10(b) does not correspond to the temporal region of the electron temperature minimum in figure 7.10(a), unlike the 1.6 Pa discharge. This might be due to different neutral tungsten dynamics in the discharges.

A key difference between the profiles acquired in the magnetic trap (figure 7.3) and at the substrate position (figure 7.10) is that the effect of varying the discharge pressure is more extreme for the substrate position in terms of both electron temperature and electron density measurements. This is expected because gas rarefaction is stronger closer to the target; hence, the magnetic trap region is more metal dominated and less sensitive to changes in argon gas pressure. Furthermore, the transport of plasma generated in the magnetic trap to the substrate position is influenced by collisions with the background gas. At a higher argon pressure, the electron mean free path for collisions with argon atoms is reduced, which could result in further ionisation and cooling of the EEDF.

The exponential decay constants for both electron temperature and electron density are summarised in table 7.5. There was a faster initial electron temperature decay at 0.8 Pa ($\tau_{T1} = 15$ $\mu$s) compared to 1.6 Pa ($\tau_{T1} = 20$ $\mu$s). These results are consistent with a higher electron temperature at the end of the pulse-on time at lower pressure. The initial decay of the electron density was similar at both pressures ($\tau_{n1} = 25$ $\mu$s). The long-term decay constants for electron density were of the order of hundreds of microseconds. This suggests a slow long-term decay of the plasma density outside of the last closed flux surface boundary, where the plasma density exceeds typical DC magnetron values of $n_e \leqslant 10^{17}$ $\mathrm{m}^{-3}$ for, at least, hundreds of microseconds after the termination of the target voltage pulse. During this period, a negatively biased substrate will receive an enhanced ion flux compared to conventional magnetron operation [129], which is beneficial for film properties [85, 86]. In addition, the remnant plasma will aid the re-ignition of the discharge from the subsequent target voltage pulse.

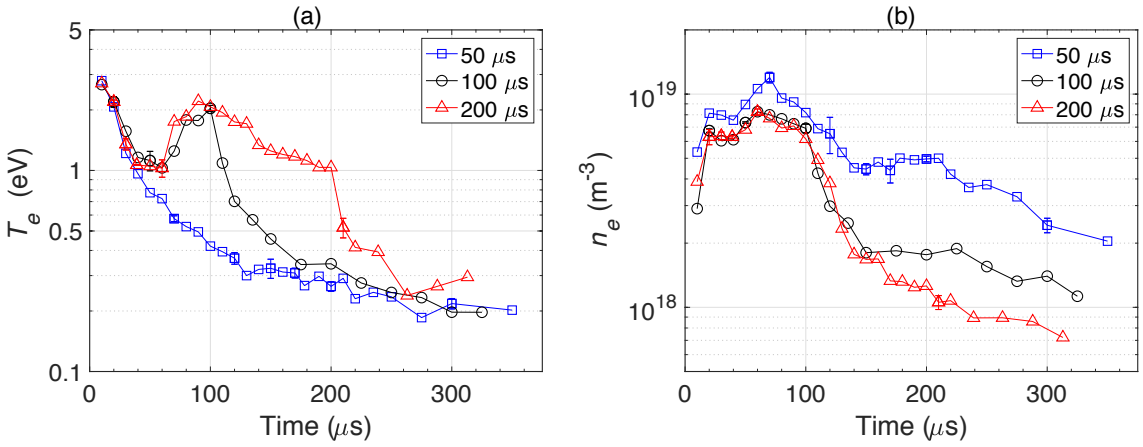


Figure 7.11: Comparison of (a) electron temperature and (b) electron density as a function of time for discharge conditions of 400 W average power, a 50 Hz repetition rate, an argon gas pressure of 1.6 Pa, and a pulse-width of either 50 $\mu$s, 100 $\mu$s or 200 $\mu$s. Measurements were performed at ($r = 0$ mm, $z = 70$ mm, $P1$).

#### 7.3.3.2 Pulse-width variation

The electron temperature results for the HiPIMS pulse-width investigation are shown in figure 7.11(a). The corresponding discharge current-voltage waveforms are shown in figure 7.1(b). All three discharges had a similar peak in electron temperature of $T_e \approx 2.7$ eV at $t = 10$ $\mu$s. The electron temperature for the 50 $\mu$s pulse-width discharge decreased during the pulse-on time, whereas a minimum occurred for both the 100 $\mu$s and 200 $\mu$s pulse-widths at $t \approx 60$ $\mu$s and then the electron temperature increased. Furthermore, the 200 $\mu$s pulse-width discharge had a peak at $t = 90$ $\mu$s of $T_e = 2.2$ eV and then a decline in electron temperature until termination of the target voltage pulse.

As discussed in section 7.3.1.2, a possible explanation as to why the electron temperature does not increase for the 50 $\mu$s pulse-width discharge is that the target voltage pulse terminates before a significant reduction in discharge power. A high discharge power, and hence a high plasma density, is associated with a metal-rich plasma because of the high sputtering rate. A high metal density favours cooling of the EEDF through inelastic collisions.

The corresponding electron density results are shown in figure 7.11(b). The electron density produced by the 50 $\mu$s pulse-width discharge exceeded the values produced by the other two discharges at all times, which is consistent with a greater peak target power

density for the 50 $\mu$s pulse-width discharge. All of the profiles have a double-peak structure, with the first electron density peak at $t = 20$ $\mu$s for all of the discharges. The second peak occurred at $t = 70$ $\mu$s for the 50 $\mu$s pulse-width discharge, which is during the pulse-off period, and at $t = 60$ $\mu$s for the other two discharges. The longer temporal delay between the first and second peaks for the 50 $\mu$s pulse-width discharge is consistent with EEDF cooling after pulse termination, so the diffusion speed of the dense plasma from the magnetic trap is reduced.

For the 200 $\mu$s pulse-width discharge, the electron density decreased during $90 < t[\mu\text{s}] < 200$ at both the substrate position (figure 7.11(b)) and in the magnetic trap (figure 7.5(b)). In contrast to the substrate position, the electron temperature increased in the magnetic trap during this period. Moreover, the target voltage ($\sim -300$ V) was comparable to DC magnetron conditions. The results in chapter 6 show that there is a cold electron population with a temperature of $T_e \sim 0.5$ eV, which dominates the total electron density, both inside and outside of the last closed flux surface boundary in the DC magnetron. Therefore, the electron temperature at the substrate position during the HiPIMS discharge is probably tending to this value, and the pulse-on period was too short to observe the eventual decay of electron temperature in the magnetic trap.

The cooling of the EEDF at the substrate position during $90 < t[\mu\text{s}] < 200$ in the 200 $\mu$s pulse-width discharge could be due to argon gas refill, which results in a greater collision frequency between argon neutrals and electrons. The timescale for this process is greater in the magnetic trap region for several reasons: gas rarefaction is strongest close to the target, especially above the racetrack; argon gas has to travel a greater distance to refill the volume close to the target, since the sputter wind kick-out predominately pushes the gas in the direction of the substrate; and gas rarefaction is always occurring during the pulse-on time but to a lesser extent as the discharge power decreases. The time required for argon gas of temperature 500 K to travel directly from the substrate position to the measurement position in the magnetic trap ($r = 41$ mm, $z = 10$ mm) is $\sim 130$ $\mu$s. Therefore, argon gas refill is not important during the pulse-on time in the magnetic trap, if one assumes that argon gas refill begins at $t \approx 90$ $\mu$s at the substrate position. Note that argon refill from the side of the magnetron has been ignored, which could reduce the refill time.

The exponential decay constants for the pulse-off period of the discharges are summarised in table 7.5 (displayed at the start of section 7.3.3). The 50 $\mu$s and 100 $\mu$s pulse-width discharges had a two-fold decay for both electron density and electron temperature. For the 200 $\mu$s pulse-width discharge, only initial decay constants were measured because,

after this period, the electron density fell below the detection limit of the laser Thomson scattering system.

The initial electron temperature decay constants for the 50 $\mu$s, 100 $\mu$s and 200 $\mu$s pulse-widths were $\tau_{T1}$ = 85 $\mu$s, 20 $\mu$s and 20 $\mu$s, respectively. The slower initial decay for the 50 $\mu$s pulse-width discharge might be due to the absence of high energy electrons at the measurement position when the pulse terminates. The 50 $\mu$s pulse-width discharge had the lowest electron temperature and highest electron density at pulse termination, which implies the highest metal density.

The initial electron density decay constants for the 50 $\mu$s, 100 $\mu$s and 200 $\mu$s pulse-widths were $\tau_{n1}$ = 80 $\mu$s, 25 $\mu$s and 245 $\mu$s, respectively. The faster initial decay for the 100 $\mu$s pulse-width discharge is associated with a higher electron temperature at the end of the pulse-on time. However, the dense plasma generated in the magnetic trap arrives during the pulse-off period for the 50 $\mu$s pulse-width discharge (the decay constant was calculated after the electron density maximum), so it is not a fair comparison. All of the discharges exhibit a slow long-term decay of the electron density.

#### 7.3.3.3 Comparison with other studies

Extensive Langmuir probe measurements have been performed by other researchers to characterise the electron plasma properties at a typical substrate position. To the authors knowledge, however, measurements using a tungsten target have not been reported in the literature. Nevertheless, the general features of the electron temperature and electron density temporal profiles in this research are consistent with those observed in previous Langmuir probe studies, namely: two peaks in a temporal profile of electron density [39, 122–125]; a high electron temperature at the start of the pulse, an electron temperature minimum during the pulse-on time, and a rise in electron temperature towards the end of the pulse-on time [122, 128, 129]; a lower electron density during the pulse-on time at lower pressure for the same average discharge power [124]; and a greater electron density as instantaneous discharge power density increases at a constant gas pressure [122, 123, 127, 129]. It should be emphasised, again, that the laser Thomson scattering system is insensitive to high temperature populations of electrons with low densities ($< 10^{16}$ $^{-3}$), which have been observed by Langmuir probes at the start of the pulse ($T_e > 10$ eV) [122, 127, 128]. Possible reasons as to why these energetic populations were not observed in this research, using laser Thomson scattering, are discussed in section 7.3.1.3.

The slow plasma density decay during the pulse-off time of HiPIMS discharges has been highlighted by other researchers in Langmuir probe [39, 122, 129] and mass spectrometry [116] studies. In particular, Poolcharuansin and Bradley [122] performed Langmuir probe measurements at a typical substrate position for the entire duration of the pulse-off period. They observed a two-fold decay of both electron temperature and electron density. The exponential decay constants are similar to this research, except for $\tau_{n2}$, which was of the order of milliseconds in their study, compared to hundreds of microseconds. The accuracy of the long-term decay constants in this research, however, is unknown because of the limited temporal range of Thomson scattering measurements in the pulse-off period. In addition, a two-fold decay of both electron temperature and electron density was observed in the afterglow of pulsed-RF [167] and kHz pulsed-DC [170] magnetron discharges. In these cases, the long-term density decay constants were of the order of tens to hundreds of microseconds.

## 7.4 Cross-magnetic field transport rate of electrons

The fundamental aim of the HiPIMS discharge is to generate a large flux of metal ions at the substrate. The cross-magnetic field transport rate of electrons is important because it influences the electron density in the region between the magnetic trap and the substrate. A high conductivity in this region is favourable for transporting ions to the substrate [161]. Furthermore, cross-magnetic field mechanisms can affect both electrons and ions. For example, Lundin *et al.* [171] propose that a modified two-stream instability in the magnetic trap generates an oscillating azimuthal electric field, which leads to enhanced electron transport in the $\mathbf{E}\times\mathbf{B}$ direction and enhanced ion transport in the radial direction.

In magnetron discharges, the cross-magnetic field transport rate is usually characterised by the Hall parameter: $\omega_{g,e}\tau_e$, where $\omega_{g,e} = eB/m_e$ is the angular frequency of the electron gyration and $\tau_e$ is the electron momentum-exchange collision time. Lower values of the Hall parameter are associated with faster cross-magnetic field transport. The Hall parameter can be determined from the macroscopic ratio of the Hall and discharge current densities ($J_H/J_D$) in the magnetic trap. The Hall current density $J_H$ is calculated using the Hall conductivity ($\sigma_H$: drift perpendicular to both electric and magnetic fields) and $J_D$ is calculated using the Pedersen conductivity ($\sigma_P$: drift parallel to the electric field and perpendicular to the magnetic field); hence [6, p. 97]:

$$\frac{J_H}{J_D} = \frac{E\sigma_H}{E\sigma_P} = \omega_{g,e}\tau_e. \tag{7.3}$$

It is assumed that the currents are driven by a uniform electric field of strength $E$, a uniform magnetic field of strength $B$ which is aligned perpendicular to the electric field, and density gradient driven diffusional transport is negligible.

Experimental investigations, however, have generally measured the azimuthal current density ($J_\phi$) as opposed to $J_H$. Components of the azimuthal drift velocity include $\mathbf{E}\times\mathbf{B}$, diamagnetic, $\nabla\mathbf{B}$ and curvature drifts. Both Lundin *et al.* [162] and Bohlmark *et al.* [164] have concluded that all of these drifts are in the same direction and the relative contribution of each component is important. This leads to:

$$\frac{J_\phi}{J_D} \geqslant \frac{J_H}{J_D} = \omega_{g,e}\tau_e. \tag{7.4}$$

Previous studies have measured values of $1.5 < J_\phi/J_D < 12$ during HiPIMS [120, 162–164] and $8 < J_\phi/J_D < 30$ during DC magnetron operation [41, 42], using intrusive electric and magnetic probes. It was concluded that the cross-magnetic field transport of electrons is anomalously fast compared to classical theory based on collisions, especially for HiPIMS discharges.

In this section, the results of using laser Thomson scattering to determine $J_\phi/J_D$ are presented. The novelty of this research is measuring $J_\phi$ using a non-intrusive technique, unlike the previous probe studies mentioned above. Moreover, the reliable measurements of $n_e$ and $T_e$ in the magnetic trap, detailed in sections 7.3.1 and 7.3.2, enable an accurate theoretical calculation of $\omega_{g,e}\tau_e$ based on Coulomb collisions for comparison. The discharge current density $J_D$ can be estimated by measuring the axial current density using laser Thomson scattering in the magnetic trap region ($J_z \approx J_D$); however, these measurements were not performed since they would have required major modifications to the experimental setup. It should be noted that the previous probe studies have not directly measured $J_D$ either, except for Lundin *et al.* [163], instead the spatial distribution of the discharge current was estimated. A similar approach was implemented in this research.

The laser Thomson scattering diagnostic provides a one-dimensional EVDF measurement in the direction of the wavevector $\mathbf{k}$=$\mathbf{k}_s$-$\mathbf{k}_i$. Measurements performed in the magnetic trap with the scattering geometry in the $P2$ configuration were sensitive to the component of the EVDF in the azimuthal direction. A global electron drift velocity ($v_d$) for a

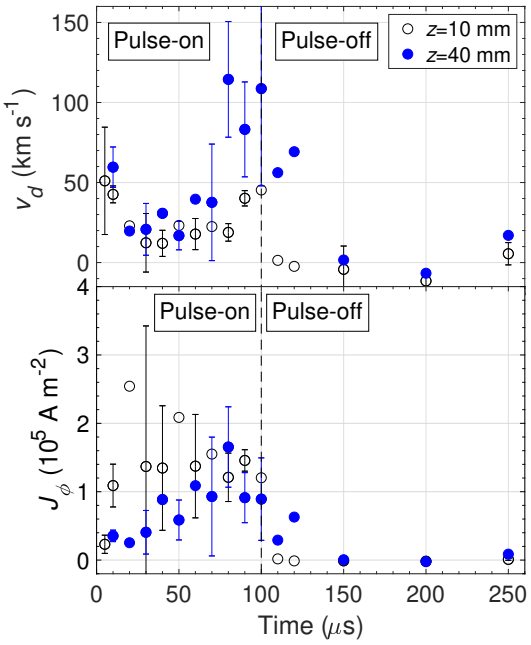


Figure 7.12: Drift velocity ($v_d$) and azimuthal current density ($J_\phi$) as a function of time for discharge conditions of 400 W average power, a 50 Hz repetition rate, a pulse-width of 100 $\mu$s and an argon gas pressure of 1.6 Pa. Measurements were performed at ($r = 41$ mm, $z = 10$ and 40 mm, $P2$).

Maxwellian EVDF is identified by the shift of the centre of the Gaussian spectrum from the laser wavelength $\lambda_i = 532$ nm; this is explained in section 3.2.3.2. In the $P2$ configuration, a positive value of $v_d$ indicates that the azimuthal drift is in the $\mathbf{E} \times \mathbf{B}$ direction.

The drift velocity of the EVDF in the $P2$ configuration was determined by re-analysing the data collected for sections 7.3.1 and 7.3.2 using a CCD pixel bin of 1 in the MATLAB analysis code, rather than 4, to improve the spectral resolution. The spectral resolution with a pixel bin of 4 is $\sim 0.071$ nm; whereas the resolution for a pixel bin of 1 is $\sim 0.020$ nm, which is limited by the 1.15 pixel resolution of the camera intensifier. The resolution of the system in terms of drift velocity is calculated using equation 3.38, which gives a resolution of 8 km·s$^{-1}$ for a pixel bin of 1.

Figure 7.12 shows the azimuthal drift velocity and the azimuthal current density ($J_\phi = en_e v_d$) in the magnetic trap ($r = 41$ mm, $z = 10$ mm and 40 mm, $P2$) for the following discharge conditions: an average power of 400 W, a 50 Hz repetition rate, a pulse-width

of 100 $\mu$s and an argon gas pressure of 1.6 Pa. The error bars, shown for some of the data points, represent the standard deviation from multiple measurements. At the $z = 10$ mm measurement position, there was a positive drift velocity of 10-50 km·s$^{-1}$ during the pulse-on time and no drift velocity during the pulse-off time. A temporal dependence on drift velocity is expected due to the non-steady state electric field generated by the voltage waveform applied to the target. Additional results, not shown here, indicated that the drift velocity at $z = 10$ mm for the other discharge conditions in section 7.3.1 were the same order of magnitude. The results for the $z = 40$ mm position were similar to the $z = 10$ mm position during the start and middle phases of the pulse-on time. Towards the end of the pulse-on time, the drift velocity was $v_d \sim 100$ km·s$^{-1}$, which is double the drift velocity at $z = 10$ mm, and the drift velocity did not tend to zero immediately after pulse termination. The latter implies that the contribution of the diamagnetic, $\nabla\mathbf{B}$ and curvature drifts are important because these are independent of the applied electric field strength. For comparison, the root mean square speed of a one-dimensional Maxwellian EVDF with $T_e = 1$ eV and zero drift velocity is $(k_B T_e/m_e)^{1/2} = 419$ km·s$^{-1}$. Therefore, the thermal speed of the electrons was dominant over the electron drift velocity.

In another laser Thomson scattering study, Tsikata *et al.* [137] measured a drift velocity of the order of 25 km·s$^{-1}$ in the magnetic trap. In this case, the direction of sensitivity for the EVDF measurements had components both parallel and perpendicular to the magnetic field in the target surface-plane. A direct comparison with the results presented in this chapter is, therefore, not possible, but it is noted that the magnitude of the drift velocity is similar.

The azimuthal current density, shown in figure 7.12, was of the order of $10^4 - 10^5$ A·m$^{-2}$, and had both a spatial and temporal dependence. The lower limit is in agreement with measurements performed using magnetic probes by other researchers [163, 164]. The ratio $J_\phi/J_D$ can be calculated once the discharge current density has been estimated. It is assumed that the discharge current flows through each closed magnetic flux surface, and the current is uniformly distributed across the flux surface [130]. The perimeter of the closed flux surfaces for the ($r = 41$ mm, $z = 10$ mm and 40 mm) measurement positions in the radial-height plane of the magnetron are shown in figure 7.13. These were calculated by tracking the path of a test particle, which moves parallel to the magnetic field, from the measurement position to the target surface using MATLAB. The surface area of the flux surface ($A_f$) was calculated by the following line integral along the perimeter ($P$):

$$A_f = \int_P 2\pi r ds, \tag{7.5}$$

where $ds$ is a small length along the perimeter.

Figure 7.14 shows the experimentally determined $J_\phi/J_D$ and the theoretical values of the Hall parameter based on Coulomb collisions between electrons and room temperature, singularly charged ions. The Coulomb collision time was estimated by dividing the mean free path (section 5.2.3.2 for formulae) by the average electron speed: $(8k_BT_e/(\pi m_e))^{1/2}$ for a three-dimensional Maxwellian EVDF [7, p. 37]. Moreover, the electron density and electron temperature were taken from the laser Thomson scattering results in sections 7.3.1 and 7.3.2. The angular frequency of the electron gyration was calculated using $B = 33$ mT and 7.6 mT at $z = 10$ mm and 40 mm, respectively. The results indicate anomalously fast electron transport across the magnetic field at the start of the pulse ($t < 20$ $\mu$s at $z = 10$ mm, $t \leqslant 20$ $\mu$s at $z = 40$ mm), otherwise there is reasonable agreement between the theoretical and experimental curves. For reference, the theoretical Hall parameter corresponding to collisions between electrons and argon neutrals at a temperature of $T_i = 500$ K [153] is $\omega_{g,e}\tau_e > 435$ during $t < 20$ $\mu$s at $z = 10$ mm. The lower limit at $z = 40$ mm during $t \leqslant 20$ $\mu$s is $\omega_{g,e}\tau_e > 100$.

It should be emphasised that the main source of error in the $J_\phi/J_D$ measurements is that the spatial distribution of the discharge current across the magnetic flux surfaces is unknown. Lundin *et al.* [163] have measured local current densities, $J_\phi$ and $J_z$, in a HiPIMS discharge using a Rogowski probe. They propose that the majority of the discharge current passes radially, through the closed flux surfaces, to the anode shield surrounding the target at the start of the pulse, and the relative contribution passing perpendicular to the target surface increases as the pulse progresses. This implies that $J_D$ is overestimated, and hence $J_\phi/J_D$ is underestimated, at the start of the pulse in this research when the electron transport appears anomalously fast. A more accurate estimate of $J_D$ is required in order to draw reliable conclusions from figure 7.14. A relatively simple option is to use a Rogowski probe, but the measurement error is $\sim 50\%$ [163] and they are inherently perturbing: Lundin *et al.* [163] could not place the probe closer than $z = 40$ mm without significantly perturbing the plasma. Laser Thomson scattering measurements of both $J_\phi$ and $J_z \approx J_D$ could be the focus of a future study.

The study using the Rogowski probe [163] found $1.5 < J_\phi/J_D < 12$ above the racetrack for $40 < z$[mm]$< 80$, which indicates faster transport across the magnetic field than Bohm

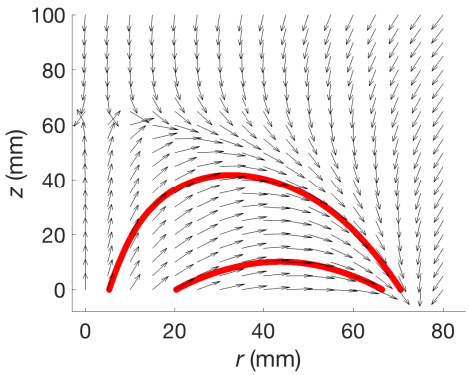


Figure 7.13: Magnetic field configuration of the unbalanced planar magnetron in the radial-height ($r - z$) plane. The arrows show the direction of the magnetic field rather than its magnitude. The origin of the system corresponds to the centre of the target surface. The closed magnetic flux surfaces passing through ($r = 41$ mm, $z = 10$ and 40 mm) are highlighted. The area of these surfaces were $A_f = 0.0140$ m$^2$ and 0.0256 m$^2$, respectively.

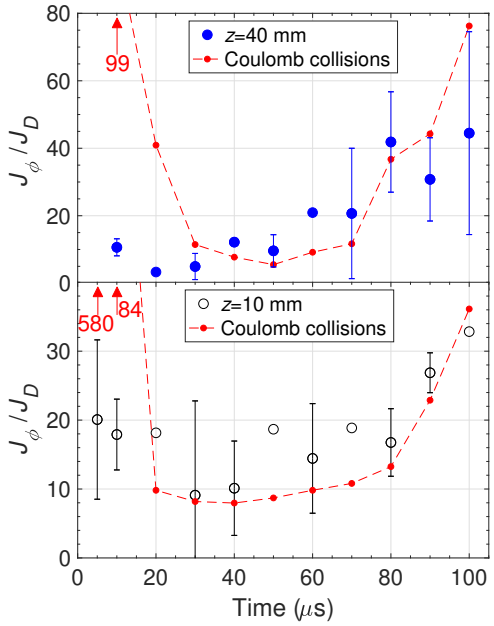


Figure 7.14: Ratio of the azimuthal and discharge current densities as a function of time for discharge conditions of 400 W average power, a 50 Hz repetition rate, a pulse-width of 100 $\mu$s and an argon gas pressure of 1.6 Pa. Measurements were performed at ($r = 41$ mm, $z = 10$ mm and 40 mm, $P2$). The theoretical Hall parameter based on electron-ion Coulomb collisions is plotted for comparison.

diffusion ($\omega_{g,e}\tau_e \equiv 16$). This is consistent with other HiPIMS investigations [120, 162, 164], where the spatial distribution of the discharge current density was estimated. These studies have concluded that the cross-magnetic field transport is anomalously fast given a theoretical Hall parameter of $\omega_{g,e}\tau_e \approx 15$ based on Coulomb collisions [162].

The results of this research, however, gave larger values of the experimentally determined Hall parameter: $J_\phi/J_D \gtrsim 10$. Moreover, the temporal evolution of the theoretical Hall parameter based on Coulomb collisions, from accurate laser Thomson scattering measurements, was compared to $J_\phi/J_D$ for the first time in the magnetic trap, showing reasonable agreement. This was also the case for the additional results, not shown here, from the different discharge conditions in section 7.3.1.

A tentative conclusion from this study, in contrast to the previous work, is that the cross-magnetic field transport of electrons in HiPIMS discharges is explained by classical theory based on Coulomb collisions. As discussed above, laser Thomson scattering measurements of $J_z \approx J_D$ are required to verify this.

## 7.5 Conclusion

The aim of the research in this chapter was to provide a detailed overview of electron dynamics in HiPIMS discharges. Laser Thomson scattering was used to determine the electron temperature and electron density. The main advantages of laser Thomson scattering are that it is a non-intrusive technique, and it provides a direct localised-measurement of the electron velocity distribution function (EVDF); therefore, data interpretation is straightforward. The disadvantages are that the measurements are insensitive to high temperature electron populations at low density, and the experimental setup is expensive and complicated. This study was the first spatio-temporal resolved survey, including measurements inside and outside of the last closed flux surface boundary, of both electron temperature and electron density. In addition, optical emission spectroscopy measurements were performed to provide information about excited atomic and ionic states. By combining these two diagnostics, a better understanding of electron-heavy species interactions was obtained.

The magnetron, equipped with a tungsten target, was operated at an average power of 400 W with a pulse repetition rate of 50 Hz, using a commercial HiPIMS power supply. The pulse-width of the target voltage waveform (50 $\mu$s, 100 $\mu$s and 200 $\mu$s) and the argon gas pressure (0.8 Pa and 1.6 Pa) were varied for measurements performed at a single location in the magnetic trap and at a single substrate position. This was the first study to investigate

the effect of discharge conditions on both electron temperature and electron density in the magnetic trap using a non-intrusive diagnostic. Axial spatial-scans were also performed above the racetrack region and along the centre axis for a single set of discharge conditions (100 $\mu$s pulse-width, 1.6 Pa).

The main outcome from this research is experimental confirmation of the expected features of HiPIMS discharges using the reliable laser Thomson scattering technique, and thereby providing a solid basis for conclusions drawn by others. These general features include: an electron density of $n_e = 10^{19} - 10^{20}$ m$^{-3}$ in the magnetic trap; a greater electron density above the racetrack region compared to the centre axis; a more uniform distribution of electron density farther from the target; a greater electron density as instantaneous discharge power increases; a greater electron temperature as argon gas pressure decreases; and a lower electron temperature as both the emission intensity from metal species and the electron density increase due to EVDF cooling via inelastic collisions. In addition, the laser Thomson scattering results may be useful for HiPIMS modelling, whether as an input or for benchmarks.

There have been extensive reports of intrusive Langmuir probe measurements at a typical substrate position in the literature. The laser Thomson scattering measurements in this research have verified some of the trends observed by the probes. These include: a peak in electron temperature at the start of the pulse, followed by EVDF cooling; a double-peak structure in a temporal profile of electron density; and a slow long-term decay of the electron density during the pulse-off period. The electron density exceeded that of DC magnetron operation ($n_e \leqslant 10^{17}$ m$^{-3}$) for, at least, hundreds of microseconds in the pulse-off period. During this time, a substrate will continue to receive substantial ion bombardment, which is beneficial for film properties.

The laser Thomson scattering measurements, however, were unable to confirm the presence of multiple electron populations in the discharge, which were detected in previous probe studies by other researchers. Future laser Thomson scattering experiments could investigate this possibility by using longer data integration times and a detection system with a wider spectral range. Furthermore, higher resolution measurements, both temporally and spatially in the radial direction, are required to investigate the origin of the first electron density peak at the substrate position. A final point is that for the lowest pressure discharge (0.8 Pa) at the substrate position, the maximum in electron density did not correlate well with the temporal location of the electron temperature minimum during the pulse-on time, unlike the other higher pressure discharges. This could be investigated

further by performing axial spatial-scans for the lower pressure conditions.

Another aim of this research was to investigate the cross-magnetic field transport rate of electrons. This was assessed by calculating the ratio between the azimuthal and discharge current densities ($J_\phi/J_D$) above the racetrack region. Laser Thomson scattering was used to provide the first non-intrusive measurement of $J_\phi$ in a HiPIMS discharge; however, the experimental setup in this study could not be easily configured for measurements of $J_D$ so this parameter had to be estimated. A tentative conclusion from this research is that the cross-magnetic field transport rate of electrons is consistent with classical theory based on Coulomb collisions. In contrast, previous studies concluded that the electron transport was anomalously fast. Future laser Thomson scattering measurements of $J_D$ could resolve this disagreement.

# Chapter 8

# Conclusions & future work

## 8.1 Summary and main conclusions

The research in this thesis was about two main topics: a diagnostic comparison study in weakly magnetised plasma involving Langmuir probes and laser Thomson scattering in chapters 5 and 6, and an investigation of electron dynamics in high power impulse magnetron sputtering (HiPIMS) using a combination of laser Thomson scattering and optical emission spectroscopy (OES) in chapter 7.

The aim of the first part of the research was to assess the reliability of unmagnetised Langmuir probe theories for electron plasma property measurements in weakly magnetised plasma. In this regime, electrons are the only magnetised species in the plasma. The plasma source for the investigation was a magnetron, which was operated using two separate power supplies in order to cover a wide electron density range: a lower-density DC mode ($10^{16} < n_e[\mathrm{m}^{-3}] \lesssim 10^{17}$) and HiPIMS ($n_e \lesssim 10^{20}$ m$^{-3}$). The discharge physics of these two modes of operation is significantly different because the HiPIMS discharge undergoes a transition from being dominated by background gas species to a metal-rich plasma during the pulse-on time. The DC mode, on the other hand, is dominated by background gas processes. The maximum magnetic field strength at a measurement position was $B = 33$ mT.

A laser Thomson scattering system was designed and installed on the magnetron rig to benchmark the Langmuir probe measurements. The advantages of laser Thomson scattering are that data interpretation is straightforward and independent of magnetic field strength; it is a non-intrusive technique; it provides measurements of both electron density

and electron temperature; and the spatial resolution of the system in this research was comparable to the probe tip length. The disadvantages are that the measurements are insensitive to high temperature electron populations at low density, and a complicated and expensive experimental setup is required. Consequently, laser Thomson scattering is not routinely applied to discharge plasmas. Previous investigations assessing the reliability of Langmuir probe measurements in weakly magnetised plasma did not use a non-intrusive diagnostic for comparison, rather different Langmuir probe theories were compared.

In chapter 5, the results of the time-resolved diagnostic comparison study in HiPIMS discharges were presented. The electron temperature and electron density measurements had good agreement when the magnetic field strength was negligible at the measurement position ($B \lesssim 1$ mT). Measurements were also performed at a position in the magnetic trap, where the magnetic field strength was significant for electron magnetisation ($B = 33$ mT). In this case, the current-voltage characteristics measured by the probe were distorted. Nevertheless, careful analysis of the probe data resulted in reasonable electron temperature agreement during the pulse-on time. Moreover, the probe determined electron density was only a factor of $\sim 2.5$ lower than the laser Thomson scattering results during this period. During the pulse-off time, the electron temperature in the discharge decreased; consequently, electrons became more magnetised and the accuracy of the Langmuir probe measurements degraded.

The research in chapter 5 demonstrated that Langmuir probe measurements can provide reasonable estimates of both electron temperature and electron density during the pulse-on time of HiPIMS discharges, including in the magnetic trap. This is a significant outcome because previous investigations of HiPIMS discharges using Langmuir probes were generally restricted to regions where the magnetic field strength was insignificant for electron magnetisation, due to the difficulty of interpreting probe data and concerns over plasma perturbation.

In chapter 6, the results of the diagnostic comparison study in DC magnetron discharges were presented. When the magnetic field strength was negligible at the measurement position ($B \lesssim 1$ mT), there was reasonable electron temperature agreement; however, the plasma density determined from the Langmuir probe measurements, using both ion and electron collection theories, was up to an order of magnitude lower than the laser Thomson scattering results. In regions of higher magnetic field strength, the Langmuir probe did not provide an accurate electron temperature for characterising the bulk population of electrons, but the agreement between the diagnostics for electron density measurements

improved. The latter was unexpected and is opposite to the trend that was observed in the HiPIMS comparison study of chapter 5, where the best agreement for electron density measurements was when the magnetic field strength was negligible. In addition, the low energy part of the electron energy distribution function determined by the probe was depleted at all of the measurement positions during DC magnetron operation.

The conclusion from the results in chapters 5 and 6 was that a significant plasma perturbation was induced by the probe stem during DC magnetron operation, but this effect was not observed in HiPIMS discharges for an unknown reason that may be linked to the shorter Debye length in the higher-density pulsed discharge and the different discharge physics of the two operating modes. The Langmuir probe is a standard laboratory diagnostic so understanding its limitations is of significant interest. Future work could investigate whether the large discrepancies reported in this research are unique to the magnetron by repeating the comparison study using a different weakly magnetised discharge, which can produce a wide plasma density range without changing the plasma generation technique.

The aim of the second part of the research was to provide a comprehensive overview of electron dynamics in HiPIMS discharges using a combination of laser Thomson scattering and optical emission spectroscopy. These results were presented in chapter 7. The novelty of this research was performing electron plasma property measurements both inside and outside of the last closed flux surface boundary using the reliable laser Thomson scattering technique. Moreover, this was the first study to investigate the dependence on discharge conditions of both electron temperature and electron density in the magnetic trap region, which is located inside of the last closed flux surface boundary, using a non-intrusive technique. In addition, OES measurements were performed to provide information about excited atomic and ionic states in the plasma. The interpretation of this data benefited from knowledge of the electron plasma properties.

The results showed that a dense plasma ($n_e = 10^{19} - 10^{20}$ m$^{-3}$) was generated in the magnetic trap, which propagated in the axial direction towards a typical substrate position. A strong emission signal from metal ions was associated with a high electron density and low electron temperature. This indicates a high metal ion density in the propagating electron density wave, and cooling of the electron energy distribution function due to inelastic collisions between electrons and metal species. During the pulse-off period, the electron density had a slow decay throughout the discharge. A substrate would continue to receive substantial ion bombardment for at least hundreds of microseconds after the termination of the discharge voltage pulse, which is beneficial for producing high-density

films with a columnar-less microstructure.

The main outcomes from the research in chapter 7 were experimental confirmation of the expected features of HiPIMS discharges and validation of trends identified by Langmuir probe studies at a typical substrate position. The laser Thomson scattering results give a solid basis for more wide ranging studies. An aside, a tentative conclusion from the laser Thomson scattering results is that the cross-magnetic field transport of electrons in HiPIMS discharges is consistent with classical theory based on Coulomb collisions. In contrast to this work, previous studies using intrusive diagnostics found that the electron cross-magnetic field transport rate was anomalously fast. Further laser Thomson scattering experiments, using a different scattering geometry to this research, are required to investigate this discrepancy.

## 8.2 Future work

Several suggestions for future work that are directly related to the research presented in this thesis are discussed below:

- Large discrepancies for electron property measurements made by Langmuir probes and laser Thomson scattering in DC magnetron discharges were reported in this research. This has motivated the need for similar studies to be carried out in other types of weakly magnetised plasma sources. An inductively coupled plasma (ICP) with an external magnetic field would be a suitable environment for several reasons: (i) previous comparison studies using an ICP in the absence of an external magnetic field found reasonable agreement between the diagnostics for electron temperature and electron density measurements [35–37]; (ii) the electron density in these devices is $n_e = 10^{17} - 10^{18}$ m$^{-3}$, and so the lower limit is comparable to the DC magnetron; (iii) the external magnetic field is not essential for igniting/sustaining the discharge so there is a lot of flexibility regarding the magnetic field configuration.

- HiPIMS produces a significant metal ion density in the bulk plasma, and the characteristic energy of a sputtered atom or ion is of the order of an electronvolt. In this research, both the ionic abundance in the plasma and the ion energy distribution function of each species was unknown. Therefore, the accuracy of ion collection theories for plasma density measurements by a Langmuir probe could not be assessed in HiPIMS discharges. A future diagnostic comparison study, involving Langmuir

probes for plasma density measurements, could use a mass spectrometer to determine these unknown quantities.

- There have been reports of Langmuir probe measurements at a typical substrate position being consistent with non-Maxwellian electron velocity distribution functions (EVDFs) during the pulse-on time of HiPIMS discharges (section 2.3.3.3). Moreover, accurate measurements of the EVDF in the magnetic trap region using a Langmuir probe are difficult due to the relatively strong magnetic field for electron magnetisation. Laser Thomson scattering could verify the probe results and explore the possibility of non-Maxwellian EVDFs in the magnetic trap region. This would require longer data integration times and a wider spectral range covered by the detector, compared to the experiments performed in this research.

- In this research, the cross-magnetic field transport rate of electrons in HiPIMS discharges was assessed by calculating the ratio of the azimuthal to discharge current densities ($J_\phi/J_D$). Laser Thomson scattering can provide direct measurements of the current densities, but each component requires rearrangement of the scattering geometry. In this research, only $J_\phi$ was directly measured and so $J_D$ was estimated. The results, however, were not consistent with previous studies, which had used intrusive diagnostics. Future work could develop a laser Thomson scattering system that can readily measure both current density components.

## 8.3 Outlook

Each plasma diagnostic has its own strengths and weaknesses in terms of measurement accuracy/sensitivity and practical considerations, such as cost and the complexity of the experimental setup. It is desirable to implement a variety of diagnostic techniques in each study, and perform plasma modelling, in order to improve the credibility of conclusions. Often, however, researchers do not have the luxury of corroboration so they are reliant on the results from only a single diagnostic. For this reason, dedicated comparison studies for assessing the accuracy of standard laboratory diagnostics are of great value to the plasma physics community. A reliable benchmark diagnostic is necessary for these comparison studies, and in general, these are more expensive, and require more effort to design and operate compared to standard diagnostics.

The outcome from this type of comparison study is either it provides a solid foundation for the modelling of plasma behaviour based on the results from standard diagnostics; or it highlights the limitations of studies, including their conclusions, which are reliant on standard diagnostics. As demonstrated by this research and in previous studies, the conclusions drawn from a diagnostic comparison study cannot be arbitrarily extended to completely different discharge conditions or a different type of plasma source. For this reason, it is hoped that there will be an increase in the number of diagnostic comparison studies in the future because, at present, there have been relatively few. Without reliable experimental measurements, it is difficult to draw deep conclusions about the discharge physics.

In the past two years, there has been the first reports of reliable electron plasma property measurements in the magnetic trap region of HiPIMS discharges through the application of THz time-domain spectroscopy [136] and laser Thomson scattering [2, 137]. A next step is to compare the experimentally determined electron density, electron temperature and electron energy distribution function with numerical models and simulations. Obvious beneficiaries would be studies that investigate the metal ionisation fraction and electron heating mechanisms. Moreover, models could be developed as to accept spatio-temporal resolved experimental data as an input. This would be useful because self-consistent dimensional models incorporating metal into the plasma for a typical HiPIMS pulse-width are still under development.

One of the key challenges of HiPIMS is improving the deposition rate whilst maintaining a high ionised flux fraction at the substrate. A better understanding of the spokes phenomenon would help to achieve this because of the intrinsic link to the ion dynamics. There have been no direct measurements of the electron plasma properties inside a spoke yet. A future project could investigate the potential of a single-shot laser Thomson scattering system for this purpose. The expected electron density inside a spoke ($n_e \sim 10^{20}$ $\mathrm{m}^{-3}$) is comparable to that found in magnetic confinement fusion devices, where single-laser-shot Thomson scattering systems are utilised (e.g. [72]). A final point is that the novel application of a positive voltage to the target immediately after termination of the conventional HiPIMS (negative) pulse has been shown to increase the deposition rate and improve film properties [172]. Detailed plasma characterisation during the positive 'kick pulse' has not been performed yet, which is important for gaining a better understanding of the ion transport, and ultimately, optimising the discharge parameters. Laser Thomson scattering could be employed for this purpose.

# Bibliography


1. Ryan, P. J., Bradley, J. W. & Bowden, M. D. Comparison of Langmuir probe and laser Thomson scattering for electron property measurements in magnetron discharges. *Physics of Plasmas* **26,** 073515 (2019).
2. Ryan, P. J., Bradley, J. W. & Bowden, M. D. Comparison of Langmuir probe and laser Thomson scattering for plasma density and electron temperature measurements in HiPIMS plasma. *Physics of Plasmas* **26,** 040702 (2019).
3. Bräuer, G., Szyszka, B., Vergöhl, M. & Bandorf, R. Magnetron sputtering - Milestones of 30 years. *Vacuum* **84,** 1354 (2010).
4. Langmuir, I. Oscillations in ionized gases. *Proceedings of the National Academy of Sciences of the United States of America* **14,** 627 (1928).
5. Chen, F. *Introduction to Plasma Physics and Controlled Fusion* Third edition (Springer, Cham, 2015).
6. Piel A. *Plasma Physics: an Introduction to Laboratory, Space, and Fusion Plasmas* Second edition (Springer International Publishing AG, Cham, 2017).
7. Lieberman, M. A. & Lichtenberg, A. J. *Principles of Plasma Discharges and Materials Processing* Second edition (Wiley, Hoboken, 2005).
8. Laroussi, M., Lu, X. & Keidar, M. Perspective: The physics, diagnostics, and applications of atmospheric pressure low temperature plasma sources used in plasma medicine. *Journal of Applied Physics* **122,** 020901 (2017).
9. Penkov, O. V., Khadem, M., Lim, W.-S. & Kim, D.-E. A review of recent applications of atmospheric pressure plasma jets for materials processing. *Journal of Coatings Technology and Research* **12,** 225 (2015).

10. Kelly, P. J. & Arnell, R. D. Magnetron sputtering: a review of recent developments and applications. *Vacuum* **56,** 159 (2000).

11. Wagenaars, E. *Plasma breakdown of low-pressure gas discharges* PhD thesis (Eindhoven University of Technology, 2006).

12. Simon, A. H. *Handbook of Thin Film Deposition: Sputter Processing* Fourth edition (eds Seshan, K. & Schepis, D.) chap. 7 (William Andrew Publishing, Oxford, 2018).

13. Von Keudell, A. & Schulz-Von der Gathen, V. Foundations of low-temperature plasma physics - an introduction. *Plasma Sources Science and Technology* **26,** 113001 (2017).

14. Gueron, S. & Deutsch, M. A fast Abel inversion algorithm. *Journal of Applied Physics* **75,** 4313 (1994).

15. Gudmundsson, J. T., Brenning, N., Lundin, D. & Helmersson, U. High power impulse magnetron sputtering discharge. *Journal of Vacuum Science & Technology A* **30** (2012).

16. Langmuir, I. The pressure effect and other phenomena in gaseous discharges. *Journal of the Franklin Institute* **196,** 751 (1923).

17. Mott-Smith, H. M. & Langmuir, I. The theory of collectors in gaseous discharges. *Physical Review* **28,** 727 (1926).

18. Swift, J. D. & Schwar, M. J. R. *Electrical Probes for Plasma Diagnostics* (Iliffe Books Ltd., London, 1970).

19. Chung, P., Talbot, L. & Touryan, K. J. *Electric probes in stationary and flowing plasmas: theory and application* (Springer-Verlag, New York, 1975).

20. Godyak, V. A., Piejak, R. B. & Alexandrovich, B. M. Measurements of electron energy distribution in low-pressure RF discharges. *Plasma Sources Science and Technology* **1,** 36 (1992).

21. Tichý, M., Kudrna, P., Behnke, J., Csambal, C. & Klagge, S. Langmuir Probe Diagnostics for Medium Pressure and Magnetised Low-Temperature Plasma. *Journal de Physique IV Colloque* **7,** C4–397 (1997).

22. Bryant, P., Dyson, A. & Allen, J. E. Langmuir probe measurements of weakly collisional electropositive RF discharge plasmas. *Journal of Physics D: Applied Physics* **34,** 1491 (2001).

23. Allen, J. E., Boyd, R. L. F. & Reynolds, P. The Collection of Positive Ions by a Probe Immersed in a Plasma. *Proceedings of the Physical Society. Section B* **70,** 297 (1957).

24. Chen, F. F. Numerical computations for ion probe characteristics in a collisionless plasma. *Journal of Nuclear Energy. Part C* **7,** 47 (1965).

25. Laframboise, J. G. *Theory of spherical and cylindrical Langmuir probes in a collisionless, Maxwellian plasma at rest* tech. rep. UTIAS Report No. 100 (University of Toronto, 1966).

26. Andersson, L. *et al.* The Langmuir Probe and Waves (LPW) Instrument for MAVEN. *Space Science Reviews* **195,** 173 (2015).

27. Matthews, G. F. Tokamak plasma diagnosis by electrical probes. *Plasma Physics and Controlled Fusion* **36,** 1595 (1994).

28. Chen, F. F., Evans, J. D. & Zawalski, W. Calibration of Langmuir probes against microwaves and plasma oscillation probes. *Plasma Sources Science and Technology* **21,** 055002 (2012).

29. Neumann, G., Bänziger, U., Kammeyer, M. & Lange, M. Plasma-density measurements by microwave interferometry and Langmuir probes in an rf discharge. *Review of Scientific Instruments* **64,** 19 (1993).

30. Hopwood, J., Guarnieri, C. R., Whitehair, S. J. & Cuomo, J. J. Langmuir probe measurements of a radio frequency induction plasma. *Journal of Vacuum Science & Technology A* **11,** 152 (1993).

31. Tuszewski, M. & Tobin, J. A. The accuracy of Langmuir probe ion density measurements in low-frequency RF discharges. *Plasma Sources Science and Technology* **5,** 640 (1996).

32. Sudit, I. D. & Woods, R. C. A study of the accuracy of various Langmuir probe theories. *Journal of Applied Physics* **76,** 4488 (1994).

33. Shih, C. H. & Levi, E. Effect of Collisions on Cold Ion Collection by Means of Langmuir Probes. *AIAA Journal* **9,** 1673 (1971).

34. Overzet, L. J. & Hopkins, M. B. Comparison of electron-density measurements made using a Langmuir probe and microwave interferometer in the Gaseous Electronics Conference reference reactor. *Journal of applied physics* **74,** 4323 (1993).

35. Bowden, M. D. *et al.* Comparison of electron property measurements in an inductively coupled plasma made by Langmuir probe and laser Thomson scattering techniques. *Journal of Vacuum Science & Technology A* **17,** 493 (1999).

36. Moshkalyov, S. A., Thompson, C., Morrow, T. & Graham, W. G. Diagnostic of rf discharge plasma by Thomson scattering with gated intensified charge coupled device detectors. *Journal of Vacuum Science & Technology A* **18,** 1395 (2000).

37. Noguchi, M. *et al.* Comparative studies of the laser Thomson scattering and Langmuir probe methods for measurements of negative ion density in a glow discharge plasma. *Plasma Sources Science and Technology* **12,** 403 (2003).

38. Field, D., Dew, S. & Burrell, R. Spatial survey of a magnetron plasma sputtering system using a Langmuir probe. *Journal of Vacuum Science & Technology A* **20,** 2032 (2002).

39. Vetushka, A. & Ehiasarian, A. P. Plasma dynamic in chromium and titanium HIPIMS discharges. *Journal of Physics D: Applied Physics* **41,** 015204 (2007).

40. Singh, S. B., Chand, N. & Patil, D. S. Langmuir probe diagnostics of microwave electron cyclotron resonance (ECR) plasma. *Vacuum* **83,** 372 (2008).

41. Rossnagel, S. M. & Kaufman, R. Induced drift currents in circular planar magnetrons. *Journal of Vacuum Science & Technology A* **5,** 88 (1987).

42. Bradley, J. W., Thompson, S. & Gonzalvo, Y. A. Measurement of the plasma potential in a magnetron discharge and the prediction of the electron drift speeds. *Plasma Sources Science and Technology* **10,** 490 (2001).

43. Simon, A. Ambipolar diffusion in a magnetic field. *Physical Review* **98,** 317 (1955).

44. Dote, T., Amemiya, H. & Ichimiya, T. Effect of a Magnetic Field upon the Saturation Electron Current of an Electrostatic Probe. *Japanese Journal of Applied Plasma Physics* **3,** 789 (1964).

45. Passoth, E. *et al.* An experimental study of plasma density determination by a cylindrical Langmuir probe at different pressures and magnetic fields in a cylindrical magnetron discharge in heavy rare gases. *Journal of Physics D: Applied Physics* **30,** 1763 (1997).

46. Tagle, J. A., Stangeby, P. C. & Erents, S. K. Errors in measuring electron temperatures using a single Langmuir probe in a magnetic field. **29,** 297 (1987).

47. Laframboise, J. G. & Rubinstein, J. Theory of a cylindrical probe in a collisionless magnetoplasma. *Physics of Fluids* **19,** 1900 (1976).

48. Usoltceva, M. *et al.* Effective collecting area of a cylindrical Langmuir probe in magnetized plasma. *Physics of Plasmas* **25,** 063518 (2018).

49. Bohm, D., Burhop, E. H. & Massey, H. S. *Characteristics of Electrical Discharges in Magnetic Fields* (eds Guthrie, A. & Wakerling, R. K.) chap. 2 (McGraw-Hill, New York, 1949).

50. Stangeby, P. C. Effect of bias on trapping probes and bolometers for Tokamak edge diagnosis. *Journal of Physics D: Applied Physics* **15,** 1007 (1982).

51. Guenther, K., Herrmann, A., Laux, M., Pech, P. & Reiner, H. D. Characteristics of electric probes in the tokamak SOL: influences of the magnetic field. *Journal of Nuclear Materials* **176,** 236 (1990).

52. Stangeby, P. C. Determination of $T_e$ from a Langmuir probe in a magnetic field by directly measuring the probe's sheath drop using a pin-plate probe. *Plasma Physics and Controlled Fusion* **37,** 1337 (1995).

53. Binwal, S., Gandhi, S., Kabariya, H. & Karkari, S. Parametric study of a pin-plane probe in moderately magnetized plasma. *Measurement Science and Technology* **26,** 125015 (2015).

54. Pitts, R. A. & Stangeby, P. C. Experimental tests of Langmuir probe theory for strong magnetic fields. *Plasma Physics and Controlled Fusion* **32,** 1237 (1990).

55. Sudit, I. D. & Chen, F. F. RF compensated probes for high-density discharges. *Plasma Sources Science and Technology* **3,** 162 (1994).

56. Spolaore, M. *et al.* Automatic Langmuir probe measurement in a magnetron sputtering system. *Surface and Coatings Technology* **116,** 1083 (1999).

57. Kudrna, P. & Passoth, E. Langmuir Probe Diagnostics of a Low Temperature Non-Isothermal Plasma in a Weak Magnetic Field. *Contributions to Plasma Physics* **37,** 417 (1997).

58. Annaratone, B. M., Allen, M. W. & Allen, J. E. Ion currents to cylindrical Langmuir probes in RF plasmas. *Journal of Physics D: Applied Physics* **25,** 417 (1992).

59. Brown, I. G., Compher, A. B. & Kundel, W. B. Response of a Langmuir Probe in a Strong Magnetic Field. *Physics of Fluids* **14,** 1377 (1971).

60. Okamoto, A., Kado, S., Iida, Y. & Tanaka, S. Comparison of langmuir probe and laser thomson scattering methods in the electron temperature measurement in divertor simulator MAP-II. *Contributions to Plasma Physics* **46,** 416 (2006).

61. Bowden, M. D. *et al.* Study of the effect of a probe on the plasma in the source region of an electron cyclotron resonance discharge. *Journal of Vacuum Science & Technology A* **11,** 2893 (1993).

62. Maurmann, S., Kadetov, V. A., Khalil, A. A. I., Kunze, H. J. & Czarnetzki, U. Thomson scattering in low temperature helium plasmas of a magnetic multipole plasma source. *Journal of Physics D: Applied Physics* **37,** 2677 (2004).

63. Van der Meiden, H. *Thomson scattering on low and high temperature plasmas* PhD thesis (Eindhoven University of Technology, 2011).

64. Prunty, S. L. A primer on the theory of Thomson scattering for high-temperature fusion plasmas. *Physica Scripta* **89,** 128001 (2014).

65. Bílková, P. *et al.* Scaling Thomson scattering to big machines. *Journal of Instrumentation* **11,** C03023 (2016).

66. Van de Sande, M. J. *Laser scattering on low temperature plasmas-high resolution and stray light rejection* PhD thesis (Eindhoven University of Technology, 2002).

67. Evans, D. E. & Katzenstein, J. Laser light scattering in laboratory plasmas. *Reports on Progress in Physics* **32,** 207 (1969).

68. Muraoka, K. & Kono, A. Laser Thomson scattering for low-temperature plasmas. *Journal of Physics D: Applied Physics* **44,** 043001 (2011).

69. Carbone, E. & Nijdam, S. Thomson scattering on non-equilibrium low density plasmas: principles, practice and challenges. *Plasma Physics and Controlled Fusion* **57,** 014026 (2015).

70. Bowden, M. D. *et al.* Detection limit of laser Thomson scattering for low density discharge plasmas. *Japanese Journal of Applied Physics* **38,** 3723 (1999).

71. Peacock, N. J., Robinson, D. C., Forrest, M. J., Wilcock, P. D. & Sannikov, V. V. Measurement of the Electron Temperature by Thomson Scattering in Tokamak T3. *Nature* **224,** 488 (1969).

72. Scannell, R. *et al.* A 130 point Nd:YAG Thomson scattering diagnostic on MAST. *Review of Scientific Instruments* **81,** 10D520 (2010).

73. Uchino, K., Muraoka, T., Muraoka, K. & Akazaki, M. Studies of an impulse breakdown process in an atmospheric air using ruby-laser scattering diagnostics. *Japanese Journal of Applied Physics* **21,** L696 (1982).

74. Sakoda, T. *et al.* Thomson scattering diagnostics of an ECR processing plasma. *Japanese Journal of Applied Physics* **30,** L1425 (1991).

75. Muraoka, K., Uchino, K. & Bowden, M. D. Diagnostics of low-density glow discharge plasmas using Thomson scattering. *Plasma Physics and Controlled Fusion* **40,** 1221 (1998).

76. ElSabbagh, M. A. M., Koyama, H., Bowden, M. D., Uchino, K. & Muraoka, K. A laser Thomson scattering system for low density glow discharge plasmas. *Japanese Journal of Applied Physics* **40,** 1465 (2001).

77. Kurzan, B. & Murmann, H. D. Edge and core Thomson scattering systems and their calibration on the ASDEX Upgrade tokamak. *Review of Scientific Instruments* **82,** 103501 (2011).

78. Maslov, M., Beurskens, M. N. A., Kempenaars, M. & Flanagan, J. Status of the JET LIDAR Thomson scattering diagnostic. *Journal of Instrumentation* **8,** C11009 (2013).

79. Vincent, B., Tsikata, S., Mazouffre, S., Minea, T. & Fils, J. A compact new incoherent Thomson scattering diagnostic for low-temperature plasma studies. *Plasma Sources Science and Technology* **27,** 055002 (2018).

80. Helmersson, U., Lattemann, M., Bohlmark, J., Ehiasarian, A. P. & Gudmundsson, J. T. Ionized physical vapor deposition (IPVD): A review of technology and applications. *Thin Solid Films* **513,** 1 (2006).

81. Anders, A. Tutorial: Reactive high power impulse magnetron sputtering (R-HiPIMS). *Journal of Applied Physics* **121,** 171101 (2017).

82. Serikov, V. V. & Nanbu, K. Monte Carlo numerical analysis of target erosion and film growth in a three-dimensional sputtering chamber. *Journal of Vacuum Science & Technology A* **14,** 3108 (1996).

83. Goehlich, A., Niemöller, N. & Döbele, H. F. Determination of angle resolved velocity distributions of sputtered tungsten atoms. *Journal of Nuclear Materials* **266,** 501 (1999).

84. Thompson, M. W. The energy spectrum of ejected atoms during the high energy sputtering of gold. *Philosophical Magazine* **18,** 377 (1968).

85. Rossnagel, S. M. & Cuomo, J. J. Ion beam bombardment effects during films deposition. *Vacuum* **38,** 73 (1988).

86. Colligon, J. S. Energetic condensation: Processes, properties, and products. *Journal of Applied Physics* **13,** 1649 (1995).

87. Wang, Z., Zhang, D., Ke, P., Liu, X. & Wang, A. Influence of Substrate Negative Bias on Structure and Properties of TiN Coatings Prepared by Hybrid HIPIMS Method. *Journal of Materials Science and Technology* **31,** 37 (2015).

88. Velicu, I. L. *et al.* Enhanced properties of tungsten thin films deposited with a novel HiPIMS approach. *Applied Surface Science* **424,** 397 (2017).

89. Hagstrum, H. D. Theory of auger ejection of electrons from metals by ions. *Physical Review* **96,** 336 (1954).

90. Anders, A., Andersson, J. & Ehiasarian, A. High power impulse magnetron sputtering: Current-voltage-time characteristics indicate the onset of sustained self-sputtering. *Journal of Applied Physics* **102,** 113303 (2007).

91. Window, B. & Savvides, N. Unbalanced dc magnetrons as sources of high ion fluxes. *Journal of Vacuum Science & Technology A* **4,** 453 (1986).

92. Rossnagel, S. M. & Kaufman, H. R. Langmuir probe characterization of magnetron operation. *Journal of Vacuum Science & Technology A* **4,** 1822 (1986).

93. Sheridan, T. E., Goeckner, M. J. & Goree, J. Observation of two-temperature electrons in a sputtering magnetron plasma. *Journal of Vacuum Science & Technology A* **9,** 688 (1991).

94. Seo, S.-H., In, J.-H. & Chang, H.-Y. Measurements of electron energy distribution functions and electron transport in the downstream region of an unbalanced dc magnetron discharge. *Plasma Sources Science and Technology* **13,** 409 (2004).

95. Kelly, P. J., Abu-Zeid, O. A., Arnell, R. D. & Tong, J. The deposition of aluminium oxide coatings by reactive unbalanced magnetron sputtering. *Surface and Coatings Technology* **86,** 28 (1996).

96. Kouznetsov, V., Macák, K., Schneider, J. M., Helmersson, U. & Petrov, I. A novel pulsed magnetron sputter technique utilizing very high target power densities. *Surface and Coatings Technology* **122,** 290 (1999).

97. Hopwood, J. & Qian, F. Mechanisms for highly ionized magnetron sputtering. *Journal of Applied Physics* **78,** 758 (1995).

98. Bohlmark, J., Gudmundsson, J. T., Alami, J., Latteman, M. & Helmersson, U. Spatial electron density distribution in a high-power pulsed magnetron discharge. *IEEE Transactions on Plasma Science* **33,** 346 (2005).

99. Bohlmark, J., Alami, J., Christou, C., Ehiasarian, A. P. & Helmersson, U. Ionization of sputtered metals in high power pulsed magnetron sputtering. *Journal of Vacuum Science & Technology A* **23,** 18 (2005).

100. Samuelsson, M. *et al.* On the film density using high power impulse magnetron sputtering. *Surface and Coatings Technology* **205,** 591 (2010).

101. Munteanu, D. *et al.* Enhanced properties of tungsten thin films deposited with a novel HiPIMS approach. *Applied Surface Science* **424,** 397 (2017).

102. Alami, J., Bolz, S. & Sarakinos, K. High power pulsed magnetron sputtering: Fundamentals and applications. *Journal of Alloys and Compounds* **483,** 530 (2009).

103. Alami, J. *et al.* Phase tailoring of Ta thin films by highly ionized pulsed magnetron sputtering. *Thin Solid Films* **515,** 3434 (2007).

104. Ehiasarian, A. P., Wen, J. G. & Petrov, I. Interface microstructure engineering by high power impulse magnetron sputtering for the enhancement of adhesion. *Journal of Applied Physics* **101** (2007).

105. Gudmundsson, J. T. Ionization mechanism in the high power impulse magnetron sputtering (HiPIMS) discharge. *Journal of Physics: Conference Series* **100,** 082013 (2008).

106. Butler, A. *et al.* On three different ways to quantify the degree of ionization in sputtering magnetrons. *Plasma Sources Science and Technology* **27,** 105005 (2018).

107. Huo, C. *et al.* On sheath energization and Ohmic heating in sputtering magnetrons. *Plasma Sources Science and Technology* **22,** 045005 (2013).

108. Huo, C. *et al.* Particle-balance models for pulsed sputtering magnetrons. *Journal of Physics D: Applied Physics* **50,** 354003 (2017).

109. Rossnagel, S. M. Gas density reduction effects in magnetrons. *Journal of Vacuum Science & Technology A* **6,** 19 (1988).

110. Huo, C. *et al.* Gas rarefaction and the time evolution of long high-power impulse magnetron sputtering pulses. *Plasma Sources Science and Technology* **21,** 045004 (2012).

111. Hala, M., Viau, N., Zabeida, O., Klemberg-Sapieha, J. E. & Martinu, L. Dynamics of reactive high-power impulse magnetron sputtering discharge studied by time- and space-resolved optical emission spectroscopy and fast imaging. *Journal of Applied Physics* **107,** 043305 (2010).

112. Oks, E. & Anders, A. Evolution of the plasma composition of a high power impulse magnetron sputtering system studied with a time-of-flight spectrometer. *Journal of Applied Physics* **105,** 093304 (2009).

113. Mishra, A., Kelly, P. J. & Bradley, J. W. The evolution of the plasma potential in a HiPIMS discharge and its relationship to deposition rate. *Plasma Sources Science and Technology* **19,** 045014 (2010).

114. Konstantinidis, S., Dauchot, J. P., Ganciu, M., Ricard, A. & Hecq, M. Influence of pulse duration on the plasma characteristics in high-power pulsed magnetron discharges. *Journal of Applied Physics* **99,** 013307 (2006).

115. Anders, A., Čapek, J., Hála, M. & Martinu, L. The recycling trap: A generalized explanation of discharge runaway in high-power impulse magnetron sputtering. *Journal of Physics D: Applied Physics* **45,** 012003 (2012).

116. Hecimovic, A. & Ehiasarian, A. P. Time evolution of ion energies in HIPIMS of chromium plasma discharge. *Journal of Physics D: Applied Physics* **42,** 135209 (2009).

117. Kozyrev, A. V., Sochugov, N. S., Oskomov, K. V., Zakharov, A. N. & Odivanova, A. N. Optical studies of plasma inhomogeneities in a high-current pulsed magnetron discharge. *Plasma Physics Reports* **37,** 621 (2011).

118. Hecimovic, A. & von Keudell, A. Spokes in high power impulse magnetron sputtering plasmas. *Journal of Physics D: Applied Physics* **51,** 453001 (2018).

119. Maszl, C., Breilmann, W., Benedikt, J. & von Keudell, A. Origin of the energetic ions at the substrate generated during high power pulsed magnetron sputtering of titanium. *Journal of Physics D: Applied Physics* **47,** 224002 (2014).

120. Hecimovic, A. Anomalous cross-B field transport and spokes in HiPIMS plasma. *Journal of Physics D: Applied Physics* **49,** 18LT01 (2016).

121. Biskup, B. *et al.* Influence of spokes on the ionized metal flux fraction in chromium high power impulse magnetron sputtering. *Journal of Physics D: Applied Physics* **51,** 115201 (2018).

122. Poolcharuansin, P. & Bradley, J. W. Short- and long-term plasma phenomena in a HiPIMS discharge. *Plasma Sources Science and Technology* **19,** 025010 (2010).

123. Alami, J., Gudmundsson, J. T., Bohlmark, J., Birch, J. & Helmersson, U. Plasma dynamics in a highly ionized pulsed magnetron discharge. *Plasma Sources Science and Technology* **14,** 525 (2005).

124. Gudmundsson, J. T., Alami, J. & Helmersson, U. Spatial and temporal behavior of the plasma parameters in a pulsed magnetron discharge. *Surface and Coatings Technology* **161,** 249 (2002).

125. Macák, K., Kouznetsov, V., Schneider, J., Helmersson, U. & Petrov, I. Ionized sputter deposition using an extremely high plasma density pulsed magnetron discharge. *Journal of Vacuum Science & Technology A* **18,** 1533 (2000).

126. De Poucques, L. *et al.* Study of the transport of titanium neutrals and ions in the post-discharge of a high power pulsed magnetron sputtering device. *Plasma Sources Science and Technology* **15,** 661 (2006).

127. Pajdarová, A. D., Vlček, J., Kudláček, P. & Lukáš, J. Electron energy distributions and plasma parameters in high-power pulsed magnetron sputtering discharges. *Plasma Sources Science and Technology* **18,** 025008 (2009).

128. Poolcharuansin, P., Liebig, B. & Bradley, J. Plasma parameters in a pre-ionized HiPIMS discharge operating at low pressure. *IEEE Transactions on Plasma Science* **38,** 3007 (2010).

129. Čada, M., Hubička, Z., Adámek, P., Klusoň, J. & Jastrabík, L. Time-resolved plasma parameters in the HiPIMS discharge with Ti target in $Ar/O_2$ atmosphere. *Surface and Coatings Technology* **205,** S317 (2011).

130. Bradley, J. W., Bäcker, H., Kelly, P. J. & Arnell, R. D. Time-resolved Langmuir probe measurements at the substrate position in a pulsed mid-frequency DC magnetron plasma. *Surface and Coatings Technology* **135,** 221 (2001).

131. Gudmundsson, J. T., Sigurjonsson, P., Larsson, P., Lundin, D. & Helmersson, U. On the electron energy in the high power impulse magnetron sputtering discharge. *Journal of Applied Physics* **105,** 123302 (2009).

132. Sigurjónsson, P. *Spatial and temporal variation of the plasma parameters in a high power impulse magnetron sputtering (HiPIMS) discharge* Technical Report RH-14-2008. MA thesis (University of Iceland, 2008).

133. Druyvesteyn, M. J. Der Niedervoltbogen. *Zeitschrift für Physik* **64,** 781 (1930).

134. Lockwood Estrin, F., Karkari, S. K. & Bradley, J. W. Triple probe interrogation of spokes in a HiPIMS discharge. *Journal of Physics D: Applied Physics* **50,** 295201 (2017).

135. Hecimovic, A. *et al.* Probing the electron density in HiPIMS plasmas by target inserts. *Journal of Physics D: Applied Physics* **50** (2017).

136. Meier, S. M., Hecimovic, A., Tsankov, T. V., Luggenhölscher, D. & Czarnetzki, U. First measurements of the temporal evolution of the plasma density in HiPIMS discharges using THz time domain spectroscopy. *Plasma Sources Science and Technology* **27,** 035006 (2018).

137. Tsikata, S., Vincent, B., Minea, T., Revel, A. & Ballage, C. Time-resolved electron properties of a HiPIMS argon discharge via incoherent Thomson scattering. *Plasma Sources Science and Technology* **28,** 03LT02 (2019).

138. Raadu, M., Axnäs, I., Gudmundsson, J. T., Huo, C. & Brenning, N. An ionization region model for high-power impulse magnetron sputtering discharges. *Plasma Sources Science and Technology* **20,** 065007 (2011).

139. Stancu, G. D., Brenning, N., Vitelaru, C., Lundin, D. & Minea, T. Argon metastables in HiPIMS: validation of the ionization region model by direct comparison to time resolved tunable diode-laser diagnostics. *Plasma Sources Science and Technology* **24,** 045011 (2015).

140. Minea, T. M., Costin, C., Revel, A., Lundin, D. & Caillault, L. Kinetics of plasma species and their ionization in short-HiPIMS by particle modeling. *Surface and Coatings Technology* **255,** 52 (2014).

141. Revel, A., Minea, T. & Costin, C. 2D PIC-MCC simulations of magnetron plasma in HiPIMS regime with external circuit. *Plasma Sources Science and Technology* **27,** 105009 (2018).

142. Pfau, S. & Tichý, M. *Low Temperature Plasmas. Fundamentals, Technologies and Techniques* Second edition (eds Ellmer, K., Hippler, R., Kersten, H., Schmidt, M. & Schoenbach, K.) chap. 7 (Wiley-VCH, Berlin, 2008).

143. Schott, L. *Plasma Diagnostics: Electrical Probes* (ed Lochte-Holtgreven, W.) chap. 11 (North-Holland Publishing Company, Amsterdam, 1968).

144. Woods, R. C. & Sudit, I. D. Theory of electron retardation by Langmuir probes in anisotropic plasmas. *Physical Review E* **50,** 2222 (1994).

145. Bernstein, I. B. & Rabinowitz, I. N. Theory of electrostatic probes in a low-density plasma. *Physics of Fluids* **2,** 112 (1959).

146. Chen, F. F. Langmuir probe analysis for high density plasmas. *Physics of Plasmas* **8,** 3029 (2001).

147. Chudáček, O., Kudrna, P., Glosík, J., Šícha, M. & Tichý, M. Langmuir Probe Determination of Charged Particle Number Density in a Flowing Afterglow Plasma. *Contributions to Plasma Physics* **35,** 503 (1995).

148. Kramida, A., Ralchenko, Y., Reader, J. & NIST ASD Team. *NIST Atomic Spectra Database (version 5.6.1)* National Institute of Standards and Technology, Gaithersburg, 2018 (accessed August 8, 2019).

149. Aymar, M. & Crance, M. Theory of two- and three-photon ionisation of metastable helium atoms. *Journal of Physics B: Atomic and Molecular Physics* **13,** 2527 (1980).

150. Schott, L. *Plasma Diagnostics: The laser as a tool for plasma diagnostics* (ed Lochte-Holtgreven, W.) chap. 9 (North-Holland Publishing Company, Amsterdam, 1968).

151. Lobbia, R. B. & Gallimore, A. D. Temporal limits of a rapidly swept Langmuir probe. *Physics of Plasmas* **17,** 073502 (2010).

152. Savitzky, A. & Golay, M. J. Smoothing and Differentiation of Data by Simplified Least Squares Procedures. *Analytical Chemistry* **36,** 1627 (1964).

153. Buckman, S. J. & Lohmann, B. Low-energy total cross section measurements for electron scattering from helium and argon. *Journal of Physics B: Atomic and Molecular Physics* **19,** 2547 (1986).

154. Phelps, A. V. Cross Sections and Swarm Coefficients for Nitrogen Ions and Neutrals in $N_2$ and Argon Ions and Neutrals in Ar for Energies from 0.1 eV to 10 keV. *Journal of Physical and Chemical Reference Data* **20,** 557 (1991).

155. Godyak, V. A., Piejak, R. B. & Alexandrovich, B. M. Probe diagnostics of non-Maxwellian plasmas. *Journal of Applied Physics* **73,** 3657 (1993).

156. Usoltceva, M. *et al.* Theory of a cylindrical Langmuir probe parallel to the magnetic field and its calibration with interferometry. *Review of Scientific Instruments* **89,** 10J124 (2018).

157. Fantz, U. Basics of plasma spectroscopy. *Plasma Sources Science and Technology* **15,** S137 (2006).

158. Magnus, F. & Gudmundsson, J. T. Digital smoothing of the Langmuir probe I-V characteristic. *Review of Scientific Instruments* **79,** 073503 (2008).

159. Kersten, H., Deutsch, H., Steffen, H., Kroesen, G. M. W. & Hippler, R. The energy balance at substrate surfaces during plasma processing. *Vacuum* **63,** 385 (2001).

160. Desecures, M., de Poucques, L., Easwarakhanthan, T. & Bougdira, J. Characterization of energetic and thermalized sputtered atoms in pulsed plasma using time-resolved tunable diode-laser induced fluorescence. *Applied Physics Letters* **105,** 181120 (2014).

161. Konstantinidis, S., Dauchot, J., Ganciu, M. & Hecq, M. Transport of ionized metal atoms in high-power pulsed magnetron discharges assisted by inductively coupled plasma. *Applied physics letters* **88,** 021501 (2006).

162. Lundin, D., Helmersson, U., Kirkpatrick, S., Rohde, S. & Brenning, N. Anomalous electron transport in high power impulse magnetron sputtering. *Plasma Sources Science and Technology* **17,** 025007 (2008).

163. Lundin, D., Sahab, S. A., Brenning, N., Huo, C. & Helmersson, U. Internal current measurements in high power impulse magnetron sputtering. *Plasma Sources Science and Technology* **20,** 045003 (2011).

164. Bohlmark, J. *et al.* Measurement of the magnetic field change in a pulsed high current magnetron discharge. *Plasma Sources Science and Technology* **13,** 654 (2004).

165. Samuelsson, M. *Fundamental aspects of HiPIMS under industrial conditions* PhD thesis (Linköping University, 2012).

166. Thornton, J. A. Influence of apparatus geometry and deposition conditions on the structure and topography of thick sputtered coatings. *Journal of Vacuum Science and Technology* **11,** 666 (1974).

167. Bäcker, H., Bradley, J. W., Kelly, P. J. & Arnell, R. D. Using Langmuir probes to measure the plasma decay rates in pulsed RF magnetron discharges. *Journal of Physics D: Applied Physics* **34,** 2709 (2001).

168. Hechtl, E., Yang, H., Wu, C. & Eckstein, W. An experimental study of tungsten self sputtering. *Journal of Nuclear Materials* **176,** 874 (1990).

169. Lieberman, M. A. & Ashida, S. Global models of pulse-power-modulated high-density, low-pressure discharges. *Plasma Sources Science and Technology* **5,** 145 (1996).

170. Seo, S.-H., In, J.-H. & Chang, H.-Y. Temporal evolution of electron energy distribution function and plasma parameters in the afterglow of drifting magnetron plasma. *Plasma Sources Science and Technology* **14,** 576 (2005).

171. Lundin, D. *et al.* Cross-field ion transport during high power impulse magnetron sputtering. *Plasma Sources Science and Technology* **17,** 035021 (2008).

172. Wu, B. *et al.* Cu films prepared by bipolar pulsed high power impulse magnetron sputtering. *Vacuum* **150,** 216 (2018).

# Appendix A

# Circuit for externally triggering the laser flashlamps during HiPIMS

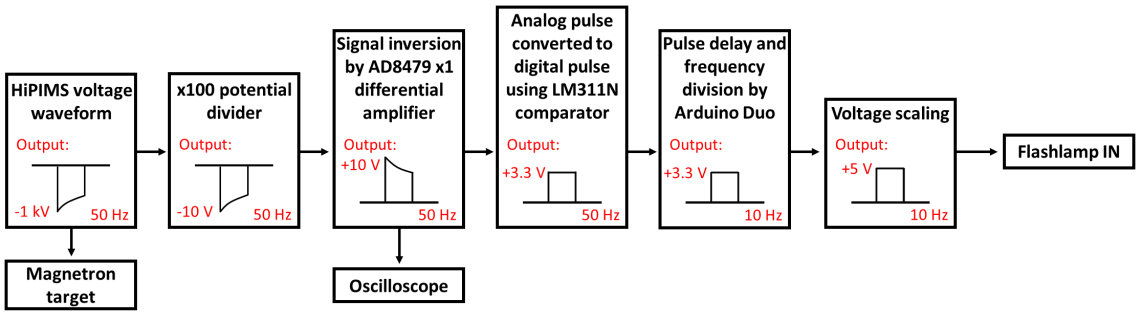


Figure A.1: Block diagram of the circuit that derives a trigger pulse for the laser flashlamps from the HiPIMS voltage waveform. The first stage is to attenuate the HiPIMS voltage using a potential divider in parallel with the connection to the target; next, the signal is inverted using a x1 differential amplifier; the analogue signal is converted to a digital signal using a comparator; a programmable Arduino Duo performs frequency division and adds an adjustable time delay; the final stage is to scale the output from the Arduino to 5 V.

# Appendix B

# Centre of mass energy

The centre of mass energy is given by [7, p. 54]:

$$W_R = \frac{m_1 m_2 v_R^2}{2(m_1 + m_2)}, \tag{B.1}$$

where $v_R$ is the relative speed between particles 1 and 2, and $m$ denotes mass. The relative speed satisfies:

$$v_R^2 = \mathbf{v}_R \cdot \mathbf{v}_R, \tag{B.2}$$

where $\mathbf{v}_R = \mathbf{v}_1 - \mathbf{v}_2$ is the relative velocity vector.

## B.1 $m_2 \gg m_1$

Consider particle 1 to be an electron and particle 2 to be an ion. Since $m_i \gg m_e$, the mean centre of mass energy is:

$$\langle W_R \rangle \approx \frac{m_e \langle v_R^2 \rangle}{2}. \tag{B.3}$$

Since the electron temperature ($T_e$) is much greater than the ion temperature ($T_i$), one can set the mean relative square speed to the mean electron square speed, $\langle v_e^2 \rangle$:

$$\langle W_R \rangle \approx \frac{m_e \langle v_e^2 \rangle}{2}. \tag{B.4}$$

For a Maxwellian velocity distribution, the mean electron square speed in three-dimensions is:

$$\langle v_e^2 \rangle = \frac{3k_B T_e}{m_e}, \tag{B.5}$$

where $k_B$ is the Boltzmann factor. Hence:

$$\langle W_R \rangle \approx \frac{3k_B T_e}{2}. \tag{B.6}$$

## B.2 $m_1 = m_2$

Consider the case of two identical ions ($m_1 = m_2 = m_i$). The mean centre of mass energy is:

$$\langle W_R \rangle \approx \frac{m_i \langle v_R^2 \rangle}{4}. \tag{B.7}$$

The mean relative square speed is:

$$\langle v_R^2 \rangle = \langle \mathbf{v}_1 \cdot \mathbf{v}_1 \rangle - 2\underbrace{\langle \mathbf{v}_1 \cdot \mathbf{v}_2 \rangle}_{=0} + \langle \mathbf{v}_2 \cdot \mathbf{v}_2 \rangle = 2\langle {v_i}^2 \rangle, \tag{B.8}$$

where $\langle {v_i}^2 \rangle$ is the mean square speed of the ion distribution (analogous to equation B.5 but with $T_e \to T_i$ and $m_e \to m_i$). The mean centre of mass energy is therefore:

$$\langle W_R \rangle \approx \frac{3k_B T_i}{2}. \tag{B.9}$$